University of Strathclyde

Department of Pure and Applied Chemistry

Functionalisation of Hollow Gold Nanospheres for use as Stable, Red-shifted SERS Nanotags in Bio-imaging

By

Samantha Moreton

A thesis submitted to the Department of Pure and Applied Chemistry, University of Strathclyde, in fulfilment of the requirements for degree of Doctor of Philosophy.

2016

This thesis is the result of the author's original research. It has been composed by the author and has not been previously submitted for examination which has led to the award of a degree.

Signed: Date:

Acknowledgements

Firstly, I would like to thank my supervisors Professor Duncan Graham and Professor Karen Faulds for their support, guidance and for the opportunity to carry out this research.

I would like to acknowledge the Defence Science and Technology Laboratory (DSTL) for providing funding and advice. In particular I would like to thank Professor Neil Shand for all the helpful discussions and encouragement throughout the project. I extend my thanks to Matthew Bedics and Professor Michael Detty at the University at Buffalo for providing the Raman reporters used within this thesis.

I would like to say a huge thank you to all the members of the Centre for Molecular Nanometrology for all their help and advice and for all the fun times. I would particularly like to thank Dr. Samuel Mabbott for electron microscopy analysis and for help with thesis corrections and Corinna Wetherill for performing cell culture and incubation. To Alexandre Girard, 'merci beaucoup' for all your help particularly with the PCA and cell mapping work. I would also like to thank Hayleigh and Tara for all the work and non-work related chats, especially within those last six stressful months. Last but definitely not least I would like to say a massive thank you to my best pal Dr. Kirsten Gracie not only for correcting my entire thesis but for pushing me through the tough times and most importantly for always being there.

Finally, I would like to thank my amazing family for their continued support in everything I do. To my brother Ryan, for always knowing just what to say to put things into perspective and for being proud even if he doesn't always show it. To Steven, for his endless love and support, for helping me through my weakest moments and always making me smile. Most of all I would like to thank my mum and dad for always believing in me, I wouldn't have come as far as I have today without your love and encouragement and I will always be grateful to you for that.

Abstract

Hollow gold nanospheres (HGNs) exhibit a unique combination of properties, in particular their tunable localised surface plasmon resonance (LSPR) from the visible to near infrared (NIR), which provide great scope for their use in many biomedical applications. However, they are highly unstable to changes in their surrounding environment and have a tendency to aggregate, particularly when exposed to high salt concentrations or changes in pH which is not ideal for applications such as bio-imaging and drug delivery where stable solutions are required for efficient cellular uptake.

An improved method for stabilising HGNs which simultaneously shifts the LSPR from around 700 nm to 800 nm or greater has been developed. Three different materials which are commonly used as stabilising agents; polymers, sugars and silica have been compared in order to determine the optimum stabilising agent for use with HGNs. Results showed PEG to be the most suitable stabilising agent for HGNs displaying both an increased stability to changes in salt concentration and pH as well as increased long term stability in solution.

The stabilised HGNs developed were investigated as potential surface enhanced Raman scattering (SERS) substrates for the development of stable nanotags which could be used in future bio-applications. Using a newly synthesised class of chalcogenpyrylium reporter molecules SERS detection has been achieved at four different excitation wavelengths; 633 nm, 785 nm, 1064 nm, and 1280 nm. The stabilised nanotags displayed excellent stability and produced consistent, reproducible SERS spectra in varying external environments. Furthermore, their potential for use in future bio-applications has been demonstrated at 785 nm to provide a basis for future bio-imaging at longer wavelengths.

This combination of improved stability, with a LSPR in the NIR region along with SERS detection at longer wavelengths demonstrates the great potential for the nanotags developed within this work to be used in applications such as biological SERS imaging and drug delivery.

Abbreviations

APTMS	3-aminopropyl trimethoxysilane
AuNPs	gold nanoparticles
AZPY	4,4-azopyridine
BPE	1,2-bis(2-pyridyl)ethylene
CHO	Chinese hamster ovarian
Con A	concanavalin A
CoNPs	cobalt nanoparticles
CTAB	cetyltrimethylammonium bromide
DLS	dynamic light scattering
DMF	dimethylformamide
DNA	deoxyribose nucleic acid
EGFR	epidermal growth factor receptor
EM	electromagnetic
EtOH	ethanol
HER2	human epidermal growth factor receptor 2
HGNs	hollow gold nanospheres
IR	infrared
LSPR	localised surface plasmon resonance
MBA	mercaptobenzoic acid
MG-ITC	malachite green isothiocyanate
MPTMS	mercaptopropyl trimethoxysilane

MSH	α-melanocyte-stimulating hormone
N.A.	numerical aperture
Nd:YAG	neodymium-doped yttrium aluminium garnet
NIR	near infrared
NTA	nanoparticle tracking analysis
PAM	polyacrylamide
PBS	phosphate buffered saline
PCA	principal component analysis
PCs	principal components
PEG	polyethylene glycol
PEI	poly(ethyleneimine)
PTA	photothermal ablation therapy
PVP	poly(vinylpyrrolidone)
RRS	resonance Raman scattering
SEM	scanning electron microscopy
SERS	surface enhanced Raman spectroscopy
SERRS	surface enhanced resonance Raman spectroscopy
SHE	standard hydrogen electrode
SPR	surface plasmon resonance
TEM	transmission electron microscopy
TEOS	tetraethyl orthosilicate

Contents

1 Introduction

Nanotechnology represents an intriguing area of research involving nanomaterials which are extensively studied due to their unique optical, electronic, physical and chemical properties.[1, 2] In particular, gold nanoparticles (AuNPs) exhibit a range of properties including high surface to volume ratios and low toxicity which, along with their ease of functionalisation, has facilitated their use in many potential applications including biomedical diagnostics, drug delivery, and catalysis.[3-5]

1.1 Metallic Nanostructures

Metallic nanostructures generally range in size from 1 nm to 100 nm and possess a number of unique physical and chemical properties compared to their bulk metal counterparts.[2, 6, 7] One of their most intriguing aspects is their plasmonic properties which are directly dependent upon the size and shape of the nanomaterials.[8, 9] The ability to tune their optical properties provides scope for use in a wide variety of applications including biological imaging and sensing,[10-12] drug delivery,[13, 14] and photothermal imaging and therapy.[15-17]

1.1.1 Plasmonic Optical Properties

Nanomaterials consisting of the coinage metals, such as gold, silver and copper, display a strong surface plasmon band in their extinction spectra due to their unique interaction with incident light. This surface plasmon resonance (SPR) arises due to the collective oscillation of valence electrons on the surface of the nanoparticle which occurs in the presence of an applied electric field (Figure 1.1).[18, 19]

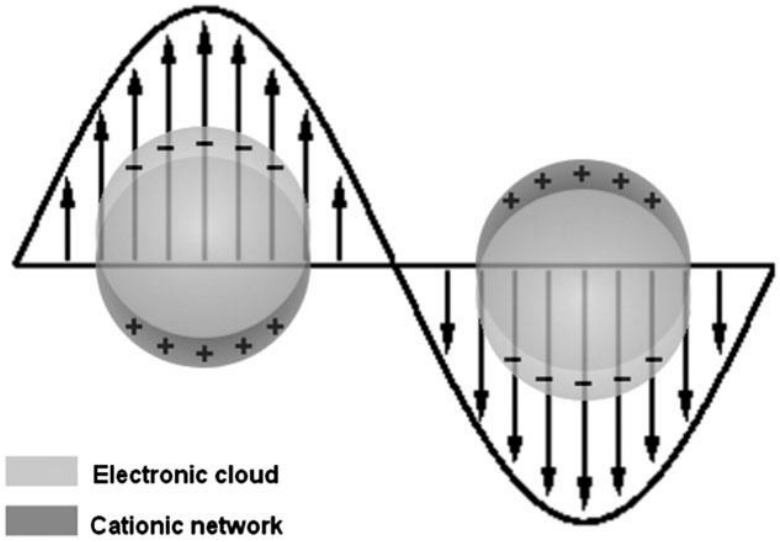

Figure 1.1: Schematic representation of the electron cloud displacements in nanoparticles under an applied electric field.[19] Reproduced from Ref. 19 with permission from the Centre National de la Recherche Scientifique (CNRS) and The Royal Society of Chemistry.

Extinction spectra (a combination of scattering and absorption) of spherical particles can be described and interpreted by Mie theory.[20, 21] It specifies that the resulting SPR is sensitive to changes in size, shape, and particle homogeneity as well as the dielectric constant of the surrounding media. As a result, changes in nanoparticle functionality can be closely monitored using extinction spectroscopy.[17, 21]

In spherical particles all modes are degenerate and result in a single plasmon resonance, however in more complex nanostructures such as nanorods or core/shell nanoparticles nondegenerate bands may arise and form multiple bands over a broad spectral range.[22]

1.1.2 Core/Shell Nanoparticles

In order to maximise the potential applications for metallic nanostructures, broad tunability in SPRs from the visible to the near infrared (NIR) region of the electromagnetic spectrum is required. This is achieved through controlling the size and shape of nanoparticles, thus allowing control of their optical properties. Solid nanoparticles such as silver and gold have a single resonance at around 400 nm and 520 nm respectively.[23] These can only be varied slightly through changes in size or dielectric environment and therefore have limited versatility.[23] Greater control of

optical properties was initially reported in core/shell systems.[24] These systems are composite nanoparticles which consist of a dielectric nanoparticle core coated with a thin metallic shell and typically have SPRs which can shift to much longer wavelengths by varying the core size and shell thickness.[25, 26] For example, silver shell-silica core particles can exhibit SPRs in the range of 500-750 nm while gold shell-silica core particles can display SPRs greater than 800 nm.[26] As a result, these nanostructures are ideal for use in therapeutic and photothermal applications where NIR absorption is desirable for greater tissue penetration.[25, 27, 28] Additionally, control of optical properties is beneficial in surface enhanced Raman scattering (SERS) based applications as the SERS enhancement factor is maximised when the SPR is in resonance with the excitation frequency.[29, 30]

Following this initial work, numerous metallic nanostructures based on biocompatible gold nanoparticles which possessed highly tunable SPRs were developed and are discussed in the following sections.

1.1.3 Hollow Gold Nanospheres (HGNs)

Hollow gold nanospheres (HGNs) are unique nanostructures which consist of a thin gold shell with a hollow interior.[23] They possess a highly tunable SPR, where careful control of particle size and wall thickness during the synthesis can result in SPRs from 550 nm to 1320 nm.[23, 31, 32] This is a notable advantage over solid gold nanoparticles which have a SPR absorption of between 510 nm to 560 nm depending on size.[33] This tunability to near-IR (NIR) wavelengths along with their small size and spherical shape makes HGNs of great interest for use in many potential biomedical applications including photothermal ablation therapy (PTA) and drug delivery.[17, 34] Their NIR SPR also gives them great scope for use as substrates in surface-enhanced Raman scattering (SERS) which is a highly sensitive spectroscopic technique used to detect molecules in close proximity to a metal surface.[35] For further discussion on SERS refer to Section 1.3.3.

1.1.3.1 HGN Synthesis

HGNs are synthesised via a galvanic reaction; reacting template nanoparticles with a gold salt solution.[36] Previously, silver nanoparticles have been used as sacrificial templates in the synthesis[37-39] however more recently methods have been developed using cobalt nanoparticles (CoNPs).[23, 31] It is the latter of these two methods which was used for the HGNs synthesised within this research.

A simplified schematic of the main processes involved in the synthesis is illustrated in Figure 1.2. In brief, CoNPs are formed by reacting $CoCl_2$ with $NaBH_4$ which reduces Co^{2+} to Co^0. Gold shells are then formed via a galvanic reaction before the solution is exposed to air, oxidising any remaining CoNPs from the inner core, and resulting in a hollow interior.

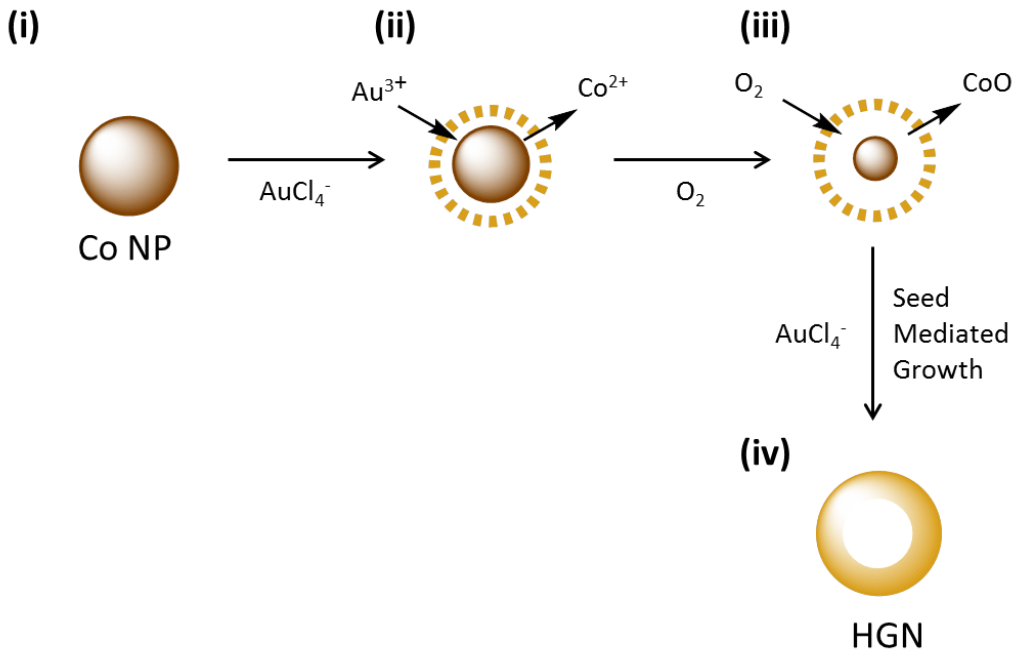

Figure 1.2: A schematic representation of the main stages involved in HGN synthesis. (i) Cobalt nanoparticles (CoNPs) function as sacrificial templates; (ii) reduction of $AuCl_4^-$ by CoNPs resulting in formation of initial porous gold shell; (iii) oxidation of remaining CoNPs following exposure to air; and (iv) complete shell formation through seed mediated growth.[9, 40]

In 2005, the first HGNs synthesised using CoNPs as sacrificial templates were reported by Liang et al.[31] The galvanic reaction takes place because the reduction

potential of the $AuCl_4^-$/Au redox couple (0.935 V *vs* standard hydrogen electrode (SHE)) is much higher than that of the Co^{2+}/Co redox couple (-0.377 V *vs* SHE). As a result the Au^{3+} ions will be reduced to Au^0 atoms almost instantaneously on exposure to the CoNP templates.[31] The redox equation for the galvanic reaction that takes place is shown in equation 1.1.

$$3Co + 2AuCl_4^- \rightarrow 2Au + 3Co^{2+} + 8Cl^- \qquad (1.1)$$

The reduced Au atoms will then begin to form a thin shell around the CoNPs, which will be porous at first to allow the diffusion of both Co^{2+} and $AuCl_4^-$ across the shell. A secondary reaction, whereby Co is continually oxidised by H^+ from the $HAuCl_4$ solution, takes place in combination with the galvanic reaction to result in complete oxidation of the Co core.[31] The thickness of the gold shell increases inwards as more gold salt is reduced, therefore as a result of this growth mechanism the outer diameter of the resultant HGNs is determined by the size of the initial CoNP templates. The shell thickness or inner core shell diameter is solely dependent on the ratio of $HAuCl_4$ to reducing agents.[23] Therefore, the outer diameter and shell thickness of the resulting HGNs can be controlled within each synthesis which in turn leads to varied optical properties as will be discussed in the following section. Consequently, the formation of the initial template CoNPs is an integral part within the synthesis of these nanostructures.[31, 41]

Schwartzberg et al. investigated the different parameters which control initial CoNP size and therefore the outer diameter of the resulting HGNs.[23] CoNPs are formed by the reduction of cobalt chloride with sodium borohydride in the presence of sodium citrate. In the standard preparation of gold colloid, sodium citrate is used as the reducing agent[42] however, the cobalt salt is relatively stable and consequently a much stronger reducing agent is required. In this instance, the citrate is alternatively employed as the capping agent to prevent the formation of aggregates.[23] Due to the strength of the reducing agent used it is imperative that complete reduction of Co^{2+} has taken place before the gold salt is added. This is to ensure that the gold salt is reduced by the CoNPs as opposed to the sodium borohydride, to begin formation of the gold shell. It was found that altering the citrate concentration did little to affect the size of the CoNPs and that the particle size was more dependent on the rate of

reduction, as kinetic processes will dominate due to the strength of sodium borohydride reducing agent. The most effective method for controlling the reaction rate and hence particle size was found to be the alteration of the sodium borohydride concentration. A reduction in the amount of sodium borohydride added will increase particle size due to an increase in reaction time. However, if the concentration is too low the particles formed will be highly unstable and the sodium citrate concentration will also need to be changed. This is because as the reaction rate slows it will become more thermodynamically driven and the capping agent will become a more significant factor as only as many seed particles can form as can be stabilised by the citrate.[23]

As the CoNPs are extremely sensitive to oxygen the entire synthesis must be completed under an inert atmosphere. CoNP oxidation prior to gold shell formation will lead to the formation of inhomogeneous HGNs which are undesirable for future applications such as cellular imaging or SERS.[23] However, this property is utilised in the final stage of the synthesis to ensure complete removal of Co remaining in the interior cavity. Exposure to air subsequent to the formation of the gold shell allows for the oxidation of the Co core by O_2, this along with the initial oxidation of Co across the porous shell will allow for complete removal of the Co from the nanostructure resulting in the hollow interior.[31]

Following complete removal of CoNPs from the inner core, complete shell formation is achieved through seed mediated growth. Porous HGNs can act as seeds which function as nucleation centres for the reduction of Au^{3+} by sodium citrate,[31] which normally occurs in boiling solutions.[43] This will result in full shell formation when excess gold salt is present following complete removal of CoNPs, and in turn more porous structures when less gold salt is present. The resultant effect on the optical properties of the HGNs is discussed in the following section.

1.1.3.2 HGN Properties

As previously mentioned, one of the most useful properties hollow gold nanospheres (HGNs) possess is the broad tunability of their surface plasmon resonance (SPR) achieved through control of particle diameter and shell thickness during the

synthesis. The effect of different aspect ratios on resultant SPRs of the HGNs has been reported (Figure 1.3). Generally, HGNs with SPRs in the NIR region tend to have larger particle diameters and thinner shells than HGNs at lower wavelengths which are slightly smaller in size with thicker outer shells.[23] The reason thicker shells shift to higher energies can be attributed to the fact that as the shell becomes thicker the HGNs become more characteristic of solid AuNPs which have approximate SPRs of 520 nm.[23] Additionally, HGNs with SPRs at longer wavelengths exhibit broader extinction spectra that were reported to be a result of the increased number of aggregates, due to less stabilising agent being available to stabilise the larger HGNs, and inhomogeneity within the red-shifted particles.[23, 40]

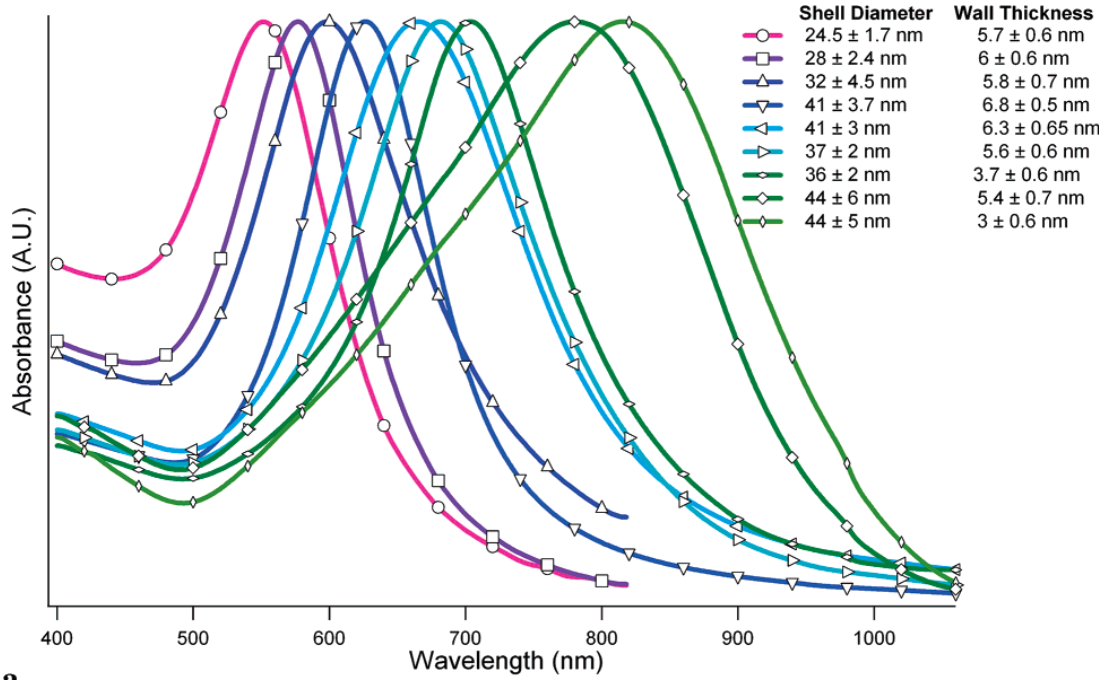

Figure 1.3: Extinction spectra of nine HGN samples with varying aspect ratios (detailed in the legend).[23] Adapted with permission from A. M. Schwartzberg, T. Y. Oshiro, J. Z. Zhang, T. Huser and C. E. Talley, Anal Chem, 2006, 78, 4732-4736. Copyright (2006) American Chemical Society.

More recently, HGNs with SPRs of 1320 nm have been reported.[32] In addition to a slight increase in particle size compared to HGNs at lower wavelengths, it was reported that they exhibited extremely porous structures with hole sizes of up to 25 nm. These less well-defined structures also contribute to the broader extinction spectra exhibited at longer wavelengths.[32]

Optical properties can also be altered by aggregation of HGNs, normally induced by addition of a simple inorganic salt which screens the Coulombic repulsion energy between the nanoparticles.[44] HGN aggregation profiles vary significantly from those of solid metallic nanoparticles, exhibiting a dampening in SPR along with a shift to shorter wavelengths as opposed to the red-shift in SPR expected in solid spherical nanostructures. The blue shift observed is a result of interparticle coupling between the aggregates where surface electrons can delocalise over multiple particles forming a new SPR which is similar to that of solid gold nanoparticles.[45] This results from a change in electron-phonon scattering lifetimes in each of the systems. Isolated HGNs possess an SPR which arises from electrons contained within an extremely thin outer shell resulting in ultrafast electron-phonon coupling times. Upon aggregation, interparticle coupling initiates electron scattering over multiple particles which increases the electron-phonon coupling time to a value similar to that for solid AuNPs.[45]

Further beneficial properties exhibited by HGNs include small size and spherical shape. HGNs with a NIR SPR have been synthesised in the region of 30 – 90 nm by careful control of the particle size and wall thickness during the synthesis.[23, 32] This is particularly beneficial for biological imaging applications where monodisperse nanoparticles below 100 nm in size are required for efficient cellular uptake.[46] A notable advantage over the core/shell systems where nanoshells with red-shifted SPRs can be up to 200 nm in diameter which hinders cellular uptake.[47]

1.1.3.3 HGN Applications

The combination of unique properties exhibited by HGNs has led to their use in a range of applications including sensitive SERS-based immunoassays,[48, 49] drug delivery,[34, 50] photothermal ablation therapy,[51] and pH sensing.[52]

Surface-enhanced Raman scattering (SERS) is a highly sensitive spectroscopic technique used to detect molecules in close proximity to a metal surface.[35] HGNs display greater sensitivity and consistency in SERS based applications than their solid counterparts.[52] This can be attributed to the ability to achieve single particle SERS from HGNs with an outer diameter of 30 nm which removes the need for

induced aggregation to form 'hot-spots' (areas of highly localised electromagnetic fields) which can lead to inconsistent results.[52] This increased enhancement is likely to derive from pinholes and surface roughness in the HGNs,[23] however as the HGNs become more red-shifted and the pinholes increase in size, this effect is somewhat reduced as the surface cavities are considered too large to produce an enhancement in the surface electric field.[32] In addition, SERS enhancements can also result from the greater extension of the electromagnetic field in metallic shells compared to solid nanoparticles.[53]

HGNs are very popular for use in photothermal therapies due to their ability to convert incident photons into heat allowing for use in non-invasive treatment of cancerous tissue.[51, 54] Their tunability to NIR wavelengths allows for selective heating of cancerous tissues with minimal damage to healthy tissues that contain organic chromophores, which absorb in the visible region and are therefore transparent to NIR irradiation.[25, 51] Targeted therapy can be achieved by functionalising HGNs with an antibody that is specific to the tumour that is to be targeted, resulting in specific cell death in the desired area. Once the functionalised HGNs bind to the tumour, NIR light can be applied to the tissue causing localised heating and subsequently cell death. Using this method the surrounding tissue will contain no HGNs and so no damage will occur to healthy cells.[9, 27] The HGN response to NIR irradiation can also be utilised in drug delivery applications where short intense bursts of NIR light will allow for controlled release of drugs at desired sites.[54]

1.1.4 Related Structures

There are many other forms of gold nanostructures reported in the literature, which have been somewhat more extensively studied than HGNs. These range from solid gold nanoparticles through to gold nanocages creating a diverse range of applications due to the varied optical properties associated with these different types of nanostructure.

1.1.4.1 Gold Nanoworms

Gold nanoworms are an interesting extension of the hollow gold nanospheres. Successful synthesis of gold nanoworms was achieved by exposing the HGNs to an electromagnetic field during their synthesis. This results in a chain of connected HGNs with partial tube-like formation but where the gold wall is still present between each nanoparticle in most cases (Figure 1.4).[36]

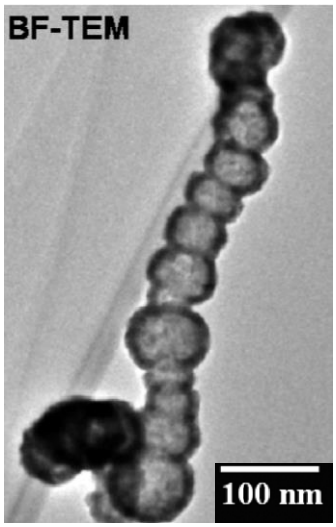

Figure 1.4: Bright field TEM image of single nanoworm chain with darker outlines highlighting the presence of thin walls between the individual HGNs.[36] Adapted with permission from H. Xie, I. A. Larmour, V. Tileli, A. L. Koh, D. W. McComb, K. Faulds and D. Graham, J. Phys. Chem. C, 2011, 115, 20515-20522. Copyright (2011) American Chemical Society.

It was initially proposed that the interaction between the individual HGNs could provide sufficient 'hot-spots' to enhance the SERS signals of these nanostructures. However, the significant SERS signal enhancements provided by these structures were found to be a result of the interaction between several nanoworms and not the individual particles due to the absence of gaps between each HGN that are required to provide effective areas of localised electromagnetic enhancements.[36]

1.1.4.2 Gold Nanorods

Gold nanorods are generally synthesised by seed-mediated synthesis. The nanorod is built up from gold seed particles, which are formed by the reduction of a gold salt

solution by a strong reducing agent such as sodium borohydride. Resulting seed particles are then added to a growth solution containing gold salt with a weaker reducing agent such as ascorbic acid and cetyltrimethylammonium bromide (CTAB) which is used as both a template to direct rod formation and as the stabilisation agent for these nanostructures.[42, 55] Due to the elongated shape of these nanostructures two absorption bands will be observed in the extinction spectra as opposed to the single resonance observed for solid spherical nanospheres. This is because the induced dipole can oscillate along two axes; the longitudinal mode and the transverse mode. The longitudinal mode has a lower energy and is therefore more red-shifted than the weaker transverse mode which is usually resonant at around 520 nm.[23, 56] By varying the amount of gold seeds with respect to the gold precursor the nanorod aspect ratio can be controlled to tune wavelengths of the nanostructures which can span most of the visible and NIR regions of the electromagnetic spectrum.[57] This control of the optical properties gives these nanorods the potential for applications in sensing and nanophotonics.[23]

1.1.4.3 Gold Nanocages

Gold nanocages represent an intriguing area for investigation with similar properties to HGNs. They possess a tunable SPR, hollow interiors and porous outer shells similar to those observed in extreme red-shifted HGNs.[32, 58] They are synthesised by galvanic replacement of a silver nanocube template with a gold salt solution based on the spontaneous reaction in Equation 1.2.[58, 59]

$$3Ag + AuCl_4^- \rightarrow Au + 3Ag^+ + 4Cl^- \qquad (1.2)$$

Similar to HGNs the SPR can be tuned in the region of 600 to 1200 nm by simply controlling the amount of gold solution added to the reaction to determine the wall thickness of the nanocage.[58] As this lies within the optimum region for *in vivo* applications due to the increased tissue penetration at these wavelengths,[25, 60] these nanostructures are ideal for use in biomedical applications in addition to SERS based applications.[58] Analogous to HGNs they possess beneficial photothermal properties for use in cancer therapy and can also act as drug delivery systems due to the porous nature of the outer wall.[58, 61]

1.1.5 Nanoparticle Characterisation

Effective techniques for nanoparticle characterisation are required to maximise their impact in potential applications. As previously stated, the characteristic SPR in metallic nanoparticles is sensitive to changes in size, shape, and particle homogeneity and therefore changes in nanoparticle functionality can be closely monitored by extinction spectroscopy.[17, 21] Other techniques commonly employed to characterise nanoparticles include zeta potential, particle sizing and scanning electron microscopy (SEM).

1.1.5.1 UV-Visible (Extinction) Spectroscopy

When particles are exposed to incident light, the photons can either be absorbed and converted to heat energy or re-radiated as scattered light or both.[62] Gold nanoparticles will both absorb and resonantly scatter visible and NIR light,[63] a combination of which is known as light extinction.[62, 64] Extinction spectra, therefore, describe a combination of absorption and scattering properties of the sample. The spectra observed are highly dependent on particle sizes,[63, 65] with the intensity of scattering with respect to absorption increasing as the size increases from 20 to 80 nm.[64] AuNPs with a diameter smaller than 20 nm essentially show absorption, with negligible scattering observed.[64]

Extinction spectroscopy can also provide the molar extinction coefficient (ε) value of a particle if the concentration is known. The molar extinction value is constant for a given molecule at a given wavelength and can be calculated using the Beer-Lambert Law (Equation 1.3) where A is the absorption value at λ_{max}, ε is the molar extinction coefficient, c is the concentration of the nanoparticle solution and l is the distance the light travels through the solution.[66]

$$A = \varepsilon c l \tag{1.3}$$

Additionally, nanoparticle concentrations can be determined through extinction spectroscopy if the molar extinction value is known. This is useful in spherical gold nanoparticles where molar extinction values are readily available within the literature

however no such study has been undertaken using HGNs. Therefore, alternative methods for determining concentrations are required such as Nanoparticle Tracking Analysis (NTA) described in Section 7.4.3.

1.1.5.2 Zeta Potential

Zeta potential is a measurement of nanoparticle stability in terms of the degree of repulsion of charged particles in a colloidal suspension. Around each particle there exists an inner region, or Stern layer, of tightly bound ions and an outer layer, or diffuse region, of ions which are less firmly attached. Within the diffuse layer there is a boundary known as the slipping plane where ions will move with (if inside the boundary) the particle. The potential difference at this boundary is known as the zeta potential and is calculated by determining the electrophoretic mobility of the nanoparticles through electrophoresis. Stable colloidal suspensions exhibit high zeta potential values in the region of ±30 mV, where repulsion is sufficient to maintain a stable dispersion. However when the zeta potential values are between 0 and ±5 mV attraction forces will dominate and the colloidal suspension will flocculate.[67, 68]

1.1.5.3 Particle Sizing

The size of nanoparticle suspensions can be measured by a technique known as dynamic light scattering (DLS). DLS measures the Brownian motion[69] of nanoparticles and through analysing the intensity of the fluctuations in the scattered light from the incident laser the relative size of the nanoparticles can be determined using the Stokes-Einstein equation (Equation 1.4) where D is the diffusion constant, k_B is the Boltzmann's constant (1.38×10^{-23} JK^{-1}), T is the absolute temperature, η is the dynamic viscosity and r is the hydrodynamic radius.[68]

$$D = k_B T/6\pi\eta r \qquad (1.4)$$

As DLS measures the diameter of the sphere around a particle that diffuses at the same velocity as the measured particle, otherwise known as the hydrodynamic diameter, measurements are only suitable for relative comparisons.[68] For direct measurement of the metallic radius of nanoparticles other techniques such as

scanning electron microscopy (SEM) or transmission electron microscopy (TEM) are required.

1.1.5.4 Scanning Electron Microscopy (SEM)

In SEM the sample to be imaged is irradiated with a focused electron beam resulting in the production of backscattered electrons, secondary electrons and other photons which can be used to determine the sample's surface topography, composition and crystallography among others. Topographic images can be obtained for magnifications of 10 – 10, 000 x and for materials ranging from nanometer (nm) to micrometer (μm) in size.[70] Images can subsequently be used to determine the metallic radius of nanoparticles using complementary software such as ImageJ.

1.2 Nanoparticle Functionalisation

In order to exploit the advantageous properties of nanoparticles for use in bioapplications, the surface functionality needs to be carefully controlled to provide both stability and biocompatibility to the nanostructures. Currently, gold nanoparticles (AuNPs) have been widely functionalised with a range of materials including silica, polymers and sugars, however minimal work has been reported on the functionalisation of HGNs. The following section will review some of the main materials commonly employed for nanoparticle stabilisation and biocompatibility.

1.2.1 Surface Chemistry and Stability

Control of the surface chemistry of metallic nanoparticles is a fundamental aspect in both improving colloidal stability and enabling a diverse range of future applications. Citrate stabilised colloids have a tendency to aggregate when exposed to changes in external environment such as high salt concentrations, changes in pH or due to the presence of biological molecules.[71] Although aggregation can prove advantageous in applications based on biomolecular binding events or SERS, nanoparticles must be readily dispersed within solution to allow for effective cellular uptake and reproducibility in SERS signals.[35, 46]

Stabilisation of nanoparticles is predominately achieved through either charge or steric approaches.[72] Charge stabilisation creates stable dispersions based on electrostatic repulsion, frequently utilised in nanoparticle synthesis where citrate is added to provide added surface stability. Citrate stabilised nanoparticles can remain stable for many years however changes in external conditions such as the addition of salt can induce aggregation through charge screening effects.[44, 72] Steric stabilisation is achieved through surface functionalisation with polymers and occurs when the size of the polymer exceeds the London interaction range. In polymer coated particles salt will not induce nanoparticle aggregation, therefore this stabilisation method is preferred for use in future applications.[72] For increased stability, charge and steric stabilisation can be combined, a property observed in DNA functionalised AuNPs.[73]

The majority of functionalised gold surfaces exploit the widely developed gold-thiolate chemistry available.[74-77] The sulfhydryl group (SH) in thiols has a high affinity for gold surfaces and when deprotonated will form a strong covalent bond with a strength similar to that of the gold-gold bond.[76] Protonated SH groups can only react through the sulphur lone-pair electrons by weaker coordinative bonding.[76]

Alkylamines are another surface ligand commonly used to functionalise gold nanoparticles. They can bind electrostatically through the protonated amine and the anionic gold surface or through a weaker covalent interaction than that for gold-thiolate bonds.[78-80]

1.2.2 Sugar Functionalisation

There is little evidence within the literature for work on sugar functionalisation of HGNs however a significant contribution has been made in this area using solid gold nanoparticles.

The majority of work published has focused on functionalisation using thiocarbohydrate derivatives, and most predominantly thioglucose, due to the strength of the gold-sulphur bond created.[81, 82] Watanabe et al. reported the first thioglucose-capped gold nanoparticles. These were prepared by using

1-thio-β-$_D$-glucose as both the reducing and stabilising agent to yield nanoparticles similar to those shown in Figure 1.5.[83]

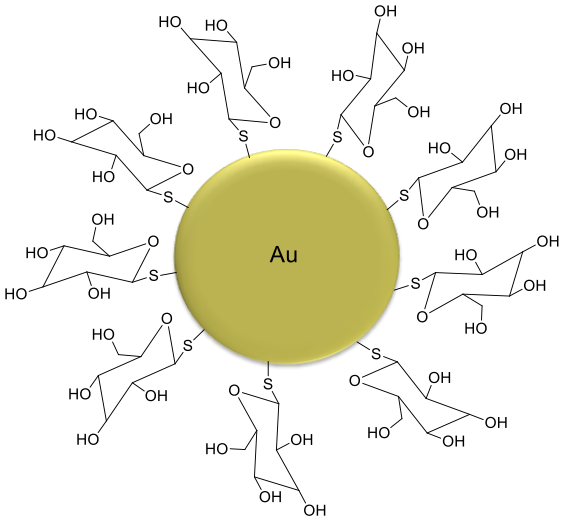

Figure 1.5: Schematic representation of thioglucose-capped gold nanoparticles.[83] Adapted from S. Watanabe, H. Seguchi, K. Yoshida, K. Kifune, T. Tadaki and H. Shiozaki, Tetrahedron Lett., 2005, 46, 8827-8829. Copyright (2005), with permission from Elsevier.

The layer of sugar molecules surrounding the nanoparticles provides a hydrophilic monolayer which should aid stabilisation against aggregation.[17, 83] The covalent bond between thioglucose and the nanoparticle surface should also provide an increased stabilisation to unmodified nanoparticles which are stabilised through the weaker electrostatic interaction with citrate.[84]

This initial work led to the development of a number of different methodologies for the production of thioglucose-capped nanoparticles. One commonly used procedure uses sodium borohydride as the reducing agent and thioglucose as the stabilising agent as opposed to citrate.[85, 86] This alternative methodology has the potential to be used for HGN functionalisation, through alteration of only the capping agent in the synthesis.

Glucose capped nanoparticles are readily taken up by cancer cells at a much faster rate than in healthy tissues and remain localised within the cytoplasm, which allows for applications including targeted cancer therapy and diagnosis.[84, 85, 87]

Polysaccharides, such as dextran, have also been widely studied as lectin-carbohydrate interactions play integral roles in many biological processes and they can therefore be used in diagnostic applications.[88] Concanavalin A (Con A) is one such lectin which is known to have an affinity for both glucose and polysaccharides and with four binding sites it can potentially cross-link at least two dextran coated nanoparticles resulting in aggregation of the samples. [89, 90] This interaction is not only important in biological applications but the potential to control the aggregation of dextran coated gold nanoparticles or HGNs could be beneficial in SERS characterisation of these nanostructures.

The main diagnostic use for dextran modified gold nanoparticles is for glucose sensing in the detection of diabetes. The mechanism of action of these sensors is based on the lectin-carbohydrate interactions. Addition of Con A to dextran coated gold nanoparticles leads to the formation of aggregates as previously described, however it was found that addition of glucose to these aggregated systems caused a change in the absorbance spectrum observed for the samples. This was thought to be due to a dissociation of aggregates when the glucose is added, as it will cause competitive dissociation from the glycoligand. Thus, the presence of glucose in a sample can easily be observed through changes in absorbance.[90-92]

1.2.3 Polymer Coatings

Polymers have long been used as effective stabilisation agents in the synthesis of nanoparticles. Coating gold nanoparticles in a polymer shell has previously been shown to improve long term stability and increase their stability to high salt concentrations similar to those found *in vivo*.[93, 94] In addition to this, the polymer shell can provide a good platform for further functionalisation, providing an additional advantage for their biological applications.[95]

There are an abundance of polymers frequently used for nanoparticle stabilisation, including; polyethylene glycol (PEG), polyvinylpyrrolidone (PVP), polyethyleneimine (PEI) and polyacrylamide (PAM), all of which can provide advantageous properties for use in future biomedical applications.

PEG is a linear polymer composed of $–CH_2CH_2O-$ repeating units and is commercially available in a vast range of molecular weights, however longer chain lengths have previously been reported to show an increased stability over shorter chains.[96] For effective conjugation to the gold surface, thiol modified PEG is most commonly used and has been shown to be compatible for use in SERS studies as it will not displace Raman reporters or other small molecules from the nanoparticle surface.[94, 97]

Salt environments *in vivo* are around 155 mM, thus nanoparticles that can remain stable at concentrations higher than this are particularly desirable in SERS based applications where stability against aggregation can improve the consistency in the measured signals. PEG has been found to be effective at maintaining nanoparticles' stability at concentrations greatly exceeding this value. For instance, silver nanoparticles functionalised with thiol-PEG-5000 have a reported stability in up to 2 M NaCl.[94]

As a result of the long term stability the PEG layer provides to AuNPs, the resultant functionalised nanoparticles are ideal for use in drug delivery systems as they are able to circulate within the body for long periods of time without degradation of the system or dissociation of molecules from the nanoparticle surface.[98]

Recently research has moved towards hollow gold nanospheres, the combination of high stability afforded by PEG along with the photothermal properties associated with HGNs is an attractive property for use in drug delivery and drug therapy.[17, 54] As an example, HGNs stabilised with PEG have been used in photothermal therapy of tumours. As the PEG layer can easily be further functionalised the HGN-PEG complex can be linked to an agonist of a specific tumour to promote uptake at the site that requires treatment. α-Melanocyte-stimulating hormone (MSH) is an agonist for the melanocortin type-1 receptor, which is overexpressed in melanoma. This agonist has been linked to pegylated HGNs to actively target melanoma for efficient photothermal therapy to take place.[17]

PVP is the other commonly used hydrophilic polymer for stabilisation and further conjugation. It has been reported that gold nanoparticles encapsulated with PVP have

an enhanced stability to organic solvents compared to unmodified particles. Gold nanoparticles prepared through the reduction of Au^{3+} in dimethylformamide (DMF) have utilised PVP as a stabilising agent with the resultant nanoparticles remaining readily dispersed and stable in ethanol for several months.[96]

Zhang *et al.*, showed that poly(vinylpyrrolidone) (PVP) can effectively stabilise HGNs resulting in both an increase in nanoparticle stability and a shift in SPR to longer wavelengths.[40] However, it was reported that this method solely worked for PVP and other polymers tested were unsuccessful.[40] This work has been expanded upon within Chapter 3.

Polymers less frequently used than PEG and PVP within nanoparticle functionalisation include PAM and PEI. Within the literature PAM has mainly been used as a coating for magnetic nanoparticles due to its low toxicity *in vitro*.[99] This allows for applications in molecular imaging, where PAM has been shown to be an effective imaging agent using MRI due to its high sensitivity which is a result of its high relaxivity.[100] Polyacrylamide nanoparticles have also been used as effective drug delivery systems, as they can be specifically targeted to cells through specific peptide conjugation or liposomal delivery, however they have also been reported to accumulate in cells after a sufficient period of time.[101] This allows for delivery of photosensitizers for use in photodynamic therapy and some initial *in vivo* success has been reported in this area.[101, 102]

PEI is a highly branched cationic polymer which contains primary, secondary and tertiary amines.[103] The cationic nature of this polymer allows for electrostatic binding to the negatively charged nanoparticle surface. This will in turn render the nanoparticle surface positively charged which is advantageous for a number of different applications.

PEI-coated nanoparticles have been widely reported in the literature as their cationic surface allows for effective cellular uptake and DNA binding.[103, 104] DNA binding occurs due to the positive charge on the PEI surface which can interact with negatively charged phosphate backbone of DNA molecules, this binding gives potential applications in gene therapy and nucleic acid delivery.[105] However, PEI

coated silver nanoparticles have been reported to be more toxic than both the citrate and PVP coated analogues and therefore there are some limitations with the use of PEI due to its cytotoxicity.[106] This cytotoxicity arises because PEI acts as a proton 'sponge', the primary amines of the polymer will buffer protons involved in proton pump activity within the cell. This will lead to an increase in proton pump activity and osmotic swelling, endosomal rupture and ultimately cell death will result.[105] This buffering effect could however prove useful in increasing nanoparticle stability to acidic solutions.[103] There are reports that the cytotoxicity of this polymer can be overcome while maintaining cellular uptake by using lower molecular weights of the polymer. Nel *et al.* demonstrated that low molecular weight PEI coated silica nanoparticles were effective delivery agents for the chemotherapeutic agent, paclitaxel, to pancreatic cancer cells without causing any toxicity *in vivo*.[105]

1.2.4 Silica Encapsulation

Silica is a chemically inert material, which can provide an alternative source of stabilisation to metallic nanoparticles and it's highly understood surface chemistry can be further manipulated to produce nanostructures with a high biocompatibility. Other properties that make silica an excellent coating material for nanoparticles are its high stability to most organic solvents and its optical transparency which allows for spectroscopic monitoring of surface chemical reactions.[107-109] Previous studies have shown that silica encapsulated gold nanoparticles are stable in both aqueous and organic solvents whereas their unmodified counterparts readily aggregate when dispersed in organic solvents. Additionally, the silica shell can provide an efficient layer of protection for small molecules attached to the nanoparticle surface. This is a particularly useful property in SERS based applications as Raman reporter molecules adsorbed on to the nanoparticle surface will be protected from displacement by other molecules and desorption of these reporters over time will also be prevented. Therefore, an increased long term stability of these nanotags has been reported with high spectroscopic activity maintained after long term storage of the nanoparticles.[110, 111]

The first reported synthesis of silica encapsulated gold nanoparticles was published by Mulvaney *et al.* in 1996.[112] Gold nanoparticles are commonly stabilised with anionic agents such as citrate to prevent aggregation however this makes the surface vitreophobic and therefore it will have little affinity for silica. In order to render the gold nanoparticles vitreophilic, in other words receptive towards silica, silane coupling agents such as 3-aminopropyltrimethoxysilane (APTMS) or 3-mercaptopropyltrimethoxysilane (MPTMS) are initially conjugated to the nanoparticle surface. Monolayer coverage of these vitreophilising agents serves two purposes; firstly to render the surface suitable for silica growth and secondly to provide added stability allowing the nanoparticles to withstand the harsh conditions necessary for silica growth.

In Mulvaney's early methodology sodium silicate was then added; the silanol groups acted as starting points for growth of the initial layer of the silica shell.[112] To produce thicker shells, condensation of additional silica particles onto the initial glass layer using the Stöber method is required.[113] This involves the base-catalysed hydrolysis of tetraethyl orthosilicate (TEOS) (Equation 1.5) to give monodisperse silica particles, which then condense (Equation 1.6) onto the preformed silica layer. This is achieved by using an alcohol/ammonia mixture where the ammonia acts as the catalyst for the hydrolysis.[108, 113] The reaction scheme presented (Equations 1.5 and 1.6)[114, 115] is a simplified version of the complex condensation which takes place in the formation of the silica particles ($R=C_2H_5$ when TEOS is used as the alkoxysilane).

$$Si(OR)_4 + H_2O \xrightarrow[\text{Alcohol}]{NH_3} (OR)_3Si(OH) + ROH \qquad (1.5)$$

$$(OR)_3Si(OH) + H_2O \xrightarrow[\text{Alcohol}]{NH_3} SiO_2\downarrow + 3ROH \qquad (1.6)$$

More recently, PEG has been utilised as an alternative to the silane coupling agents in the synthesis. Liz-Marzán *et al.* reported that methoxy-poly(ethylene glycol)-thiol (mPEG-SH) could be used as an alternative coupling agent prior to shell growth by the standard Stöber process. A layer of PEG surrounding AuNPs or gold nanorods of

various sizes provides sufficient stabilisation to prevent nanoparticle aggregation on transfer to ethanolic solutions.[116]

1.3 Raman Spectroscopy

Raman spectroscopy provides an alternative technique for molecular diagnostic detection to the more widely used fluorescence based methods. Fluorophores exhibit a number of drawbacks, which limits their detection capabilities including photobleaching and the production of broad, overlapping emission spectra in multiplexed experiments. Raman scattering can overcome these limitations by producing unique fingerprint spectra with narrow peak widths allowing for the simultaneous detection of multiple analytes, while Raman tags can resist photobleaching.[117, 118]

1.3.1 Raman Scattering

Raman scattering is a form of vibrational spectroscopy, which measures the inelastic scattering of light from an analyte molecule. When photons of light interact with a molecule they can either be absorbed, scattered, or pass through the molecule without any interaction.[119] The molecular vibrations that result from light absorption are monitored in infrared (IR) spectroscopy. Absorption will occur when the energy of the incident photon is equal to the difference in energy between the ground state and first vibrational excited state of a molecule. For molecules to be IR active they must have a permanent dipole which is altered by molecular vibrations and therefore asymmetric vibrations are most intense in the observed signals.[119] Light which is scattered is monitored in Raman spectroscopy and occurs in polarisable molecules where symmetric vibrations produce the strongest signals.[119] Initial studies on the scattering of light focussed on a process known as Rayleigh scattering, which is an elastic process where scattered photons will be radiated with no change in energy from the incident light.[120] The first observation of Raman scattering was reported by Raman and Krishnan in 1928 and can be described as an inelastic process where scattered radiation was found to have a higher or lower energy to that of the incident light.[121]

When light interacts with a molecule, the electron cloud is polarised resulting in the formation of a short-lived virtual state. Scattering occurs when the distorted electron cloud relaxes. The majority of the scattered light will undergo Rayleigh scattering, which involves the distortion of the electron cloud without affecting the nucleus and results in minimal changes in frequency. When nuclear motion is induced Raman scattering occurs where energy is either transferred from the incident photon to the molecule (Stokes scattering) or from the molecule to the scattered photon (anti-Stokes scattering). A summary of the energy level transitions which occur during absorption and scattering processes is illustrated in Figure 1.6.[119]

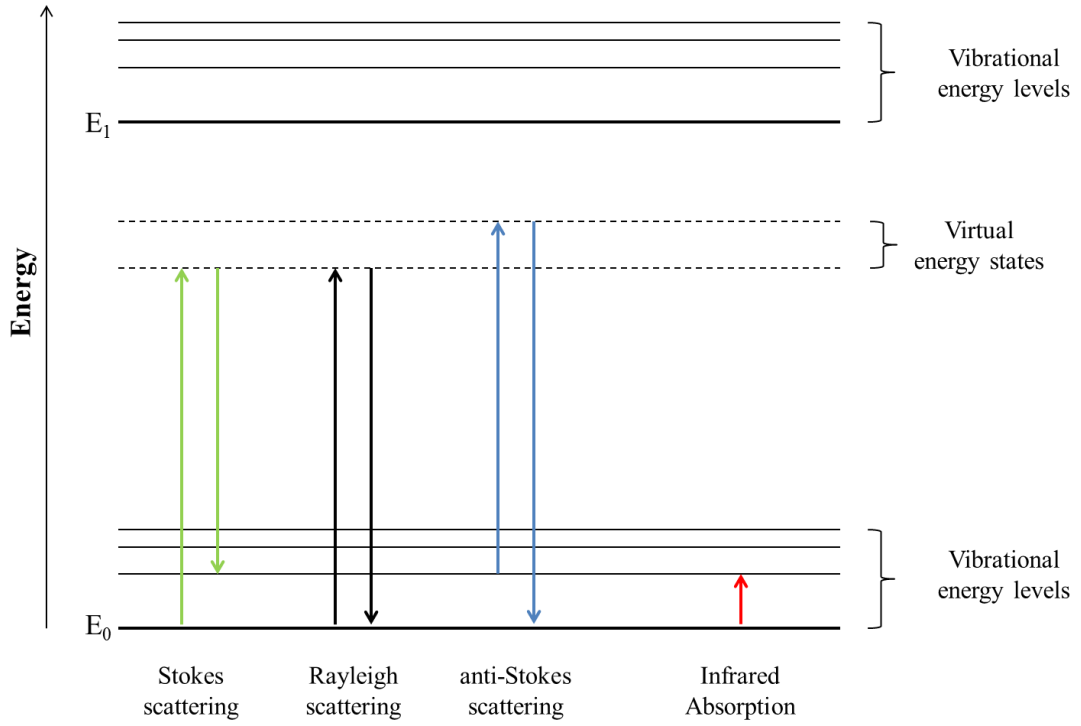

Figure 1.6: A Jablonski diagram representing the energy transitions which occur in scattering and absorption processes.

In Stokes scattering energy is absorbed from incident photons, resulting in promotion of the molecule to a higher energy vibrational state and scattering at a lower energy than that of the incident photons. Under normal circumstances a higher proportion of molecules will be found in the lowest energy ground vibrational state and therefore Stokes is the stronger and more widely used of the two Raman processes. A change in conditions such as the introduction of thermal energy will result in a higher

proportion of molecules residing in a higher energy vibrational state before interaction with a photon. This results in anti-Stokes scattering where energy is lost from the molecule and transferred to the scattered photon on return to the ground state.[119] The measurement of anti-Stokes scattering is preferred when Stokes scattering is masked by fluorescence interference.

The ratio of the intensities of Stokes and anti-Stokes scattering can be calculated using the Boltzmann distribution equation (Equation 1.7) where N_1 is the number of molecules in the excited energy state E_1, N_0 is the number of molecules in the ground energy state E_0, g is the degeneracy of the levels, ΔE is the difference in energy between states E_1 and E_0, k is the Boltzmann's constant (1.3807×10^{-23} JK^{-1}) and T is temperature (K).[119]

$$\frac{N_1}{N_0} = \frac{g_1}{g_0} e^{\left[\frac{-\Delta E}{kT}\right]} \tag{1.7}$$

The peaks in a Raman spectrum represent the shift in energy between the incident laser beam and the scattered energy (Raman shift) and correspond to vibrational modes within the analyte molecule. The total number of vibrations for a particular molecule is related to the number of atoms in the molecule and the frequency of the vibration is resultant on the bond strength and mass of the atoms involved.

Raman scattering is a relatively weak process as only one in every 10^6-10^8 photons is Raman scattered. As the intensity is dependent on the fourth power of the excitation frequency, shorter laser excitation wavelengths are desirable for the production of intense Raman spectra however at high energy sample degradation and fluorescence can result.[119] This has led to successive developments in Raman spectroscopy including resonance Raman, SERS and SERRS, which allow for improvements in signal intensity at longer wavelengths.

1.3.2 Resonance Raman Scattering (RRS)

By using an incident laser line that has an energy which corresponds to the frequency of an electronic transition within a molecule the intensity of the Raman bands can be enhanced by a factor of 10^3-10^4 in a process known as resonance Raman scattering.[119]

RRS differs from Raman scattering in that the absorption of a photon results in the excitation of a molecule to the vibrational energy levels of the first excited state as opposed to the virtual excited state. As a result, more intense spectra are observed as vibrations associated with electronic transitions within a molecule are greatly enhanced. However, co-occurrence of fluorescence is a significant issue within this technique and results in high fluorescence backgrounds in the resulting spectra. It is possible to minimise this interference by using a pulsed laser or by monitoring the anti-Stokes scattering as previously mentioned.[119, 122, 123]

1.3.3 Surface Enhanced Raman Scattering (SERS)

Surface enhanced Raman scattering (SERS) is a highly sensitive spectroscopic technique which exploits the optical properties of metallic nanostructures to overcome the limitations of RRS and provide significant spectral enhancements from analyte molecules in close proximity to a metal surface.[35, 119] The first observation of SERS was reported by Fleischmann *et al.* in 1974.[124] They reported an enhancement in Raman signals from pyridine molecules adsorbed on a roughened silver electrode whereas the use of a smooth silver electrode did not yield the same enhancement.[124] The enhancement mechanism was not immediately apparent and was initially attributed to an increase in surface area of the roughened silver electrode however this was soon disputed as it was proposed that the signal enhancement observed was too large to be solely attributed to an increased surface area and was in fact a result of surface enhancement from the metallic electrode.[125, 126] To date it is generally widely accepted that the enhancement arises from a combination of both electromagnetic and chemical effects.

1.3.3.1 Electromagnetic Enhancement

Electromagnetic (EM) enhancement is the dominant enhancement mechanism in SERS, which arises when localised surface plasmon resonances (LSPRs) on a metal surface are excited.[119, 127] Laser irradiation on a metallic nanoparticle surface will induce oscillation of the LSPRs which will increase the surface electromagnetic field and substantially enhance the polarisation experienced by analyte molecules in close proximity to the metallic surface.[128] When the LSPR of the metallic substrate is in resonance with the incident laser the plasmon oscillates perpendicular to the surface and a further enhancement can be observed. Controlled aggregation of nanoparticles is commonly employed to further enhance the SERS signals achieved. The interaction between nanoparticles results in 'hot-spots', which are areas of highly localised electric fields which can result in SERS enhancements of up to 10^{11} with respect to conventional Raman scattering.[129]

1.3.3.2 Chemical Enhancement

Chemical enhancement, or the charge transfer effect, is a result of the formation of a bond between the analyte and the surface, which allows for charge transfer between the two components. It is thought that on formation of the bond the incident radiation is absorbed by the metal and that this is followed by a charge transfer to the analyte and back to the metal before scattering occurs. As a result, the polarisability of the analyte molecule is greatly increased which subsequently increases the scattering and signal intensities observed.[119, 130]

1.3.4 Surface Enhanced Resonance Raman Scattering (SERRS)

Surface-enhanced resonance Raman scattering (SERRS), first reported by Stacy *et al.* in 1983, can result in further electronic enhancements when a reporter molecule in resonance with the excitation laser is used.[131, 132] SERRS is effectively a combination of both RRS and SERS and it is therefore reasonable to assume that the enhancement

mechanism can be explained by both surface enhancement and through enhancement from molecules in resonance with the interrogating laser frequency. Enhancement factors using this technique have been reported to be as high as 10^{14} when compared to normal Raman scattering.[119]

This technique overcomes the fluorescence limitations associated with resonance Raman as the metallic nanoparticle substrates will quench any fluorescence emission and additionally the intense Raman peaks will dominate over any background fluorescence signal in the spectra. As a result of the increased sensitivity of this technique the measurement can be obtained at lower laser powers and with reduced acquisition times, which significantly reduces the risk of sample degradation.

1.4 Bio-imaging using Raman and SERS

The application of Raman and SERS spectroscopies in the detection of specific biological species and interactions within biological environments has significantly progressed in recent years. This is attributed to the molecularly specific detailed information that can be obtained in comparison to alternative bio-imaging techniques such as fluorescence and magnetic resonance imaging and is also due to successive improvements in instrument sensitivity.[133]

1.4.1 Raman bio-imaging

Raman is a non-invasive analysis technique which has been used to identify cellular components[134] and for discrimination between healthy and cancerous cells (Figure 1.7).[135]

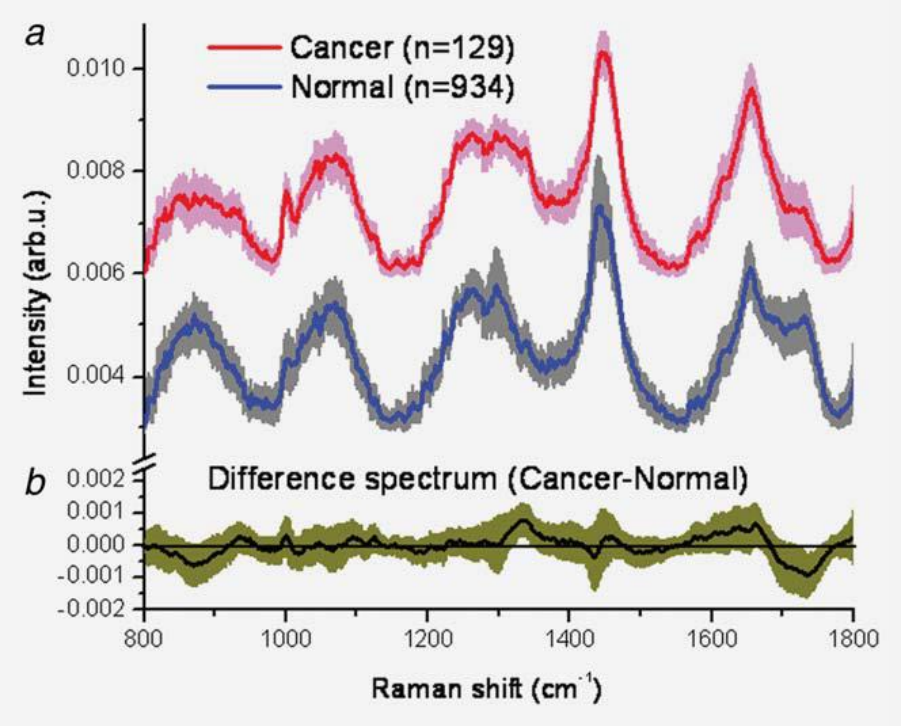

Figure 1.7: Discrimination between normal and cancerous gastric tissues at 785 nm laser excitation; (a) *In vivo* average Raman spectra of normal (red) and cancerous (blue) gastric tissues, and (b) corresponding difference spectrum calculated from the average Raman spectra between normal and cancerous tissues.[135] M. S. Bergholt, W. Zheng, K. Lin, K. Y. Ho, M. Teh, K. G. Yeoh, J. B. Yan So and Z. Huang, Int. J. Cancer, 2011, 128, 2673-2680. Copyright (2011) The Union for International Cancer Control (UICC).

Additionally, Raman spectroscopy used in combination with multivariate analysis techniques can be used to identify different pathologies and types of tissues with high specificity and sensitivity.[135-137] It is important to note that these studies were carried out using NIR laser excitation wavelengths. This is because at NIR wavelengths there is a significant reduction in tissue autofluorescence and an increase in water absorption which allows for deeper light penetration depths compared to visible excitation sources.[137, 138]

The sensitivity of this technique can be further improved *via* Raman enhancement techniques described within the previous section. Resonance Raman spectroscopy has been effectively utilised for the analysis of haemozoin in malaria diagnosis.[139] Introduction of metallic nanoparticle based systems can also result in large signal enhancements through SERS.

1.4.2 SE(R)RS bio-imaging

The sensitivity in bio-imaging afforded by SERS renders this technique particularly suitable for analysis of complex biological systems. The majority of the work reported within SERS imaging is based on solid gold nanoparticles however the emphasis within the following sections will be placed on hollow gold nanospheres (HGNs), which allow for biological imaging within the transparent NIR sensing window.

1.4.2.1 Nanoparticle uptake and cell toxicity

Metallic nanoparticles used within SERS imaging, particularly those composed of gold, are generally considered to be biocompatible materials.[140, 141] However, the level of toxicity can vary depending on the surface chemistry, charge and size of the nanoparticles.[142] Goodman *et al.* reported that cationic gold nanoparticles were more toxic than their anionic counterparts and it was proposed that the interaction of cationic nanoparticles with the anionic cellular membrane could result in membrane disruption.[142, 143]

To further improve biocompatibility, coatings such as PEG can be added to the nanoparticle surface which can improve absorption and blood circulation times and decrease immunogenic responses.[144, 145] You *et al.* reported that HGNs coated with a layer of PEG and a mean diameter of 63 nm displayed no adverse toxicity within kidney or liver cells after a 48 hour incubation period.[146]

Intracellular imaging studies require efficient nanoparticle uptake into cells, which can occur through direct interaction with membrane receptors or through indirect association with the plasma membrane. Cellular uptake is then subsequently achieved through various forms of endocytosis.[147] Direct interaction is achieved by functionalising the nanoparticles with specific ligands that selectively target the cell surface. To provide an example, HGNs modified with an anti-epidermal growth factor receptor (EGFR) antibody can be selectively engulfed by cancer cells, which exhibit overexpression of EGFR on the cell surface. The efficient nanoparticle uptake subsequently resulted in the effective destruction of the tumour cells both *in*

vivo and *in vitro* by photothermal ablation therapy.[51] Indirect interaction does not require functionalisation with specific targeting ligands as it involves the interaction of nanoparticles with the membrane by hydrophobic and electrostatic interactions.[147]

Additionally, passive diffusion mechanisms can result in efficient cellular uptake, particularly in tumour cells where blood vessels exhibit increased porosity. PEG coated gold shell-silica core nanoshells around 130 nm in diameter have been shown to preferentially accumulate in tumour cells over normal tissues due to this enhanced permeability in tumour vessels.[148]

1.4.2.2 *In vitro* and *in vivo* SERS imaging applications

In biological SERS imaging, detection of analytes can be achieved through direct detection methods where the characteristic SERS spectrum of the analyte is produced or through indirect detection methods where the SERS spectrum of the Raman reporter in the nanoparticle tags is used to determine the presence of the analyte.[149] As a result of its high sensitivity and specificity SERS imaging has been utilised in a wide variety of applications including the determination of different cellular components,[133] intracellular pH sensing,[150] and for tumour targeting and detection.[151]

Indirect cellular imaging of human epidermal growth factor receptor (HER2) which is over expressed in breast cancer tissues has been achieved using antibody conjugated HGNs functionalised with crystal violet to produce a Raman spectrum (Figure 1.8). This result demonstrated selective targeting to cancerous tissues and supports the use of HGNs in combination with SERS imaging to sensitively detect cancer markers over expressed in cells.[152]

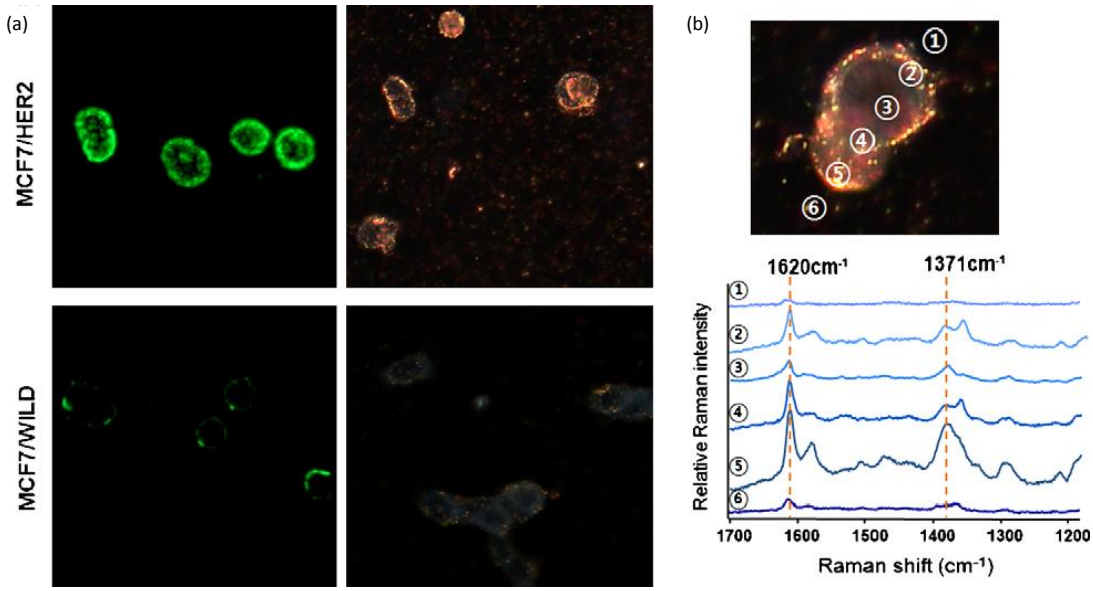

Figure 1.8: (a) Fluorescence and dark-field images of MCF7/WILD and MCF7/HER2 cells with quantum dot labelled fluorescence images on the left compared to HGN-labelled light scattering images on the right. (b) Raman profiles obtained at 633 nm excitation of an HGN-labelled MCF7/HER2 cell and corresponding Raman spectra at six different spots.[152] S. Lee, H. Chon, M. Lee, J. Choo, S. Y. Shin, Y. H. Lee, I. J. Rhyu, S. W. Son and C. H. Oh, Biosens. Bioelectron., 2009, 24, 2260-2263. Copyright (2009), with permission from Elsevier.

One drawback of using metallic nanoparticles is that they may undergo uncontrollable aggregation in biological environments that leads to inconsistencies in SERS results.[13] Therefore efforts should be made to address this; encapsulation of a stabilising layer such as PEG is frequently employed to prevent aggregation while allowing the reporter molecule to remain in close proximity to the metallic surface.

Antibody conjugated gold nanoparticles stabilised with a layer of PEG have been used for successful *in vivo* targeting of cancer cells at NIR excitation wavelengths (785 nm). In addition to targeted detection of tumour cells through EGFR, estimated penetration depths of 1-2 cm were reported.[151] (Figure 1.9)

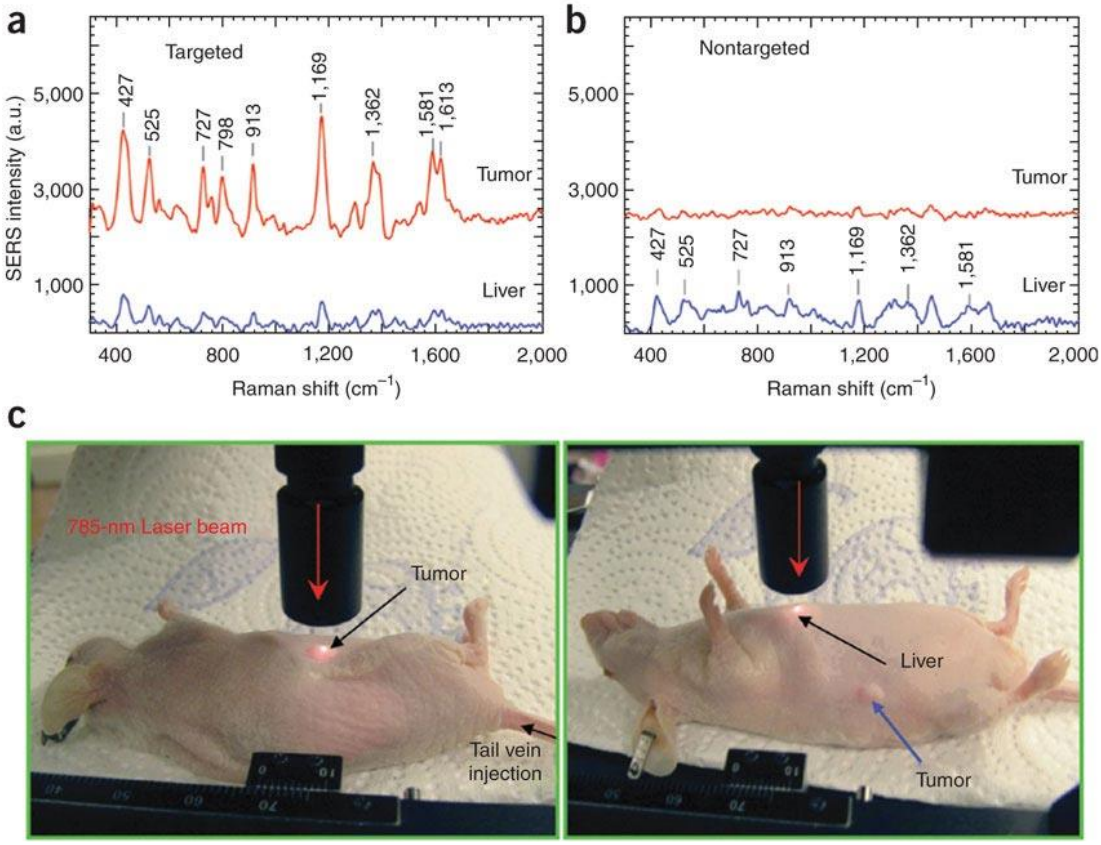

Figure 1.9: *In vivo* cancer targeting and SERS detection using antibody conjugated gold nanoparticles specific to the tumour biomarker EGFR. SERS spectra obtained from the tumour (red) and the liver (blue) locations by using targeted (a) and nontargeted (b) nanoparticles at a 785 nm excitation. Particles were administered to nude mice bearing head and neck squamous cell carcinoma (Tu686) xenograft tumour (3 mm diameter) via tail injection. (c) Photographs showing a laser beam focussed on the tumour site or on the liver.[151] X. Qian, X.-H. Peng, D. O. Ansari, Q. Yin-Goen, G. Z. Chen, D. M. Shin, L. Yang, A. N. Young, M. D. Wang and S. Nie, Nat. Biotechnol., 2008, 26, 83-90. Copyright (2008), permission from Nature Publishing Group.

Multiplexing capabilities associated with SERS allow for simultaneous detection of multiple analytes or components within a sample. *In vivo* detection of five distinct SERS markers has been reported using silica encapsulated gold nanoparticles,[153] while more recently SERS imaging and 3D Raman has been combined for multiple component detection of SERS nanotags.[133]

2 Aims

The principle aim of this thesis was to develop a stable SERS nanotag which had potential for use in bio-imaging applications within the uncongested spectral window of the NIR region. Hollow gold nanospheres (HGNs) represent a unique nanostructure with a highly tunable LSPR from the visible to the NIR region and were therefore considered ideal substrates for bio-imaging at longer excitation wavelengths. However, HGNs have a tendency to aggregate and are highly unstable to changes in their surrounding environment such as high salt concentrations or changes in pH, thus limiting their potential biological applications. Therefore, there is a significant need to find a suitable stabilising agent for HGNs which provides improved stability to a range of conditions whilst maintaining surface accessibility in order to render them suitable for use as stable, NIR active SERS substrates.

To achieve this objective the thesis was divided into two main sections. The main aim of the work within chapter 3 was to investigate the most suitable stabilising agent for use with HGNs. This initially involved the development of an improved method for stabilising HGNs with LSPRs in the NIR region. Three frequently used stabilising agents were to be evaluated for use with HGNs and their stability to changing external environments was to be systematically compared.

Chapter 4 aimed to investigate the suitability of the stabilised HGNs developed within chapter 3 as potential surface enhanced Raman scattering (SERS) substrates across a range of excitation wavelengths ranging from 633 nm to 1280 nm. The stability of the nanotags developed was then to be investigated in varying external environments using SERS. The final objective was to investigate the potential use of the stabilised nanotags developed within bio-imaging applications. This was to be evaluated at 785 nm with the aim of providing the basis for future work at longer excitation wavelengths where better penetration depths and reduced autofluorescence could be achieved.

3 Surface Functionalisation of Hollow Gold Nanospheres for Improved Stability

3.1 Introduction

Hollow gold nanospheres (HGNs) exhibit a unique combination of properties which provide great scope for their use in many potential biomedical applications including photothermal ablation therapy (PTA) and drug delivery.[17, 34] Along with their small size and spherical shape they possess a highly tunable surface plasmon resonance (SPR), where careful control of particle size and wall thickness during the synthesis can result in SPRs from 550 nm to 1320 nm.[23, 31, 32]

However, their use in these aforementioned applications may be hindered by the fact that they are highly unstable to changes in their surrounding environment and have a tendency to aggregate, particularly when exposed to high salt concentrations or changes in pH. Stability to changes in pH is of particular importance in biomedical applications due to the large variations in pH throughout the body, ranging from pH 2 in the stomach, pH 5.4 - 7.4 in cancerous tissues and pH 5 - 8 in the intestine.[154] Although aggregation can prove advantageous for applications such as surface-enhanced Raman scattering (SERS), uncontrolled aggregation will cause limited reproducibility in SERS signals.[35] Additionally, stable colloids are particularly desirable in applications such as drug delivery where monodispersed nanoparticles below 100 nm in size are required for efficient cellular uptake.[46]

There are a wide variety of materials frequently used to functionalise nanoparticles which provide increased stability and improved biocompatibility. For example, polymers such as polyethylene glycol (PEG) have previously shown to improve long term stability of gold nanoparticles and increase their stability to high salt concentrations similar to those found *in vivo*.[93, 94] In addition to this, the polymer shell can provide an ideal platform for further functionalisation, providing an added advantage for future bio applications.[95] Sugars such as thioglucose can enhance

cellular uptake and provide the nanoparticles with a hydrophilic monolayer which aids stabilisation against aggregation.[17, 83, 84] Silica is another excellent coating material for nanoparticles due to its highly understood surface chemistry which can be further manipulated to produce nanostructures with a high biocompatibility, as well as its high stability to most organic solvents and optical transparency.[108, 118, 155] Additionally, silica coated nanoparticles can maintain high spectroscopic activity after long term storage as the protective shell limits the desorption of Raman reporter molecules from the surface.[110, 111]

As previously mentioned in section 1.1, HGNs are generally stabilised by using citrate as a final capping agent however within this work it was found that citrate stabilised HGNs showed a degree of instability both over time and in response to external stimuli such as high salt concentrations or changes in pH. Previous work in this area, reported by Zhang *et al.*, showed that poly(vinylpyrrolidone) (PVP) can effectively stabilise HGNs.[40] PVP was added to stabilise cobalt nanoparticles (CoNPs) prior to the addition of gold in the synthesis in order to slow down the growth of the shell, resulting in both an increase in nanoparticle stability and a shift in SPR to longer wavelengths. However, it was reported that this method solely worked for PVP and other polymers tested were unsuccessful.[40]

The work in this chapter presents an improved methodology for stabilising HGNs which provides much more flexibility in stabilising agents which can be used compared to the previously published method,[40] allowing for tailoring to specific applications. This improved methodology not only provides stabilisation to the HGNs but also significantly shifts their SPR into the NIR region of the electromagnetic spectrum. A systematic investigation was then carried out to determine the most effective stabilising agent for use with HGNs which would provide improved stability under a range of conditions.

3.2 HGN Synthesis

Initial work focussed on the development of a general method for the synthesis of standard citrate stabilised HGNs which could subsequently be adapted to provide additional functionality and added stability to the nanostructures.

The method developed was modified from previously reported methods by varying the volume of cobalt chloride and sodium citrate used in the synthesis of the initial cobalt nanoparticle (CoNP) templates.[23, 35] This varied the particle diameter of the CoNP templates which ultimately determines the resultant HGN particle size. Schwartzberg *et al.* reported that HGNs with an LSPR at longer wavelengths will tend to have a larger particle diameter and thinner gold shell than those at shorter wavelengths. These are generally less stable, due to the reduction in the ratio of stabilising agent to gold shell, and less suited to further functionalisation.[23] With this in mind conditions were optimised in order to provide HGNs which had a relatively small particle diameter and corresponding thicker shell which would therefore be more stable, proving advantageous for further functionalisation. Under the conditions employed, standard citrate HGNs synthesised for this work typically had an LSPR of 700 ± 50 nm and a particle size of 63 ± 6.2 nm. Representative extinction spectra for four different batches of citrate stabilised HGNs synthesised using this methodology are shown in Figure 3.1.

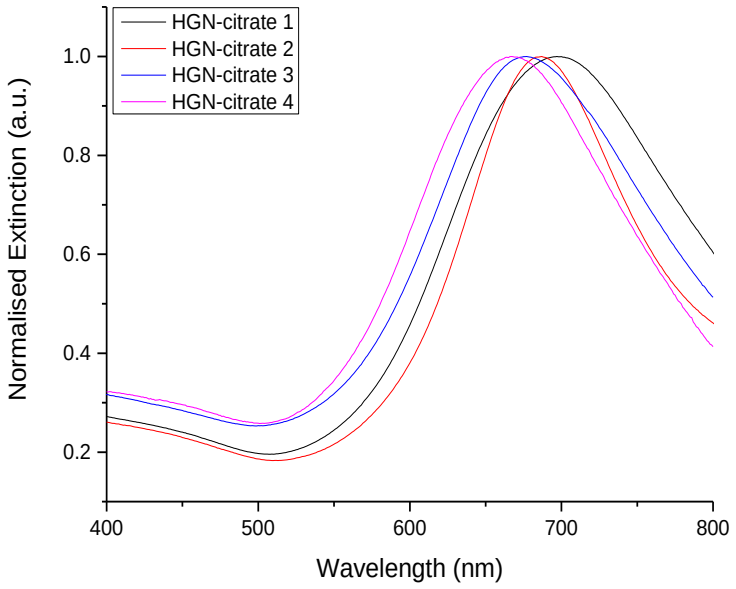

Figure 3.1: Normalised extinction spectra for four batches of citrate stabilised HGNs synthesised using the standard methodology developed.

As observed in Figure 3.1, one of the main limitations within the synthesis of HGNs is the limited inter-batch reproducibility. There are a number of factors which could explain the variation in LSPR observed between the different batches. The quality of the initial CoNPs as sacrificial templates will ultimately determine the quality of the HGNs produced. This stage of the synthesis is extremely sensitive to oxygen so it is imperative that the system is thoroughly deoxygenated before sodium borohydride ($NaBH_4$) is added to the reaction mixture as any air within the flask could cause oxidation of the CoNPs and an increase in inhomogeneity in the resultant HGNs will be observed. Secondly, slight deviations in shell thickness from batch to batch could be a result of slight variances in reaction time for CoNP formation or insufficient quenching of the $NaBH_4$ from the solution before the gold salt is added. If the $NaBH_4$ is not left to fully hydrolyse before addition of the gold salt then the gold will be reduced by the remaining $NaBH_4$ in solution as opposed to the CoNPs which in turn will lead to thinner shell formation and more red-shifted LSPRs. Additionally, deviations in reaction time for CoNPs to form before any remaining $NaBH_4$ is quenched from the solution will result in slight changes in particle diameter between batches and thus slight changes in the LSPR of the resultant HGNs. Finally, the rate at which the gold salt is added to the reaction mixture can have a significant effect on the shell thickness of the HGNs produced. When the gold salt is added to the reaction it will almost immediately react with the cobalt forming an initial shell around the CoNPs which will increase in thickness as more gold is reduced by excess citrate in solution. Hence, if the gold is added too slowly it will dilute quickly into the water and less will be reduced onto the cobalt producing thinner, less well formed shells. Conversely, if the gold is added too quickly this would result in a high concentration of gold being reduced on initial CoNPs and result in more overgrown shells. Therefore the gold must be added at a steady, consistent rate which is difficult to accurately control between each synthesis. Although every effort was taken in order to increase the reproducibility between each synthesis this was somewhat difficult to control. Therefore, HGNs synthesised with an LSPR of 700 ± 50 nm were considered a suitable foundation for further functionalisation within this work.

3.3 HGN Functionalisation

Preliminary efforts to functionalise the HGN surface with different stabilising agents investigated the reproducibility of previously published methods. There is extensive work in the literature on the functionalisation of gold nanoparticles, which can easily be modified through thiol, amino or carboxyl groups.[2, 156, 157] However, HGN functionalisation is limited to a few papers[40, 108] as the majority concentrate on application.[34, 54, 152] Due to the similar surface chemistries of the solid and hollow gold nanoparticles it was hoped that methods would be transferable however due to the level of instability of the hollow gold compared to solid gold this was unlikely.

3.3.1 Polymer and Sugar Functionalisation

Polymer coatings are commonly used to provide stability and prevent flocculation in colloidal systems. Initial work carried out followed protocols published for solid gold nanoparticles where polyethylene glycol (PEG) is conjugated to the nanoparticle surface using gold-thiol chemistry. The PEG referred to within this chapter is heterobifunctional, with thiol functionality on one end for affinity to the gold surface and carboxylic acid functionality on the other to provide potential for further conjugation, and has a molecular weight of 5000 unless otherwise stated.

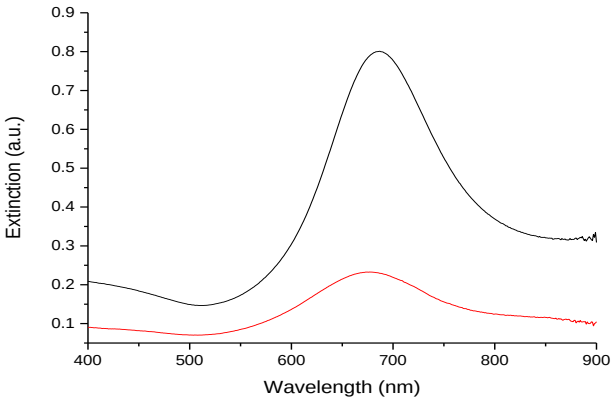

Figure 3.2: Extinction spectra of standard citrate HGNs (black) and citrate HGNs with added PEG (red) using initial method adapted from previously published methods for use with solid gold nanoparticles.

Results observed from these initial experiments (Figure 3.2) showed limited success. On addition of the PEG to the standard citrate stabilised HGNs there was a significant dampening and broadening in the extinction spectra, coupled with a blue shift in LSPR, all of which are characteristic signs that aggregation has taken place. Within these samples there were also some visible signs of aggregation after the final centrifugation step. Efforts were taken in order to try to modify the success of this method by decreasing the initial concentration of the PEG added so as to provide an initial stabilising layer on the HGN surface before additional PEG was added to create a monolayer. Additionally, varying centrifugation speeds were investigated in order to minimise any forced nanoparticle aggregation during final washing steps. However, due to limited success and varied results over multiple attempts it was concluded that due to the instability of the HGNs compared to solid gold nanoparticles, methods could not easily be transferred between the two nanostructures and alternative more efficient methods of functionalisation required investigation.

This led to the investigation of the reproducibility of a method previously published within the literature based on hollow gold where PVP was shown to effectively stabilise the HGN surface[40] and subsequently to the development of an improved methodology which provided much more flexibility in stabilising agents which can be used.[158] For clarity, a schematic diagram of the HGN synthesis modified with different stabilising agents at the final stage of the synthesis is shown in Figure 3.3. The method referred to as the sodium borohydride ($NaBH_4$) method is based on the work published by Zhang *et al.* where PVP is added to stabilise CoNPs (first step in the schematic) and the method denoted as the stabilising agent method was developed within this work and involves addition of the stabilising agent subsequent to the addition of gold in the synthesis as a final capping agent (final step in the schematic) and can be altered to be a number of different agents including PEG, polyacrylamide (PAM), dextran and thioglucose.

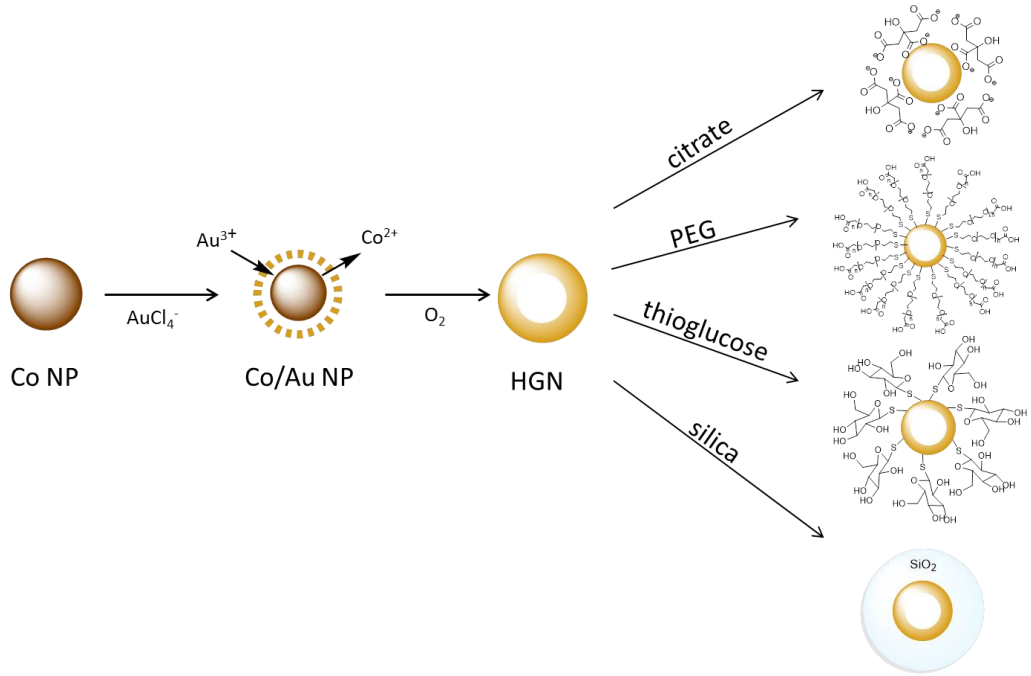

Figure 3.3: Schematic representation of the main stages in the HGN synthesis. Cobalt nanoparticles (CoNPs) are initially formed and used as sacrificial templates for growth of the gold shell. The hollow interior is formed by exposing the system to air to oxidise any cobalt remaining in the core. At the final stage a number of different stabilising agents can be introduced to provide nanoparticle stability.

Initially four polymers were chosen for investigation using these two methods, namely PEG, PVP, PAM and poly(ethyleneimine) (PEI). Successful functionalisation using each of the polymers was primarily characterised using extinction spectroscopy. Following the literature[40], a successful functionalisation was indicated by a significant shift in the SPR to longer wavelengths while unsuccessful syntheses were denoted by a complete loss in plasmon band and visible aggregation within the samples. The extinction spectra of the results using both methods with all four polymers are presented in Figure 3.4.

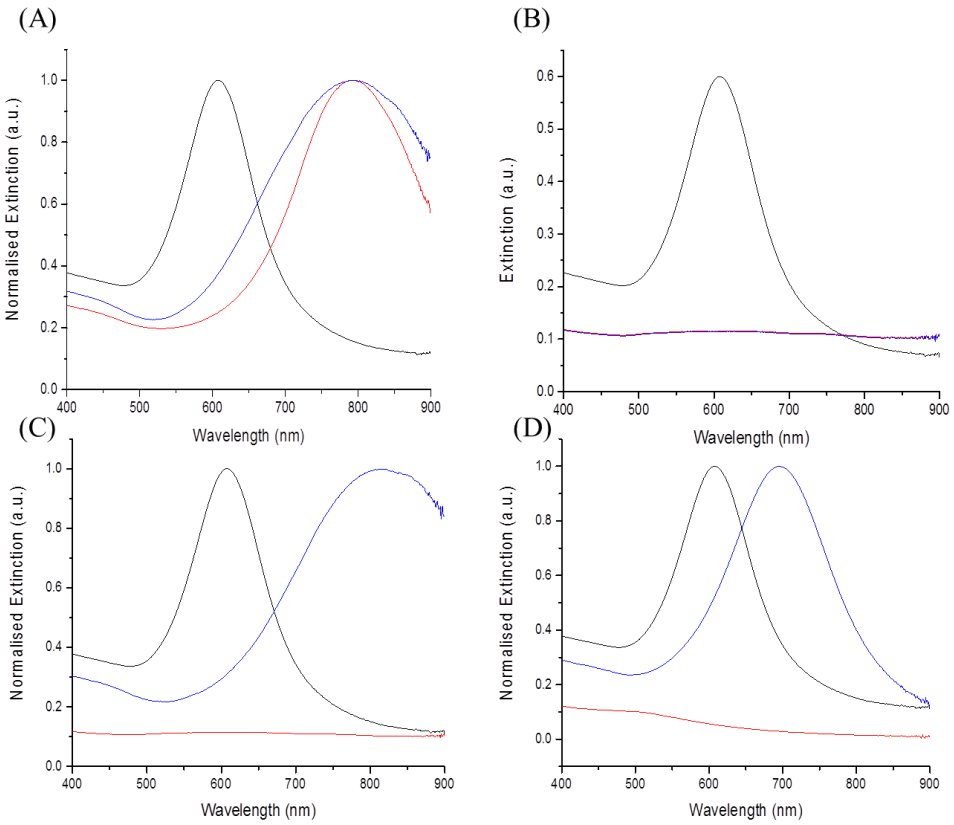

Figure 3.4: Extinction spectra of HGNs synthesised using standard citrate method (black), sodium borohydride stage addition of polymers (red) and stabilising agent method of addition of polymers (blue). Polymers used within each synthesis were (A) PVP, (B) PEI, (C) PAM and (D) PEG.

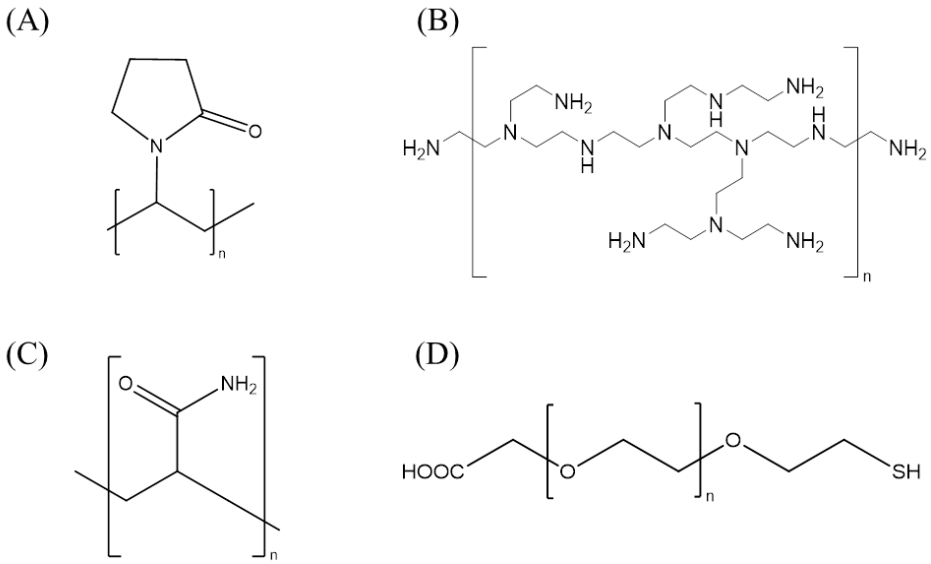

Figure 3.5: Chemical Structures of (A) PVP, (B) PEI, (C) PAM and (D) PEG.

Results using the $NaBH_4$ method were successfully reproduced and corresponded to those previously reported.[40] Using this method, PVP was the only polymer with which successful functionalisation was achieved. All other polymers investigated caused immediate precipitation from the solution and therefore no plasmon band was observed in the extinction spectra, a result which agreed with results published by Zhang *et al.* and confirmed that this method solely worked with PVP and could not be amended for use with other stabilising agents. Conversely, the stabilising agent method gave much more promising results and successful functionalisation was achieved with a further two polymers with the exception of PEI which was unsuccessful using both methods. The difference in success of the two methods can be attributed to the different chemical structures (Figure 3.5) and their coordination to the nanoparticle surface. In the $NaBH_4$ method the polymers must have an affinity for the cobalt nanoparticles (CoNPs) in order for successful functionalisation to occur. The amide moiety of PVP can create a stable colloidal solution by forming a Co^{2+}-PVP complex through coordinative bonding.[159] PEG and PAM have no reported affinity for the Co nanoparticle surface and it is proposed that they do not form a strong enough interaction to create a stable solution at this stage of the synthesis. Furthermore, in the weakly basic $CoCl_2$ and sodium citrate solution the carboxyl group on the PEG, with a pKa of around 5, will be in its deprotonated form which could induce repulsion from the negatively charged citrate-capped CoNPs. Conversely, polymers added at the final stage of the synthesis must have an affinity for the gold shell. Suitable functional groups on both PEG and PAM allowed successful functionalisation to occur through the thiol and amino groups respectively. PEI was unsuccessful using both methodologies. This was thought to be due to the positively charged species causing immediate aggregation to the nanoparticles forming in solution. Therefore, due to the added flexibility in the stabilising agents which could be used the method developed whereby the polymer was added as a capping agent at the final stage of the HGN synthesis was used as the method of choice for HGN functionalisation. After this initial success the method was developed and optimised to incorporate sugar functionalisation in addition to polymer coatings. A summary of the extinction spectra observed for all HGNs

synthesised using the improved methodology with various stabilising agents is shown in Figure 3.6.

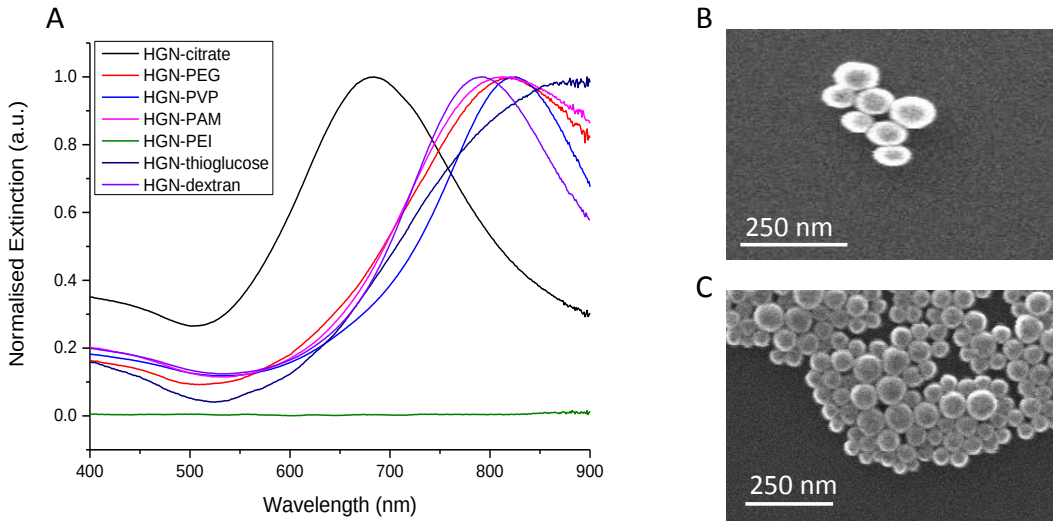

Figure 3.6: (A) Normalised extinction spectra of HGNs synthesised with various stabilising agents. Spectra were normalised in order to highlight the red-shifted SPR observed in the samples with the exception of PEI which was unsuccessful and precipitated from solution. (B) SEM image of citrate-stabilised HGNs corresponding to the extinction spectrum shown in A. (C) SEM image of PEG-stabilised HGNs corresponding to the extinction spectrum in A.

The normalised spectra clearly show that on addition of the various stabilising agents at the final stage of the HGN synthesis there is a significant red shift in the SPR of greater than 100 nm. An added advantage of this methodology was the increased reproducibility observed between each synthesis, overcoming one of the major limitations described for standard citrate stabilised HGNs (Section 3.2). To highlight the reproducibility within this method, citrate stabilised HGNs typically had an SPR of 700 ± 50 nm, while other stabilising agents shifted the SPR to 815 ± 35 nm with the exception of thioglucose which generally had an SPR of 875 ± 25 nm. The significant red-shift and greater reproducibility agree with results previously published however this method allows extension for use with other stabilising agents which were reported to be unsuccessful when added prior to the addition of gold in the synthesis. The significant red-shift in SPR could be a result of a variation in shell thickness of the stabilised HGNs synthesised. Previous studies have reported that HGNs with a SPR in the NIR region have thinner outer shells which results in a

slight increase in inhomogeneity within the samples.[23, 40] Additionally, previous work has hypothesised that the presence of a stabilising agent could slow the growth of the gold shell and results in more red-shifted particles with thinner shells.[40] Similarly, adding the stabilising agents shortly after addition of the gold salt could hinder the development of a thicker shell whereas adding citrate aids the further reduction of the gold salt, therefore resulting in thicker shell formation. The significant increase in time taken for a colour change to occur when the various stabilising agents were added to the synthesis along with evidence of increased particle inhomogeneity from the larger standard deviation values in particle size measurements of the stabilised HGNs (Table 3.1) support this hypothesis. Unlike solid gold nanoparticles, HGN aggregation can be characterised by a dampening in SPR along with a shift to shorter wavelengths[45] which again suggested the red-shift observed was due to the presence of the stabilising agent and was not a result of nanoparticle aggregation.

Representative SEM images are shown in Figures 3.6B and 3.6C for citrate-stabilised and PEG-stabilised HGNs respectively. Images for the remainder of the stabilising agents used are shown in Figure 3.7.

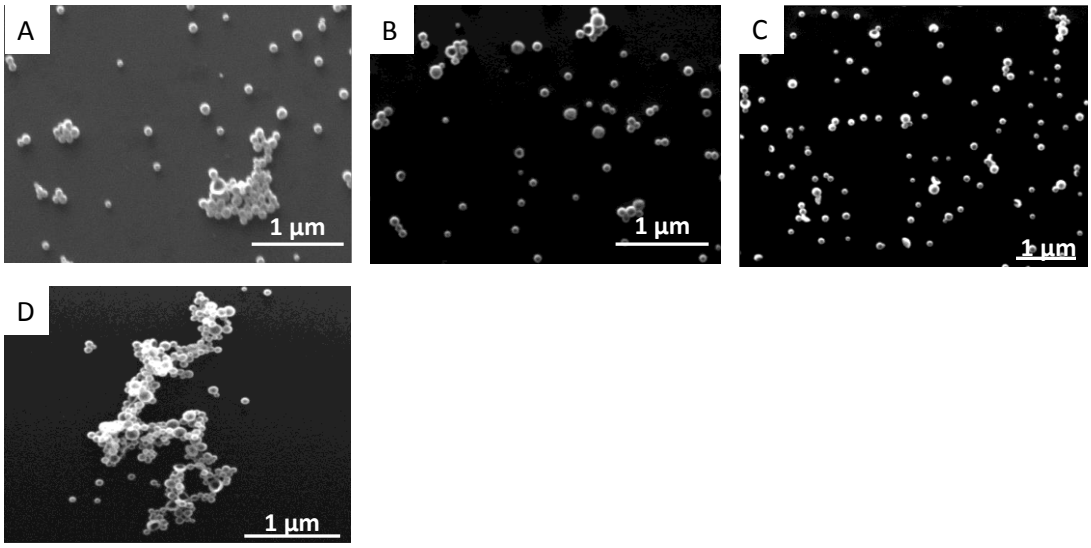

Figure 3.7: SEM images corresponding to extinction spectra in Figure 3.6, (a) PVP-stabilised HGNs, (b) PAM-stabilised HGNs, (c) thioglucose-stabilised HGNs, and (d) dextran-stabilised HGNs.

Particle size and ζ-potential data corresponding to the extinction spectra of the HGNs reported in Figure 3.6 are shown in Table 3.1. Particle size values calculated based on the metallic diameter using ImageJ software remained relatively consistent within the different stabilised HGNs as the presence of the different stabilising agents cannot be observed from the SEM images. All stabilised-HGNs synthesised were below 100 nm, ideal for cellular uptake.

Table 3.1: Summary of data obtained for HGNs synthesised with various stabilising agents corresponding to extinction spectra reported in Figure 3.6. Red-shift values were calculated with respect to citrate-stabilised HGNs. Zeta potential values are quoted as the mean of three replicates of each sample with error ± one standard deviation. Particle size values are calculated from the average size of 50 particles within each sample with error ± one standard deviation.

Stabilising Agent	λ_{max} (nm)	Red-Shift (nm)	Particle Size Diameter (nm)	Zeta Potential (mV)
Citrate	684	0	82.4 ± 9.6	-28.6 ± 1.2
PEG	820	136	76.5 ± 18.7	-32.9 ± 2.6
PVP	826	142	86.9 ± 18.9	-47.5 ± 2.1
PAM	811	127	87.5 ± 22.6	-21.8 ± 0.8
PEI	-	-	-	3.46 ± 0.62
Thioglucose	897	213	80.4 ± 19.3	-45.2 ± 3.1
Dextran	791	107	84.2 ± 24	-47.7 ± 1.4

As additional confirmation that successful functionalisation had taken place, particle size measurements were also recorded using dynamic light scattering (DLS). As measurements are based on the hydrodynamic diameter of the colloidal systems, changes in particle diameter due to the presence of an added stabilising layer should be observable. Results are presented in Figure 3.8. All successfully stabilised HGNs displayed a consistent size increase compared to standard citrate HGNs confirming the presence of the stabilising layer. PEI-stabilised HGNs showed a large increase in size when measured by DLS due to the immediate aggregation of the sample induced by the positive charge on the PEI moiety. This was supported by ζ-potential data

which indicated that this was the only positive sample out of all agents tested. All other samples showed a significant degree of colloidal stability, and the difference in ζ-potential from standard citrate-HGNs indicated that successful functionalisation had occurred.

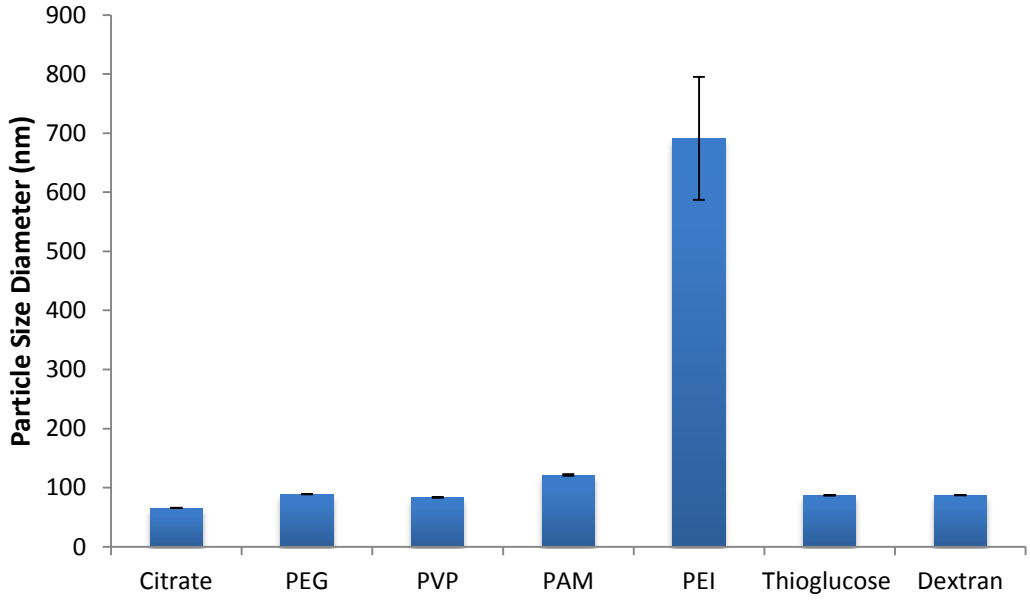

Figure 3.8: Particle size values measured by DLS corresponding to HGNs synthesised in Figure 3.6. Values are quoted as the mean of three replicates of each sample with error bars ± one standard deviation.

3.3.2 Silica Encapsulation

As silica functionalisation is slightly more complex, involving a two-stage synthesis, an alternative methodology was required for the silica encapsulation of HGNs to that outlined in Section 3.3.1. To develop a suitable methodology it was first necessary to address a number of limitations surrounding the synthesis. Firstly, as with most metallic nanoparticles the HGN surface is stabilised by citrate, an anionic agent, to prevent aggregation however this makes the surface vitreophobic and so has little affinity for silica. Secondly, the silica shell is grown under relatively harsh conditions, thus the nanoparticles need to have sufficient stability to withstand

aggregation in an alcohol / water solution required for growth of the silica shell in order to reduce the possibility of the silica shell encapsulating partial aggregates or small clusters of nanoparticles. To simultaneously address these limitations, a silane coupling agent can be added as the first stage in the silica encapsulation process.[112, 116] Monolayer surface coverage of a silane coupling agent will render the surface vitreophilic and primed for growth of the silica shell while additionally providing a sufficient stabilising layer to prevent aggregation during the second stage in the synthesis.

Initial work focussed on investigating which silane coupling agent was most effective for use with HGNs. Three silane coupling agents were considered; their chemical structures are shown in Figure 3.9.

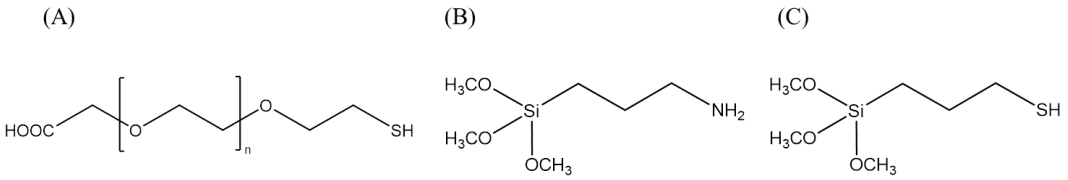

Figure 3.9: Chemical structures of silane coupling agents for silica encapsulation of HGNs; (A) polyethylene glycol (MW 5000), (B) 3-(aminopropyl)trimethoxysilane (APTMS), (C) 3-(mercaptopropyl)trimethoxysilane (MPTMS)

Thiol and amino functionality present on all coupling agents investigated would provide a high level of affinity to the gold surface allowing displacement of the current citrate stabilising layer, rendering the surface vitreophilic and suitable for silica shell growth.

Figure 3.9A represents PEG, a less conventional coupling agent than the alkoxysilane coupling agents frequently used in silica encapsulation of metallic nanostructures. As successful synthesis of PEG stabilised HGNs had already been achieved as described in Section 3.3.1 this was naturally the first coupling agent to be investigated. The method used was inspired by work by Liz-Marzán *et al.* which reported that PEG could provide sufficient stabilisation to the nanoparticles to prevent aggregation on transfer to the ethanol / ammonia solution required for silica shell growth.[116] As well as providing stabilisation, the PEG can also act as a primer for growth of the shell enabling silica condensation onto the gold surface. It was

thought that the ether oxygens present in PEG could act as hydrogen bond acceptors, therefore allowing binding of silanol groups through hydrogen bonding.[116] As a result, pre-prepared PEG-stabilised HGNs were used as a starting material for growth of the silica layer which was added using a modified Stöber method.[113]

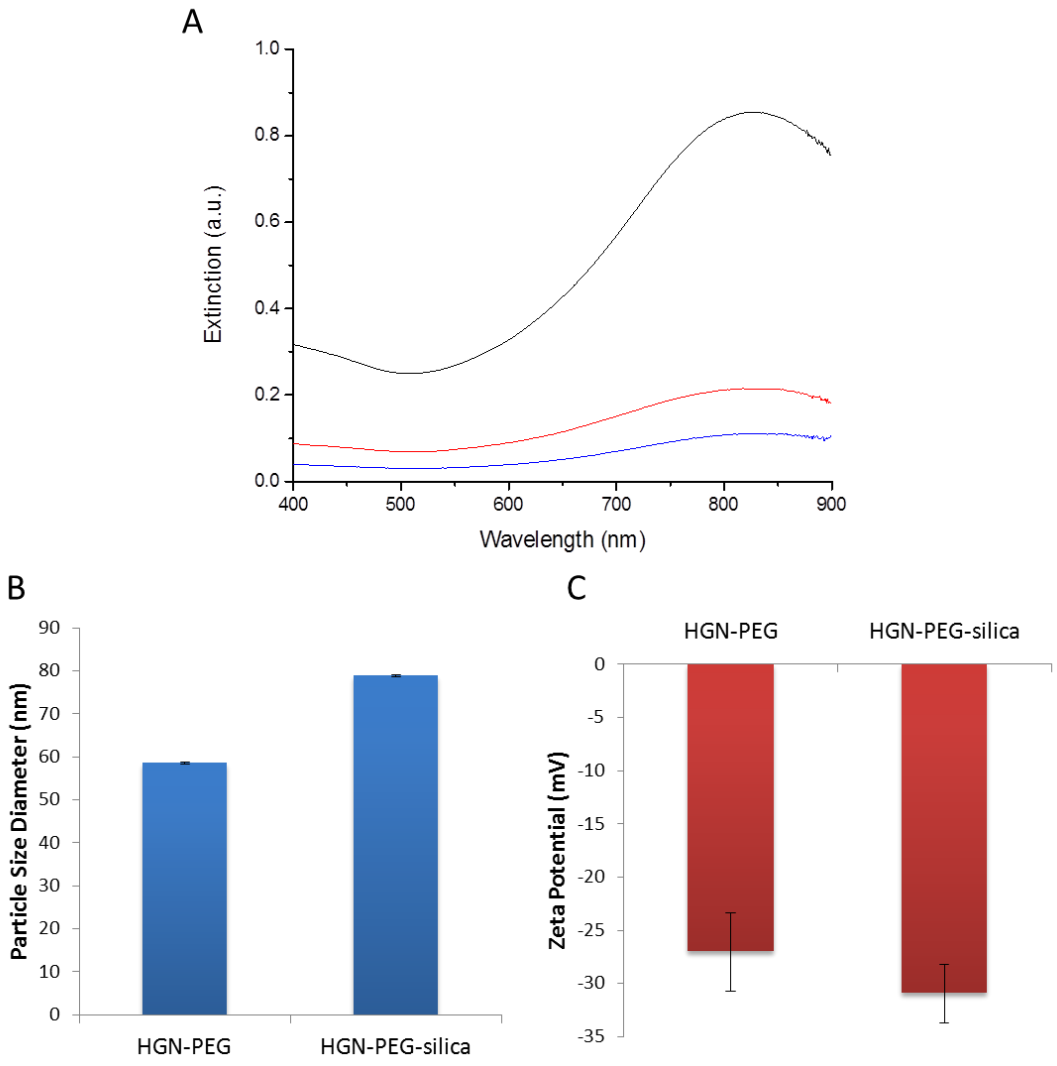

Figure 3.10: HGN-silica encapsulation using PEG as a coupling agent; (A) Extinction spectra of initial HGN-PEG starting material (black), HGN-PEG post-centrifugation step (red) and HGN-PEG after silica functionalisation, (B) Particle size measurements pre and post silica encapsulation, error bars are ± one standard deviation based on three replicate measurements and (C) Zeta potential values pre and post silica encapsulation, error bars are ± one standard deviation based on three replicate measurements.

Results obtained using PEG as an initial coupling agent are summarised in Figure 3.10. The initial stage in the synthesis involved a centrifugation step firstly to remove

any unbound PEG but additionally to concentrate the nanoparticles down into a pellet which could be redispersed into the alcohol / ammonia solution required for silica shell growth. The extinction spectra (Figure 3.10A) indicated that there was some aggregation induced within the HGNs after the initial centrifugation step, shown by both a dampening in plasmon band and blue-shift in SPR. This could have been due to the PEG layer providing insufficient stabilisation to the HGNs to protect against any forced aggregation induced by centrifugation or by inefficient removal of the supernatant from the pellet resulting in a lower concentration of nanoparticles being present in the redispersed solution. Lower centrifugation speeds were investigated to try to overcome this issue however this caused ineffective separation of the HGN solution. The final stage in the synthesis (growth of the silica shell) gave more promising results. Although there was again a slight dampening in the spectra this was accompanied by a slight red-shift in the SPR from the post-centrifuged HGNs. The red-shift observed was a characteristic indication that successful functionalisation had been achieved. The SPR is dependent upon the refractive index of the surrounding medium of the nanoparticles and so the high refractive index of silica (n = 1.57) compared to water (n = 1.33) explains the red-shift observed.[110] Particle size measurements showed a size increase of around 20 nm after the addition of the silica layer, while zeta potential measurements showed a change in surface potential after the final silica encapsulation step. This provided additional confirmation that HGNs pre-stabilised with PEG could be used as a precursor for silica encapsulation. Although results initially seemed promising, this method was not taken any further due to the limitations highlighted in the centrifugation step. Although a significant effort was taken to overcome these issues the resultant silica encapsulated HGNs were of insufficient quality and concentration to be carried forward for further studies. Therefore, PEG was disregarded as a coupling agent for use with HGNs within this work.

As a result APTMS and MPTMS, two more widely used silane coupling agents, were investigated as alternatives. They are structurally very similar, differing only by the amino and thiol functionality on APTMS and MPTMS respectively (Figure 3.9), allowing for ease of conjugation to the gold surface of the citrate-stabilised HGNs. For comparison studies, APTMS-HGN and MPTMS-HGN conjugates were prepared

and analysed using extinction spectroscopy. Following silica encapsulation, these conjugates were then re-analysed and results observed are shown in Figure 3.11.

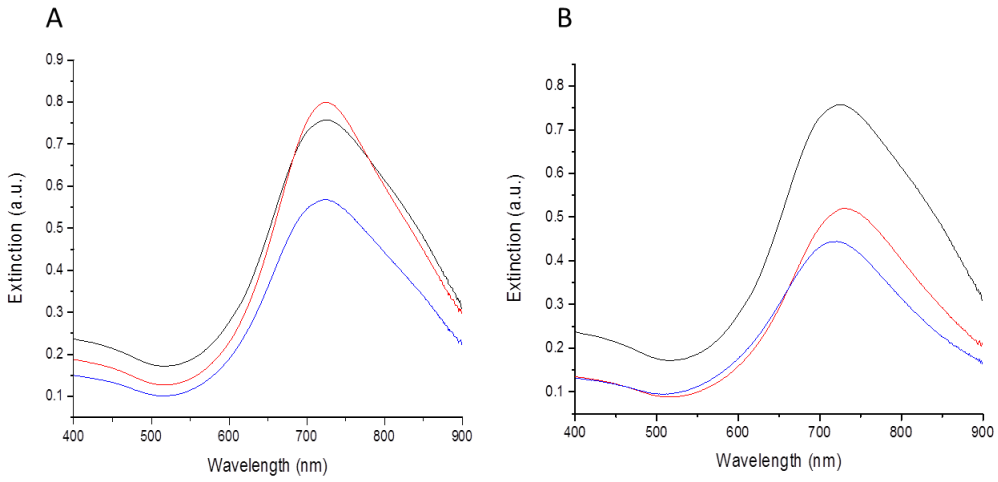

Figure 3.11: (A) Extinction spectra results for HGN (black) conjugation to APTMS (red) and MPTMS (blue) redispersed in a 1:4 H_2O:EtOH solution after initial centrifugation step, (B) original standard citrate HGNs (black) and post silica encapsulation analysis of HGN-APTMS (red) and HGN-MPTMS (blue) conjugates.

HGN-APTMS conjugates showed very little change in extinction spectra after the initial centrifugation step to remove excess coupling agent indicating that no aggregation had taken place within the sample. In contrast, a similar dampening and blue shift in SPR to that seen using PEG as a coupling agent was observed when MPTMS was added to the HGNs indicating that this did not provide a sufficient stabilising layer to protect against forced aggregation in the centrifugation step. Although extinction spectra in Figure 3.11B showed that there was a slight dampening in the plasmon band when the silica layer was added to the APTMS nanoparticle precursor this was somewhat expected due to the additional washing steps to remove free silica nuclei at the final stage of the synthesis. Therefore, at this stage APTMS was chosen as the most effective coupling agent for use with HGNs and was used in the further development of a reproducible methodology for silica encapsulation of HGNs.

In order to achieve the most efficient level of stabilisation and to provide an efficient platform for complete silica shell formation, monolayer coverage of APTMS on the

HGN surface was required. To determine the optimum concentration of APTMS for use within the synthesis, varying concentrations were added to the citrate-stabilised HGNs and the resulting conjugates were analysed using extinction spectroscopy.

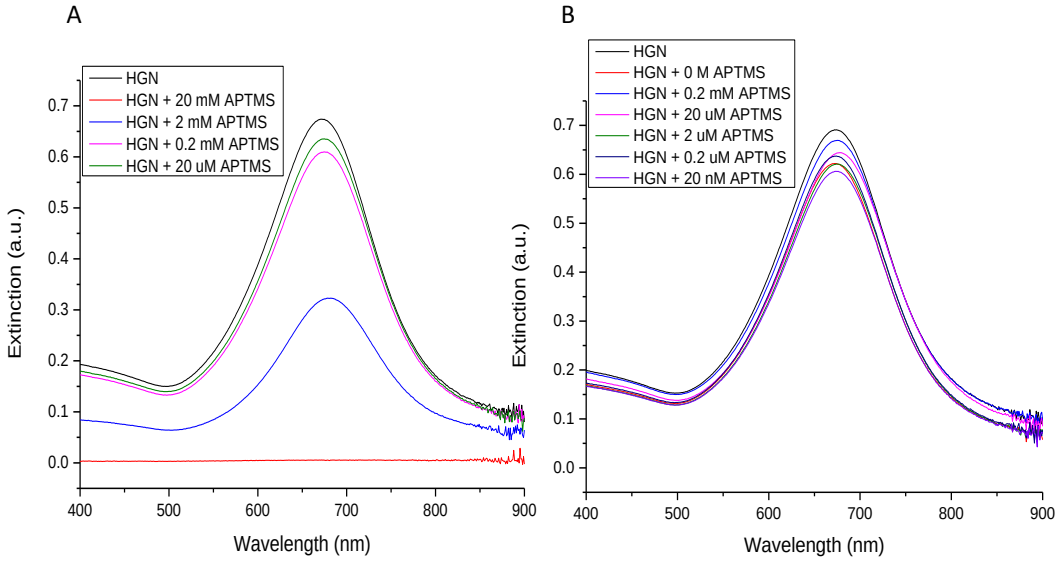

Figure 3.12: Extinction spectra of HGN-APTMS conjugates with varying APTMS concentrations (A) high concentration range from 20 µM to 20 mM (B) lower concentration range (0 M to 0.2 mM)

As previously reported in Section 3.3.1 the citrate stabilised HGNs have limited stability to post synthesis conjugation methods. Initial APTMS conjugation studies explored the maximum coupling agent concentration the HGNs could withstand (Fig 3.12A). Results showed that HGN aggregation was initiated on addition of an APTMS concentration of 2 mM or higher which equated to a final concentration of 0.2 mM in solution. Repeating the study at lower concentration increments found optimum results were observed using an APTMS concentration of 20 µM (final concentration 2 µM).

Within this work silica shells were grown using a modified Stöber method.[113] After transferring the HGN-APTMS precursor into an ethanol / water solution, ammonia was added to act as a catalyst for the hydrolysis of tetraethyl orthosilicate (TEOS); creating silica sols which could condense on the HGN surface. Both reaction time and the volume of TEOS added can be altered in order to vary the thickness of the silica shell produced. For this work as thin a silica shell as possible was required to

maintain a strong electromagnetic field between the gold surface and silica shell for further SERS characterisation so conditions were optimised based on this condition. The first parameter investigated was TEOS reaction time.

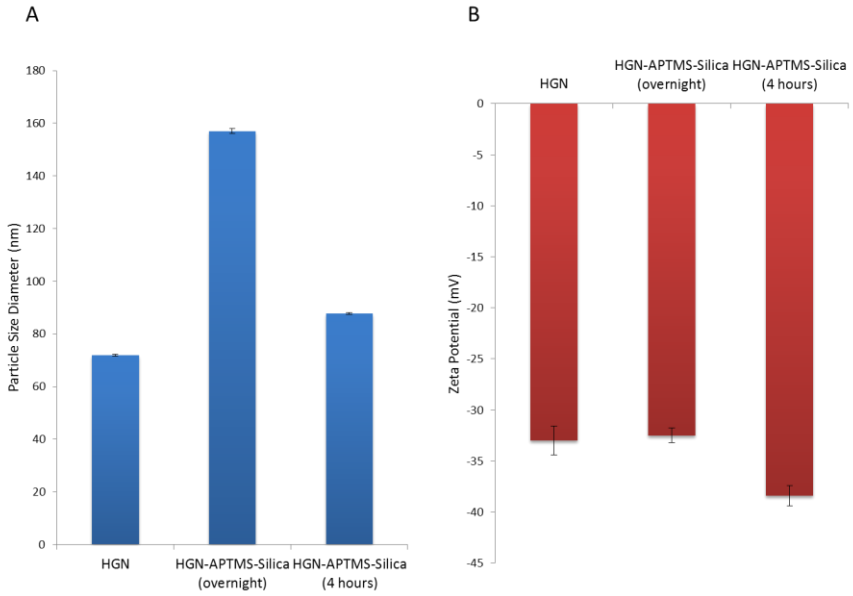

Figure 3.13: (A) Particle size measurements and (B) zeta potential values of HGNs pre and post silica encapsulation with varying TEOS reaction times. Error bars are ± one standard deviation.

Analysis was carried out on reactions terminated after sixteen hours (overnight) and four hours. Extinction spectra results showed very little difference between the two reaction times however particle size and zeta potential measurements presented in Figure 3.13 provided an added insight into the results. When TEOS was left to react overnight the resultant particle size increased by around 85 nm compared to pre functionalised HGNs. As the extinction spectra was unchanged this suggested that the large size increase was not a result of particle aggregation but was exclusively due to the presence of a thick silica layer which would be unsuited to further applications. Reducing the reaction time to four hours gave much more promising results with a particle diameter increase of 15 nm indicating a shell thickness of around 8 nm; ideal for further characterisation using SERS. Zeta potential values remained relatively consistent. The slight decrease from -33 ± 1.4 mV in the pre functionalised HGNs to -38.4 ± 1 mV in the silica encapsulated HGNs after a four hour reaction time indicated successful functionalisation had occurred.

Final optimisation steps focussed on investigating the effect of varying TEOS concentration by adding incremental volumes to concurrent experiments. (Fig 3.14)

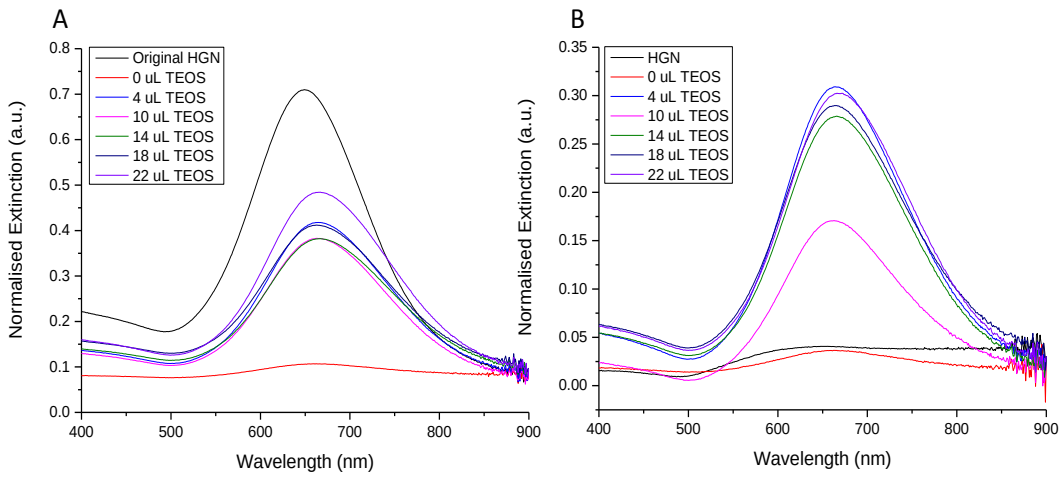

Figure 3.14: (A) Extinction spectra normalised at 900 nm of silica encapsulated HGNs using different volumes of TEOS (B) Normalised extinction spectra of silica encapsulated HGNs using varied TEOS concentrations redispersed in 100 mM NaCl 90 minutes before analysis.

Table 3.2: Summary of data obtained corresponding to extinction spectra in Figure 3.14 A; silica encapsulated HGNs with varying TEOS concentrations.

Sample	λ_{max} (nm)	Absorbance (a.u.)	Shift (nm)	Particle Size Diameter (nm)	Zeta Potential (mV)
Original HGN	649	0.710	0	69 ± 0.2	-49.8 ± 0.1
0 µL TEOS	662	0.107	13	110.9 ± 4.3	-34.7 ± 1.5
4 µL TEOS	662	0.418	13	81.1 ± 0.9	-45.4 ± 1.4
10 µL TEOS	663	0.383	14	82.7 ± 0.1	-44.7 ± 2.6
14 µL TEOS	667	0.382	18	85.6 ± 0.7	-44.8 ± 1.9
18 µL TEOS	662	0.411	13	85.6 ± 1	-43.8 ± 2.9
22 µL TEOS	667	0.484	18	79.6 ± 0.1	-45.7 ± 2

Table 3.3: Summary of data obtained corresponding to extinction spectra in Figure 3.14 B; silica encapsulated HGNs with varying TEOS concentrations redispersed in 100 mM NaCl.

Sample	λ_{max} (nm)	Absorbance (a.u.)	Shift (nm)	Particle Size Diameter (nm)	Zeta Potential (mV)
Original HGN	-	-	-	3130 ± 369.5	-37.8 ± 4.4
0 µL TEOS	663	0.037	1	122.3 ± 4	-41.8 ± 1.7
4 µL TEOS	664	0.364	2	83.7 ± 0.4	-40.5 ± 3.6
10 µL TEOS	663	0.227	0	89.4 ± 1	-40.7 ± 2.3
14 µL TEOS	666	0.318	-1	84.9 ± 0.4	-39.7 ± 1.1
18 µL TEOS	666	0.328	4	83.8 ± 0.9	-46.3 ± 1.5
22 µL TEOS	666	0.343	-1	78.2 ± 0.4	-42 ± 1.7

Detailed analysis of the results observed are summarised in Tables 3.2 and 3.3. After silica encapsulation samples were redispersed in 100 mM NaCl to determine the effectiveness of the silica layer in each of the samples; fully formed silica shells should prevent HGN aggregation.[108] In the control sample no TEOS was added to the reaction and therefore no silica shell growth should be observed. This was confirmed by the severe dampening in plasmon band in the extinction spectra and particle size increase observed within the sample however nanoparticle flocculation from the salt solution did not occur due to the slight stability afforded by the APTMS monolayer. Results of increasing TEOS concentration within the reactions showed minimal particle size changes between each sample indicating that the incremental concentration increase was not significant enough to provide a significantly thicker silica layer. All samples did however show a size increase of around 10-15 nm and slightly red-shifted SPRs with respect to the pre-functionalised HGNs indicating that a thin silica layer was present on the HGN surface. Analysis of samples redispersed in salt solution (Table 3.3) showed that all samples maintained a consistent particle size with the exception of the original HGN and the control sample. All showed minor shifts in SPR with respect to the original samples analysed with minimal

changes in extinction spectra and no evidence of nanoparticle aggregation. Considering all variables, 4 µL was chosen as the optimum concentration as this showed the least deviation in extinction spectra on initial HGN silica encapsulation and maintained stability in salt solution.

Using this optimised methodology standard citrate-stabilised HGNs can be successfully encapsulated with a thin layer of silica. A summary of the results obtained using the optimised methodology are presented in Figure 3.15 and Table 3.4. Normalised extinction spectra showed successful functionalisation had occurred from the red-shift in SPR observed. This red-shift is not as significant as the red-shift observed using the stabilisation method for polymers and sugars as the silica layer was added after the initial synthesis was completed and therefore had no effect on the resulting HGN aspect ratios. The resolution in the SEM image was not sufficient to show the presence of the silica shell, however images showed that a relatively monodispersed solution was maintained.

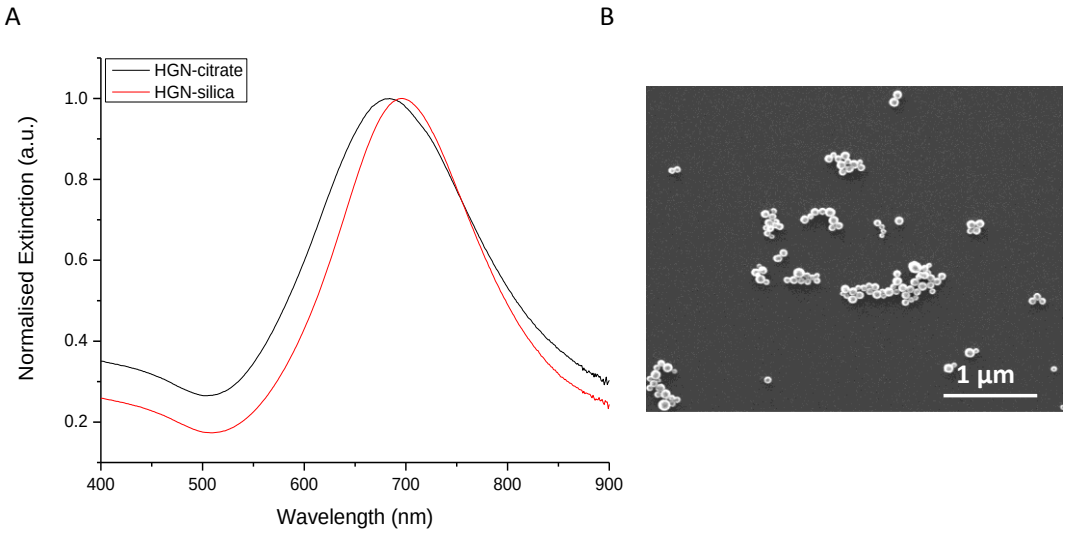

Figure 3.15 (A) Normalised extinction spectra of HGNs encapsulated with a silica shell (B) SEM image of silica encapsulated HGNs corresponding to the extinction spectrum shown in A.

Table 3.4: Summary of data obtained for silica encapsulated HGNs corresponding to extinction spectra in Figure 3.15. Red-shift values were calculated with respect to citrate-stabilised HGNs. Zeta potential values are quoted as the mean of three replicates of each sample with error ± one standard deviation. Particle size values are calculated from the average size of 50 particles within each sample (Image J) or by DLS with error ± one standard deviation.

Stabilising Agent	λ_{max} (nm)	Red-Shift (nm)	Particle Size Diameter (nm) (Image J)	Particle Size Diameter (nm) (DLS)	Zeta Potential (mV)
Citrate	684	0	82.4 ± 9.6	65.6 ± 0.3	-28.6 ± 1.2
Silica	695	11	83 ± 14.5	87.2 ± 0.5	-38.5 ± 1.7

Particle size values calculated using ImageJ software from SEM images showed no apparent change in particle diameter as the silica layer could not be detected. However, measurements taken using DLS confirmed successful functionalisation with an increase in diameter of 22 nm which indicated a shell thickness of around 10 nm surrounded the HGN surface. The change in zeta potential showed the increased colloidal stability provided by the silica stabilising layer.

For future stability testing it was imperative that a complete layer of silica was encapsulating the HGN surface to provide maximum stability. Because the silica shell synthesised using the aforementioned methodology was designed to be as thin as possible pinholes could be present on the surface which could prove problematic in future stability studies. As TEM imaging was not available for direct observation of the silica layer on the HGN surface a pyridine pinhole test using SERS was carried out. This experiment is designed on the principle that pyridine will strongly adsorb on a gold surface but has no affinity for silica.[160] Therefore if there are pinholes present in the shell, pyridine will adsorb onto the HGN surface and an enhanced pyridine peak will be observed at 1009 cm^{-1}. With a complete silica layer, pyridine will remain in solution and no SERS signal will be obtained. Results observed are presented in Figure 3.16.

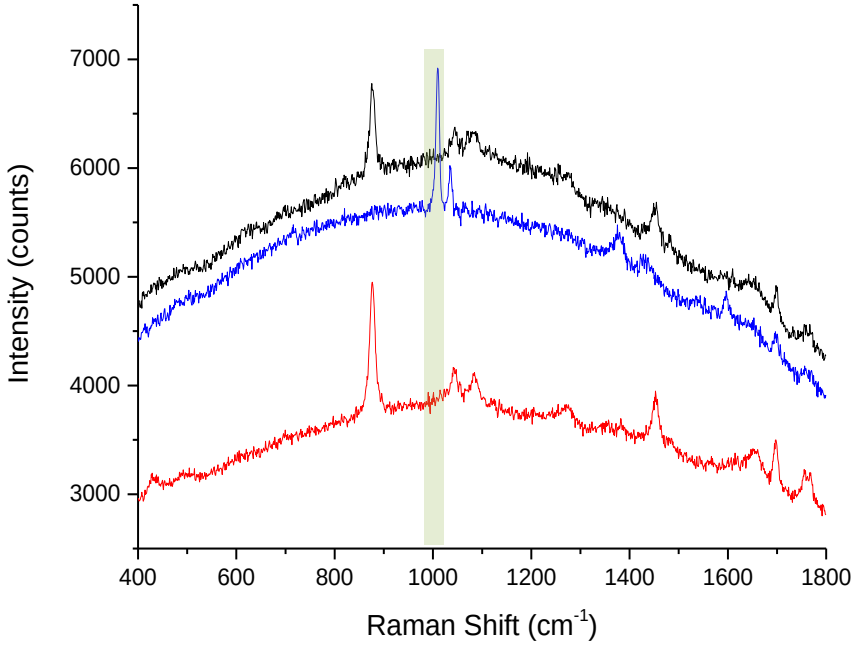

Figure 3.16: Raman spectra recorded using an excitation wavelength of 633 nm of silica encapsulated HGN (black) silica encapsulated HGN with 1 mM pyridine (red) and citrate-stabilised HGN with 1 mM pyridine (blue). Spectra were obtained by scanning three replicates of each sample with a 10s accumulation time under a laser incident power of ~12 mV. Averages are shown and error bars are ± one standard deviation.

The peak highlighted at 1009 cm^{-1} which is indicative of the presence of pyridine was only present when no silica layer was encapsulating the HGN surface which confirmed the presence of a fully formed silica layer. The dominant peak observed in the silica encapsulated HGN spectra at around 880 cm^{-1} was due to traces of ethanol (EtOH) which remained in solution after synthesis. To ensure the presence of the EtOH peaks were not obscuring any weak pyridine signal that may have been present repeated washing steps were employed and samples were reanalysed. (Figure 3.17)

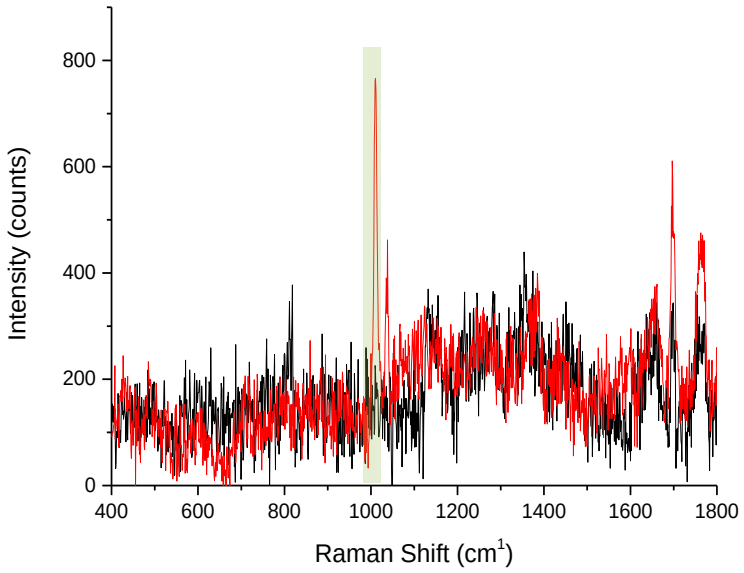

Figure 3.17: Raman spectra recorded using an excitation wavelength of 633 nm of silica encapsulated HGN with 1 mM pyridine (black) and citrate-stabilised HGN with 1 mM pyridine (red) after additional wash steps to remove EtOH. Spectra were obtained by scanning three replicates of each sample with a 10s accumulation time under a laser incident power of ~12 mV. Averages are shown and error bars are ± one standard deviation.

Although the spectra observed were very weak due to a reduction in nanoparticle concentration during washing steps the results were successfully repeated. EtOH peaks were effectively removed from the samples and the pyridine peak highlighted could only be observed in the pre-encapsulated HGN sample. This confirmed the synthesis of complete silica encapsulated HGNs which could be used in further stability tests.

3.4 HGN Stability Studies

After incorporation of stabilising agents into the HGN synthesis the successful HGNs were systematically tested for increased tolerance to different pH and salt concentrations; important considerations if these HGNs are to be used in bio-applications. In addition to this, long term stability was also investigated. For

comparable studies, the polymer and sugar functionalised HGNs were functionalised with 1% (w/v) of each of the stabilising agents using the method described in Section 3.3.1., which was thought to allow for sufficient monolayer coverage of the HGN surface by each of the stabilising agents. This was estimated by calculating the number of molecules required for monolayer coverage of HGNs with an approximate concentration of 0.15 nM and an average size of 70 nm. Based on PEG which has a reported molecular footprint of 0.35 nm^2 on a gold surface[161] it was estimated that 6.6 µM PEG was required for monolayer coverage on the HGN surface. A concentration of 1% (w/v) PEG equated to a final concentration of 7.4 µM, an excess of the estimated value to ensure full coverage of the HGN surface. For other stabilising agents no molecular footprint values were published within the literature; however due to their bulkier nature values were expected to be larger than that of PEG, therefore requiring less molecules per nanoparticle for monolayer coverage. As a result, all were added in excess of the concentration required for PEG which should consequently be more than sufficient for monolayer coverage. For confirmation that 1% (w/v) was indeed the most suitable concentration and appropriate for comparison studies, a range of concentrations were added during the synthesis and the resultant HGNs were redispersed in 1 M sodium chloride (NaCl) and analysed using extinction spectroscopy. Results are presented in Figure 3.18. These results confirmed that 1% (w/v) PEG was indeed the optimum concentration with very little change in the extinction spectrum observed on addition of 1 M NaCl indicating that an effective stabilising layer was present to protect against salt induced aggregation. Although 10% (w/v) and 5% (w/v) also showed some increased salt tolerance the quality of HGNs synthesised was very poor with broadening in the spectra indicating a level of inhomogeneity within these samples. Concentrations lower than 1% (w/v) were not sufficient to slow the growth of the gold shell and produce the significantly red-shifted SPR beneficial for use in future applications. This experiment was repeated using the further three polymer (PVP, PAM and PEI) and two sugar (dextran and thioglucose) stabilising agents however a consistent level of instability to salt was observed throughout the range of concentrations analysed. Therefore 1% (w/v) was considered an appropriate concentration for all stabilising agents for comparable stability measurements. As the stabilising agents were thought to be

added in excess, HGNs were concentrated by centrifugation and re-dispersed in d.H_2O to give final concentrations of 2 nM - 3 nM for storage and further analysis. Concentrations were obtained using Nanoparticle Tracking Analysis (NTA) which is described in Chapter 7.

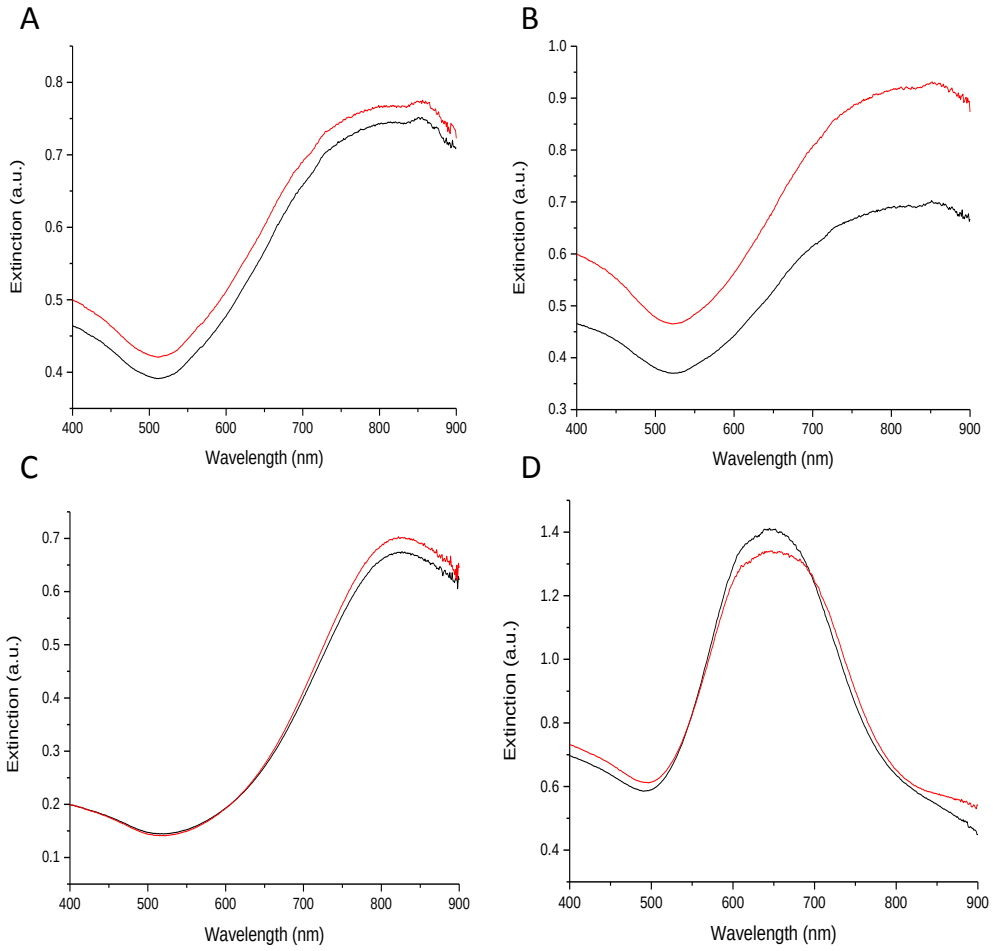

Figure 3.18: PEG-HGNs synthesised with (A) 10% (w/v) PEG, (B) 5% (w/v) PEG, (C) 1% (w/v) PEG, and (D) 0.5% (w/v) PEG (red) and resulting extinction spectra of samples exposed to 1 M NaCl (black).

3.4.1 pH Studies

Initially the HGNs tolerance to changing pH levels was investigated, which were altered by the addition of 1 M NaOH or 1 M citric acid as appropriate. Extinction spectra were recorded at the original pH of the HGN solution which ranged from pH

7.4 –9.2, acidic pH ranging from pH 2.2-2.6 and alkaline pH ranging from pH 12.6-13.1. Results for the original citrate-HGNs compared to PEG-stabilised HGNs which were found to have the most tolerance to changing conditions are shown in Figure 3.19.

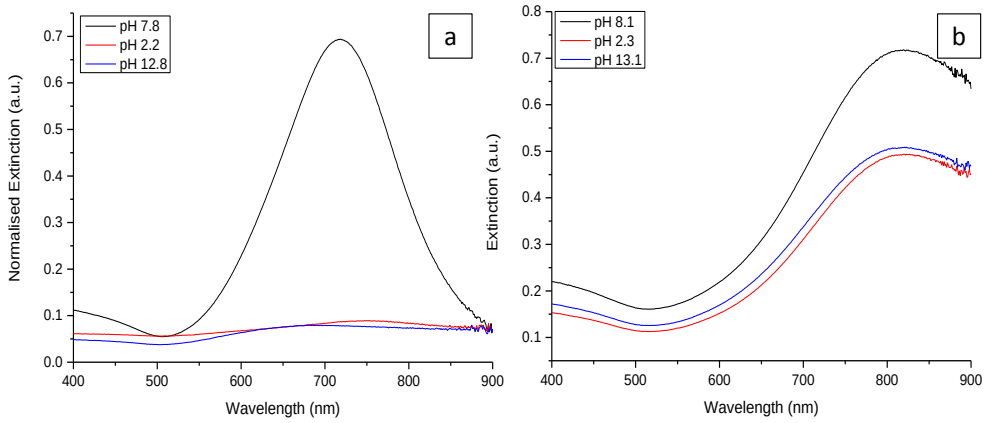

Figure 3.19: Extinction spectra of (a) citrate-stabilised HGNs and (b) PEG-stabilised HGNs measured at the original pH of the nanoparticle solution (black) and acidic (red) and alkaline pH (blue). pH was altered with the addition of 1 M citric acid or 1 M NaOH and left for four hours before analysis. Spectra (a) have been normalised at 900 nm to emphasise the plasmon dampening which is occurring.

It is clear from Figure 3.19 that citrate-capped HGNs had a very limited tolerance to changing pH and precipitated from solution due to over aggregation when exposed to extreme alkaline or acidic conditions with a complete loss of plasmon band in both environments. PEG-stabilised HGNs showed a significantly increased tolerance to both acidic and alkaline conditions with only a slight dampening in absorbance and very little line broadening indicating that aggregation was not taking place.

With PEG-HGNs showing the most promising results, their tolerance to changing pH levels were studied over one month. Results observed after a 24 hour period are shown in Figure 3.20, these were similar to results shown in Figure 3.19 however the PEG tolerance to alkaline conditions has reduced. Again, citrate HGNs were sensitive to changes in conditions and precipitated from solution as before.

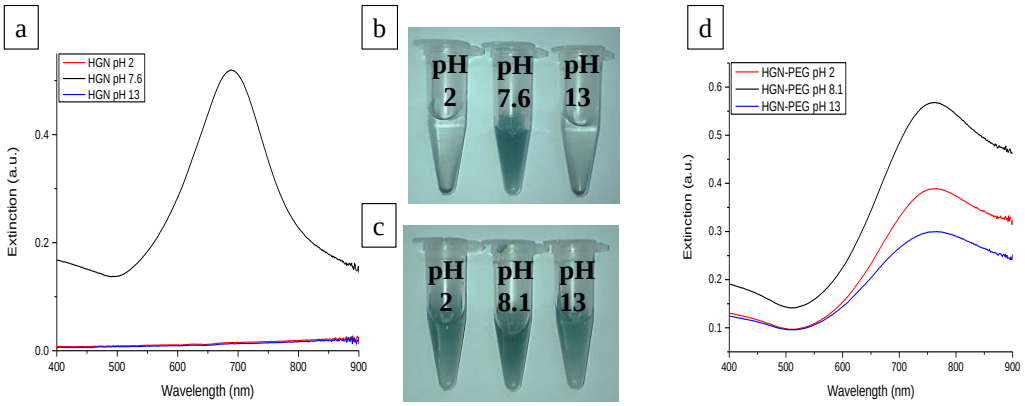

Figure 3.20: (a) Extinction spectra of citrate-stabilised HGNs after 24 hrs suspended in different pH values, (b) image of citrate-stabilised HGNs in a range of pH environments, (c) image of PEG-HGNs in a range of pH environments and (d) extinction spectra of PEG-stabilised HGNs after 24hrs suspended in different pH values.

Particle size measurements taken for PEG-HGNs were constant over the entire pH range studied (90.5 ± 0.2 nm at pH 2, 95.61 ± 2 nm at pH 8 and 91.3 ± 0.9 nm at pH 13) showing no aggregate formation. Samples were analysed again one month after initial measurements and showed no significant change compared to results taken after 24 hours (Figure 3.21).

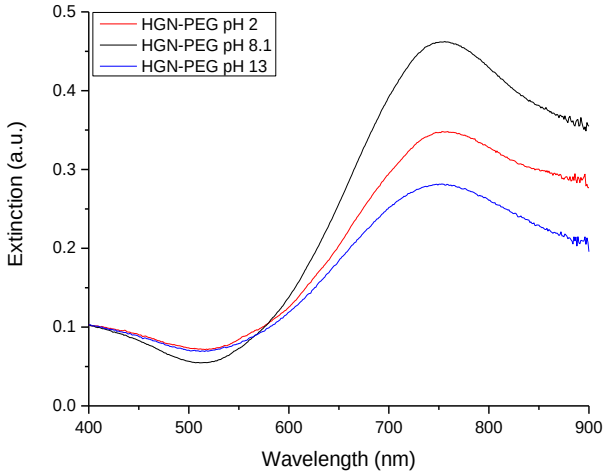

Figure 3.21: Extinction spectra of PEG-stabilised HGNs after one month suspended in different pH values.

With regards to other stabilising agents used, the spectra shown in Figure 3.22 indicated that although there was some increased tolerance to changing conditions compared to citrate, this was not to the extent of PEG. All other materials with the exception of silica showed some stability to acidic conditions however partial aggregation was indicated by the line broadening and blue-shift in SPR in the spectra. The stabilisation imparted by PEG among other agents was thought to be mainly a steric effect resulting from dense monolayer coverage due to the increased stability, to not only pH, but also to increased salt concentrations (Section 3.4.2). If this was a charge effect the salt would screen the charges and van der Waals attractions would induce aggregation.[44, 162]

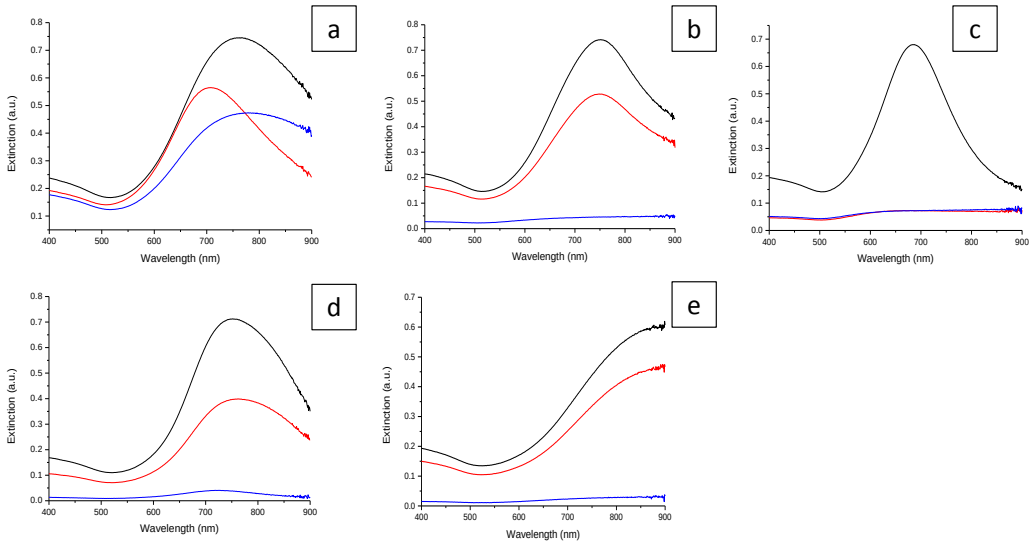

Figure 3.22: Extinction spectra of (a) PAM-stabilised HGNs, (b) PVP-stabilised HGNs, (c) silica-stabilised HGNs, (d) dextran-stabilised HGNs and (e) thioglucose-stabilised HGNs measured at original pH (black), acidic pH (red) and alkaline pH (blue).

For further investigation zeta potential measurements were carried out and showed that values varied significantly within different pH environments (Table 3.5).

Table 3.5: Zeta potential values of PEG-stabilised and citrate-stabilised HGNs measured at various pH values. Zeta potential values are quoted as the mean of three replicates of each sample with error ± one standard deviation.

pH of PEG-HGNs	Zeta Potential (mV)	pH of citrate-HGNs	Zeta Potential (mV)
pH 8.1	-41.9 ± 1.9	pH 7.8	-40.1 ± 1.7
pH 2	3.3 ± 0.5	pH 2	0.14 ± 2
pH 13	- 24.7 ± 0.6	pH 13	– 23.3 ± 0.6

This trend was observed throughout all stabilising agents tested showing no correlation to nanoparticle stability observed by extinction spectroscopy. The inherent maintenance of stability in PEG stabilised HGNs with the significant change in ζ-potential values supports the hypothesis that the stability is not solely due to charge influences but is significantly dependent on steric effects.

3.4.2 Salt Tolerance

Salt tolerance was tested using NaCl due to its presence in most biological buffers; results are shown in Figure 3.23 for the most and least stable HGNs, with PEG-HGNs showing very little change in extinction spectra with increasing salt concentration. The PEG-HGNs displayed a significantly increased tolerance to increasing salt concentrations compared to standard citrate HGNs which began to show signs of aggregation after addition of 30 mM NaCl caused by charge screening effects induced by the salt. The addition of 100 mM NaCl or greater led to visible aggregation within the samples evidenced by a loss in plasmon band in the extinction spectra shown.

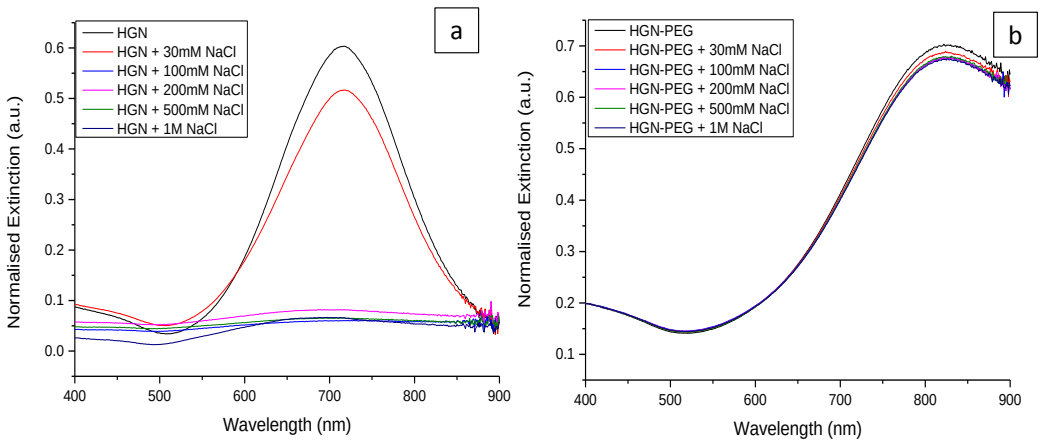

Figure 3.23: Extinction spectra of (A) citrate-stabilised HGNs and (B) PEG-stabilised HGNs measured in a range of different salt concentrations (from 0 M up to 1 M NaCl). Spectra (A) have been normalised at 900 nm and (B) at 400 nm to emphasise the plasmon dampening which is occurring.

Results of salt tolerance in up to 1 M NaCl for the remaining HGNs synthesised can be observed in Figure 3.24. Here, PAM-HGNs showed only slight aggregation on addition of up to 1 M salt indicating that the stability imparted by PAM is predominantly a steric effect. PVP was slightly more tolerant than citrate in up to 100 mM salt however the decreased stability above this concentration could be due to the weaker bond formation to the HGN surface, compared to that of the other polymers. Silica shelled HGNs have shown surprising results with limited stability compared to the polymers and sugars tested. Although no partial aggregation occurs when 30 mM salt was added the remaining results were similar to citrate-HGNs. This could indicate that the silica shell is too thin to provide sufficient shielding however adding a thicker shell for added stabilisation would not prove beneficial for future SERS based applications as described in section 3.3.2. Both sugars again showed limited stability to salt with no apparent increased stability compared to normal citrate-HGNs. Here, the steric stability may not be strong enough to overcome the screening of the charge induced by the salt.

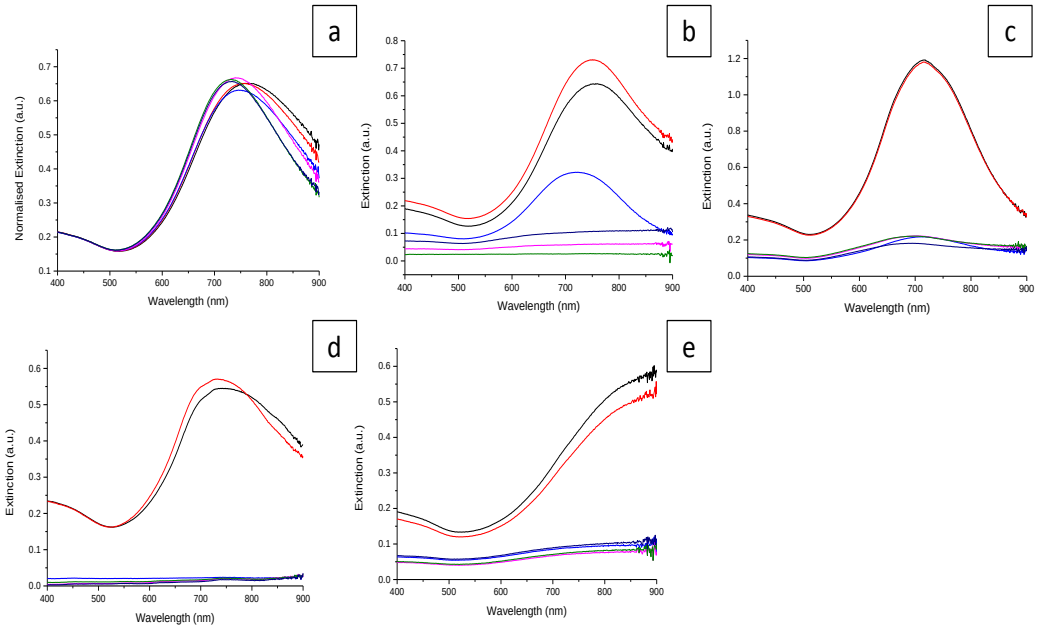

Figure 3.24: Extinction spectra of (a) PAM-stabilised HGNs, (b) PVP-stabilised HGNs, (c) silica-stabilised HGNs, (d) dextran-stabilised HGNs and (e) thioglucose-stabilised HGNs measured after dispersion in various different salt solutions of increasing concentration; 0 M (black), 30 mM (red), 100 mM (blue), 200 mM (pink), 500 mM (green) and 1 M (purple).

Producing the most promising results, maximum salt tolerance levels for PEG-stabilised HGNs were studied over one month using citrate-HGNs as a comparison.

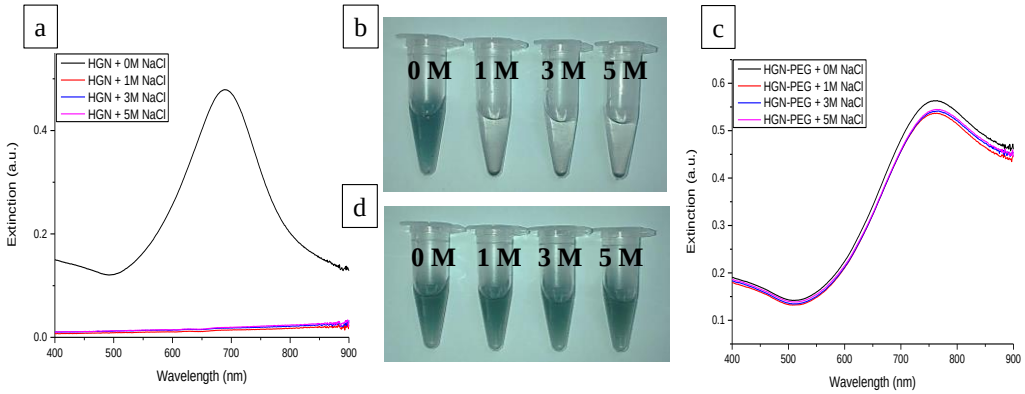

Figure 3.25: (a) Extinction spectra of citrate-stabilised HGNs after 24hrs suspended in increasing NaCl concentrations, (b) image of citrate-stabilised HGNs in increasing salt concentrations from left to right, (c) extinction spectra of PEG-stabilised HGNs after 24hrs suspended in increasing NaCl concentrations, and (d) image of PEG-HGNs in increasing salt concentrations from left to right.

Figure 3.25 shows salt tolerance levels in up to 5 M NaCl, concentrations higher than this could not be investigated as the salt solution becomes saturated above this point. For this investigation samples were left for a period of 24 hours before analysis commenced. Figure 3.25(c) shows the extinction spectra for the PEG-HGNs imaged in Figure 3.25(d). The sustained green colour of the solution along with the extinction spectra showed that the PEG-HGNs displayed no sign of aggregation in up to 5 M salt. Citrate capped HGNs however, showed no stability to salt as was shown previously. This was observed by both the loss of colour in solution due to nanoparticle precipitation and is supported by the extinction spectra in Figure 3.25(a). Measurements were repeated one month after initial analysis with very little change in results observed indicating that PEG-HGNs are stable in up to 5 M NaCl for at least one month (Figure 3.26).

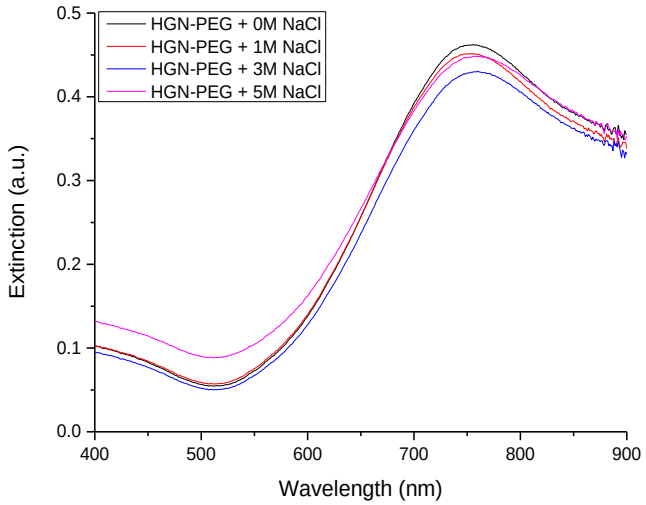

Figure 3.26: Extinction spectra of PEG-stabilised HGNs after one month suspended in increasing NaCl concentrations.

This data was supported by particle size measurements which remained consistent in PEG-HGNs over the one month period (Table 3.6) whereas citrate-HGNs formed large aggregates within the solution.

Table 3.6: Particle size and zeta potential values of PEG-stabilised HGNs measured after one month suspended in increasing NaCl concentrations. Particle size and zeta potential values are quoted as the mean of three replicates of each sample with error ± one standard deviation.

Sample	Particle Size Diameter (nm)	Zeta Potential (mV)
HGN-PEG + 0 M NaCl	95.6 ± 2	-41.8 ± 3.8
HGN-PEG + 1 M NaCl	90.9 ± 0.3	-20.1 ± 6.8
HGN-PEG + 3 M NaCl	91.9 ± 0.3	-14.7 ± 2.7
HGN-PEG + 5 M NaCl	91.5 ± 0.6	-11.6 ± 1.2

Zeta potential values of PEG-HGNs became less negative with increasing salt concentrations (Table 3.6). This was to be expected as a result of the increasing cationic proportion within the samples on increasing NaCl concentration however as previously stated this caused no adverse effect on the PEG-HGN stability as steric effects where enough to overcome the charge screening induced by the added counter ions.

3.4.3 Long Term Stability

Improvement in long term stability of colloidal systems is an important parameter to investigate as future applications may be limited if nanoparticles aggregate at a rate faster than which they can be put to suitable use. Long term stability of the HGN solutions synthesised were compared, with all HGN solutions dispersed in $d.H_2O$ and stored in glass vials out of direct sunlight. Generally, citrate HGNs can be redispersed in a citrate buffer to maintain an increased stability over time however for comparison with other HGNs $d.H_2O$ was used in this investigation. It is important to note that in citrate buffer they still do not display the same level of stability compared to PEG-HGNs redispersed in $d.H_2O$.

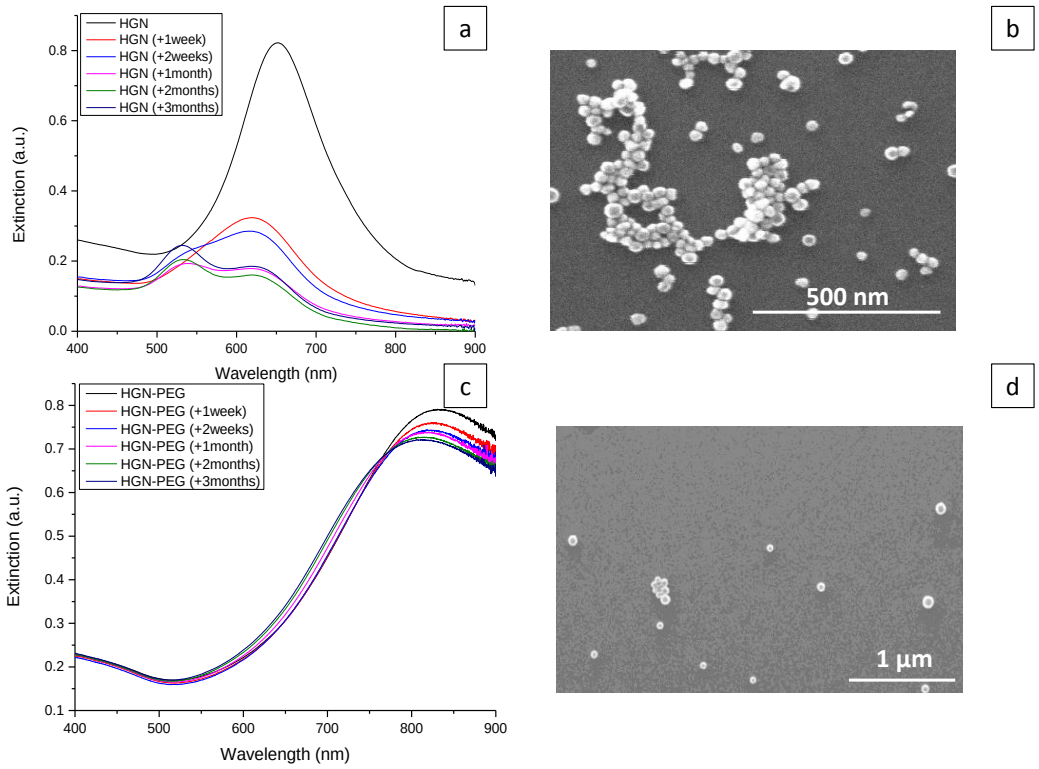

Figure 3.27: Extinction spectra and corresponding SEMs of (a), (b) citrate-stabilised HGNs and (c), (d) PEG-stabilised HGNs measured at specific time intervals after initial synthesis. SEMs were taken 3 months after initial synthesis.

Figure 3.27 compares the stability of citrate and PEG-stabilised HGNs over a three month period. The extinction spectra for citrate-HGNs (Figure 3.27a) taken at specific time intervals over a three month period show that after just one week the SPR has significantly broadened and dampened, indicating that a significant amount of aggregation has occurred. After three months there is considerable dampening in SPR at 650 nm and a new SPR band appears at around 529 nm which is more representative of solid gold nanoparticles. This could be a consequence of varied aggregation states within the sample with the red and blue shifted SPR bands resulting from large aggregates, partial aggregates and single particles co-existing within the solution. The presence of large numbers of aggregates alongside single particles was confirmed by SEM imaging taken after three months, an example of which is shown in Figure 3.27b. Although this was the most likely explanation for the change in extinction spectra observed, it was also possible that the new SPR band

at 529 nm was a result of the HGNs beginning to lose their hollow interior. Particle size and zeta potential measurements recorded concurrently over the same three month period (Figure 3.28) supported this second hypothesis with very little change in particle size and no presence of aggregates indicated. In the SEM image in Figure 3.27b it could be argued that some of the HGNs no longer appear hollow however higher resolution TEM imaging would need to be carried out to confirm this hypothesis.

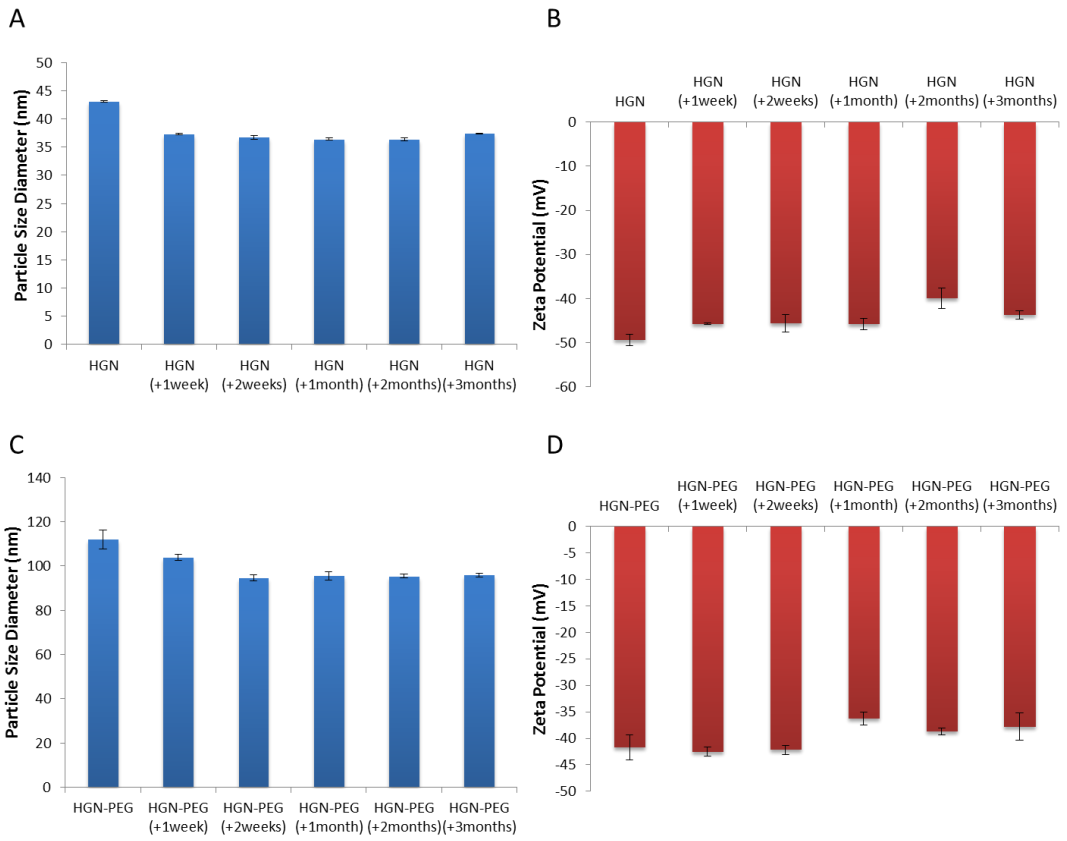

Figure 3.28: Particle size and zeta potential measurements taken at specific time intervals after initial synthesis of (A), (B) citrate-stabilised HGNs and (C), (D) PEG-stabilised HGNs. Error bars are ± one standard deviation.

In contrast, PEG-HGNs were still stable after a period of three months indicated by the lack of change in extinction spectra in Figure 3.27c and monodispersity in the sample shown in the SEM image in Figure 3.27d. Again, particle size and zeta potential values stayed relatively consistent over the three month time period studied.

Further to this study, HGNs stabilised with a shorter PEG chain length (MW 635) as opposed to the larger molecular weight PEG (MW 5000) were additionally analysed over the three month period (Figure 3.29) however these showed much reduced stability over time indicating that the steric stability from the larger chain length is fundamental to the increased stability observed within the samples. Additionally, the shorter chain PEG-stabilised HGNs did not exhibit as significant a red-shift in SPR as their longer chain length counterparts possibly as a result of a reduction in hindrance to the formation of the gold shell during the synthesis.

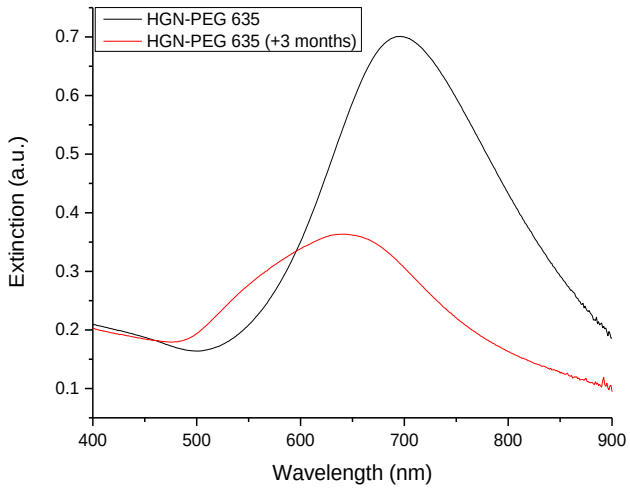

Figure 3.29: Extinction spectra of PEG(635)-stabilised HGNs measured after the initial synthesis (black) and after a period of three months (red).

Extinction spectra and corresponding SEM images for all other HGNs are shown in Figures 3.30 and 3.31. It is apparent from these that all other coatings impart a degree of stabilisation to the HGNs and maintain relatively stable solutions.

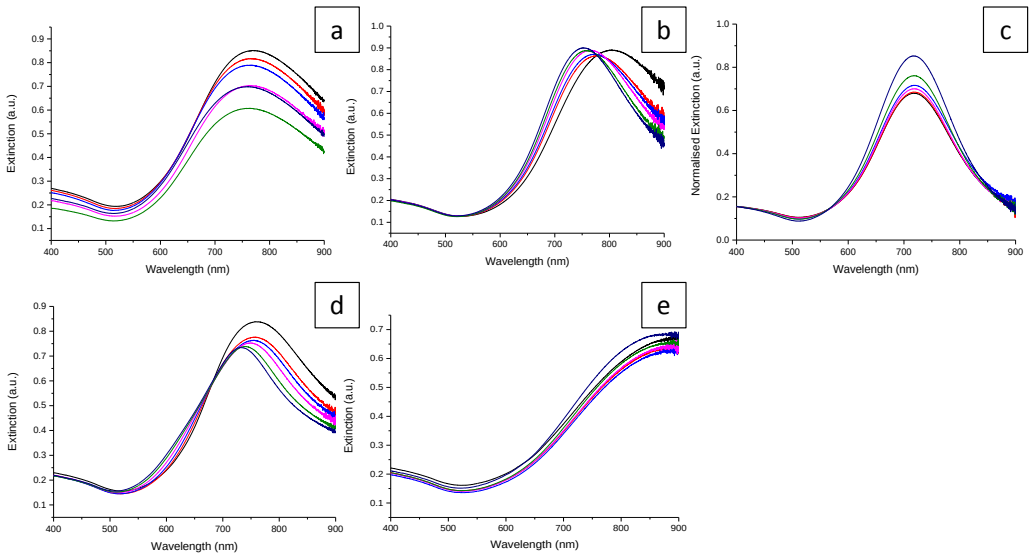

Figure 3.30: Extinction spectra of (a) PAM-stabilised HGNs, (b) PVP-stabilised HGNs, (c) silica-stabilised HGNs, (d) dextran-stabilised HGNs and (e) thioglucose-stabilised HGNs measured at specific time intervals after initial synthesis. Initial sample (black), +1week (red), +2weeks (blue), +1month (pink), +2months (green), and +3months (purple).

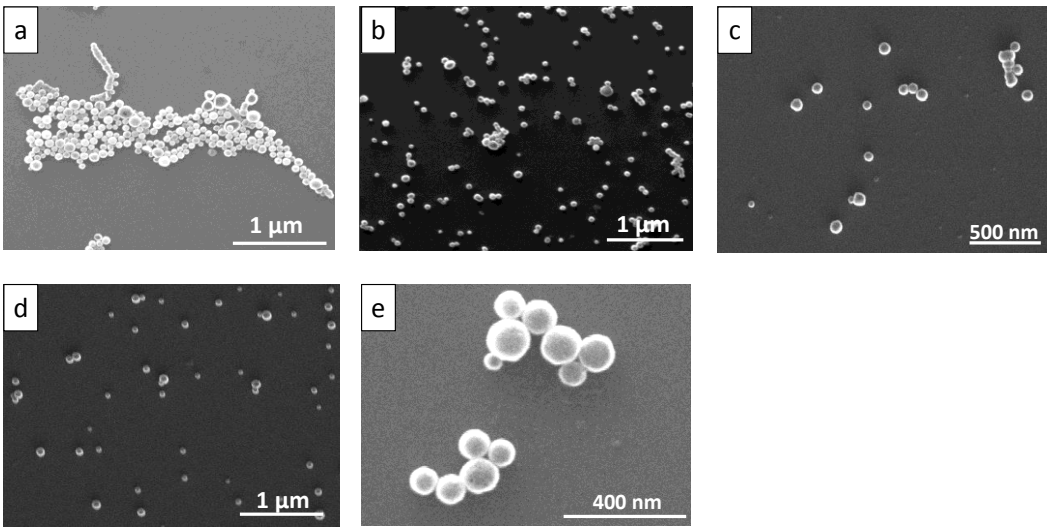

Figure 3.31: SEM images corresponding to extinction spectra in Figure 3.27 of (a) PAM-stabilised HGNs, (b) PVP-stabilised HGNs, (c) silica-stabilised HGNs, (d) dextran-stabilised HGNs and (e) thioglucose-stabilised HGNs taken three months after initial synthesis.

This provided additional confirmation that the various stabilising agents were present on all HGNs synthesised within this chapter providing increased colloidal stability over time in contrast to citrate stabilised HGNs.

3.5 Chapter Conclusions

A methodology for the general synthesis of standard citrate stabilised HGNs which could subsequently be adapted to provide additional functionality and added stability to the nanostructures was developed. However, inter-batch reproducibility within the synthesis was limited producing HGNs with a LSPR of 700 ± 50 nm.

Previously reported methods for functionalisation of solid gold nanoparticles were assessed as being non-transferable to HGNs due to a reduction in nanoparticle stability in hollow gold compared to solid gold. One previously reported method for HGN functionalisation within the literature was successfully reproduced however this was limited to use with PVP and could not be extended for use with other stabilising agents. Consequently, an improved method for HGN functionalisation was developed by incorporating polymers and sugars into the synthesis as stabilising agents. This method both improved the stability of the resultant HGNs and shifted their SPR to longer wavelengths making them advantageous for use in many biomedical applications where nanostructures with a SPR in the NIR region are desirable. Furthermore, this method increased the reproducibility between each synthesis overcoming the major limitation described for standard citrate stabilised HGNs.

An alternative methodology for the silica encapsulation of standard citrate HGNs was developed and optimised. Three silane coupling agents were investigated for use with HGNs; APTMS afforded the most stability to the nanoparticle precursors during the synthesis while MPTMS and PEG formed silica encapsulated HGNs of insufficient quality and concentration to be used in further studies. Modifications of the Stöber method were investigated. Reaction time and TEOS volume was optimised to provide thin, complete silica shells which could be used in future SERS based applications.

The stability of all functionalised HGNs were systematically compared in different salt and pH environments. The results indicated that in regards to HGNs, PEG is by far the most suitable stabilising agent increasing stability to high salt concentrations

and pH extremes with an inherent stability in both environments for up to one month. The stabilisation provided was thought to be mainly a steric effect resulting from the densely packed PEG layer on the HGN surface and less dependent on charge effects due to the sustained stability in various pH environments. Standard citrate stabilised HGNs were shown to be highly unstable both over time and to changes in surrounding environment which severely limits their potential future applications.

Overall, the stabilised HGNs synthesised within this chapter possess a combination of increased stability across a range of environments and long term stability which offers great potential for use in applications such as biological SERS imaging and drug delivery.

4 Stable, Red-shifted SERS Nanotags for use in Bio-imaging

4.1 Introduction

Surface-enhanced Raman scattering (SERS) is a highly sensitive spectroscopic technique used to detect molecules in close proximity or attached to a metal surface.[35] The development of stable, SERS substrates in the NIR region are of great interest for use in many biomedical applications as light at wavelengths between 800 and 1200 nm can penetrate human tissue and blood, thus providing a transparent sensing window.[25, 60] Additional benefits at longer excitation wavelengths include reduced autofluorescence, limited photobleaching and better penetration depth in biological tissues; useful in biological SERS imaging.[163, 164]

In the NIR region, Raman scattering is a relatively weak process as it is dependent on the fourth power of the frequency, whereas SERS can provide more enhanced signals as it is mainly dependent on electromagnetic (EM) enhancement which arises when localised surface plasmon resonances (LSPRs) on a metal surface are excited.[119, 127] Surface-enhanced resonance Raman scattering (SERRS) can result in further electronic enhancements when a reporter molecule in resonance with the excitation laser is used.[131] Therefore it is necessary to develop nanostructures with LSPRs in the NIR region such as those developed in Chapter 3, which can be used as effective SERS substrates.

Aggregation of nanoparticles is widely used to create areas of highly localised EM fields at interparticle junctions known as SERS 'hot-spots'.[44] Molecules which are confined to these areas experience large EM enhancements and intense Raman signals can be observed, specific to the molecule of interest.[165, 166] However, this aggregation (normally induced by the addition of an inorganic salt) is difficult to control and nanoparticle instability can lead to over-aggregation and precipitation from solution. This can severely limit the reproducibility in the SERS signals observed, as structural homogeneity within the sample is compromised.[23] Therefore,

there is a significant need to develop stable nanotags which can provide effective SERS signals without the need to induce aggregation.

Early work involving SERS without the need for induced aggregation involved core/shell systems.[24, 167] These consist of a dielectric core surrounded by a thin metallic shell which are monodispersed and tunable to the NIR region. It was found that single particle SERS could be achieved as the EM field can extend further from the surface than in conventional AuNPs which allows for greater enhancements. Additionally, the shells are formed from small aggregates of nanoparticles introducing a roughness in the surface not present in solid, spherical particles which allows for further enhancements.[167] Nanostructures have also been designed to include structural 'hot-spots' where exposed sharp edges can enhance the EM field.[168] However, although both these substrates remove the need for induced nanoparticle aggregation they are greater than 100 nm in particle diameter which limits cellular uptake and therefore restricts future bio-applications.[46]

Alternatively, hollow gold nanospheres (HGNs) make for excellent reproducible SERS substrates not only due to their tunable LSPR for NIR applications and small size but due to their ability to achieve single particle SERS.[52] The mechanism of HGN synthesis, where the gold shell is formed on a cobalt nanoparticle template by oxidation of cobalt and reduction of gold across the shell, creates surface pinholes which can act as efficient 'hot-spots' for SERS enhancements.[52]

As previously mentioned (Chapter 3) standard citrate-stabilised HGNs are highly unstable to changes in their surrounding environment, thus SERS reproducibility can be compromised in biological environments likely to induce nanoparticle aggregation. Therefore there is a significant need to develop stable NIR active HGNs which can act as reproducible SERS substrates in biological environments.

As a result of the combination of unique properties possessed by HGNs, and primarily their tunable plasmon absorption to the NIR region, there have been several reports demonstrating their ability for use in many biomedical applications such as photothermal ablation therapy,[51] cancer imaging and diagnosis,[48, 152] and as effective drug delivery agents.[34, 50] Additionally, PEG functionalised HGNs have previously

undergone extensive biosafety evaluations and displayed limited *in vitro* and *in vivo* toxicity.[146]

As a result of a combination of the aforementioned properties exhibited by HGNs and due to their potential for use in numerous bio applications, within this chapter the stabilised HGNs synthesised in chapter 3 were assessed as potential stable red-shifted SERS substrates and initial bio imaging work was performed to evaluate their potential for use in future biomedical applications.

4.2 Nanotag Development

Nanotags comprise of a metallic nanoparticle acting as a SERS substrate combined with a Raman active reporter molecule which can be further functionalised for targeted detection.[94, 169] Stabilised HGNs developed in Chapter 3 were investigated as potential SERS substrates for the development of stable nanotags which could be used in bio applications without the need for induced aggregation. As SERS is dependent on the number of particles within the laser interrogation volume it was important that all HGN concentrations were kept relatively consistent throughout the analysis. A Nanosight LM10 system was used to obtain approximate HGN concentrations using Nanoparticle Tracking Analysis (NTA) software. As the instrument has a limited excitation wavelength it was not sensitive enough to give accurate values for red-shifted nanoparticles so values calculated were approximate. The HGNs investigated within this chapter were dispersed in d.H_2O and stored at final concentrations of 2 nM – 3 nM for further analysis.

4.2.1 Raman Reporter Investigation

Careful selection of a Raman reporter which could be used in the stabilised nanotag system was required. It was necessary to find a suitable reporter that produced sufficiently strong signals to allow for an enhanced signal through the stabilising layer present on the HGN surface.

4.2.1.1 Commercial Reporters

Initial studies focussed on frequently used, commercially available Raman reporters. Malachite green isothiocyanate (MG-ITC) is an extensively used Raman reporter, with intense spectra reported in the presence of polymer and silica stabilising layers.[110, 170]

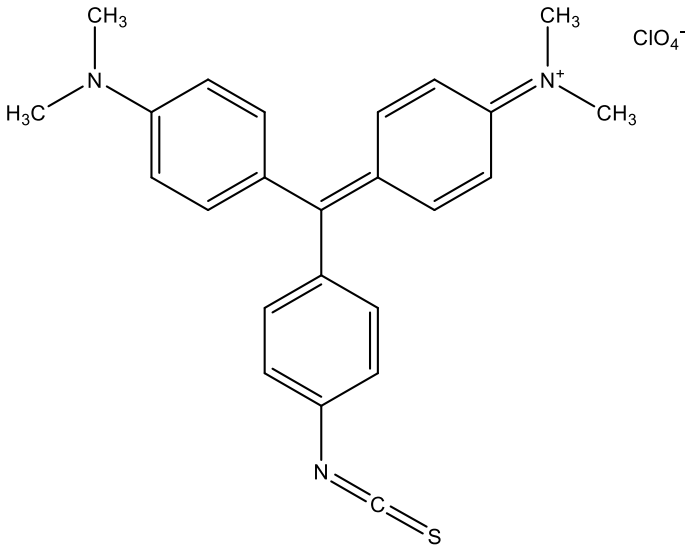

Figure 4.1: Chemical structure of malachite green isothiocynate (MG-ITC).

It has an absorption maximum at 633 nm allowing for increased signal intensities from resonance contributions at this excitation wavelength and also contains an isothiocyanate group which can strongly adsorb onto a gold surface allowing for surface enhancement. Notably, signals have previously been observed using MG-ITC with nonaggregated HGNs however only when the SPR, along with the dye, are in resonance with the excitation wavelength.[35] To study the suitability of MG-ITC as a reporter for use with the stabilised HGN substrates it was added to both PEG and citrate stabilised HGNs; respectively the most and least stable to changes in external environment as concluded from the work in Chapter 3. Conventionally, Raman reporter molecules are conjugated to the metallic substrate prior to the addition of the stabilising layer to maximise the surface EM enhancement effect. Due to the method used for adding the stabilising layer within this work (at the final stage in the HGN synthesis) the reporter was added following successful HGN functionalisation with various stabilising agents. For comparison, the reporter was also incorporated into

the HGN synthesis where it was added ten minutes prior to either the PEG or citrate stabilising agent to allow for direct binding to the HGN surface. MG-ITC was added at a final concentration of 50 nM to ensure that it did not induce aggregation when added to the citrate stabilised HGNs. Results observed at 633 nm excitation are shown in Figure 4.2.

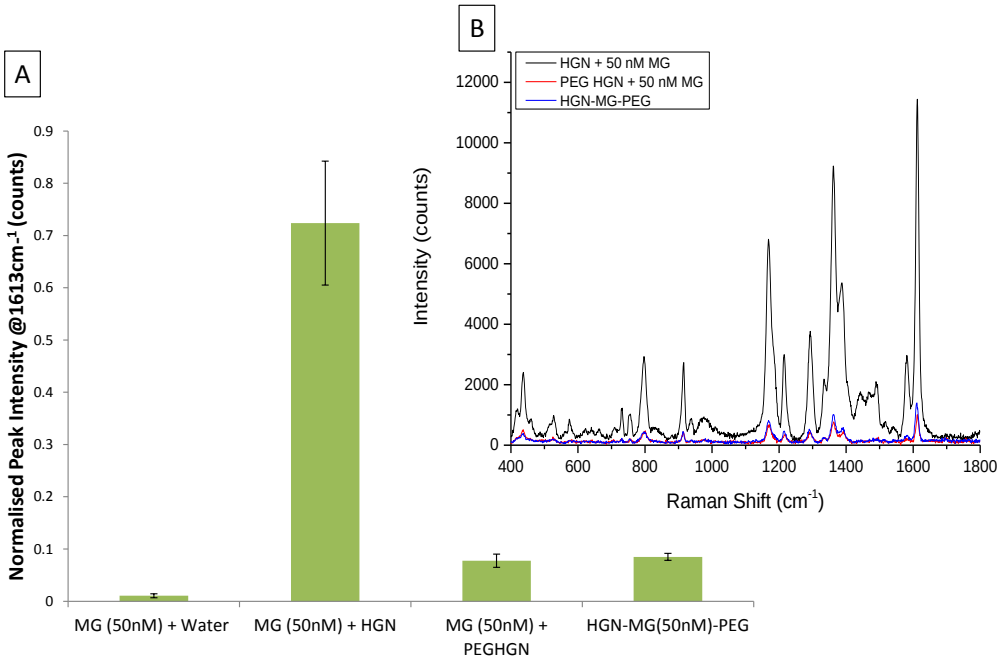

Figure 4.2: SERRS spectra recorded using an excitation wavelength of 633 nm: (A) Normalised SERS peak intensities at 1613 cm^{-1} for MG-ITC at 50 nM final concentration with standard citrate HGNs and PEG stabilised HGNs where the MG-ITC was incorporated before (HGN-MG-PEG) and after (PEG HGN + MG) the PEG layer was added, (B) SERS spectra of MG-ITC at 50 nM final concentration with standard citrate HGNs and PEG stabilised HGNs where the MG-ITC was incorporated before (HGN-MG-PEG) and after (PEG HGN + MG) the PEG layer was added. Spectra were obtained by scanning 3 replicates of each sample with a 10s accumulation time and laser incident power of 4.5mW. Averages are shown and error bars are ± one standard deviation.

Extinction spectra measured for the three HGNs used within this study showed that the citrate-stabilised HGN had an SPR closest to that of the excitation wavelength with an SPR at 692 nm. PEG stabilised HGNs with MG-ITC incorporated before and after the PEG stabilising layer was added had SPRs of 790 nm and 824 nm respectively, and thus were not in resonance with the laser. The results in Figure 4.2

revealed that the presence of the PEG stabilising layer on the HGN surface reduced the signal intensity from the MG-ITC by a factor of ten approximately. This was highlighted in Figure 4.2A where the normalised peak intensity of the prominent peak at 1613 cm^{-1}, present due to C-C ring stretching in the aromatic rings in the dye structure[171], was compared. The reduction in signal could be due to a number of factors. Firstly, the presence of the PEG layer could limit the amount of reporter in close proximity to the HGN surface irrespective of whether the reporter was added prior to or subsequent to the addition of the PEG stabilising layer. If the reporter was added after the stabilising layer the PEG could hinder the adsorption of MG-ITC on the HGN surface, increasing the distance of the reporter from the nanoparticle surface which would limit the SERS intensity observed. Conversely, if the PEG was added after the reporter this could lead to competition for binding sites resulting in a lower reporter surface coverage than for citrate stabilised HGNs where the MG-ITC can readily displace the electrostatically bound citrate stabilising layer. Secondly, the SPR of the citrate stabilised substrates is closer to the laser excitation wavelength which could increase the surface enhancement effect. However it was recently reported that the SERS performance of HGNs is more dependent on the shell thickness than if the SPR is in resonance with the laser.[35] The red-shifted HGNs, stabilised with PEG, tend to have thinner outer shells than standard citrate HGNs. Thinner shells have a lower outer electric field compared to thicker shells[172] so therefore the reduction in signal could also be due to the weaker electric field distribution in the PEG stabilised HGNs. This ultimately resulted in minimal signal variations using the two methods for adding MG-ITC to the PEG stabilised HGNs. Therefore, as the synthesis was developed and optimised for addition of stabilising agents directly on to the HGN surface in the final stage of the synthesis, and so an identical batch of stabilised HGNs could be used for multiple studies with varied reporter concentrations, reporter molecules would be added subsequent to the addition of the stabilising layer for the remainder of the studies.

MG-ITC with no HGN present gave negligible signals which indicated that the enhancement observed was a result of surface enhancement from the HGN combined with resonance from the dye and not solely from the presence of the resonant reporter molecule.

To investigate the lowest observable limit of detection which could be achieved for MG-ITC with PEG stabilised HGNs at a laser excitation of 633 nm a concentration study was undertaken. The same PEG-HGN sample was used for all measurements. Results are presented in Figure 4.3.

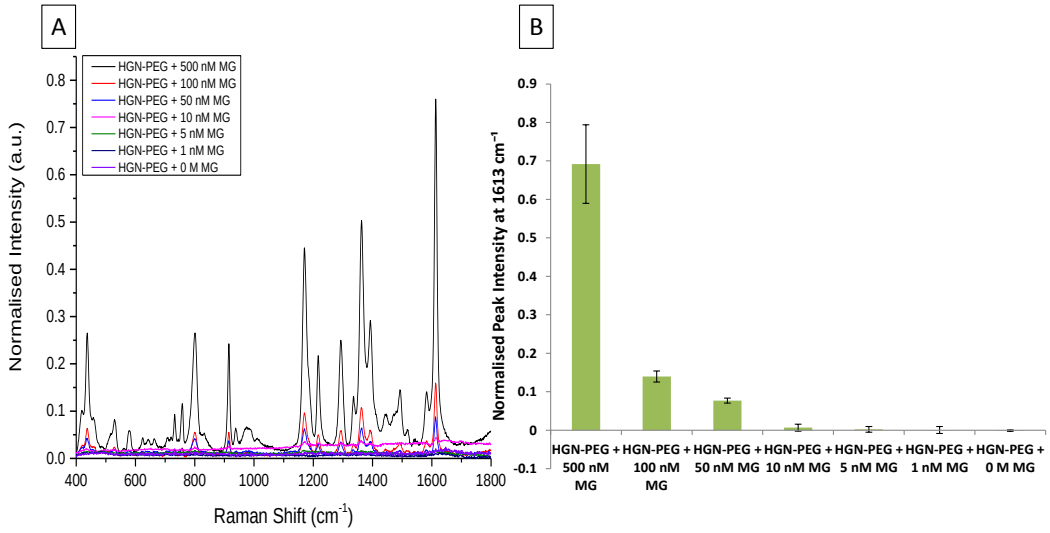

Figure 4.3: SERRS spectra recorded using an excitation wavelength of 633 nm: (A) SERS spectra of PEG stabilised HGNs with MG-ITC concentrations between 0 M and 500 nM, (B) Normalised SERS peak intensities at 1613 cm^{-1} for MG-ITC at incremental concentrations from 0 M to 500 nM final concentrations of MG-ITC. Spectra were obtained by scanning 3 replicates of each sample with a 10s accumulation time and laser incident power of 4.5mW. Averages are shown and error bars are ± one standard deviation.

Again, the peak intensity at 1613 cm^{-1} was compared (Figure 4.3B) to highlight the relative intensity changes. Results observed were promising for initial studies with a lowest observable final concentration of 50 nM for MG-ITC at 633 nm.

However, as the aim of this chapter was to exploit the NIR SPR of the stabilised HGNs for potential use in biomedical applications, the resultant MG-ITC labelled PEG stabilised nanotags would be required to give intense signals at longer wavelengths, off resonance with the reporter molecule. As a result, this nanotag system was also analysed at 785 nm laser excitation (Figure 4.4).

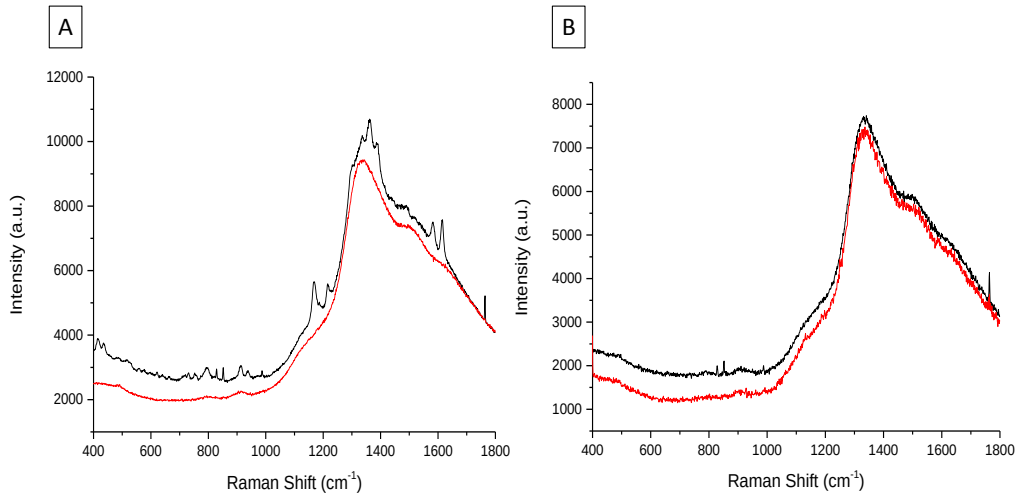

Figure 4.4: SERS spectra recorded using an excitation wavelength of 785 nm: (A) citrate stabilised HGNs with 50 nm MG-ITC (black) and PEG stabilised HGNs with 50 nM MG-ITC (red), (B) control spectra; HGN only (black) and glass cuvette only (red). Spectra were obtained by scanning 3 replicates of each sample with a 10s accumulation time and laser incident power of 41 mW.

Unfortunately, results indicated that the main enhancement in the results observed at 633 nm was from the resonance contribution of the dye at this wavelength. Thus when the excitation wavelength was moved off resonance from the dye negligible SERS signals could be observed using the PEG stabilised HGN substrates. Minimal signals could still be observed from the citrate-stabilised HGNs however both spectra had large background fluorescence signals. From the control experiments (Figure 4.4B) it was concluded that the fluorescence background could be attributed to the glass cuvettes which were used for sample analysis. This could be a result of the reporter not being sensitive enough at this wavelength to produce SERS signals strong enough to overcome the fluorescence background. Consequently, malachite green was disregarded as a Raman reporter for use with the stabilised HGN substrates as it only produced SERS signals at 633 nm.

The second commercially available Raman reporter investigated was 1,2-bis(2-pyridyl)ethylene (BPE). BPE possesses a highly conjugated π-electron system with two nitrogen atoms suitable for binding to metal surfaces which allows for electron transport and energy transfer processes to occur within the molecule.[173-175] The chemical structure is shown in Figure 4.5.

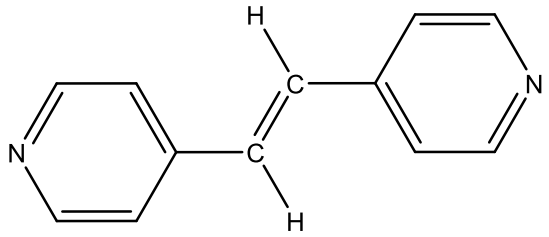

Figure 4.5: Chemical structure of 1,2-bis(2-pyridyl)ethylene (BPE).

Previous work has reported that BPE, which is non resonant at laser wavelengths used so does not contribute to resonance enhancement, gives more enhanced signals at longer wavelengths than at 633 nm when HGNs are used as substrates.[35] More recently, work has shown that BPE provides much larger enhancements than other commercially available reporters such as 4,4-azopyridine (AZPY) and 4-mercaptobenzoic acid (MBA) when used with NIR citrate stabilised HGN substrates at 1064 nm laser excitation.[174] Although partial aggregation was induced to achieve these results, BPE looked to be promising for use with the various stabilised HGNs at longer wavelengths.

Initial studies looked into comparing the SERS response of BPE at 633 nm to that of MG-ITC (Figure 4.2). For an accurate comparison the same HGNs were used, thus nanoparticle concentration and SPRs were kept consistent with the exception of PEG HGNs with BPE added before the PEG stabilising layer in the synthesis which had an SPR of 819 nm. Results obtained are shown in Figure 4.6. The SERS spectra observed were significantly weaker than for MG-ITC due to the absence of the reporter resonance contribution at this wavelength. There was a large fluorescence background present in Figure 4.6A which has not been quenched, indicating that no aggregation has taken place within the samples. Baseline corrected spectra (Figure 4.6B) and the plotted normalised peak intensity at 1635cm^{-1} (Figure 4.6C), associated with the vinyl C=C stretching mode[173, 174], highlight the reduction in SERS enhancement when the PEG stabilising layer is present.

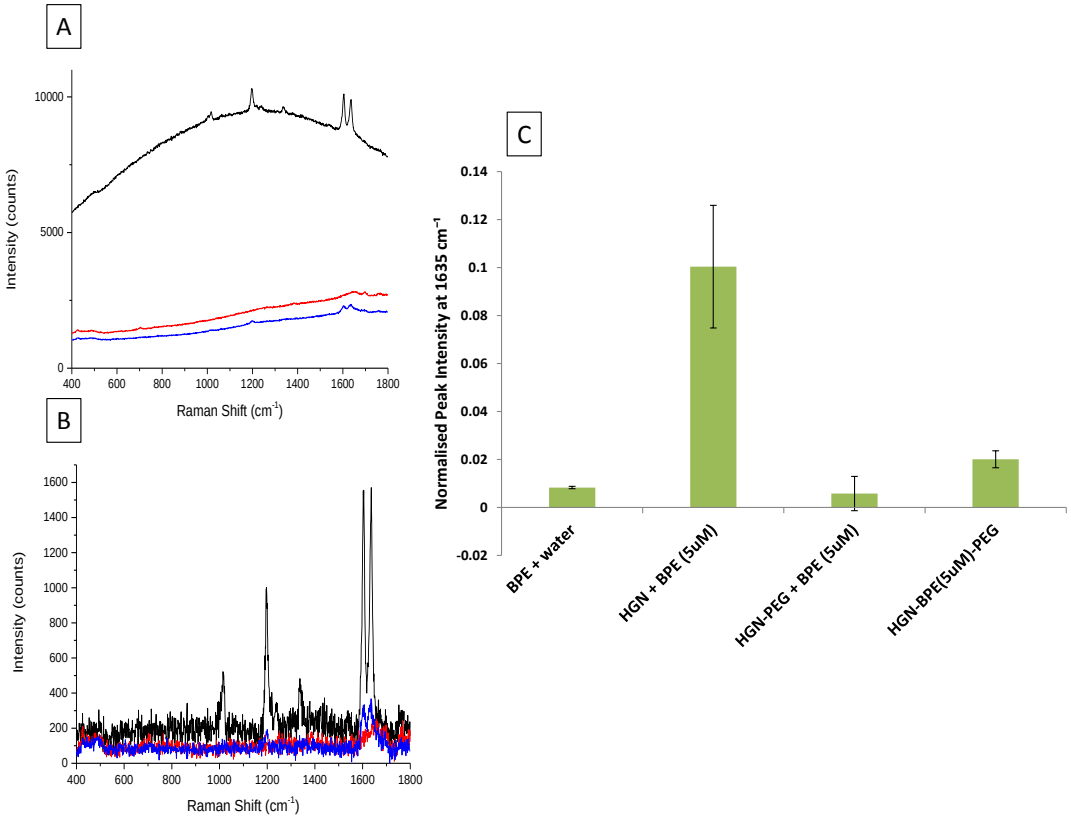

Figure 4.6: SERS spectra recorded using an excitation wavelength of 633 nm: (A) SERS spectra of BPE at 5 µM final concentration with standard citrate HGNs (black) and PEG stabilised HGNs where the BPE was incorporated before (HGN-BPE-PEG) (blue) and after (PEG HGN + BPE) the PEG layer was added (red). (B) Baseline corrected spectra for results shown in (A) HGN+BPE (black), HGN-BPE-PEG (blue) and PEG HGN + BPE (red). (C) Normalised SERS peak intensities at 1635 cm^{-1} for BPE at 5 µM final concentration with standard citrate HGNs and PEG stabilised HGNs. Spectra were obtained by scanning 3 replicates of each sample with a 10s accumulation time and laser incident power of 4.5mW. Averages are shown and error bars are ± one standard deviation.

This result was not surprising as BPE has been previously reported to show limited signals at 633 nm with red-shifted HGN substrates.[35] The reduction in signal observed in the presence of the stabilising layer was again thought to be due to the reduced interaction between BPE and the HGN surface as the SERS effect decreases exponentially as a function of distance from the nanoparticle.[176] Furthermore, it has been reported that the vinyl stretching band analysed at 1635 cm^{-1} is enhanced through interaction with the SPR,[174] which indicates that the reduction in signal when the PEG layer is present is due to the reporter molecule not being in close proximity

to the HGN surface. This was confirmed by the control where no nanoparticles were present, showing that when BPE was added to the pre-functionalised HGNs there was no increase in signal observed so no enhancement effect was involved. When the BPE was added prior to the PEG layer during the synthesis there was a slight enhancement in signal observed indicating that a small number of BPE molecules may have been trapped within the PEG layer however as stated previously this method of reporter addition was inefficient for further studies and the enhancement achieved was not significant enough to be worthwhile. Additionally, a concentration study was carried out at 633 nm with PEG stabilised HGNs as substrates however no observable limit of detection was apparent as the spectra for concentrations of 100 µM and greater were dominated by ethanol solvent peaks.

Following the unsuccessful result at 633 nm the nanotags were analysed at 785 nm where the PEG-stabilised HGNs with an SPR of 824 nm were closer to the resonance of the laser than at 633 nm. Following the success of the reported SERS of aggregated HGNs with BPE at 1064 nm it was hoped that some signals would be observed from the isolated HGNs within this work. Results observed for a final concentration of 5 µM of BPE added to both citrate and PEG stabilised HGNs are shown in Figure 4.7. Results showed minimal change in the spectra observed using standard citrate HGNs as substrates while the PEG stabilised HGNs appeared to show a slight enhancement in the signal observed indicating that there was some added enhancement from the SPR at this wavelength.

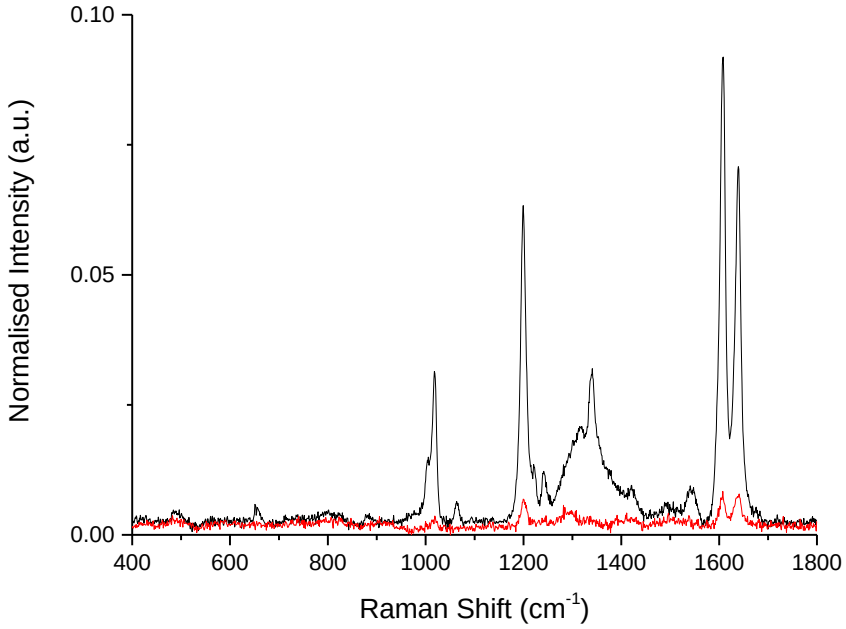

Figure 4.7: SERS spectra recorded using an excitation wavelength of 785 nm of BPE at 5 µM final concentration with standard citrate HGNs (black) and PEG stabilised HGNs (red). Spectra were obtained by scanning 3 replicates of each sample with a 10s accumulation time and laser incident power of ~75 mW.

However, the presence of the PEG layer still reduced the signal intensity by a factor of eight approximately. A concentration study was carried out at 785 nm (Figure 4.8) where the lowest observable concentration appeared to be at 5 µM however the spectra observed had a high signal to noise ratio. The BPE was not a strong enough SERS reporter to give intense signals when the stabilising layer was present due to the increased proximity from the HGN surface and the absence of SERS 'hot-spots' resulting from salt induced aggregation. For these stabilised nanotags to be used in biomedical applications such as intracellular SERS imaging the signals achieved must be significantly enhanced as signals will be further reduced within cells.[133] Therefore, BPE was not suitable for use within this nanotag system so further reporter investigations were required.

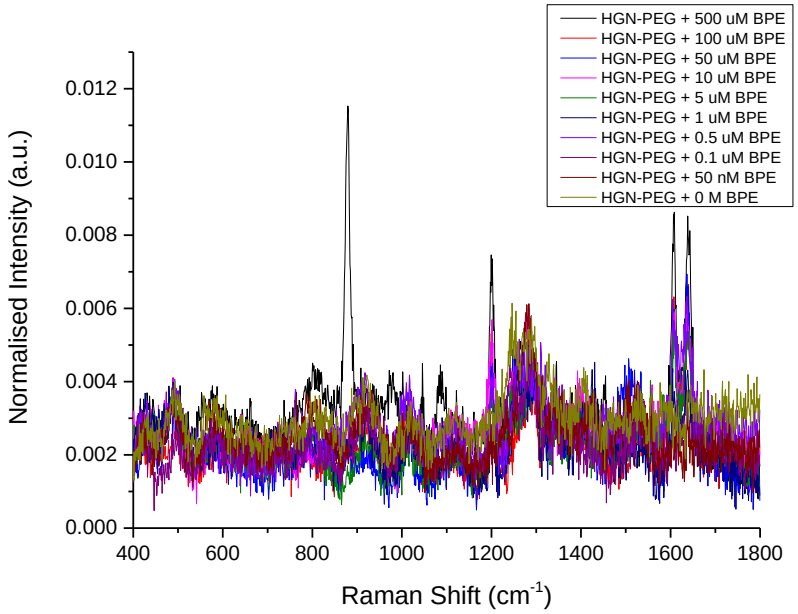

Figure 4.8: SERS spectra recorded using an excitation wavelength of 785 nm of PEG stabilised HGNs with BPE concentrations between 0 M and 500 uM. Spectra were obtained by scanning 3 replicates of each sample with a 10s accumulation time and laser incident power of ~ 140 mW. Averages are shown and error bars are ± one standard deviation.

4.2.1.2 Chalcogenpyrylium Dyes

A new class of Raman reporters, synthesised by collaborators at The University at Buffalo, which are highly aromatic and produce rich vibrational spectra[177] were investigated for use with the stabilised HGN substrates. It was reported that these dyes could produce intense SERS spectra with calculated limits of detection in the picomolar range at 1280 nm from partially aggregated HGNs that did not have an SPR which matched the laser excitation.[177] Following this work, two trimethine dyes, reported to produce more enhanced signals than their monomethine counterparts, were chosen for reporter studies. Their structures and extinction spectra in DMF are presented in Figure 4.9.

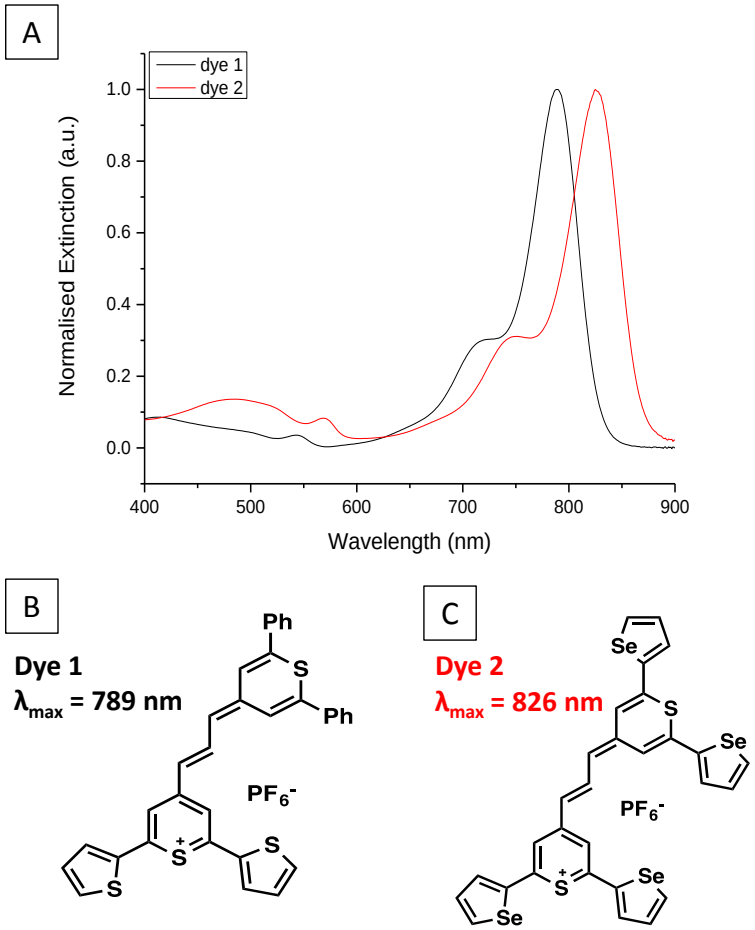

Figure 4.9: (A) Normalised extinction spectra of Raman reporters dye 1 and dye 2 with a λ_{max} of 789 nm and 826 nm respectively. Structures of (B) dye 1 and (C) dye 2.

The reporter labelled dye 1 (otherwise known as dye 073) is a sulphur-based compound with a λ_{max} of 789 nm and dye 2 (otherwise known as dye 114) is a structurally similar selenium-based compound with a λ_{max} of 826 nm. Both dyes contain sulphur atoms in the chalcogenpyrilium backbone but the change in substituents, 2-thienyl groups in dye 1 and 2-selenophenyl groups in dye 2, allows for each to possess a unique Raman fingerprint. An affinity for the HGN surface was provided by the thiophene and selenophene substituents which have previously been reported to form self-assembled monolayers on gold surfaces.[178, 179]

Initial studies using these two new reporters were carried out at a laser excitation of 633 nm in order to compare their relative signal intensities with the commercial reporters previously investigated. A final concentration of 5 µM of each of the dye

molecules was added to both citrate-stabilised HGNs (λ_{max} = 686 nm) and PEG-stabilised HGNs (λ_{max} = 757 nm) following studies with commercial reporters which concluded that little variation in signal intensities was observed when reporters were added prior to the stabilising layer. Analysis was performed at 633 nm without any induced aggregation and results observed are shown in Figure 4.10.

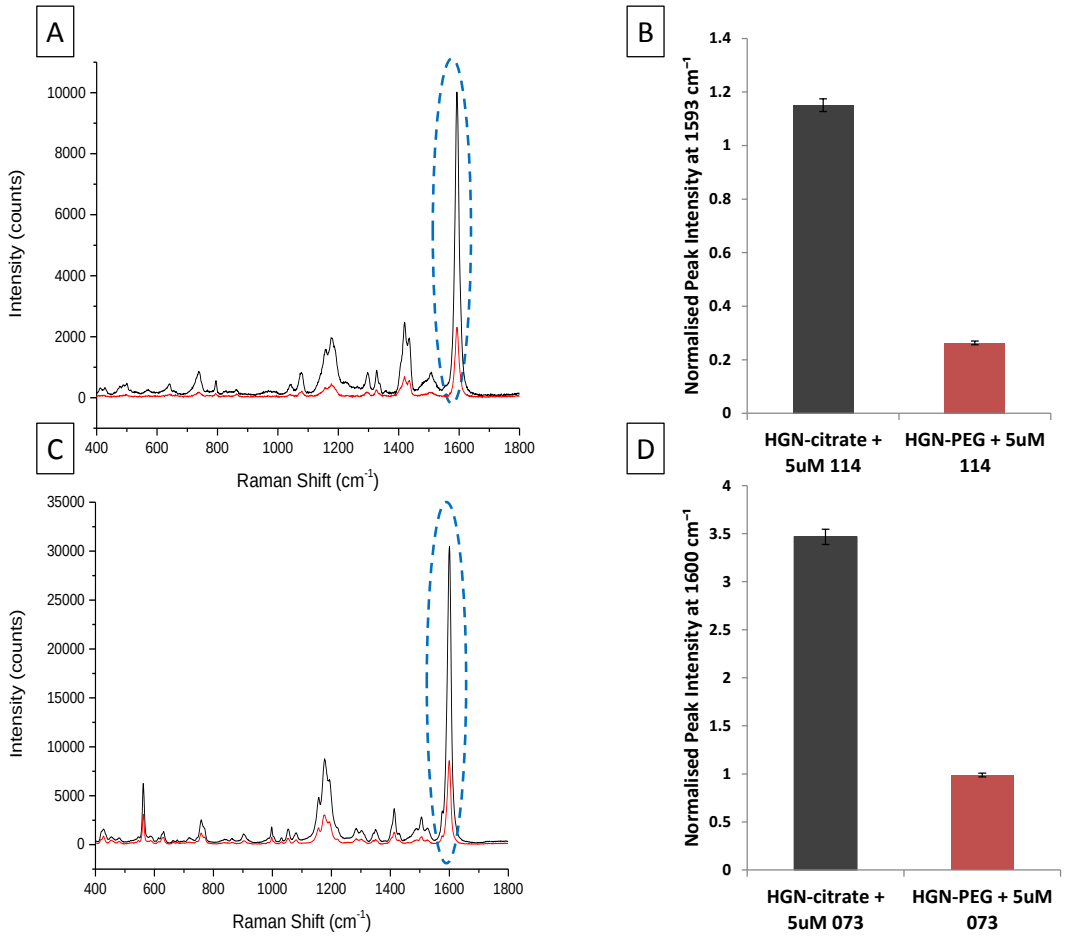

Figure 4.10: SERS spectra recorded using an excitation wavelength of 633 nm: (a) SERS spectra of dye 2 (dye 114) using standard citrate-HGNs (black) and PEG-stabilised HGNs (red); (b) SERS peak intensities at 1593 cm^{-1} for dye 2 (dye 114) at 5 µM final concentration using both HGN substrates; (c) SERS spectra of dye 1 (dye 073) using standard citrate-HGNs (black) and PEG-stabilised HGNs (red); (d) SERS peak intensities at 1600 cm^{-1} for dye 1 (dye 073) at 5 µM final concentration. Spectra were obtained by scanning 3 replicates of each sample with a 10s accumulation time and laser power of 6.2 mW. Averages are shown and error bars are ± one standard deviation.

A similar trend to that observed for both commercial reporters was apparent, with a reduction in signal intensities caused by the presence of the PEG stabilising layer, although the reduction in signal was not as significant as previously shown. This could again be explained by the reduction in the number of sites on the HGN surface available for the reporters to bind when the PEG layer was present, as well as the increased distance of the reporter from the nanoparticle surface. The prominent peak highlighted at 1600 cm^{-1} for dye 1 and slightly shifted to 1593 cm^{-1} for dye 2, which is present due to heterocyclic aromatic ring stretching within both molecules, was compared to highlight the reduction in signal intensities observed for the two dyes. Although the spectra achieved were not as intense as the results observed using MG-ITC, with normalised intensities of the prominent peaks for PEG-stabilised HGNs using a final concentration of 500 nM of each reporter calculated to be 0.69 counts, 0.14 counts and 0.06 counts for MG-ITC, dye 1 and dye 2 respectively, this was somewhat expected as no resonance contribution from dye 1 or dye 2 would be present at this wavelength.

To compare the relative intensities of the two chalcogen reporters a final concentration of 10 µM of each dye was added to PEG-stabilised HGN substrates and analysed under identical experimental conditions. Results can be observed in Figure 4.11. Importantly, the spectra shown in Figure 4.11A were not baseline corrected showing no background fluorescence was observed from the dyes at this wavelength. The spectra obtained showed improved signal to noise ratios than for BPE indicating that these reporters were more suitable for use with the stabilised HGN substrates. The intensity of the prominent peak at 1600 cm^{-1} was analysed (Figure 4.11B) and it was determined that at this wavelength dye 1 gave more enhanced signals. The reason for this was not immediately apparent and would require further investigation but could possibly be due to dye 1 being slightly more in resonance with the excitation frequency.

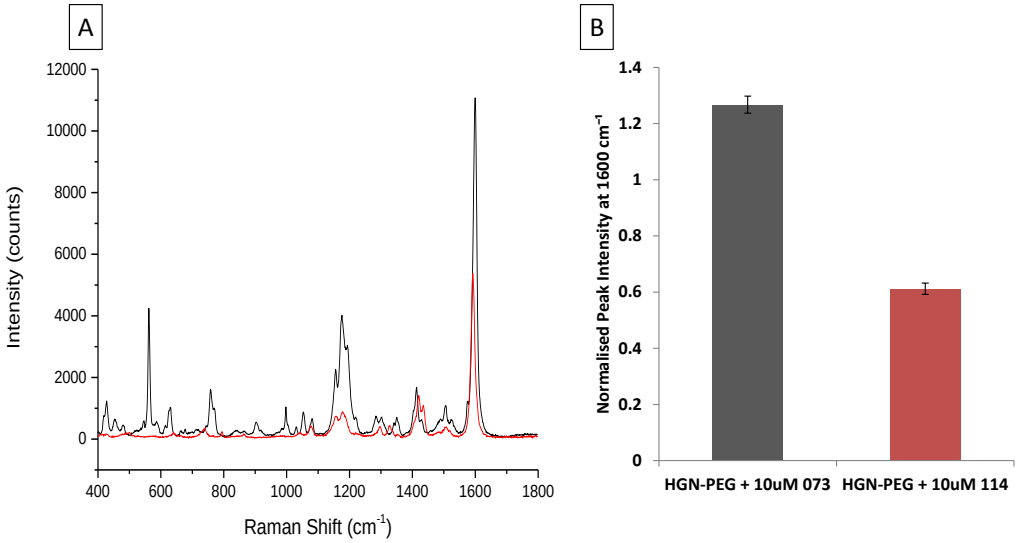

Figure 4.11: SERS spectra recorded using an excitation wavelength of 633 nm: (a) SERS spectra using PEG-stabilised HGN substrates for dye 1 (dye 073) (black) and dye 2 (dye 114) (red) (b) SERS peak intensities at 1600 cm^{-1} for dye 1 (dye 073) and dye 2 (dye 114) at 10 µM final concentration using PEG-HGNs. Spectra were obtained by scanning 3 replicates of each sample with a 10s accumulation time and laser power of 6.2 mW. Averages are shown and error bars are ± one standard deviation.

Subsequent to these promising initial results SERS analysis was also carried out at 1064 nm and 785 nm, although SERS intensities were not directly comparable as analysis was performed on different instruments. HGNs used for analysis were kept consistent across the two wavelengths, all were dispersed in d.H_2O to give final concentrations of between 2 and 2.5 nM. Their relative SPR, particle size and zeta potential values are presented in Table 4.1.

Table 4.1: Summary of characterisation data for HGNs synthesised with various stabilising agents for use in SERS at 785 nm and 1064 nm. Particle size and zeta potential values are quoted as the mean of three replicates of each sample with error ± one standard deviation.

Stabilising Agent	LSPR (nm)	Particle Size Diameter (nm)	Zeta Potential (mV)
PEG 5000	837	101.7 ± 0.6	-46.1 ± 0.9
PEG 635	696	82.8 ± 2.2	-49.9 ± 1.6
PAM	811	121.5 ± 1.4	-21.8 ± 0.8
PVP	826	83.5 ± 0.2	-47.5 ± 1.7
Citrate	704	72.1 ± 0.4	-44.2 ± 0.5
Dextran	760	91.5 ± 1.3	-45.9 ± 3.4
Thioglucose	900	86.2 ± 0.6	-45.2 ± 3.1
Silica	694	87.3 ± 0.4	-48.4 ± 1.5

As the SERS intensity was significantly reduced when the PEG stabilising layer was present, a shorter PEG unit (PEG 635) was also investigated although this did not exhibit the same level of stability as the longer PEG chain length as was reported in Chapter 3. The presence of the shorter PEG unit on the HGN surface was confirmed by the reduced particle size compared to the larger PEG but also due to the less significant red-shift in SPR compared to citrate-stabilised HGNs as it did not impede the growth of the gold shell to the same extent as the larger PEG unit. To obtain the optimum dye concentration for use with these stabilised HGNs, a concentration study was carried out using PEG5000-stabilised HGNs and dye 1 (dye 073) at 1064 nm as this was the desired working wavelength for future bio-applications. Results observed are shown in Figure 4.12.

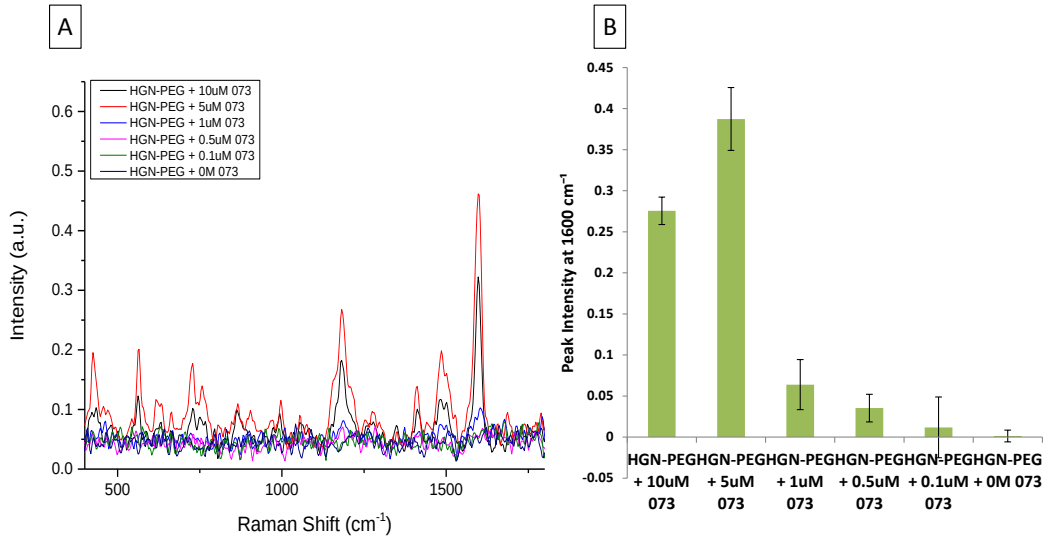

Figure 4.12: (A) SERS spectra at 1064 nm for dye 1 (dye 073) at various concentrations from 0 M to 10 µM using PEG-stabilised HGN substrates, (B) Peak intensities at 1600 cm^{-1} for incremental concentrations corresponding to the SERS spectra in (A). Spectra were obtained by scanning 3 replicates of each sample with an exposure time of 20 s under a laser power of 660 mW. Averages are shown and error bars are ± one standard deviation.

From the results shown, it was apparent that 5 µM was the optimum final concentration for use in this nanotag system. At this concentration the dye showed the greatest enhancement in signal, whereas when the concentration was increased to 10 µM and beyond the SERS intensity was reduced. This indicated that at 5 µM concentration the maximum dye molecule surface coverage was achieved and

concentrations beyond this would give no added benefit to the signals obtained. Results for standard citrate-HGNs and PEG5000-HGNs with 5 µM of each dye are presented in Figure 4.13.

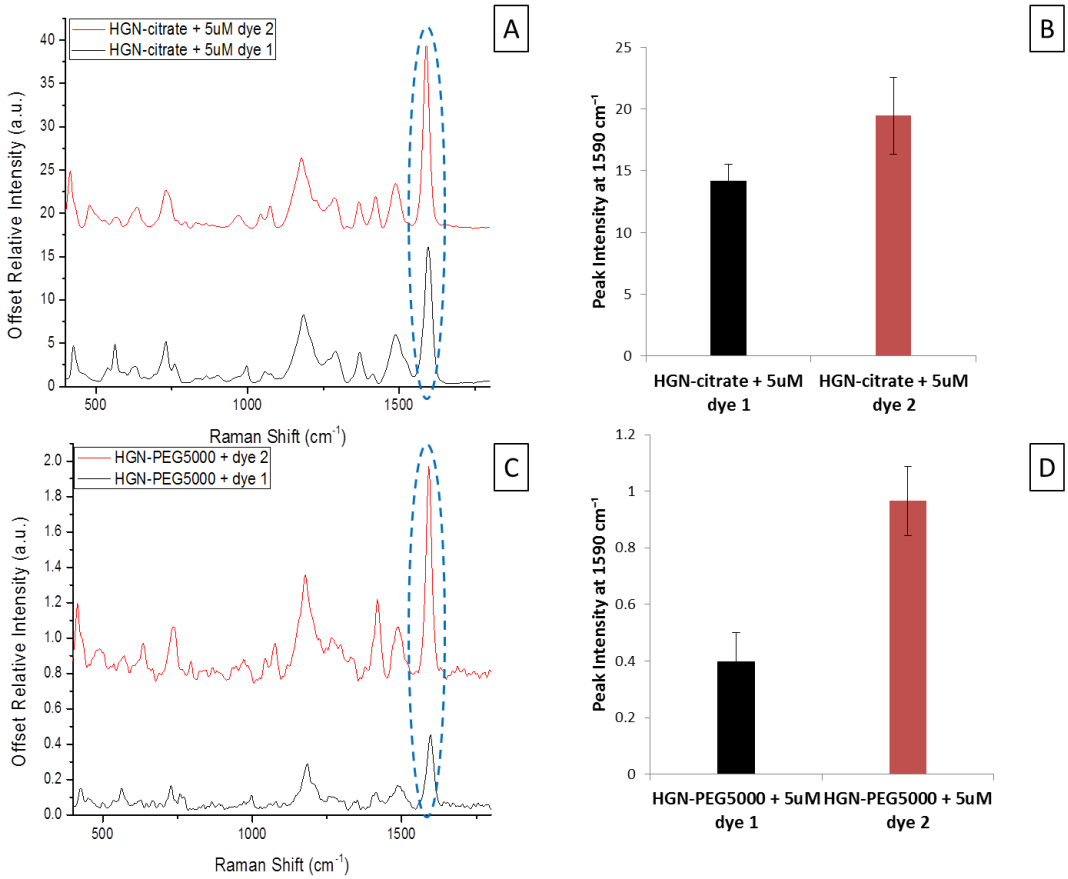

Figure 4.13: SERS spectra recorded using an excitation wavelength of 1064 nm: (A) SERS spectra of dye 2 (red) and dye 1 (black) using standard citrate-HGNs; (B) SERS peak intensities at 1590 cm^{-1} for both reporters at 5 µM final concentration; (C) SERS spectra of dye 2 (red) and dye 1 (black) using PEG-stabilised HGNs; (D) SERS peak intensities at 1590 cm^{-1} for both reporters at 5 µM final concentration. Spectra were obtained by scanning 3 replicates of each sample with 20 scans averaged per sample under a laser incident power of 600 mW. Averages are shown and error bars are ± one standard deviation.

The intensity of the prominent peak highlighted at 1590 cm^{-1} was compared. Results observed indicated that at this excitation wavelength dye 2 gave a more enhanced signal. This was thought to be a result of the difference in absorption maxima of the two dyes, as dye 2 has a λ_{max} of 826 nm it has previously been reported to be NIR

active.[177] This along with the red-shifted SPR of the PEG-stabilised HGNs could provide an ideal combination to produce the non-aggregated SERS at this excitation wavelength. Further to this, selenophene-substituted reporters were previously shown to give greater SERS enhancements than their thiophene-substituted equivalents indicating that selenolates have a greater affinity for the HGN surface than thiolates.[177] This would suggest that dye 2 would have a greater attraction for the HGN surface than dye 1, resulting in it being closer to the HGN surface and allowing for greater enhancement in SERS signals.

Although the signal intensity observed using PEG-stabilised HGNs as substrates was significantly weaker than the citrate-stabilised HGN substrates it was still readily distinguishable and showed a vast improvement compared to the commercially available Raman reporters. As previously discussed, the reduction in signal was due to the presence of the stabilising agent which hinders adsorption of reporters on the HGN surface and therefore reduces the enhancement effect provided from the metal surface. Additionally, the red-shifted stabilised HGNs possess a thinner gold shell than standard citrate HGNs. Thinner shells have a lower outer electric field compared to thicker shells[172] so therefore the reduction in signal could also be due to the weaker electric field distribution in the stabilised HGNs.

SERS spectra were also recorded for all stabilised-HGNs synthesised in Chapter 3 and are shown in Figure 4.14. The general trend observed across all stabilising agents investigated showed dye 2 (dye 114) gave the greatest enhancement at 1064 nm excitation wavelength. Figure 4.14C shows PEG-stabilised HGNs provided the least enhanced signals out of all stabilising agents used, however other coatings were previously shown to be less stable and addition of reporter molecules induced aggregation in the samples which enhanced the SERS signals. This limits future applications where stable substrates are required. Interestingly, the shorter PEG stabilising layer (PEG635) showed no increase in SERS intensities indicating that the primary explanation for the reduction in SERS intensities with the addition of the stabilising layer was the hindrance of absorption of reporter molecules at the HGN surface due to the reduction in the number of binding sites available as opposed to the reporter distance from the nanoparticle surface. Additionally, this could be due to

the red-shifted SPR of the PEG-5000 HGNs (837 nm) compared to the PEG-635 HGNs (696 nm) resulting in a greater EM enhancement from the red-shifted PEG-HGNs at this wavelength.

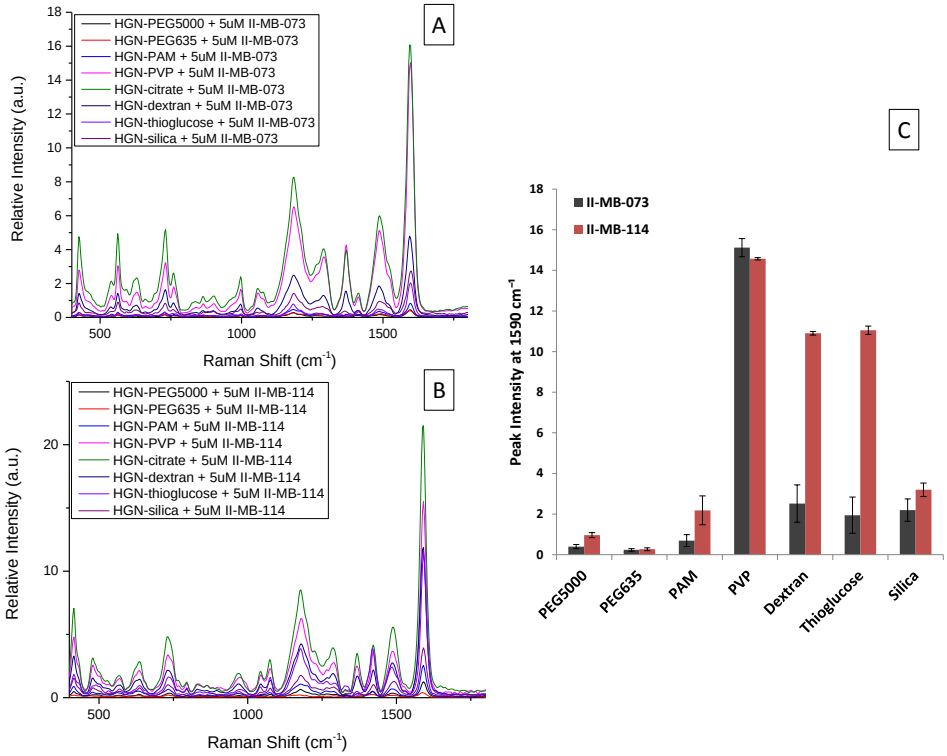

Figure 4.14: SERS spectra recorded using an excitation wavelength of 1064 nm: (a) SERS spectra of dye 1 (dye 073) for all stabilised HGNs; (b) SERS spectra of dye 2 (dye 114) for all stabilised HGNs; (c) SERS peak intensities at 1590 cm^{-1} for both reporters at 5 µM final concentration. Spectra were obtained by scanning 3 replicates of each sample with 20 scans averaged per sample under a laser incident power of 600 mW. Averages are shown and error bars are ± one standard deviation.

The experiment was then repeated at a laser excitation of 785 nm. Dye 1 (dye 073) is resonant at 789 nm and therefore an extra enhancement from the dye was expected at this wavelength. Results for standard citrate-HGNs and PEG5000-HGNs with 5 µM of each dye are presented in Figure 4.15.

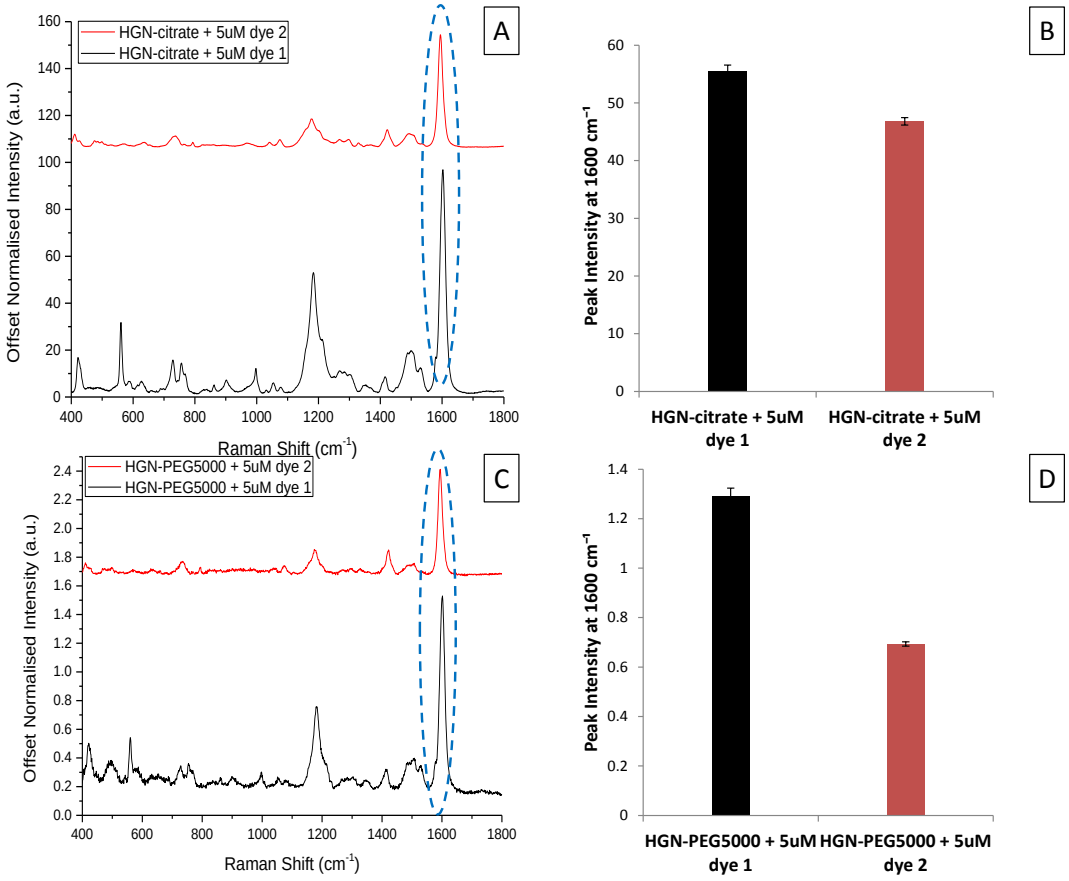

Figure 4.15: SERS spectra recorded using an excitation wavelength of 785 nm: (a) SERS spectra of dye 2 (red) and dye 1 (black) using standard citrate-HGNs; (b) SERS peak intensities at 1600 cm^{-1} for both reporters at 5 µM final concentration; (c) SERS spectra of dye 2 (red) and dye 1 (black) using PEG-stabilised HGNs; (d) SERS peak intensities at 1600 cm^{-1} for both reporters at 5 µM final concentration. Spectra were obtained by scanning 3 replicates of each sample with a 10s accumulation time and laser power of ~8 mW. Averages are shown and error bars are ± one standard deviation.

By comparing the prominent peak highlighted in the SERS spectra at 1600 cm^{-1} as before it is clear that dye 1 shows a greater enhancement at this wavelength as expected. This was thought to be due to the resonance enhancement from the dye at this wavelength, which was indicated by the large fluorescent background observed in dye 1 compared to dye 2. The raw data corresponding to the spectra presented in Figure 4.15 is shown in Figure 4.16.

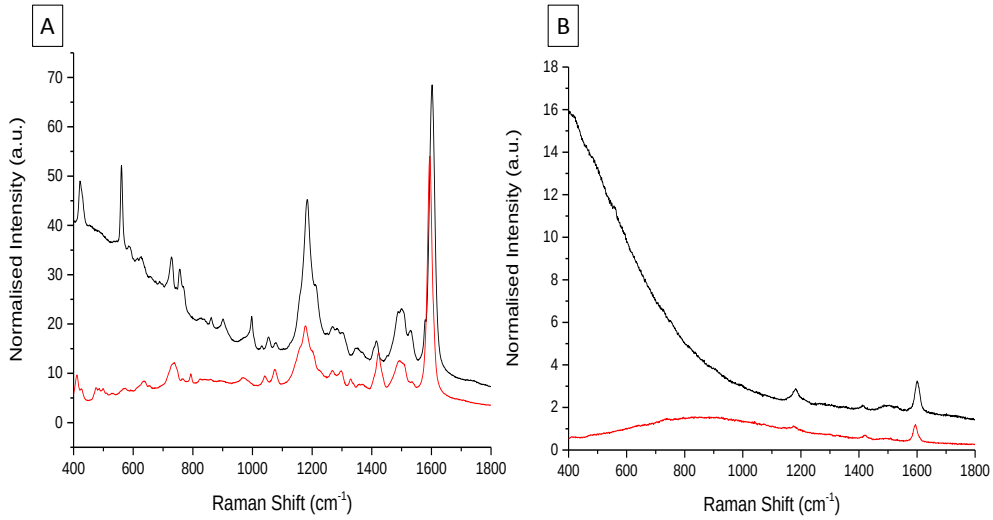

Figure 4.16: SERS spectra recorded using an excitation wavelength of 785 nm without baseline correction: (a) SERS spectra of dye 2 (red) and dye 1 (black) using standard citrate-HGNs; (b) spectra of dye 2 (red) and dye 1 (black) using PEG-stabilised HGNs. Spectra were obtained by scanning 3 replicates of each sample with a 10s accumulation time and laser power of ~8 mW. Averages are shown and error bars are ± one standard deviation.

The results observed confirmed that the larger enhancement from dye 1 at 785 nm was due to resonance enhancement from the dye. As dye 1 has an absorption maximum at 789 nm it is almost directly in resonance with the excitation wavelength which causes the large fluorescent background observed in Figure 4.16B. The decreased fluorescence in dye 2 shows that the reporter enhancement is less intense as the dye is off resonance at this wavelength. SERS can usually overcome this fluorescence issue by enhancing the Raman signal, through electromagnetic enhancement when the reporter is in close proximity to the metal surface, and simultaneously suppressing the fluorescence background. Here the SERS is not strong enough to overcome the background as the presence of the PEG stabilising layer increases the distance between the reporter and the HGN surface. Figure 4.16A shows the raw data using citrate stabilised HGNs where the SERS has overpowered the fluorescence background as the reporter is in closer proximity to the metal surface allowing for electromagnetic enhancement from the LSPR of the HGN to dominate.

As a result, to ensure that the spectra observed at 785 nm were not purely a result of resonance Raman as opposed to SERRS the normalised peak intensities at 1600 cm^{-1} for each dye were compared to blank samples which contained comparable dye concentrations with no nanoparticles present. Results are presented in Figure 4.17.

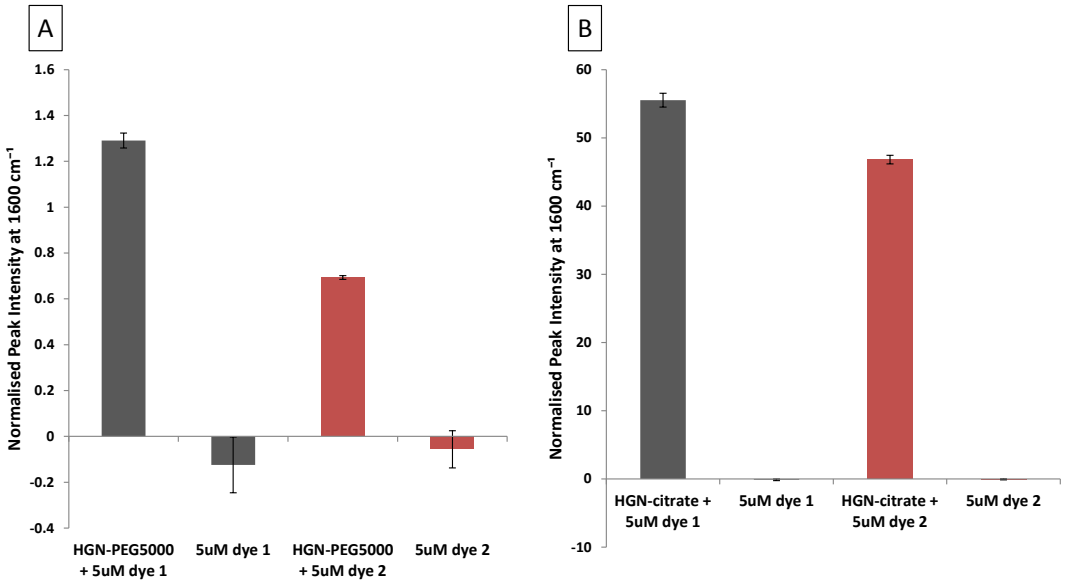

Figure 4.17: Normalised peak intensities at 1600 cm^{-1} for: (A) PEG-HGNs with 5 µM final concentration of dye 1 and dye 2 compared to blank samples with no HGNs present; (b) citrate-HGNs with 5 µM final concentration of dye 1 and dye 2 compared to blank samples with no HGNs present. Spectra were obtained by scanning 3 replicates of each sample with a 10s accumulation time and laser power of ~8 mW for HGN samples or ~0.8 mW for blank samples. Averages are shown and error bars are ± one standard deviation. Spectra were normalised to a cyclohexane standard.

The results revealed that although the EM enhancement was reduced due to the presence of the stabilising layer it still provided some signal improvement when compared to equivalent dye concentrations with no HGNs present which showed negligible signals. In fact, the fluorescence from the dye without the presence of any nanoparticles was so intense that it saturated the spectrometer at laser powers higher than 0.8 mW, a factor of ten lower than the laser power used for the analysis of the stabilised nanotag systems. This result confirmed that both reporters dye 1 and dye 2 produced effective SE(R)RS signals when used with the stabilised HGNs at 785 nm. Again, SERS spectra were also recorded for all stabilised-HGNs synthesised in Chapter 3 and are shown in Figure 4.18. The general trend observed across all

stabilising agents investigated showed dye 1 (dye 073) gave the greatest enhancement at 785 nm excitation wavelength for reasons explained above.

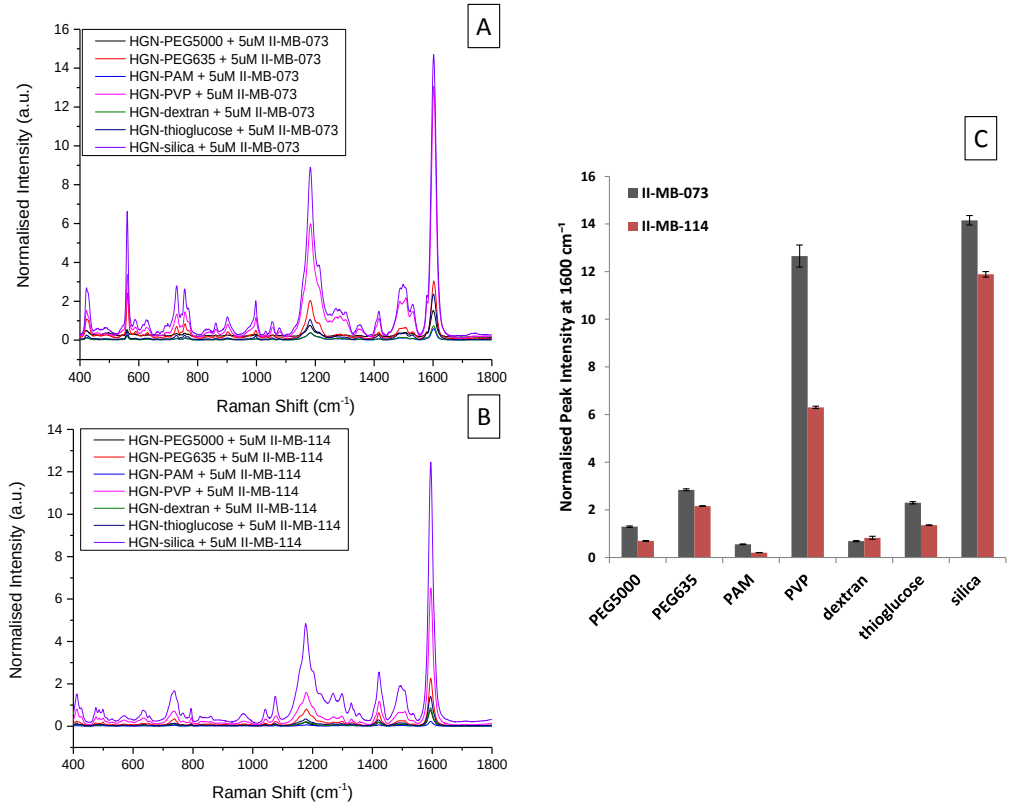

Figure 4.18: SERS spectra recorded using an excitation wavelength of 785 nm: (a) SERS spectra of dye 1 (dye 073) for all stabilised HGNs; (b) SERS spectra of dye 2 (dye 114) for all stabilised HGNs; (c) SERS peak intensities at 1600 cm^{-1} for both reporters at 5 µM final concentration. Spectra were obtained by scanning 3 replicates of each sample with a 10s accumulation time and a laser power of 8 mW. Averages are shown and error bars are ± one standard deviation.

At this wavelength the use of the shorter PEG chain length (PEG635) did give some improvement to the SERS intensities as opposed to results at 1064 nm which showed no improvement over the longer chain length. This was due to the LSPR of the PEG635 HGN being closer to the excitation wavelength than that of the PEG5000 HGN which had a more red-shifted LSPR, confirming the initial hypothesis for the difference in intensities at 1064 nm.

The success of the stabilised nanotags developed with the chalcogen reporters at both 785 nm and 1064 nm led to the analysis of these nanotags at 1280 nm where successful SERS would provide additional benefits for future bio-applications as the scattering of human tissue is at a minimum near 1300 nm allowing for better penetration depth than shorter wavelengths.[28] Although the LSPRs of the stabilised HGNs used within the nanotag systems do not match the 1280 nm excitation wavelength it has been reported previously that SERS can be achieved when the plasmon resonance does not match the excitation frequency.[174, 180]

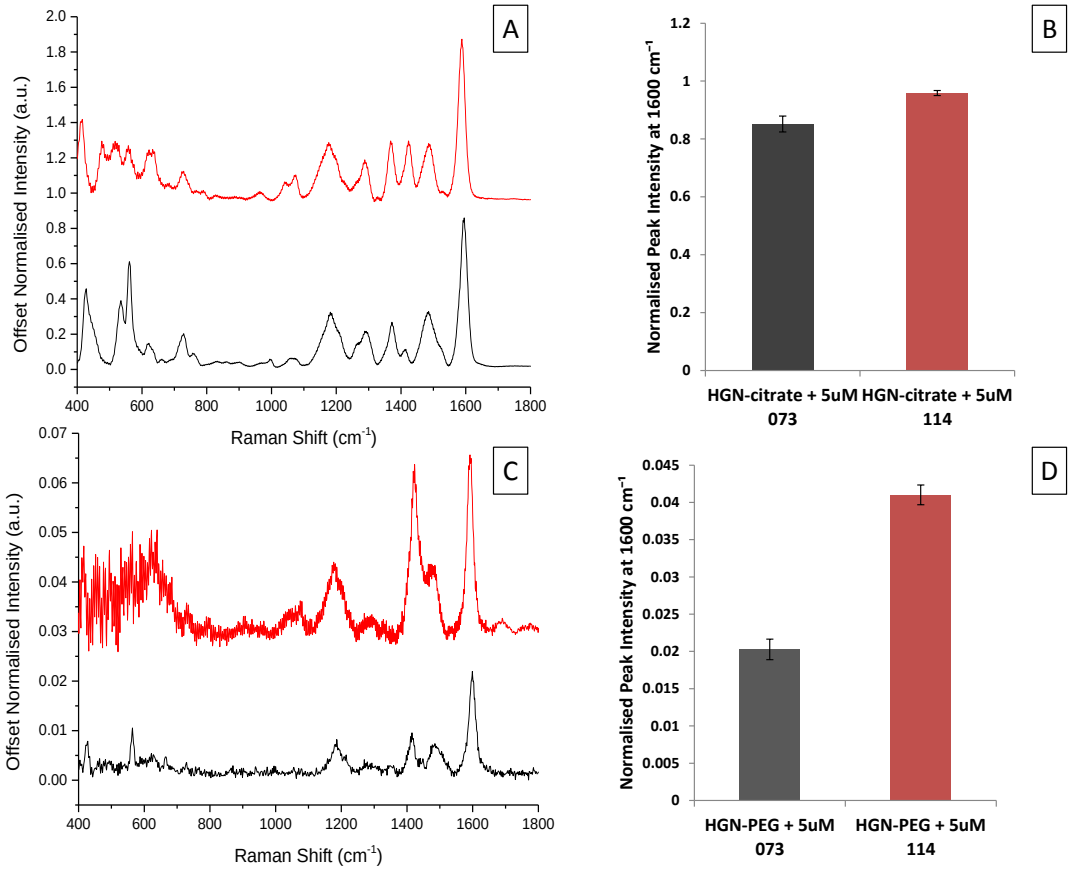

Figure 4.19: SERS spectra recorded using an excitation wavelength of 1280 nm: (a) SERS spectra of dye 2 (dye 114) (red) and dye 1 (dye 073) (black) using standard citrate-HGNs; (b) SERS peak intensities at 1600 cm^{-1} for both reporters at 5 µM final concentration; (c) SERS spectra of dye 2 (dye 114) (red) and dye 1 (dye 073) (black) using PEG-stabilised HGNs; (d) SERS peak intensities at 1600 cm^{-1} for both reporters at 5 µM final concentration. Spectra were obtained by scanning 3 replicates of each sample with a 10s accumulation time and laser power of 100 mW at the sample. Averages are shown and error bars are ± one standard deviation.

The results observed with no induced aggregation are presented in Figure 4.19. Although results showed the signals to be significantly weaker than results at shorter excitation wavelengths, characteristic peaks for each of the dyes could still be observed. The reduced signal intensities could be directly attributed to the LSPRs of the stabilised nanotags, which are too far off resonance to provide a significant EM contribution to the reporters. Successful SERS at this wavelength using aggregated red-shifted HGN substrates has previously been reported[174] and although the results for the stabilised nanotags shown here are significantly weaker in intensity this was a very promising result for future studies. With further optimisation of the nanotags, trying to further red-shift their LSPRs, effective SERS at 1280 nm could be achieved.

4.2.2 Nanotag Optimisation for bio-imaging at 785 nm

As further work within this chapter was to focus on bio-imaging of the resulting nanotags, which was to be carried out at 785 nm due to instrumental limitations, an investigation into the parameters which gave the most enhanced signals with two of the nanotag systems at this wavelength was undertaken. Although the PEG-stabilised HGNs did not produce the most intense SERS signals of all the stabilising agents investigated, chapter 3 concluded that these were the most stable to changes in external conditions out of all HGNs synthesised and would provide the most protection against aggregation in biological systems. Therefore, conditions were optimised at 785 nm based on PEG-HGN substrates and these were compared to the unstable citrate-HGN substrates.

Concentrations studies were carried out for both dye 1 (dye 073) and dye 2 (dye 114) using PEG-stabilised HGNs and citrate-stabilised HGNs as SERS substrates. Results for PEG-HGNs with incremental concentrations of dye 1 added are presented in Figure 4.20. The peak intensity plot (Figure 4.20A) indicated that 50 µM was the optimal concentration for use with PEG-HGNs, providing the most enhanced signal at this wavelength. However, the dye is diluted in a 50:50 DMF: H_2O solution which can induce aggregation at higher concentrations and after a short amount of time visible aggregation was observed when 50 µM of dye was added to the PEG-HGNs. Therefore, a final concentration of 10 µM was selected for use within the nanotag

systems as it produced the most enhanced signals without causing nanoparticle precipitation from solution.

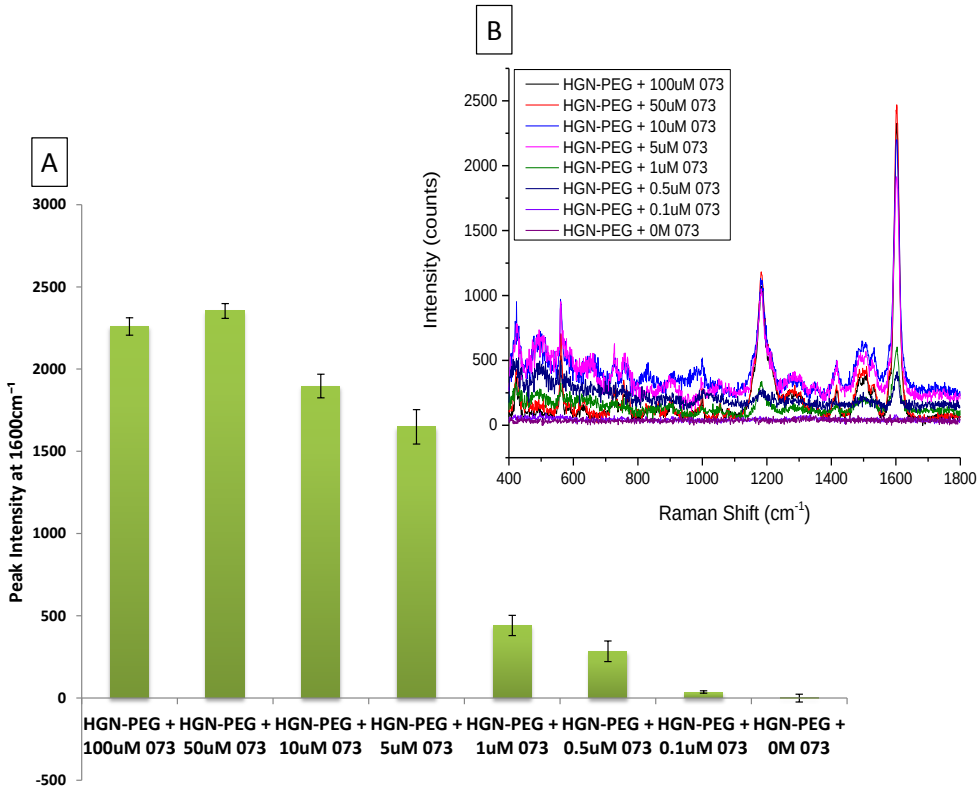

Figure 4.20: Concentration study at 785 nm for HGN-PEG-dye 1(dye073) nanotags: (A) SERS peak intensities at 1600 cm^{-1} from 0 M to 100 µM final concentration of dye 1, (B) SERS spectra corresponding to the peak intensity plot in (A). Spectra were obtained by scanning 3 replicates of each sample with a 10s accumulation time. Averages are shown and error bars are ± one standard deviation.

This study was also repeated with the alternative chalcogen reporter molecule (dye 2) and the same trend was observed with 10 µM selected as the final concentration for use within the stabilised nanotag systems.

Further to this, both concentration studies were repeated using citrate-stabilised HGNs as substrates. Again, results for dye 1 (dye 073) are presented in Figure 4.21 and results for dye 2 (dye 114) displayed a similar trend. Results showed that maximum surface coverage of the dye was achieved at 5 µM final concentration, less than that for the PEG-HGNs which was to be expected as the citrate HGNs tend to have a smaller outer diameter than the PEG-HGNs which have more red-shifted

SPRs. Therefore, lower concentrations are required to achieve full surface coverage. Particle size measurements for the PEG-HGNs and citrate-HGNs used within these experiments were 138.6 ± 1.9 nm and 109.1 ± 1.6 nm respectively.

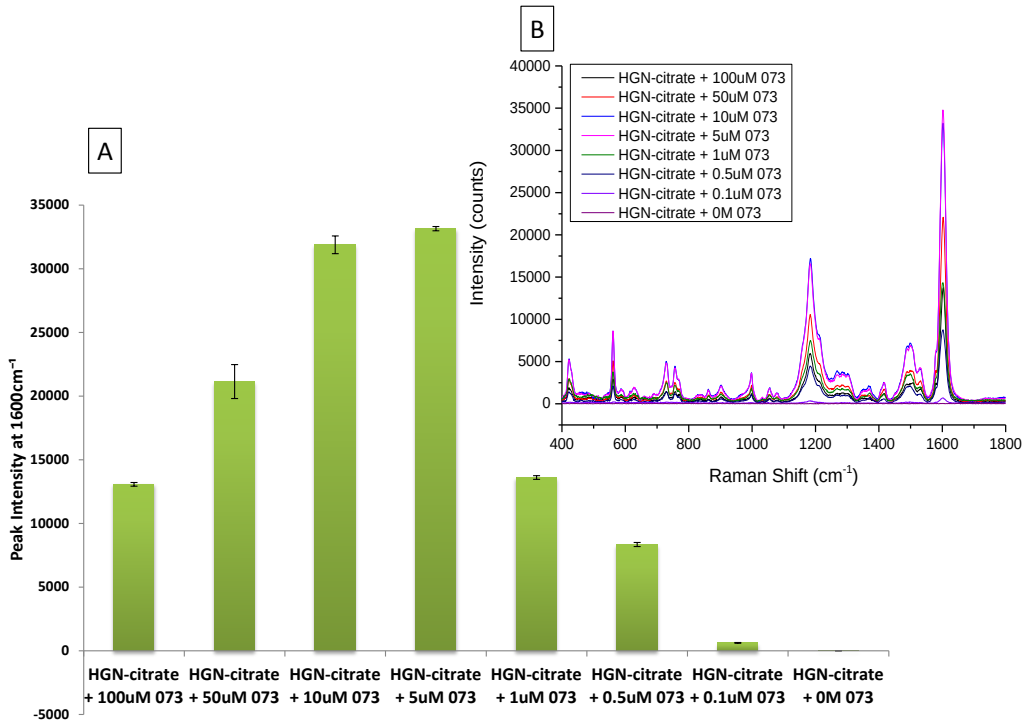

Figure 4.21: Concentration study at 785 nm for HGN-citrate-dye 1(dye073) nanotags: (A) SERS peak intensities at 1600 cm^{-1} from 0 M to 100 µM final concentration of dye 1, (B) SERS spectra corresponding to the peak intensity plot in (A). Spectra were obtained by scanning 3 replicates of each sample with a 10s accumulation time. Averages are shown and error bars are ± one standard deviation.

However, to maintain an accurate comparison between PEG and citrate stabilised HGNs, a final reporter concentration of 10 µM was selected for use within all nanotag systems at 785 nm for future studies.

In order to obtain the maximum SERS response possible from each substrate, various parameters based on the method of nanotag assembly were investigated. Firstly, the incorporation of a centrifugation step to remove any excess reporter from the HGNs before analysis was investigated to determine whether this would have any influence on the SERS response achieved. Additionally, the length of time required between incorporation of the reporter molecule and final analysis was studied. A summary of

the results obtained varying these two parameters are presented in Figure 4.22 and Figure 4.23 for PEG-HGN and citrate-HGN based systems respectively.

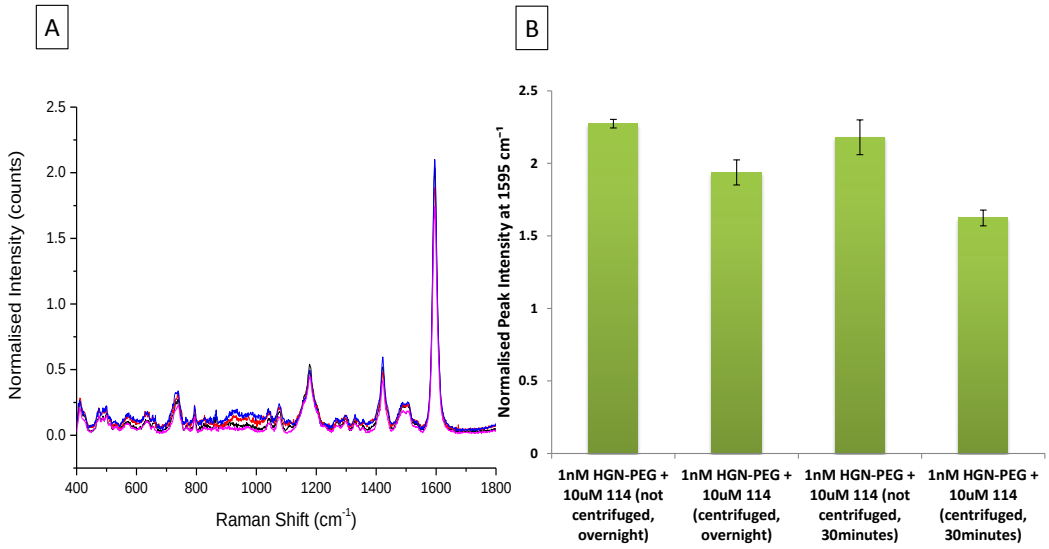

Figure 4.22: (A) SERS spectra of PEG-HGN-dye 2 (dye 114) nanotag system assembled under variable conditions; not centrifuged with overnight reporter addition (black), centrifuged with overnight reporter addition (red), not centrifuged, 30 minute reporter addition (blue), centrifuged, 30 minute reporter addition (pink), (B) Normalised peak intensities at 1595 cm^{-1} corresponding to the SERS spectra in (A). Analysis was carried out at 785 nm, scanning 3 replicates of each sample with a 10s accumulation time. Averages are shown and error bars are ± one standard deviation.

Results for PEG-HGN based systems (Figure 4.22) showed very little variation in SERS response as a consequence of altering the assembly conditions. A slight reduction in signal intensity was observed when a centrifugation step was incorporated, thought to be a result of a reduction in nanoparticle concentration after this stage. However, leaving the reporter to react with the HGN surface for a short period of time (30 minutes) or longer (overnight) before analysis revealed minimal changes in the spectra indicating that the optimum reporter response was achieved just 30 minutes after addition to the HGNs.

Conversely, results for citrate-HGN based systems (Figure 4.23) showed extensive variation within the results observed. Again a slight reduction in signal intensity was observed when a centrifugation step was incorporated, so for direct SERS analysis

this was an unnecessary stage in the nanotag assembly however for bio-imaging this would need to be incorporated to remove any free reporter from solution before adding them to the cells. Within this system, the length of time allowed for the reporter to react with the HGN surface had a significant effect on the SERS response observed. After 30 minutes a very intense signal was produced, caused by partial aggregation initiated by the addition of the reporter molecules. However, when the reporter was left to react overnight before analysis commenced there was a significant reduction in SERS signal produced. This was a result of nanoparticle flocculation, due to the reduced stability of the system compared to PEG-stabilised HGNs, which reduced the number of nanoparticles present within the laser interrogation volume.

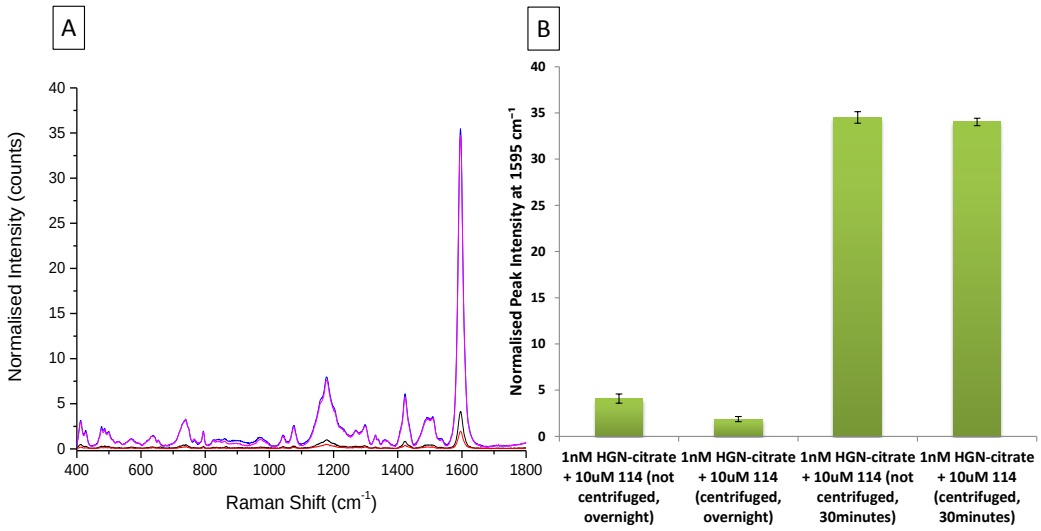

Figure 4.23: (A) SERS spectra of citrate-HGN-dye 2 (dye 114) nanotag system assembled under variable conditions; not centrifuged with overnight reporter addition (black), centrifuged with overnight reporter addition (red), not centrifuged, 30 minute reporter addition (blue), centrifuged, 30 minute reporter addition (pink), (B) Normalised peak intensities at 1595 cm^{-1} corresponding to the SERS spectra in (A). Analysis was carried out at 785 nm, scanning 3 replicates of each sample with a 10s accumulation time. Averages are shown and error bars are ± one standard deviation.

Again, results were mirrored when dye 1 was used as opposed to dye 2. Ultimately, the results revealed that for PEG-HGNs the method of nanotag preparation had no

overall bearing in the SERS response generated however this was not the case for citrate-stabilised HGNs. Therefore, taking all factors into account the optimum conditions selected for nanotag assembly at 785 nm were as follows; 10 µM final concentration of reporter molecule, 30 minute incubation time before analysis and no centrifugation step. These conditions were implemented when assembling the nanotags used for stability studies within Section 4.3 however a centrifugation step was incorporated for bio-imaging studies within Section 4.4 to remove any free reporter from solution prior to cell incubation.

4.3 Nanotag Stability Studies

As the ultimate goal of this work was to develop nanotags which produced intense and reproducible SERS in various external environments for use in bio-applications it was important to assess the SERS stability of the nanotags developed within Section 4.2. As previously discussed, nanotag stability will directly affect the reproducibility in the SERS spectra produced due to the reduction in homogeneity within the sample. Thus, avoiding over-aggregation within different external environments such as high salt concentrations or changes in pH was desirable to maximise the reproducibility and long term stability in the SERS responses of the nanotag systems.

4.3.1 Long Term Stability

Long term monitoring of SERS signals is required in both *in vivo* and *in vitro* applications and is therefore an important area to investigate if the nanotags developed within this work are to be used for bio-imaging. For analysis, both PEG-stabilised and citrate-stabilised HGNs were diluted to a comparable final concentration of 1 nM. Subsequent to the addition of 10 µM of dye 1 (dye 073) or dye 2 (dye 114) SERS spectra were recorded at incremental time periods from the initial reporter addition over one month. Extinction spectra were measured simultaneously, in order to monitor the aggregation profiles within each system. Nanotags were assembled and stored in the same vials throughout the analysis and measurements were recorded without any sample agitation. SERS spectra were

normalised against a cyclohexane standard to allow for direct comparison of spectra accumulated on different days where laser intensities would vary.

Results for citrate-stabilised HGNs with dye 1 (dye 073) are shown in Figure 4.24 as an example of the citrate-HGN based nanotags, dye 2 also exhibited the same results. Results clearly demonstrated that these nanotags were unstable and resulted in considerable reduction in SERS intensities over the one month period studied. SERS spectra recorded just one week after initial measurements showed a reduction in SERS intensity by approximately a factor of four, which was then further reduced by half in the subsequent weeks.

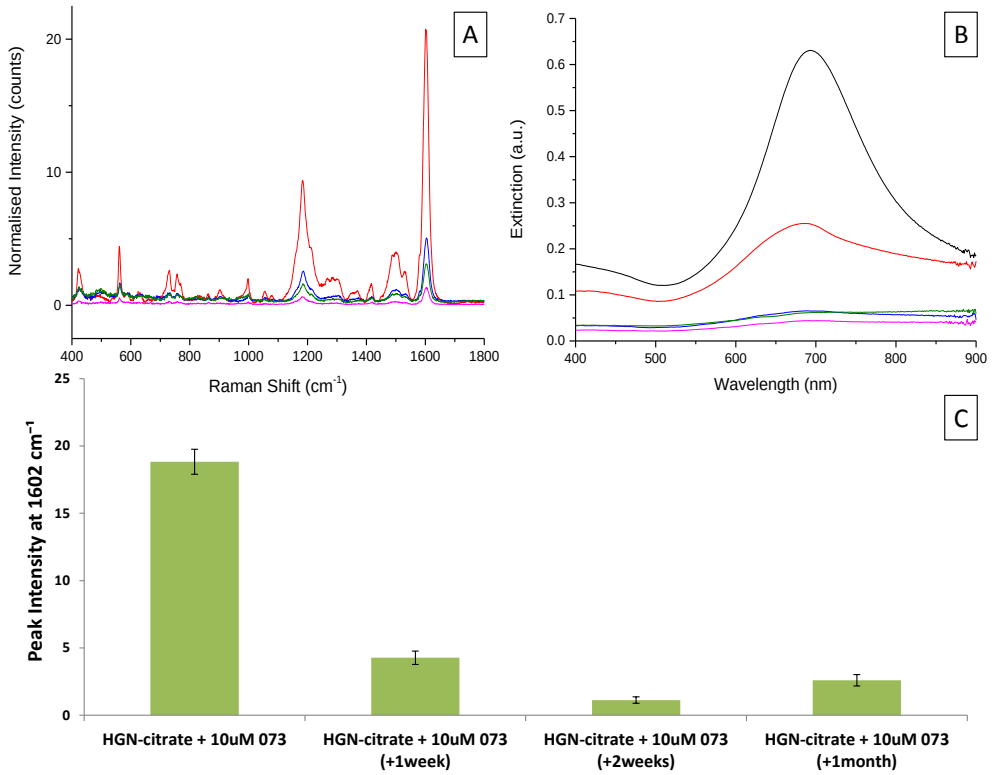

Figure 4.24: (A) SERS spectra at 785 nm of 1 nM citrate-HGNs with 10 µM dye 1 (dye 073) analysed at initial reporter addition (red), after 1 week (blue), after 2 weeks (pink) and after one month (green). (B) Extinction spectra of initial citrate-HGNs (black), citrate-HGNs immediately after addition of 10 µM dye 1 (red) and subsequently 1 week (blue), 2 weeks (pink) and one month (green) after addition of the dye. (C) SERS peak intensities at 1602 cm^{-1} corresponding to the SERS spectra in (A). Spectra were obtained by scanning 3 replicates of each sample with a 10s accumulation time at a laser power of ~1 mW. Averages are shown and error bars are ± one standard deviation.

The extinction spectra results provided a possible explanation for the reduction in SERS signals exhibited over time. After initial addition of the reporter molecule, there is evidence of partial aggregation within the sample indicated by a blue-shift and dampening in plasmon band (Figure 4.24B). This explains the occurrence of the initial intense signal, as the partial aggregation will create efficient 'hot-spots' for maximum enhancement of the signal. However, these nanotags were highly unstable and precipitated from solution fairly readily, which was observed both visibly and in the loss in plasmon band in the extinction spectra in the subsequent measurements. As a result, the HGNs formed large aggregates at the bottom of each vial which resulted in a reduced number of HGNs being present in each sample volume removed for analysis. One other possible explanation for this reduction in signal was that the reporters were not strongly bound to the HGN surface and were displaced from the surface over time which would result in weaker SERS signals however this hypothesis would require further investigation.

Results for PEG-stabilised HGNs with dye 1 (dye 073) are shown in Figure 4.25, and again dye 2 exhibited the same results. The results observed were more promising with an increase in the consistency of the SERS spectra obtained over the one month period studied. Although the SERS intensities did reduce slightly over the four weeks this was not considered to be a result of instability within the nanotags but because the nanoparticles will naturally settle to the bottom of the solution over time. As agitation of the samples between measurements was kept to a minimum to give as accurate results as possible this resulted in a slight loss of nanoparticle concentration from the sample volume removed from the initial nanotag solution each time and thus resulted in marginally reduced signals after each measurement. Extinction spectra recorded confirmed that over-aggregation was not taking place as the plasmon band was not completely diminished after the one month period. The slight hump in the spectra at around 650 nm shortly after the addition of the reporter molecule was characteristic of the dye extinction spectra and indicated that the dye had not fully conjugated to the HGN surface at the time of analysis. The extinction spectra recorded in the following weeks showed a slight dampening and broadening in the spectra which could indicate that partial aggregation was taking place.

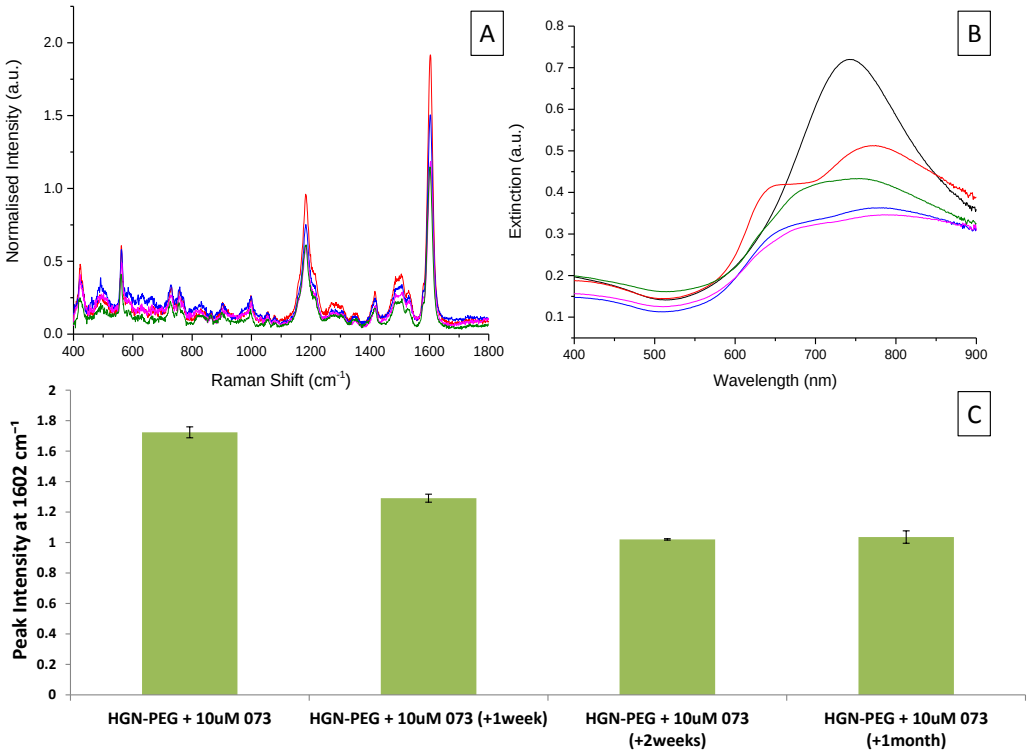

Figure 4.25:(A) SERS spectra at 785 nm of 1 nM PEG-HGNs with 10 µM dye 1 (dye 073) analysed at initial reporter addition (red), after 1 week (blue), after 2 weeks (pink) and after one month (green). (B) Extinction spectra of initial PEG-HGNs (black), PEG-HGNs immediately after addition of 10 µM dye 1 (red) and subsequently 1 week (blue), 2 weeks (pink) and one month (green) after addition of the dye. (C) SERS peak intensities at 1602 cm^{-1} corresponding to the SERS spectra in (A). Spectra were obtained by scanning 3 replicates of each sample with a 10s accumulation time at a laser power of ~1 mW. Averages are shown and error bars are ± one standard deviation.

However, as the SERS spectra remained consistent over this time and there was no blue-shift in SPR observed this was more likely a result of the reduced HGN concentration within each sample as previously described.

To investigate whether the sensitivity could be increased without the stability and reproducibility of the PEG-HGN based nanotags being compromised, a higher concentration of reporter (50 µM) was added to the initial solution and analysed over one month as previously reported. The results observed are shown in Figure 4.26. Although the initial SERS intensity was slightly enhanced, this steadily diminished over the one month period as the HGNs precipitated from solution. The reduction in

the number of nanoparticles from the sample volume was so significant after one month that a weak Raman signal from the DMF present within the system was apparent as the SERS enhancement was completely diminished. The initial extinction spectrum observed when the reporter was added to the PEG-HGNs was again the result of the dye absorbance. Nanoparticle aggregation over the one month period studied was confirmed by the loss of plasmon band in the extinction spectra over time.

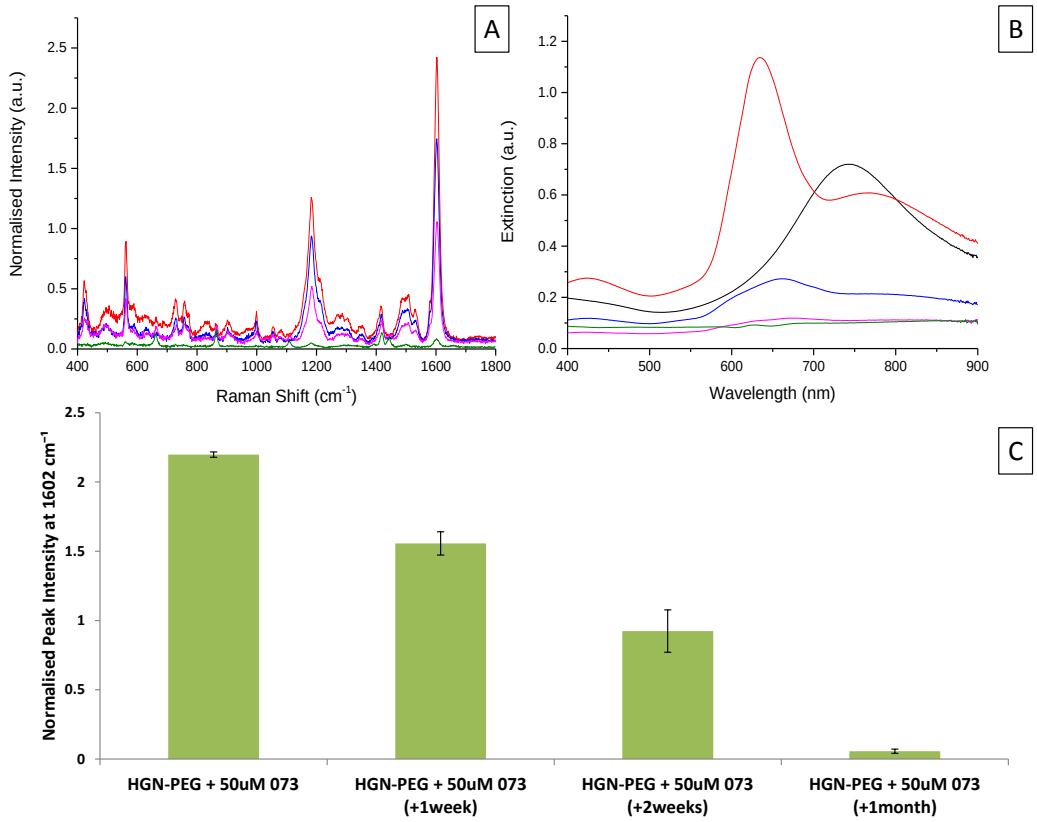

Figure 4.26: (A) SERS spectra at 785 nm of 1 nM PEG-HGNs with 50 µM dye 1 (dye 073) analysed at initial reporter addition (red), after 1 week (blue), after 2 weeks (pink) and after one month (green). (B) Extinction spectra of initial PEG-HGNs (black), PEG-HGNs immediately after addition of 50 µM dye 1 (red) and subsequently 1 week (blue), 2 weeks (pink) and one month (green) after addition of the dye. (C) SERS peak intensities at 1602 cm^{-1} corresponding to the SERS spectra in (A). Spectra were obtained by scanning 3 replicates of each sample with a 10s accumulation time at a laser power of ~1 mW. Averages are shown and error bars are ± one standard deviation.

As a result, this confirmed that the 10 µM reporter concentration was in fact the optimum selection for use with the stabilised-HGNs, with negligible SERS intensity fluctuations observed over time.

4.3.2 SERS Stability to Salt

In Chapter 3 PEG-HGNs displayed a high stability to increasing salt concentrations, with a reported stability in up to 5 M NaCl over a period of one month, compared to citrate-HGNs which began to show signs of aggregation upon addition of just 30 mM salt. Due to the presence of NaCl in many biological buffers it was necessary to study its effect on the sensitivity and reproducibility on the SERS spectra of the stabilised nanotag systems. For analysis, both citrate-HGNs and PEG-HGNs were diluted to a final concentration of 1 nM. Following addition of 10 µM of reporter, samples were concentrated and redispersed in varying concentrations of NaCl up to 1 M and left overnight before analysis. The results observed using both PEG-stabilised and citrate-stabilised HGNs are presented in Figure 4.27.

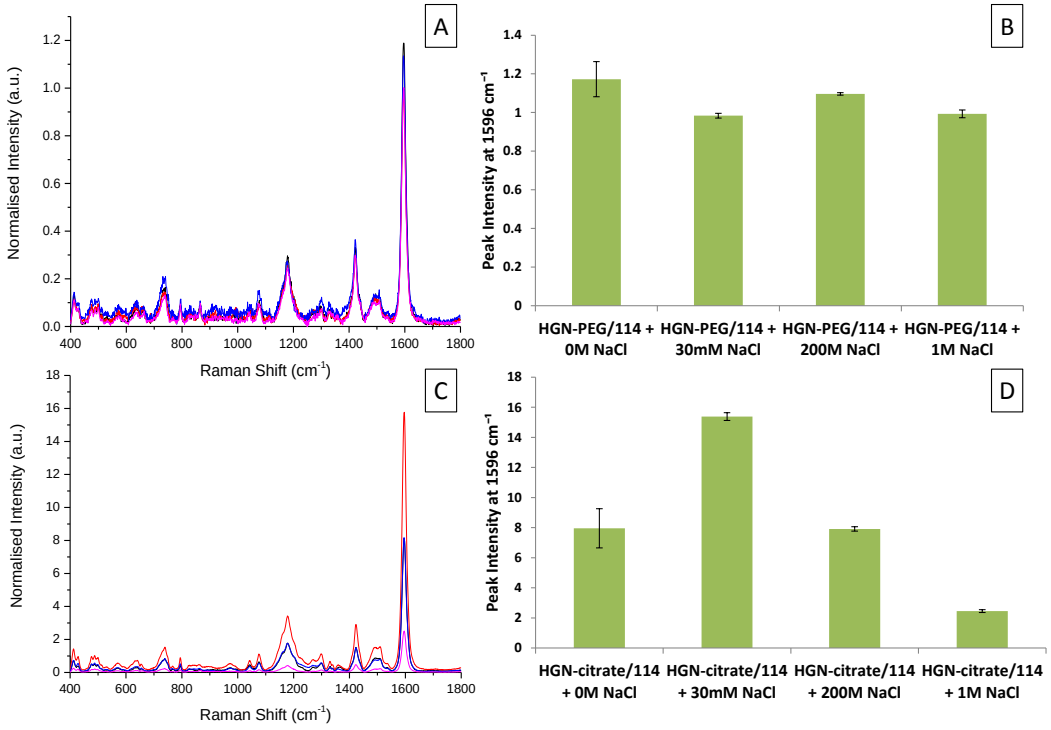

Figure 4.27: SERS spectra measured at 785 nm for (A) PEG-HGN/dye 2(dye114) and (C) citrate-HGN/dye 2 (dye114) nanotags redispersed in 0 M NaCl (black), 30 mM NaCl (red), 200 mM NaCl (blue) and 1 M NaCl (pink). Corresponding peak intensities at 1596 cm^{-1} for (B)PEG-HGNs/dye 2 and (D) citrate-HGNS/dye 2 in increasing salt concentrations. Spectra were obtained by scanning 3 replicates of each sample with a 10s accumulation time. Averages are shown and error bars are ± one standard deviation.

From the results it was clear that the presence of the PEG stabilising layer within the nanotag system produced much more reproducible SERS spectra than the citrate-stabilised system. Within the citrate-HGN based nanotags there were significant variations in signal intensities across the range of concentrations studied. The initial increase in SERS intensity on addition of the 30 mM NaCl was a result of the formation of partial aggregates within the solution which resulted in the formation of 'hot-spots' to provide an added enhancement in the signal obtained. The subsequent reduction in SERS signals in more concentrated salt solutions was due to over-aggregation within the samples, as a result of the charge screening effect induced by the salt, which resulted in a reduction in nanoparticle concentration within the sample volume. However, when the PEG stabilising layer was present within the nanotag system this signal variation was no longer observed. This indicated that the PEG layer provided sufficient stability within the system to control any partial aggregation induced by addition of the reporter molecule and protect against any further aggregation induced by the salt.

4.3.3 pH Studies

Due to large variations in pH throughout the body, ranging from pH 2 in the stomach, pH 5.4 – 7.4 in cancerous tissues and pH 5-8 in the intestine,[154] it was important that the nanotag systems developed could maintain consistent, reproducible SERS spectra in both alkaline and acidic pH environments. For analysis, both citrate-HGNs and PEG-HGNs were diluted to a final concentration of 1 nM and combined with either reporter molecule dye 1 or dye 2 at a final concentration of 10 μM. The pH of the samples was adjusted by the dropwise addition of 1 M citric acid or 1 M NaOH as appropriate. Samples were left overnight before analysis and SERS spectra were then recorded at the original sample pH and in both acidic and alkaline conditions. To assess the reproducibility within each sample, three replicate samples at each pH were prepared and each was scanned five times to provide a total of fifteen repeats of each sample at each pH value which were averaged for analysis. The resulting SERS spectra for the PEG stabilised samples are presented in Figure 4.28.

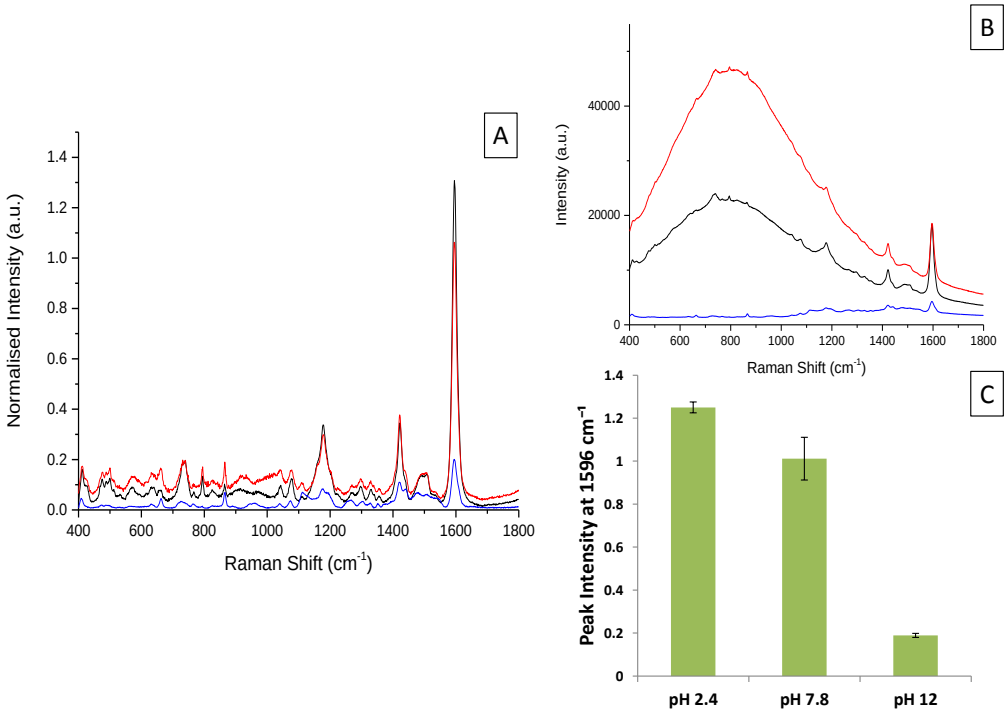

Figure 4.28: SERS spectra of PEG-HGN/dye 2(dye 114) nanotags measured at different pH values at 785 nm excitation: (A) normalised, baseline corrected spectra at pH 2.4 (black), pH 7.8 (red) and pH 12 (blue), (B) raw spectra corresponding to spectra presented in (A), (C) peak intensities at 1596 cm^{-1} calculated from raw SERS spectra in (B). Spectra were obtained by scanning 3 replicate samples 5 times with a 10s accumulation time and incident laser power of 11 mW. Averages are shown and error bars are ± one standard deviation.

In the raw spectra (Figure 4.28B) significant variations in background fluorescence between the samples was observed. It is well documented that metal nanoparticles can quench the fluorescence exhibited in molecular chromophores and that the level of quenching is dependent on the proximity of the fluorophore to the metal surface.[181-183] Therefore, at pH 7.8 (original pH of the PEG-HGN combined with dye 2) the significant background signal observed was thought to be due to the presence of the PEG stabilising layer which would limit the level of fluorescence quenching provided by the HGN surface. At acidic pH there was a slight reduction in background fluorescence combined with a slight increase in SERS intensity which indicated that some partial aggregation may have been initiated in the acidic environment. At alkaline pH the fluorescence background completely diminished

and there was a significant reduction in SERS intensity however no visible aggregation was observed within the PEG-stabilised samples. This indicated that the OH^- ions introduced into the sample may have compromised the conjugated system resulting in a loss in fluorescence and SERS intensity. However, these results required further investigation for an enhanced understanding of the results observed.

The results observed using citrate-stabilised HGNs are presented in Figure 4.29 where a similar trend in signal intensities was observed across the different pH environments.

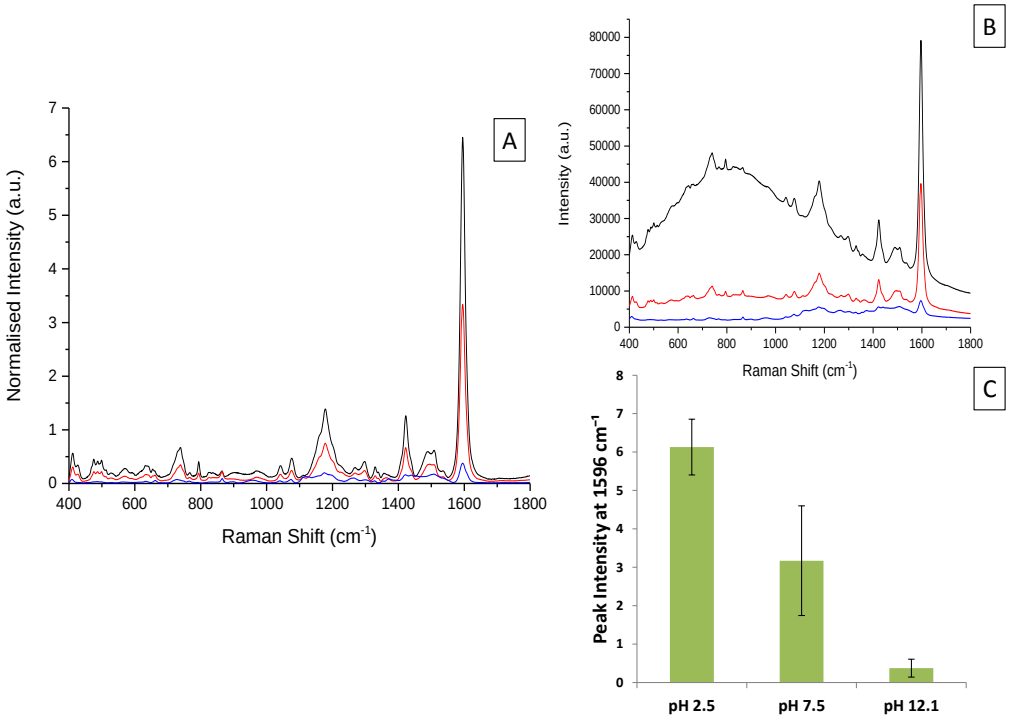

Figure 4.29: SERS spectra of citrate-HGN/dye 2(dye 114) nanotags measured at different pH values at 785 nm excitation: (A) normalised, baseline corrected spectra at pH 2.5 (black), pH 7.5 (red) and pH 12.1 (blue), (B) raw spectra corresponding to spectra presented in (A), (C) peak intensities at 1596 cm^{-1} calculated from raw SERS spectra in (B). Spectra were obtained by scanning 3 replicate samples 5 times with a 10s accumulation time and incident laser power of 11 mW. Averages are shown and error bars are ± one standard deviation.

However the background signals were significantly reduced within this system. At pH 7.5 (the original pH of the sample) the fluorescence background had almost completely diminished and was thought to be due to the formation of partial

aggregates within the solution induced by the reporter molecule which has previously been reported to be self-aggregating.[177] Without the presence of the polymer stabilising layer the reporter molecule would be in close proximity to the HGN surface and therefore partial aggregation induced within the system would cause significant fluorescence quenching with an enhanced SERS signal. At acidic pH there was again an increase in SERS intensity however this was combined with an increase in fluorescence background and visible aggregation within the solution. The increased fluorescence could be explained by displacement of the reporter from the HGN surface when significant aggregation was induced which would result in more free dye molecules in solution to contribute to the fluorescence background. Additionally, the increased SERS enhancement could be due to the presence of larger aggregates within the sample volume which would provide significant EM enhancements to the reporters directly on the HGN surface. At alkaline pH the fluorescence background completely diminished and there was a significant reduction in SERS intensity however this was now combined with visible aggregation within the citrate-HGN based samples. This indicated that the result was more dependent on the pH effect on the dye as opposed to the aggregation state of the samples with fully aggregated and non-aggregated systems displaying similar trends in results.

Focussing on the reproducibility of the samples in different pH environments, the error bars in the peak intensity plot in Figure 4.29C indicated that there were large variations in signal intensity within each sample compared to the PEG-HGN based counterparts in Figure 4.28C which exhibited much smaller error within measurements. Principal component analysis (PCA) is a technique commonly employed to reduce the dimensionality in spectroscopic data whilst retaining maximum information content from the SERS spectra.[184, 185] Within this section PCA was employed to assess the reproducibility in the SERS spectra, identifiable by high density clustering of replicate samples in the PCA scores plots. The resultant scores and loadings plots for the SERS data presented in Figures 4.28 and 4.29 are shown in Figures 4.30 and 4.31 respectively. All PCA analysis was performed by Alexandre Girard (The University of Strathclyde).

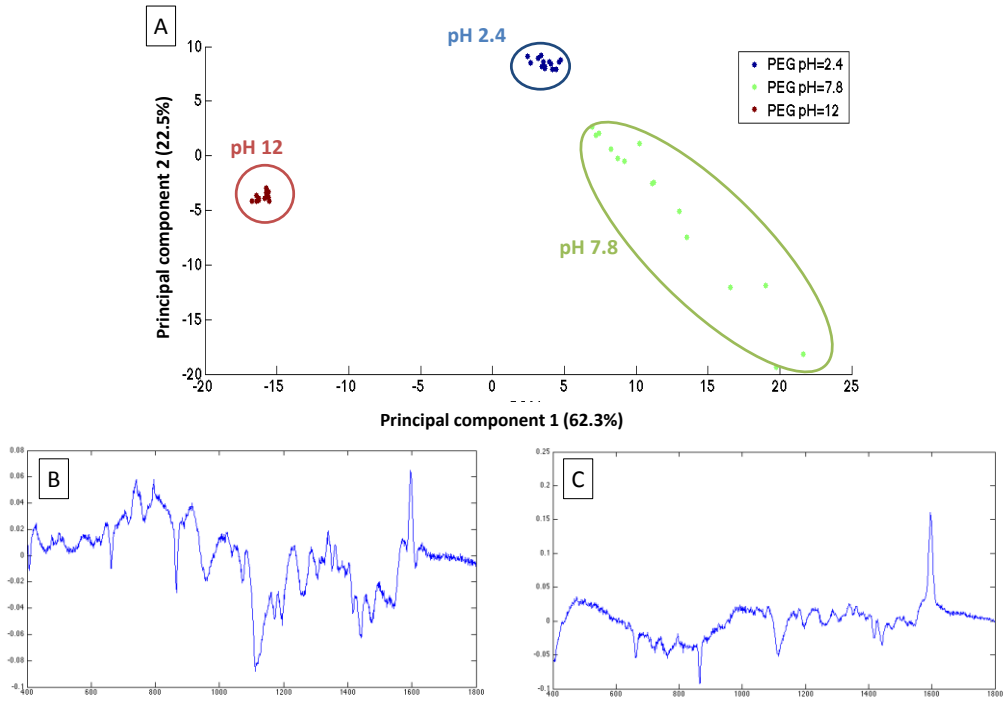

Figure 4.30: (A) PCA scores plot showing the effect different pH environments have on the reproducibility in the signal obtained using PEG-HGNs with dye 2. 5 scans of each of the 3 replicates were recorded using an excitation wavelength of 785 nm and 10 s accumulation time. The loading plots of (B) Principal Component 1 and (C) Principle Component 2 are also presented.

The scores plot for the PEG-stabilised HGN nanotags (Figure 4.30A) showed tight clustering within data sets at both acidic and alkaline pH which indicated a high level of reproducibility within these samples. These environments produced much more reproducible spectra than the samples at the original pH which showed more variation across PC2. The increased reproducibility at acidic and alkaline pH could be a result of the formation of partial aggregates controlled by the presence of the PEG stabilising layer however this would require further investigation.

Conversely, the results for citrate-stabilised HGN nanotags showed more variability within each cluster indicating that these samples produce less reproducible spectra upon changes in pH than the PEG-stabilised systems.

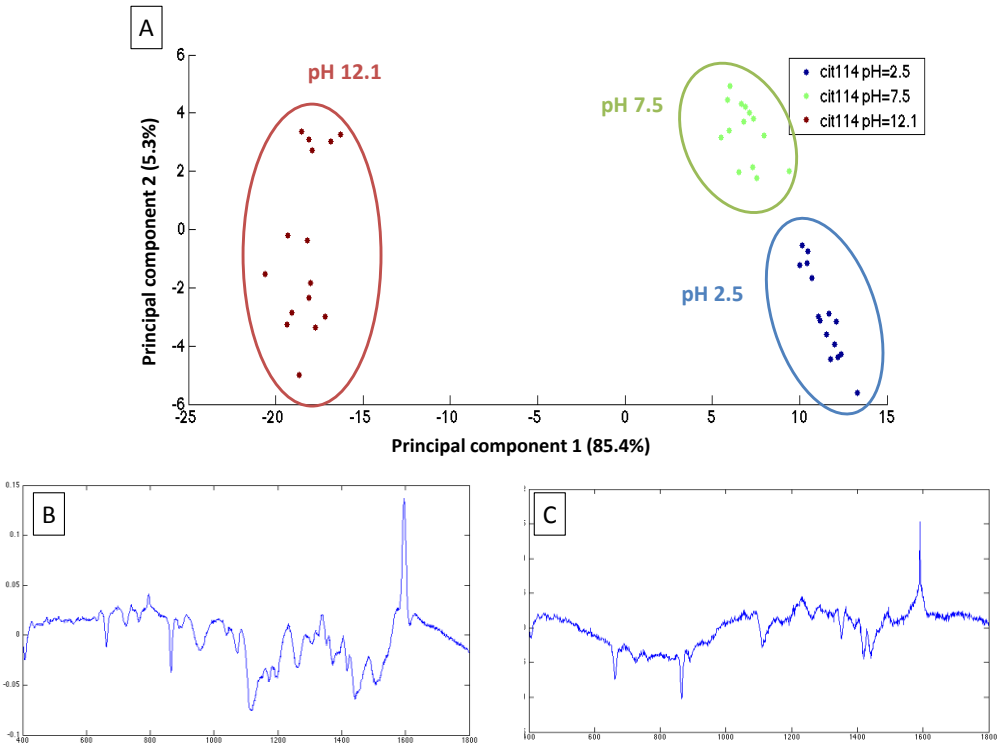

Figure 4.31: (A) PCA scores plot showing effect different pH environments have on the reproducibility in the signal obtained using citrate-HGNs with dye 2. 5 scans of each of the 3 replicates were recorded using an excitation wavelength of 785 nm and 10 s accumulation time. The loading plots of (B) Principal Component 1 and (C) Principle Component 2 are also presented.

At pH 7.5 there is more clustering within the data set observed than for the PEG-HGN samples at neutral pH. This was thought to be a result of the partial aggregation and quenched fluorescence background observed from the SERS spectra. However, in both acidic and alkaline conditions there is much more variation observed in the resulting spectra as indicated by the reduced clustering of each data set in the scores plot. This could be due to over-aggregation within each sample, induced by changes in pH, however this would again require further investigation.

In order to fully interpret the data obtained, further analysis was carried out. Firstly, the variation in the reporter fluorescence was indirectly measured by absorption spectroscopy to determine whether the change in fluorescence background was related to the change in dye fluorescence at different pH values, was a result of nanoparticle aggregation and quenching or was a combination of both. The

extinction profile of dye 2 at the three different pH environments investigated is presented in Figure 4.32.

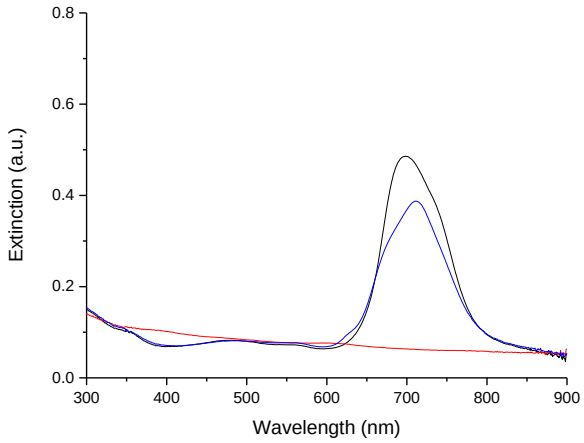

Figure 4.32: Extinction spectra measured for dye 2 (dye 114) at pH 8.3 (black), pH 12.5 (red) and pH 2 (blue). The pH was altered by the addition of 1 M NaOH or 1 M citric acid as appropriate.

The extinction profiles of the dye at both pH 8.3 and pH 2 are slightly blue-shifted compared to the profiles measured in pure DMF as the dye is less stable to aqueous conditions. However at these two pH values an absorption profile was still observed and the dye remained stable in solution confirming that the background fluorescence observed in the samples at acidic pH and neutral pH (with the exception of the citrate-HGNs at pH 7.5 in which partial aggregation quenched the fluorescence) was due to the presence of dye 2 within each system. However, at alkaline pH there was no absorption band observed and there was a complete loss of colour from the dye solution which indicated that the dye was no longer resonant or stable at this pH and explained the loss of background in the SERS spectra in both aggregated and non-aggregated samples. As previously proposed this may have been due to the addition of the OH^- ions which could disrupt the conjugated dye system and hence the chromophore, resulting in a colourless solution. The retention of the main Raman peaks from the dye at alkaline pH suggests that the dye structure is not significantly altered which indicated that the observed results may be due to differing counter ion effects on the dye. Under neutral conditions the bulky PF_6^- counter ion will be non-coordinating and will not interact with the dye molecule. However, at alkaline pH the

introduction of OH^- anions may induce a counter ion exchange allowing the OH^- anions to interact with the dye and interfere with the resonance effects within the dye molecule. This would also explain the reduction in signal intensity observed in the SERS spectra at alkaline pH.

To further evaluate the results observed, extinction spectra, particle size and zeta potential measurements were recorded in original, acidic and alkaline pH environments using both the PEG-stabilised and citrate-stabilised HGNs in order to assess the aggregation states within each sample. Results using PEG-stabilised HGNs and citrate-stabilised HGNs are presented in Figure 4.33 and Figure 4.34 respectively.

A

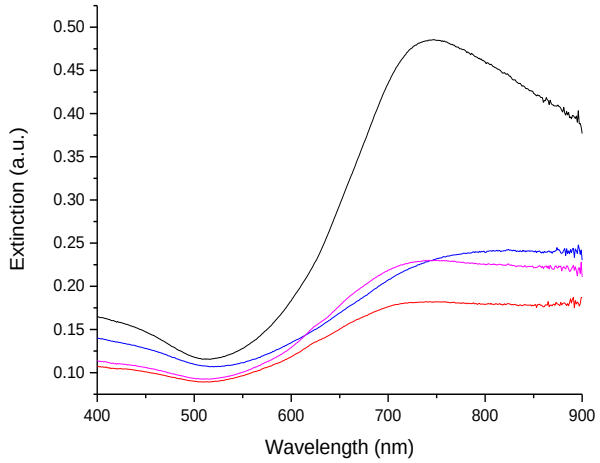

B

Sample	Particle Diameter (nm)	Zeta Potential (mV)
HGN-PEG	107 ± 0.4	-41.4 ± 4.5
HGN-PEG/dye114 pH 7.9	320.1 ± 52.1	-8.3 ± 2.8
HGN-PEG/dye114 pH 12.3	666.1 ± 140.6	-20.9 ± 0.2
HGN-PEG/dye114 pH 2.2	689.2 ± 99.3	17.9 ± 4.1

Figure 4.33: (A) Extinction spectra of original PEG-HGN (black), and HGN-PEG/dye 2 (dye 114) nanotags at pH 7.9 (red), pH 12.3 (blue) and pH 2.2 (pink). (B) Table summarising particle size and zeta potential values measured by DLS for samples presented in (A). Error bars are ± one standard deviation based on three replicate measurements.

Results indicated that on addition of dye 2 to the PEG-HGN there was a slight dampening and broadening in the extinction spectra observed. This was combined with a particle size increase of about three times the original PEG-HGN which indicated that a number of dimers and trimers may have been introduced into the sample as a result of the addition of the reporter molecule. At both acidic and alkaline pH a similar dampening and broadening in the extinction spectra was observed and the particle size measurements indicated that larger clusters were formed than at the original sample pH, however when compared to the size increase of the citrate-HGNs at both acidic and alkaline pH this was not as significant and indicated that the PEG stabilising layer provided some control over aggregation across the different pH environments.

A

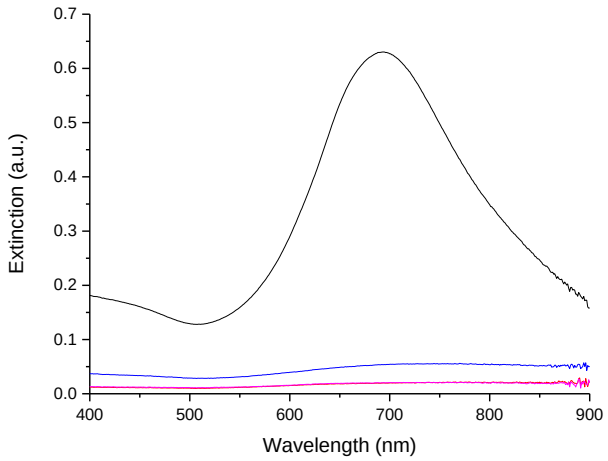

B

Sample	Particle Diameter (nm)	Zeta Potential (mV)
HGN-citrate	86.6 ± 0.5	-51.3 ± 0.5
HGN-citrate/dye114 pH 7.3	498.7 ± 134.1	-4.03 ± 3.1
HGN-citrate/dye114 pH 12.2	1148 ± 285	-24 ± 0.8
HGN-citrate/dye114 pH 2.2	899.2 ± 219	17.9 ± 4.2

Figure 4.34: (A) Extinction spectra of original citrate-HGN (black), and HGN-citrate/dye 2 (dye 114) nanotags at pH 7.3 (red), pH 12.2 (blue) and pH 2.2 (pink). (B) Table summarising particle size and zeta potential values measured by DLS for samples presented in (A). Error bars are ± one standard deviation based on three replicate measurements.

Results for nanotags based on citrate-HGNs showed that across all three pH values there was a loss of plasmon band in the extinction spectra which for acidic and alkaline environments was combined with visible precipitation from the solution. On addition of the dye molecule to the citrate-HGN surface there was a more significant size increase than for the PEG-based system which along with the proximity of the dye to the HGN surface explains the fluorescence quenching observed. At alkaline and acidic pH there was a significant size increase compared to the PEG-stabilised system which indicated that severe over-aggregation had occurred. The change in zeta potential is highly dependent upon the solution pH and therefore shows no change between the PEG and citrate stabilised systems recorded in similar pH environments.

After full investigation of the results obtained it was concluded that the reproducibility in the SERS spectra was resultant on the aggregation state of the sample being analysed. For PEG-stabilised systems the partial aggregation which was induced in both alkaline and acidic environments was sufficiently controlled by the polymer layer and resulted in extremely reproducible SERS spectra. At pH 7 the SERS was less reproducible however this was due to the large variations in fluorescence background. Conversely, the citrate-stabilised systems exhibited over-aggregation and precipitated from solution in both acidic and alkaline conditions which limited the reproducibility in the SERS signals obtained.

4.4 Bio-imaging of Stable, SERS Nanotags

Following the successful development of the PEG-stabilised nanotags, which exhibited a high level of colloidal stability and produced reproducible SERS spectra across a range of environments, both dye 1 and dye 2 labelled nanotags were applied to Chinese hamster ovarian (CHO) cell populations to determine their detectability. This experiment was carried out as a proof of concept to investigate the potential of the nanotags developed within this work for use in future cellular based applications. All cell populations were prepared by Corinna Wetherill (The University of Strathclyde) as outlined in Section 7.6.

4.4.1 Nanotag Toxicity Study

The toxicity of both the PEG-stabilised and citrate-stabilised nanotags towards CHO cells was investigated using an alamarBlue® assay[186] followed by addition of a SYTOX® green nucleic acid stain.[187]

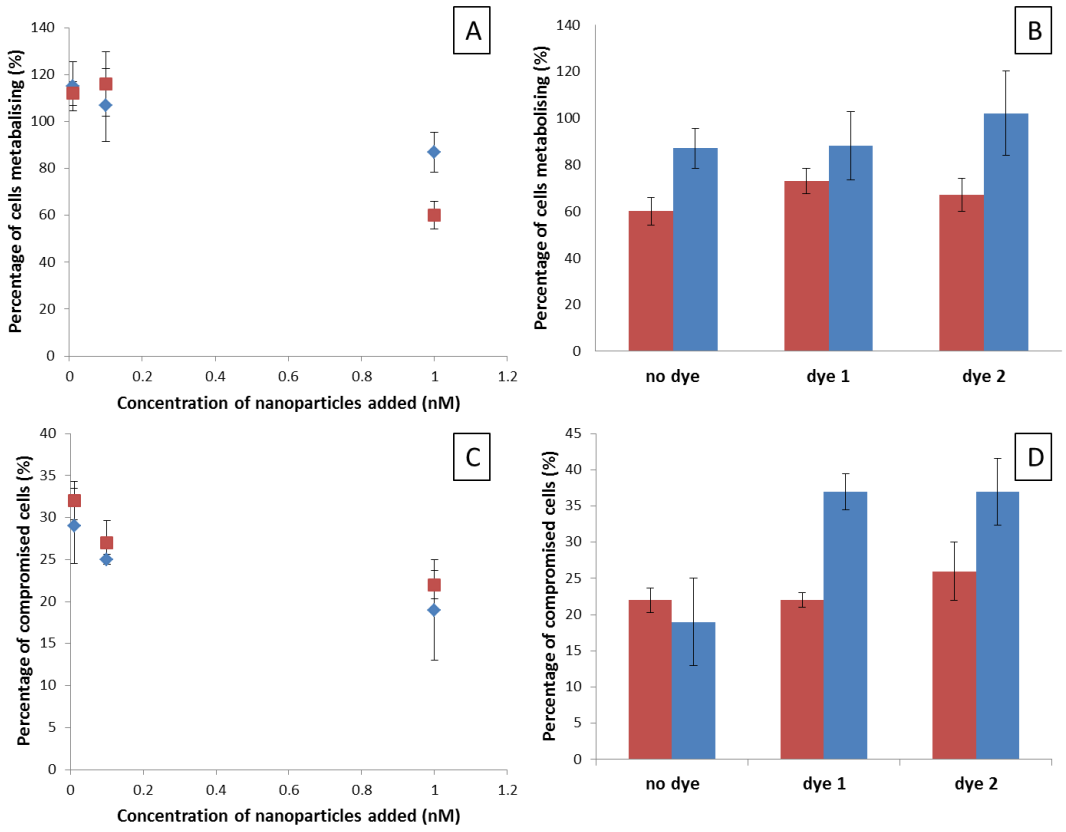

Figure 4.35: (A) and (B); Toxicity tests for PEG-stabilised (red) and citrate-stabilised (blue) HGNs evaluated using alamarBlue® (A) over varied concentrations and (B) for nanotags labelled with dye 1 and dye 2. (C) and (D); Toxicity tests for PEG-stabilised (red) and citrate-stabilised (blue) HGNs evaluated using SYTOXgreen® (A) over varied concentrations and (B) for nanotags labelled with dye 1 and dye 2. Percentages were calculated based on control samples containing cells in media (100% healthy) and cells treated with Triton X (100% compromised). Error bars are ± one standard deviation based on three replicate measurements.

AlamarBlue® is a proven indicator of healthy cells, containing a non-fluorescent active ingredient, resazurin, which is reduced to the bright red coloured, highly fluorescent molecule resorufin on entering viable cells.[186] The natural reducing power of healthy cells will continually turn over the molecule and therefore the

fluorescence signal will increase over time.[186] Conversely, SYTOX® green nucleic acid stain is a fluorescent indicator for cells with compromised plasma membranes. If cells are healthy, and thus cell walls are intact, the stain cannot cross the plasma membrane and no fluorescence signal should be observed.[187]

The cells were incubated with both labelled and unlabelled citrate-HGNs and PEG-HGNs to assess the effects of both HGNs and the reporter molecules on cell viability. Unlabelled HGNs were added to cells at three different concentrations (0.01 nM, 0.1 nM and 1 nM) while reporter molecules were added based on the optimised SERS conditions for nanotags with final concentrations of 1 nM HGN and 10 µM of reporter molecule. Following addition of alamarBlue® cells were incubated for four hours before analysis commenced. Results using alamarBlue® are presented in Figure 4.35A and Figure 4.35B, where a higher fluorescence signal was expected from cells still metabolising. The percentage values were calculated based on ideal conditions which assumed that the positive control, which contained cells in media, should contain cells which were 100% viable. A background signal was subtracted from wells which contained only media before the percentage of viable cells was calculated. The results indicated that in general the PEG-stabilised HGNs were slightly more toxic to the cells than their citrate-stabilised counterparts with a decrease in fluorescence intensity at higher concentrations. Additionally it appeared that the incorporation of the reporter molecules dye 1 and dye 2 into the system had no significant effect on cell viability. However the results observed over the two assays were variable as after incubation with SYTOX green®, which should show a decreased fluorescence signal in healthy cells, it appeared that although the PEG-HGNs still showed a slightly larger percentage of compromised cells the incorporation of the reporter molecules to the citrate-stabilised HGNs had a significant effect on the integrity of the cell membranes. For this study the percentage values were calculated with respect to a negative control, which contained cells treated with 0.1 % Triton X, where cells should be 100 % compromised.

The variation in results in combination with the reduction in cell viability of PEG-stabilised HGNs which should, according to current literature, increase the

biocompatibility of the HGNs indicated that the nanoparticles were interfering with the results of the assay.[188, 189] An additional control containing nanoparticles with no cells would have been beneficial to investigate this. However, by visual inspection of the cells under a microscope in addition to the viability assay results obtained it was concluded that the labelled nanotags were not particularly toxic to the CHO cells.

4.4.2 Nanotag Incubation Method

To investigate the most efficient method of preparing the nanotags for cell imaging, two methods of incubation were trialled and subsequently analysed by Raman mapping. Within this subsection the samples were interrogated using a Renishaw inVia Raman spectrometer/ Leica DMI 5000 M microscope with a 785 nm diode laser excitation source and 50x objective (NA 0.75) at 5% laser power (6.6 mW).

Nanotags were prepared as previously described, using PEG-stabilised HGNs labelled with either dye 1 or dye 2. In initial attempts the resulting nanotags were incubated for one hour with cells which were grown directly on to the coverslips to be analysed. The results for PEG-stabilised HGNs with dye 1 incubated using this initial method are shown in Figure 4.36. The false colour map calculated based on the intensity of the signal at 1602 cm^{-1}, the prominent peak within dye 1, indicated that there were large areas outside the cell where a measurable signal was produced. Areas of intense signal, highlighted in black, were restricted to a few localised areas within the mapping area both within and outside the cell perimeter. This enhanced signal may be due to clusters of nanotags forming on the glass coverslip due to the method of incubation, as nanotags have an affinity for glass coverslips and could easily bind to these preferentially to the cells. Additionally, the level of non-specific binding observed may have also been a result of the absence of a targeting moiety on the nanotags as they would have no specific affinity for any particular component of the cell.

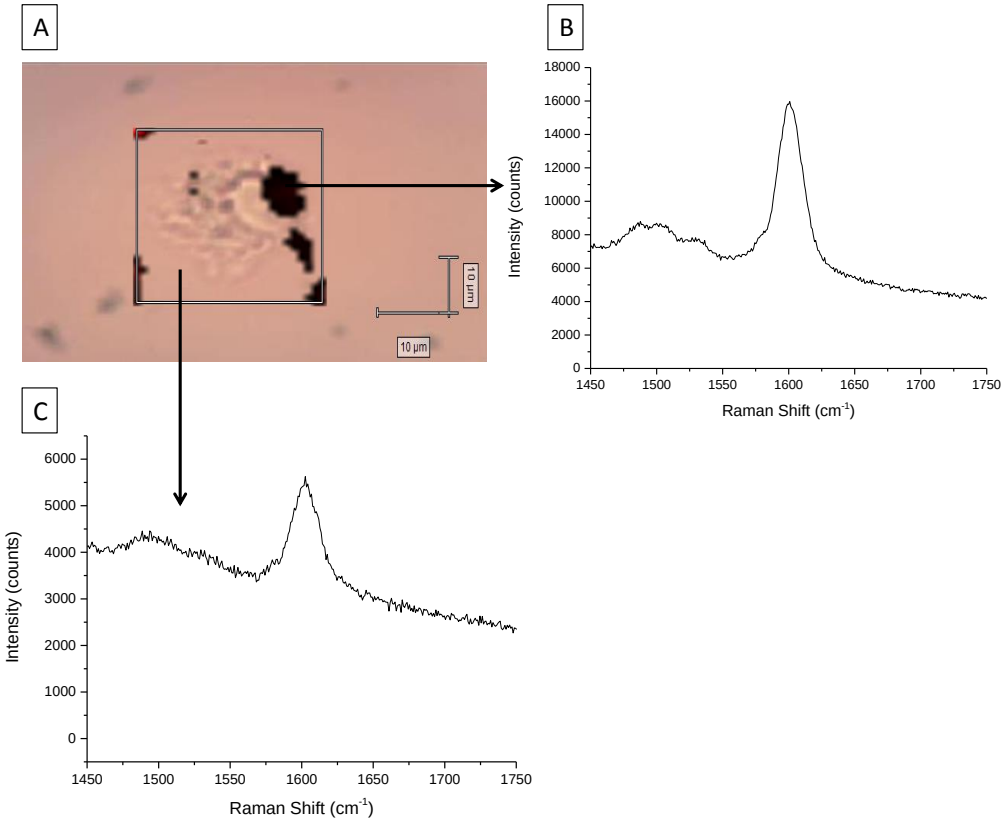

Figure 4.36: PEG-stabilised nanotags labelled with dye 1 (10 uM) and incubated with cells directly on to glass coverslips– A) white light image of cell to be mapped overlaid with a false colour intensity map calculated from the peak at 1602 cm^{-1}, the black rectangle represents the total area mapped, B) representative cell spectrum from the mapped cell at a point of intense signal, C) representative cell spectrum from the mapped cell from an area of low signal outside the cell. Samples were analysed at 785 nm, 5% laser power (~ 6.6 mW), 5 s accumulation time and centred at 1600 cm^{-1}.

In the second method of incubation the nanotags were added to cells and incubated in a flask for 24 hours before being mounted to glass coverslips. Additional wash steps were added to remove any extracellular or unbound nanotags. This method has been previously reported to be much more effective[190] than the initial method evaluated. The results using this method of incubation (Figure 4.37) were much more promising with reporter signal localised to areas within the cell boundary. The three prominent peaks corresponding to the reporter molecule label dye 2 at 1593 cm^{-1}, 1493 cm^{-1} and 1177 cm^{-1} were used to create a false colour map and results showed that each peak gave intense signals within the same areas of the cell confirming the presence of the nanotags.

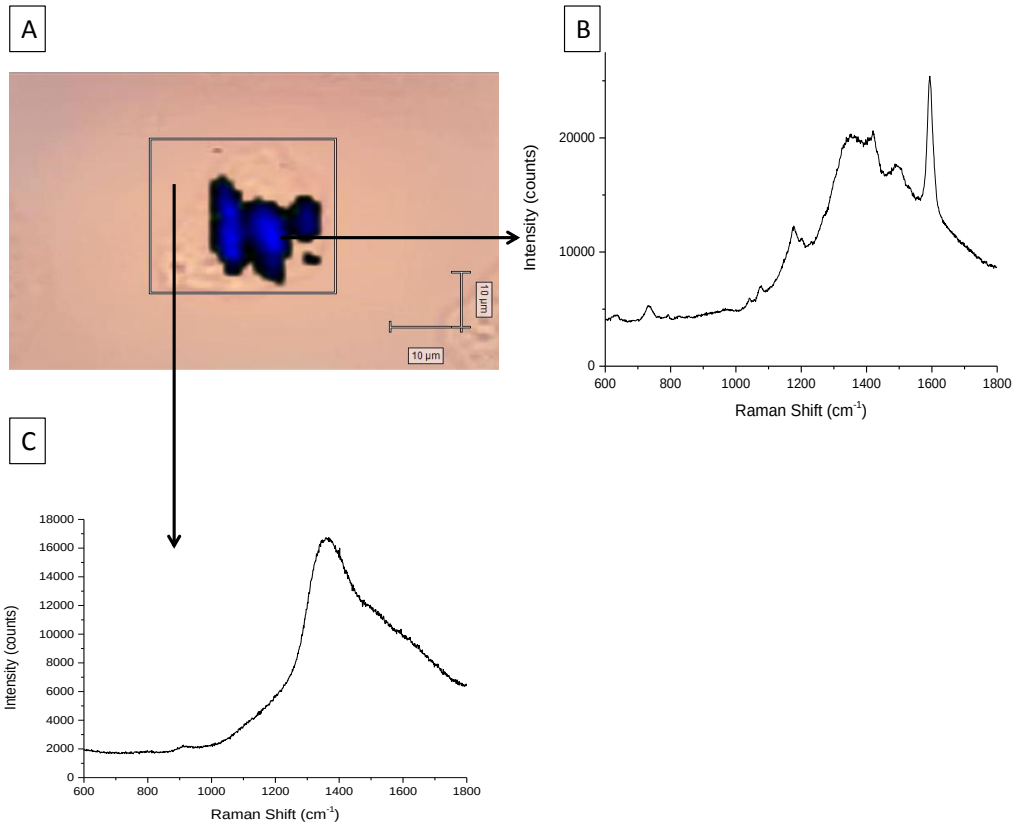

Figure 4.37: PEG-stabilised nanotags labelled with dye 2 (10 uM) and incubated with cells in a flask for 24 hrs prior to being mounted on to glass coverslips– A) white light image of cell to be mapped overlaid with a false colour intensity map calculated from a combination of the main peaks at 1593 cm^{-1}, 1493 cm^{-1} and 1177 cm^{-1}. The black rectangle represents the total area mapped, B) representative cell spectrum from the mapped cell at a point of intense signal, C) representative cell spectrum from the mapped cell from an area outside the cell. Samples were analysed at 785 nm, 5% laser power (~ 6.6 mW), 10 s accumulation time and spectral range of 600 cm^{-1} to 1800 cm^{-1}.

As previously suggested, this method proved much more successful than the initial incubation method with the successful removal of any unbound nanotags from the glass coverslip. The background fluorescence observed in both the background signal and the nanotag signal was a result of the glass fluorescence at 785 nm however moving the excitation wavelength to 1064 nm, where future mapping studies would ideally be undertaken, or use of calcium fluoride (CaF_2) windows should remove this.

Although the nanotag signal was only present within the cell perimeter, and additional wash steps within the slide preparation should have been sufficient to

remove any extracellular nanotags it could not be ascertained whether the nanotags had been successfully engulfed by the cells using 2D Raman mapping. Solution spectra of the nanotags pre and post cell incubation were analysed under the same conditions and example spectra are presented in Figure 4.38.

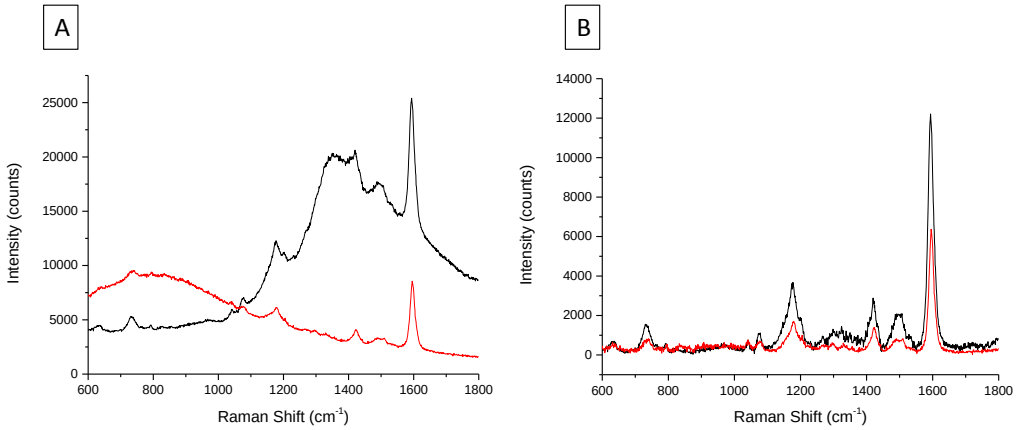

Figure 4.38: PEG-stabilised nanotags labelled with dye 2 (10 uM): A) representative cell spectrum from the mapped cell at a point of intense signal (black) and spectrum of nanotags prior to cell incubation (red), B) baseline corrected spectra of mapped cell at a point of intense signal (black) and of nanotags prior to cell incubation (red). Samples were analysed at 785 nm, 5% laser power (~ 6.6 mW), 10 s accumulation time and spectral range of 600 cm^{-1} to 1800 cm^{-1}.

Prominent peaks from dye 2 were still readily observed after cell incubation however the signal was largely dominated by the glass fluorescence background. Baseline corrected spectra are shown in Figure 4.38B to highlight the intensity difference between the two spectra. If the nanotags had been successfully engulfed by the cells a lower SERS signal intensity would be expected as previous work has shown that signals can decrease 10-100 fold succeeding cellular uptake.[133] However, data observed indicated that the solution based spectrum of the nanotags prior to cell incubation gave a lower signal intensity than the nanotags after incubation with cell populations. This suggested that partial aggregation was taking place during cellular incubation or that the spectra observed were a result of clustered areas of intense signal from nanotags on the cell surface which had not been effectively removed with washing steps and that the laser was focussed on the cell surface rather than within the cell. For further understanding, SEM imaging was carried out on nanotags

prepared in an identical way as for Raman mapping analysis. All SEM imaging was carried out by Dr. Samuel Mabbott (The University of Strathclyde).

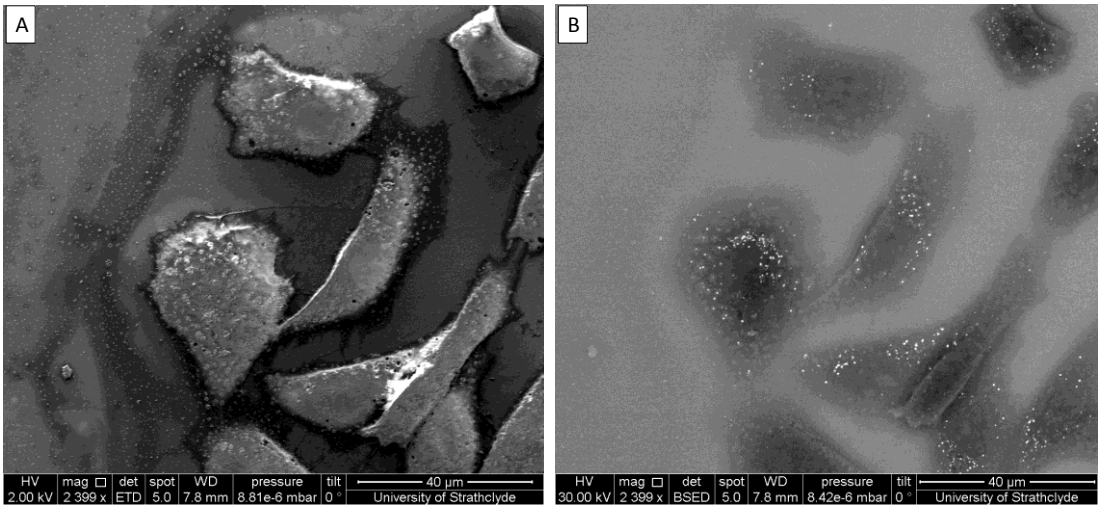

Figure 4.39: SEM images of CHO cells incubated with PEG-HGN nanotags labelled with dye 1 (10 uM): (A) focussed on cell surface and (B) focussed within cells.

In Figure 4.39A the surface of the cells were imaged and very few areas containing nanoparticles could be observed. In Figure 4.39B an image of the identical cell area to 4.39A, but focussed within the cell is presented. This appeared to show a significantly higher proportion of nanotags within the cells and they seemed to be relatively evenly distributed throughout the cells. This result indicated that the stabilised nanotags were being successfully engulfed by the cell populations and not purely bound to the cell surface. Although a very promising result this was not sufficient evidence to confirm the effective uptake of nanotags in cells and further analysis in the form of 3D Raman and SERS imaging[133] or cross sectioning followed by TEM analysis would need to be carried out.

Control measurements were carried out using cells which contained no nanotags or cells with unlabelled PEG-HGNs. False colour maps were generated based on the same conditions as for the labelled nanotags. Results are presented in Figure 4.40.

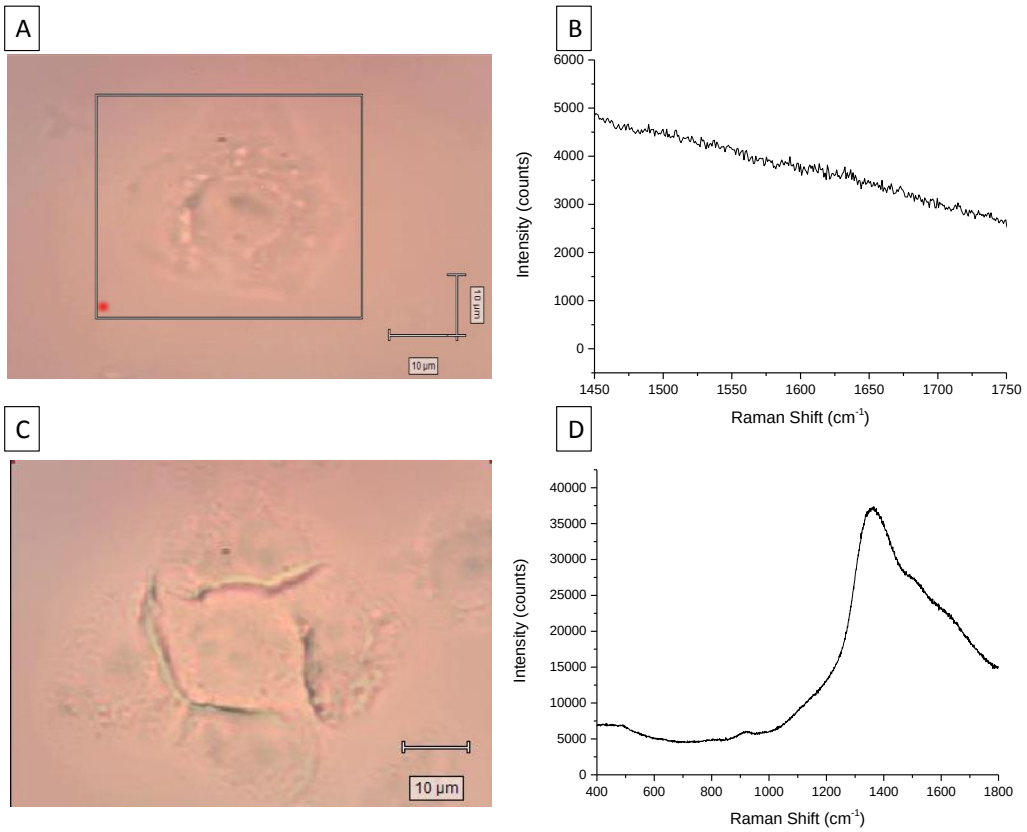

Figure 4.40: Control samples containing no nanotags (A) and (B) and unlabelled nanotags (C) and (D). (A) White light image of cell to be mapped overlaid with a false colour intensity map calculated from the peak at 1602 cm^{-1}, the black rectangle represents the total area mapped, (B) representative cell spectrum from the mapped cell, (C) white light image of cell to be mapped containing PEG-HGNs overlaid with a false colour intensity map calculated from the peak at 1602 cm^{-1}, (D) representative cell spectrum from the mapped cell. Samples were analysed at 785 nm, 5% laser power (~ 6.6 mW), 5 s accumulation time and centred at 1600 cm^{-1} (A and B), and 10 s acc. time with spectral range 400 – 1800 cm^{-1} (C and D).

The results observed confirmed that all peaks present within the previous samples were due to the presence of the labelled nanotags and no cell signal was observed at this wavelength. This may be a result of the large background fluorescence produced by the glass slide which could potentially be reduced by moving to longer excitation wavelengths or reducing the laser power.

4.4.3 *In-vitro* Analysis of Stabilised Nanotags at 785 nm

Due to the numerous bio-imaging, therapeutic and diagnostic applications of HGNs there is a great need for stable, SERS nanotags which produce sensitive intracellular signals at NIR excitation wavelengths. Although ideally analysis of the stabilised nanotags would be carried out at 1064 nm, due to instrumental constraints this was not a possibility so samples were analysed using a 785 nm excitation source.

Within this subsection the samples were interrogated using a WITec Alpha300-R instrument with a 785 nm diode laser excitation source and 100x objective (NA 0.9) at 25% laser power (270 μW) to produce higher resolution images than in the previous section. False colour images were generated in a similar way to those in the previous section however to give a more accurate representation of areas of intense signal peak ranges were used to generate the image as opposed to a single point. For nanotags labelled with dye 1 the areas analysed were 1569-1630.1 cm^{-1} and 1129.7-1234.2 cm^{-1}, with dye 2 were 1558.6 -1619 cm^{-1} and 1157.2-1206.7 cm^{-1}, and for a mix of both dyes were 1557-1628.5 cm^{-1} and 1117.1-1238.1 cm^{-1}. These two areas represented the areas of most intense signal within the two reporter molecules.

In order to reduce the background fluorescence observed from the glass coverslips in the previous section and to minimise sample degradation the conditions were further optimised from the previous study to reduce the integration time and laser power while still retaining a measurable SERS signal from within the cells. Previous studies involving HGNs have reported that too high a laser power can destroy the optical properties of the nanostructures and signals became unreliable.[36] Thus the laser power was reduced from 6.6 mW to 270 μW within this section.

Results for PEG-HGN nanotags labelled with dye 1 and dye 2 are presented in Figure 4.41 and 4.42 respectively.

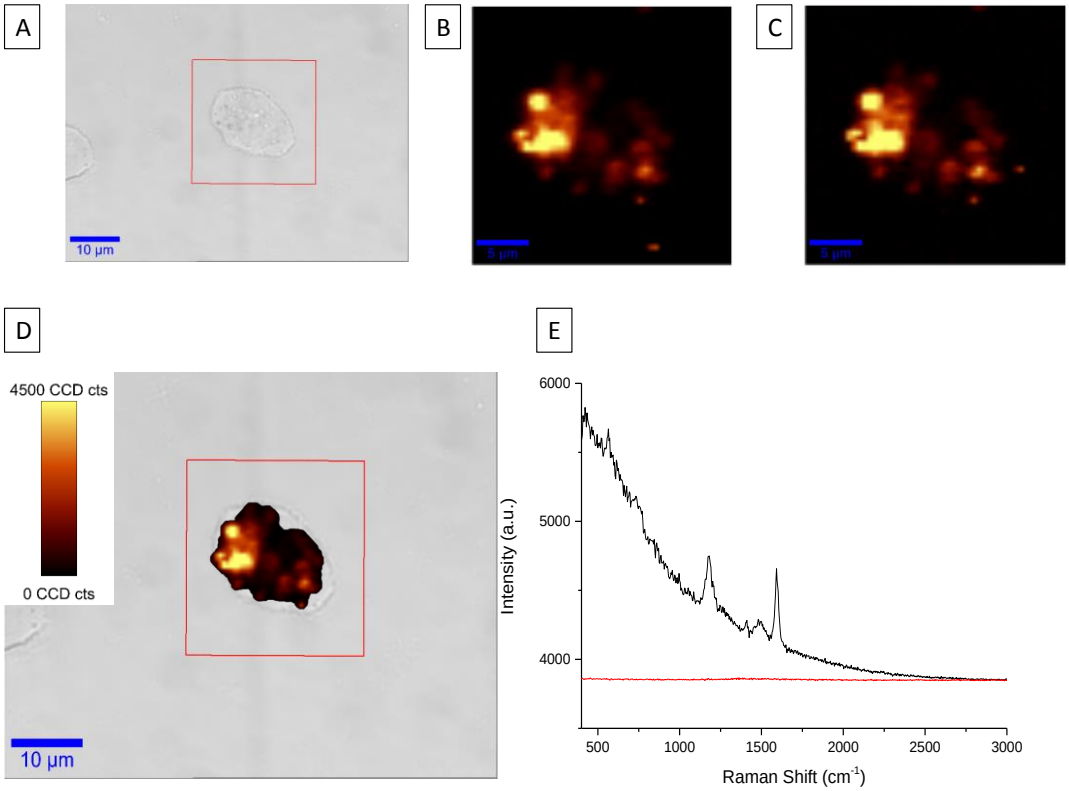

Figure 4.41: Analysis of dye 1 labelled nanotags: (A) optical bright field image of cell mapping area highlighted by the red square, (B) false colour intensity map for peak at 1593 cm^{-1}, (C) false colour intensity map for the peak at 1180 cm^{-1}, (D) false colour map overlaid on cell mapping area with scale bar for false colour maps inset, (E) SERS spectra produced from areas of intense signal (black) and background SERS spectra observed from out with the cell wall. Samples were analysed at 785 nm, 25% laser power (~ 270 µW), 0.5 s integration time with spectral range 400 - 3000 cm^{-1}.

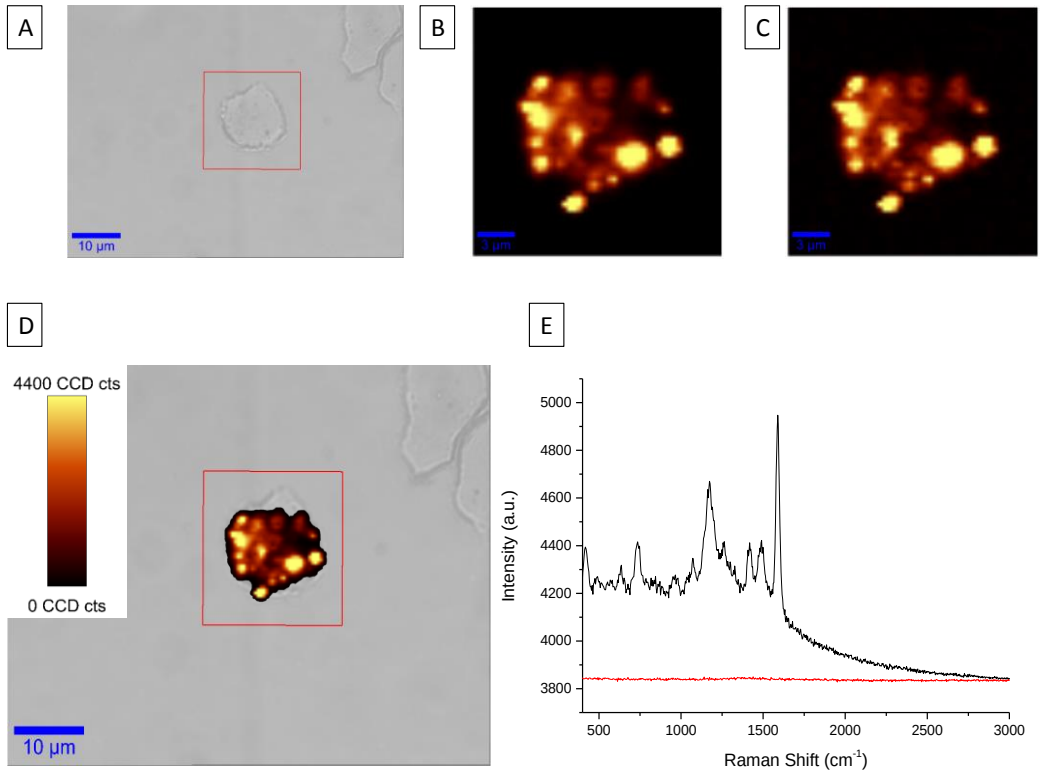

Figure 4.42: Analysis of nanotags labelled with dye 2: (A) optical bright field image of cell mapping area highlighted by the red square, (B) false colour intensity map for peak at 1588 cm^{-1}, (C) false colour intensity map for the peak at 1173 cm^{-1}, (D) false colour map overlaid on cell mapping area with scale bar for false colour maps inset, (E) SERS spectra produced from areas of intense signal (black) and background SERS spectra observed from out with the cell wall. Samples were analysed at 785 nm, 25% laser power (~ 270 µW), 0.5 s integration time with spectral range 400 – 3000 cm^{-1}.

Results observed for both dyes indicated that successful uptake of both nanotags had occurred with the presence of highly localised intense signals from within the cell boundary and no background signals present from out with the cell walls. The representative SERS spectra obtained for each nanotag are shown in Figure 4.41E and 4.42E and these correlate well with the solution based spectra previously shown in Section 4.2.1 (Figure 4.15). Additionally, reduction in the laser power has eliminated the background fluorescence obtained from the glass slide however there is still some background signal present from the dye fluorescence, much more intense in the resonant reporter dye 1 than in dye 2.

To determine whether these two nanotag systems could be used simultaneously in future targeting applications, both reporters were added to the same batch of PEG-stabilised HGNs at equimolar concentrations. The mixed dye labelled nanotags were then incubated with CHO cells and analysed as previously described.

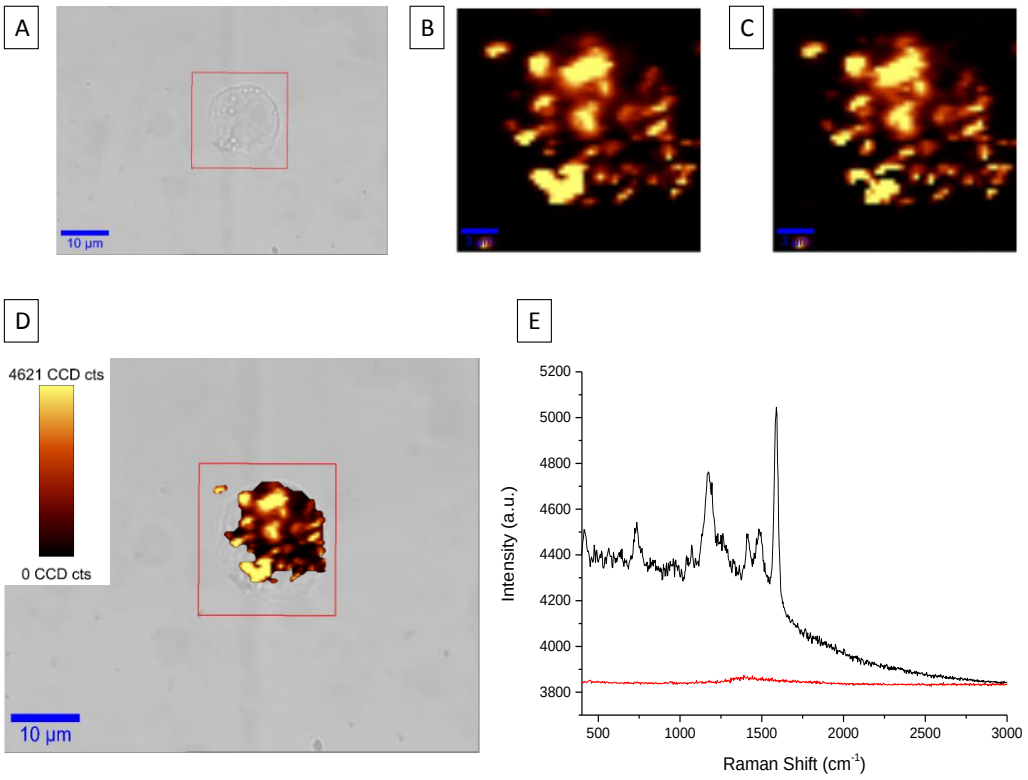

Figure 4.43: Analysis of nanotags labelled with a 50:50 mix of dye 1 and dye 2: (A) optical bright field image of cell mapping area highlighted by the red square, (B) false colour intensity map for peak at 1588 cm^{-1}, (C) false colour intensity map for the peak at 1173 cm^{-1}, (D) false colour map overlaid on cell mapping area with scale bar for false colour maps inset, (E) SERS spectra produced from areas of intense signal (black) and background SERS spectra observed from out with the cell wall. Samples were analysed at 785 nm, 25% laser power (~ 270 µW), 0.5 s integration time with spectral range 400 – 3000 cm^{-1}.

Results are presented in Figure 4.43 and again indicate effective cellular uptake has occurred with areas of intense signal within the cell walls and minimal background signals. By eye, the SERS spectrum observed appeared to be similar to the dye 2 labelled nanotags however for more accurate analysis PCA was carried out to separate out the spectra and understand if each nanotag could be identified based on their individual components. For analysis 20 replicate spectra from random areas of

intense signal within the cell for each system were analysed. Control samples contained cells with no nanotags added. The data was normalised and scaled before PCA was performed. The resulting principal component (PC) scores plot is presented in Figure 4.44.

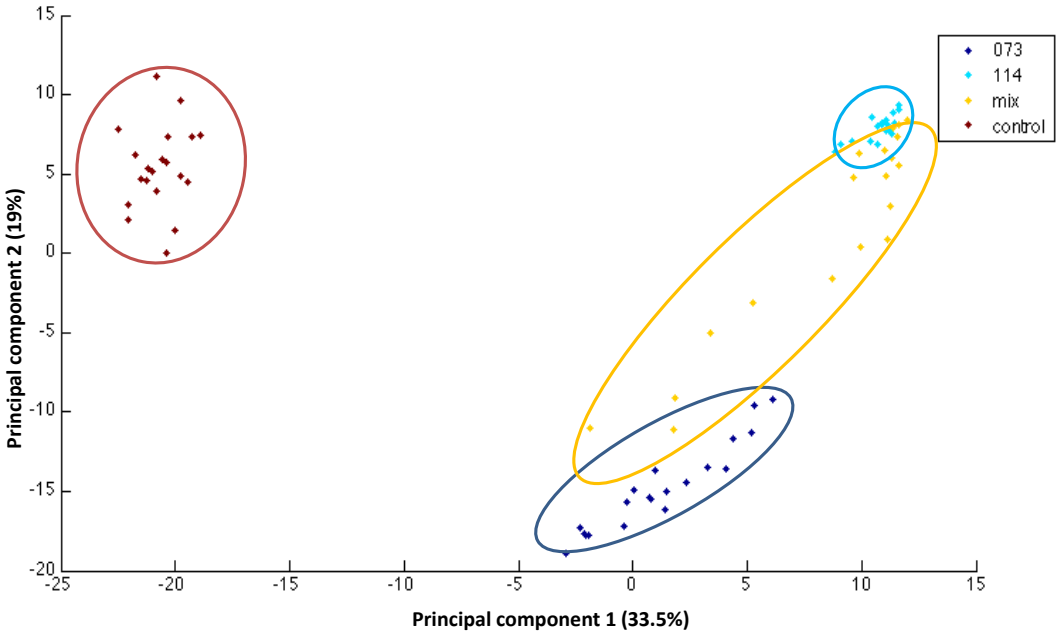

Figure 4.44: PCA scores plot discriminating between the two dyes used within the nanotag systems, and results of the duplex dye nanotag (yellow) which shows characteristic features of both dye 2 (light blue) and dye 1 (blue). The control sample consisted of cells with no nanotags added. 20 replicates of each sample were analysed, with an excitation wavelength of 785 nm.

The PCA scores plot clearly shows a distinction between nanotags labelled with dye 2 (highlighted in light blue) and nanotags labelled with dye 1 (highlighted in dark blue). The tight clustering observed in the data set for dye 2 compared to dye 1 showed that dye 2 labelled nanotags exhibited greater reproducibility in SERS spectra across the mapped area. The mixed dye labelled nanotags (highlighted in yellow) were spread between the two dyes which indicated that the mix contained characteristics of both nanotag systems. However, a higher proportion appeared to exhibit more spectral characteristics of dye 2 which would indicate that dye 2 may have a greater surface affinity for the HGNs than dye 1. The PC loading plots for both components and representative SERS spectra of each nanotag within the cell population are shown in Figure 4.45.

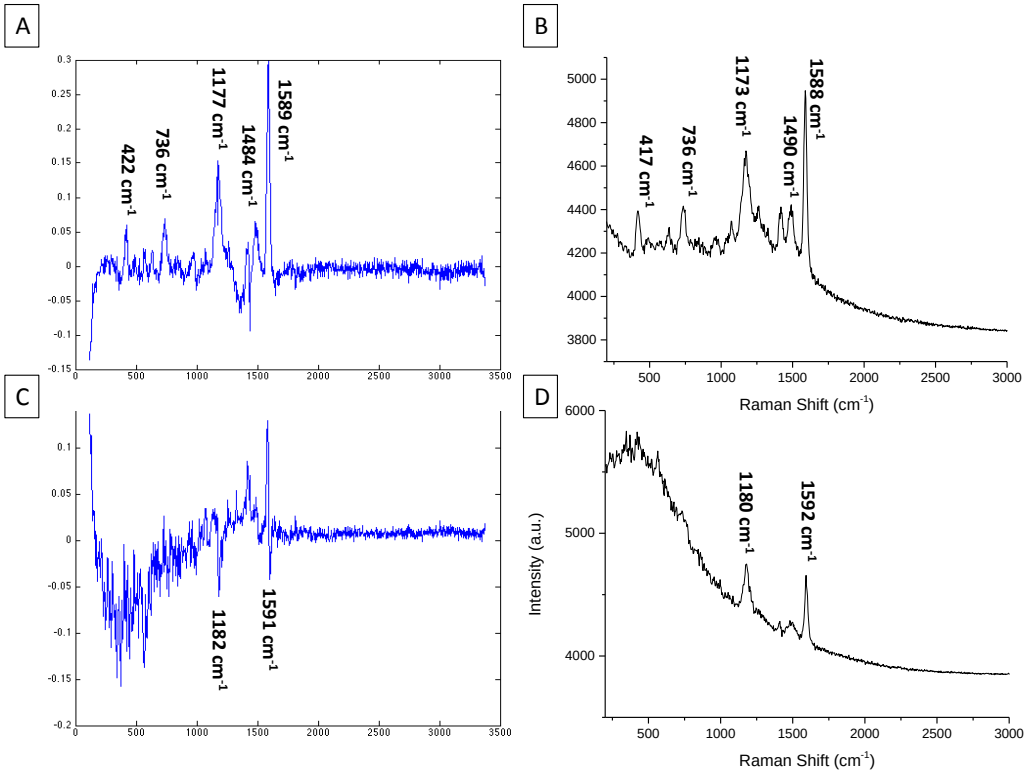

Figure 4.45: (A) Loadings plot for PC 1 with positive peak labelling, (B) representative SERS spectrum from cells incubated with nanotags labelled with dye 2, (C) loadings plot for PC 2 with negative peak labelling, (D) representative SERS spectrum from cells incubated with nanotags labelled with dye 1.

PC 1 explained 33.5 % of the variance in the data and represents the x-axis in the PC scores plot. Peak assignments revealed that PC 1 was characterised by Raman bands which corresponded to dye 2 labelled nanotags (Figure 4.45B). PC 2 represents the y-axis in the PC scores plot and explained 19 % of the variance in the data. The labelled peaks in the negative region corresponded to the Raman bands in the nanotags labelled with dye 1, which are shifted from 1177 cm^{-1} to 1182 cm^{-1} and 1589 cm^{-1} to 1591 cm^{-1} compared to dye 2. PC 3 accounted for 2.7 % of the variance in the data and along with the remainder of the PCs showed no variance in loadings plots so were not employed in the analysis.

Although further optimisation needs to be carried out to provide more enhanced clustering and better discrimination between the dye labelled nanotags this was a

very promising initial result and indicated that the two nanotag systems developed could potentially be used in combination for cellular targeting applications.

4.5 Chapter Conclusions

Stabilised HGNs developed in Chapter 3 were investigated as potential SERS substrates for the development of stable nanotags which could be used in future biological applications. A Raman reporter investigation was performed to find a suitable reporter which could produce rich vibrational spectra through the stabilising layers present on the HGN surface.

Initial studies focussed on the commercial reporters malachite green isothiocyanate (MG-ITC) and 1,2-bis(2-pyridyl)ethylene (BPE). MG-ITC showed promising initial results with both PEG-stabilised and citrate-stabilised HGNs at 633 nm however this was attributed to the extra resonance contribution from the dye at this wavelength and results could not be extended to longer wavelengths. BPE showed limited signals at 633 nm whereas at 785 nm a slight enhancement in the SERS signal from PEG-stabilised HGNs was observed. However the reporter was not strong enough to give intense signals when the stabilising layer was present due to the increased proximity from the HGN surface and the absence of SERS 'hot-spots' resulting from the non-aggregated system. Consequently, the commercial reporter labelled nanotags were disregarded for use with stabilised HGN substrates.

Additionally, two methods of reporter addition to the PEG stabilised HGNs were investigated, with results showing minimal signal variations between reporters added subsequent or prior to the addition of the stabilising layer. Therefore, as the synthesis was developed and optimised for addition of stabilising agents directly on to the HGN surface in the final stage of the synthesis, reporter molecules were added subsequent to the addition of the stabilising layer for all further studies.

A newly synthesised class of Raman reporters consisting of a highly conjugated chalcogenpyrilium backbone with 2-thienyl (dye 1) and 2-selenophenyl (dye 2) substituents were investigated for use with stabilised HGN substrates across four

different excitation wavelengths. A similar trend to that observed for both commercial reporters was apparent, with a reduction in signal intensities caused by the presence of the PEG stabilising layer, although the reduction in signal was not as significant. The spectra obtained at 633 nm showed much improved signal to noise ratios than BPE; however the observed Raman peaks were not as intense as results observed using MG-ITC as no resonance contribution from the dyes were present at this wavelength. Spectra obtained at 785 nm for all stabilised HGNs again showed promising results. At both 785 nm and 633 nm it was determined that dye 1, resonant at 789 nm, showed a greater enhancement in signals as a result of the resonance enhancement from the dye at both wavelengths, particularly at 785 nm where a large fluorescent background was observed in dye 1 compared to dye 2. Moving to longer wavelengths, desirable for future biological applications, successful SERS was obtained at 1064 nm and 1280 nm. At longer wavelengths dye 2, reported to be NIR active, produced greater enhancements in SERS signals across all stabilised HGNs investigated.

Nanotag optimisation for bio-imaging at 785 nm based on PEG-stabilised HGNs labelled with chalcogen reporters was carried out and compared to citrate-stabilised HGN substrates. In order to obtain the maximum SERS response possible from each substrate, various parameters based on the method of nanotag assembly were investigated. The results for PEG based systems showed that the method of nanotag preparation had no overall bearing on the SERS response generated however this was not the case for citrate-stabilised HGNs which showed extensive variations in the signals observed. Therefore, taking all factors into account the optimum conditions selected for nanotag assembly at 785 nm were as follows; 10 μM final concentration of reporter molecule, 30 minute incubation time before analysis and no centrifugation step.

Further to this work the SERS stability of both stabilised PEG-HGN and citrate-HGN based nanotags in various external environments and over time were assessed to investigate the reproducibility and long term stability in the SERS responses of the nanotag systems developed. PEG-stabilised HGN substrates produced consistent SERS signals over a one month period whereas citrate-stabilised HGN substrates

were highly unstable, resulting in considerable reduction in SERS intensities over the time frame studied. With regards to stability to salt, PEG-stabilised nanotags again produced much more reproducible SERS spectra than their citrate-stabilised counterparts in up to 1 M NaCl. This indicated that the PEG layer provided sufficient stability within the system to control any partial aggregation induced by addition of the reporter molecule and protect against any further aggregation induced by the salt. Finally, nanotag stability to different pH environments was investigated and the reproducibility in the SERS responses for each nanotag system was assessed using PCA. A similar trend in signal intensities was observed for both PEG and citrate-stabilised systems with a significant reduction in signals observed at alkaline pH. For PEG-stabilised systems the presence of the polymer layer sufficiently controlled the aggregation in both alkaline and acidic environments resulting in extremely reproducible SERS spectra. At pH 7 the SERS was less reproducible however this was due to the large variations in fluorescence background. Conversely, the citrate-HGN based systems exhibited over-aggregation in both acidic and alkaline conditions which limited the reproducibility in the SERS signals obtained.

As a proof of concept, PEG-stabilised nanotags developed within this chapter were applied to CHO cells and imaged at 785 nm. Toxicity tests revealed that PEG-stabilised HGNs were slightly more toxic to cells than their citrate-HGN counterparts while the effects of incorporation of reporter molecules into the system showed varied results and therefore the viability experiments were not conclusive. However, by visual inspection of the cells under a microscope in addition to the viability assay results obtained it was concluded that the labelled nanotags were not particularly toxic to the CHO cells. Two methods of nanotag incubation were assessed. Nanotags which were added to cells and incubated in a flask for 24 hours before being mounted to glass coverslips produced the most effective results with a reduction in non-specific binding observed and resulting in reporter signals being localised to areas within the cell boundary. SEM imaging indicated that nanotags were being successfully engulfed by the cell populations and not purely bound to the cell surface however further analysis in the form of 3D Raman and SERS imaging would need to be carried out for confirmation.

Effective SERS intensity maps were obtained for PEG-stabilised nanotags labelled with dye 1 and with dye 2 showing highly localised intense signals from within the cell boundary and no background signals present from out with the cell walls. Bio-imaging of nanotags labelled with a mixture of dye 1 and dye 2 in combination with PCA revealed that nanotags labelled with dye 1 and dye 2 could be clearly distinguished from one another with the mixed dye label exhibiting character from both dyes.

Overall, the nanotags developed within this chapter showed excellent stability and reproducibility in SERS signals over a one month period and in response to external environments such as changing salt concentrations or pH values. Additionally, their potential for use in future bio-applications has been demonstrated at 785 nm to provide a basis for future bio-imaging at longer wavelengths.

5 Conclusions

An improved methodology for HGN functionalisation which incorporates various polymer and sugar stabilising agents into the synthesis has been developed. This method provided a number of advantages over previously published methods including improved inter-batch reproducibility, a significant shift in SPR to longer wavelengths and increased stability to extreme salt and pH environments.

The stability of three different materials; namely polymers, sugars and silica, commonly used as stabilising agents were systematically compared both over time and in response to high salt concentrations or extreme pH values. The results indicated that in regards to HGNs, PEG is the most suitable stabilising agent with an inherent stability over one month in up to 5 M NaCl and in both acidic and alkaline environments. Additionally, HGNs stabilised with PEG exhibited a greater long term stability than standard citrate stabilised HGNs with no reduction in stability over the three month period studied.

PEG-stabilised HGN substrates were used to develop nanotags, labelled with novel chalcogenpyrilium based dyes, which produced effective SERS with no salt induced aggregation across four excitation wavelengths; 633 nm, 785 nm, 1064 nm and 1280 nm. The stabilised nanotags displayed excellent stability and produced consistent, reproducible SERS spectra over a one month period and in varying external environments such as high salt concentrations or extreme pH values.

Effective bio-imaging at 785 nm excitation using the stabilised nanotags was achieved. Initial toxicity testing revealed that the nanotags were biocompatible and SEM imaging indicated that successful cellular uptake was attained. These preliminary results suggest that the SERS detectable PEG-stabilised HGNs are capable of imaging target molecules within biological environments.

The stabilised nanotags developed offer great scope for use in a wide variety of biological applications such as photothermal ablation therapy or as drug delivery agents. The preliminary bio-imaging work undertaken at 785 nm excitation will

provide the basis for future biological SERS imaging at longer wavelengths such as 1064 nm which is a highly desirable working wavelength in bio-applications and is an area not currently well documented within the literature.

6 Future Work

The work presented within this thesis has focussed on the development of stable, NIR active SERS nanotags which provide an ideal platform for further application based research.

With regards to HGN functionalisation, the presence of the various stabilising agents was confirmed by extinction spectroscopy, particle size and zeta potential measurements while the significant red-shift in SPR observed in the polymer and sugar stabilised HGNs was attributed to the formation of a thinner gold shell compared to standard citrate-HGNs. Further characterisation by TEM would be beneficial for additional confirmation of the presence of each stabilising agent and to investigate the relationship between variations in shell thickness and the corresponding LSPR of the HGN.

The stable nanotags developed produced effective SERS across four excitation wavelengths. However, signals observed at 1280 nm were significantly weaker than results produced at shorter excitation wavelengths. An excitation source of 1280 nm is an idealistic working wavelength for future bio-imaging applications due to the increased tissue penetration depth and reduced autofluorescence experienced within this transparent spectral window. Therefore, in order to exploit the advantageous properties described further nanotag optimisation is required to improve the SERS signal at this wavelength. This could involve further development of the initial synthesis of the stabilised HGN substrates to provide HGNs with extreme red-shifted LSPRs which would be closer in resonance to the NIR laser excitation sources, enabling the provision of a significant electromagnetic contribution to the reporters. With an improvement in signal intensities effective SERS imaging at 1064 nm and 1280 nm could be readily achieved based on the initial bio-imaging work undertaken at 785 nm.

As a proof of concept preliminary bio-imaging work was carried out at 785 nm laser excitation. Cell toxicity studies performed were inconclusive as it was proposed that the nanoparticles may have interfered with the fluorescence results, therefore it

would be beneficial to repeat these experiments with an additional nanoparticle control in order to determine their effect on the toxicity indicators. Colorimetric indicators such as a Trypan Blue dead stain could also be used as an alternative to fluorescence detection based assays.

SEM imaging indicated that nanotags were being successfully engulfed by the cell populations and not purely bound to the cell surface. SERS intensity maps showing highly localised intense signals from within the cell boundary also indicated that cellular inclusion had been achieved however further analysis is required to support this initial data. This could be achieved using a combination of 3D Raman and SERS imaging which would determine the specific intracellular location of the nanotags without the need for invasive TEM imaging.

Bio-imaging of nanotags labelled with a mixture of both reporter molecules in combination with PCA revealed that nanotags could be clearly distinguished from one another, making them ideal reporters for future multiplex analysis. Furthermore, the PEG functionality on the nanotags creates an ideal platform for further conjugation of cell targeting ligands to increase the specificity of the nanotag system and create efficient targeting agents which could be used for biological sensing and cancer cell detection.

7 Experimental

All chemicals were purchased from Sigma-Aldrich, unless otherwise stated, and used without further purification.

7.1 HGN Synthesis

The synthesis developed was modified from previously reported methods.[23, 35, 40] All glassware was cleaned with aqua regia and rinsed thoroughly with deionised water before use. The synthesis was carried out under argon on a standard Schlenk line to keep the reaction free from oxygen. In a typical synthesis, trisodium citrate dihydrate (600 µL, 0.1 M) and cobalt (II) chloride hexahydrate (Acros Organics) (100 µL, 0.4 M) were added to deionised water (100 mL) in a three-necked round-bottom flask and degassed several times. While maintaining constant stirring, sodium borohydride (Acros Organics) (1 mL, 0.1 M) (freshly prepared with degassed, deionised water) was injected into the solution and left to react under argon for a further 20 minutes. At this stage the solution turned from a pale pink colour to brown indicating the formation of cobalt nanoparticles. Any remaining borohydride was quenched from the reaction mixture before the gold salt was added. Chloroauric acid trihydrate (ACS reagent grade) (33 mL, 0.25 mM) was then transferred into the solution, maintaining an air free environment, and stirred for a further 10 minutes. The solution was subsequently exposed to air and sodium citrate (500 µL, 0.1 M) was added as a stabilising agent. After 5 minutes the solution turned from brown to green and was left to stir for a further two hours. The resulting HGNs were then concentrated through centrifugation (3466 g) and redispersed in 8-10 mL of 2 mM sodium citrate solution for storage and further analysis.

7.2 HGN Functionalisation

7.2.1 Stabilising Agent Method

Modification of the HGN synthesis was achieved by replacing 500 µL of 0.1 M sodium citrate with 500 µL of 1 % (w/v) CM-PEG-SH (M_w 5000, Laysan Bio Inc.), 1 % (w/v) PVP (M_w 10 000), 1 % (w/v) PAM (M_w 5 000 000-6 000 000), 1 % (w/v) (PEI), 1 % (w/v) dextran from *Leuconostoc mesenteroides* (M_w 9000-11 000) or 1 % (w/v) 1-Thio-β-D-glucose sodium salt dihydrate (>98%, Santa Cruz Biotechnology) depending on the desired stabilising agent. Following addition of a stabilising agent the solution turned from brown to green within 5 minutes when citrate was added but increased to roughly 30 minutes when other stabilising agents were used. The resulting HGN solution was left to stir for a further two hours and was then concentrated through centrifugation (3466 g) and redispersed in 8-10 mL of d.H_2O for storage and further analysis.

7.2.2 Sodium Borohydride Method

The standard HGN synthesis was modified by simultaneously injecting 500 µL of 1 % (w/v) CM-PEG-SH (Mw 5000, Laysan Bio Inc.), 1 % (w/v) PVP (Mw 10 000), 1 % (w/v) PAM (Mw 5 000 000-6 000 000), or 1 % (w/v) (PEI) and sodium borohydride (Acros Organics) (1 mL, 0.1 M) into the solution which was then left to react under argon for a further 20 minutes. At this stage the solution turned from a pale pink colour to brown indicating the formation of cobalt nanoparticles. Any remaining borohydride was quenched from the reaction mixture before the gold salt was added. Chloroauric acid trihydrate (ACS reagent grade) (33 mL, 0.25 mM) was then transferred into the solution, maintaining an air free environment, and stirred for a further 10 minutes. The solution was subsequently exposed to air and no stabilising agent was added at this stage. When PEG, PAM and PEI were used in the initial step there was no colour change on exposure to air and the solutions remained brown in colour. For PVP, after 5 minutes the solution turned from brown to green and was

left to stir for a further two hours.[40] The resulting HGNs were then concentrated through centrifugation (3466 g) and redispersed in 8-10 mL of d.H_2O for storage and further analysis.

7.2.3 Post Synthesis Method (Initial PEG protocol)

To a concentrated HGN (citrate-stabilised) solution (960 µL), CM-PEG-SH (Mw 5000, Laysan Bio Inc.) (20 µL, 10 µM) was added. After shaking for one hour a higher concentration of PEG was added to the solution (20 µL, 1 mM) and left shaking for an additional two hours. The resulting HGNs were then concentrated through centrifugation (1585 g) and redispersed in 1 mL of d.H_2O for storage and further analysis.

7.2.4 Silica Encapsulation

7.2.4.1 PEG Method

PEG-stabilised HGNs (500 µL) were centrifuged (1585 g) for 15 minutes and the resulting pellet was redispersed in a water:ethanol (1:4) solution (5 mL) and ammonia (28-30%, 80 µL) to allow for growth of the silica shell using a modified Stöber method.[113] After 5 minutes, tetraethyl orthosilicate (TEOS) (12 µL, 10.7 mM) was added in four equal portions over 1 hour. The mixture was left to react overnight.

The resultant solution was then concentrated through centrifugation (1585 g) for 15 minutes and the precipitate was redispersed in d.H_2O (1 mL) for further analysis.

7.2.4.2 APTMS/MPTMS Coupling Agent Method

To a citrate stabilized HGN solution (1 mL) was added 3-aminopropyltrimethoxysilane (APTMS) (100 µL, 20 µM) or 3-mercaptopropyltrimetoxysilane (MPTMS) (100 µL, 20 µM). This solution was shaken for 10 minutes and left to equilibrate for a further 20 minutes. The resulting solution was centrifuged (1585 g) for 15 minutes. The silica shell was then grown

using a modified Stöber's method.[113] The APTMS-HGN pellet was redispersed in a water:ethanol (1:4) solution (10 mL) and ammonia (28-30%, 160 µL) was added under stirring as a catalyst for the hydrolysis. After 5 minutes, tetraethyl orthosilicate (TEOS) (4 µL, 1.8 mM) was added in 2 equal portions over 1 hour. The mixture was left to react for 4 hours. The resultant solution was then concentrated through centrifugation (1585 g) for 15 minutes and the precipitate was redispersed in d.H2O (1 mL) for further analysis.

7.3 Stability Testing

HGN solutions (700 µL) were altered to acidic pH ranging from pH 2.2-2.6 with dropwise addition of citric acid (1 M) or alkaline pH ranging from pH 12.6-13.1 with dropwise addition of NaOH (1 M). Readings were recorded using a portable pH meter which was calibrated before use. For salt stability studies, HGN solutions (270 µL) were added to NaCl (300 µL, 30 mM – 1 M). Control samples were prepared using d.H_2O (300 µL).

7.4 HGN Characterisation

7.4.1 Extinction Spectroscopy

Extinction spectroscopy was carried out on a Cary 300 Bio UV-vis spectrophotometer within the range of 400 – 900 nm. Spectra were baseline corrected using d.H_2O as a blank.

7.4.2 Particle Size and Zeta Potential Measurements (Dynamic Light Scattering)

DLS measurements were obtained using a Malvern Zetasizer Nano ZS system. For particle size measurements 1 mL of the appropriate solution was analysed in a 1 cm path length cell. For zeta potential measurements 800 µL of the appropriate sample was analysed using a dip cell.

7.4.3 HGN Concentration

HGN concentrations were calculated using a Nanosight® LM10 and analysed using Nanoparticle Tracking Analysis (NTA 2.1) software. The original concentrated HGN solutions were diluted with filtered d.H_2O until 5 - 20 nanoparticles per CCD frame were obtained. Imaging videos were recorded for 60 seconds, providing concentrations in particles/L which were subsequently converted to molar concentrations.

7.4.4 SEM Imaging

SEM imaging was used to obtain particle sizes by using ImageJ software based on the measurement of 50 particles per HGN sample. SEM samples were prepared on silicon wafers using previously reported methods.[35, 36] Briefly, wafers were washed with water and acetone, then dried under a flow of nitrogen and placed in an oxygen plasma cleaner for 60 seconds. Poly(diallyldimethylammonium chloride) (PDDA) solution (30 µL PDDA dissolved in 1 mL of 1 mM NaCl) was applied to the wafer and left for 30 minutes to render the surface positively charged. 50 µL of the HGN sample to be imaged was added to the wafer and left for 5-7 minutes before being removed; this process was repeated 3 times. After the third addition the sample was removed and the wafer washed with water and dried under N_2. SEM imaging was carried out on a Hitachi S-3000N variable pressure SEM with EDX 6″ tungsten electron source at an acceleration voltage of 30 kV.

7.5 SERS Analysis

7.5.1 Preparation of SERS Nanotags

Samples for SERS analysis were prepared by mixing functionalised HGNs (135 µL) with Raman reporters: dye 1 (15 µL, 1 x 10^{-4} M) or dye 2 (15 µL, 1 x 10^{-4} M) and d.H_2O (150 µL). Samples were left for 30 minutes before SERS measurements were recorded.

For commercial reporters functionalised HGNs (135 µL) were mixed with Raman reporters: Malachite green isothiocyanate (MG) (15 µL, 1 x 10^{-6} M) or 1,2-bis(4-pyridyl)ethylene (BPE) (15 µL, 1 x 10^{-4} M) and d.H_2O (150 µL). Samples were left overnight before SERS measurements were recorded.

7.5.2 Solution Based SERS Analysis

For all samples a cyclohexane standard was used to optimise the signal collection and to provide an intensity reference for data normalisation based on the peak at 800 cm^{-1}. Spectra were baseline corrected using a multipoint polynomial fit and level and zero mode in Grams software (AI 7.00).

633 nm

633 nm solution SERS spectra were recorded using a Renishaw inVia microscope system with a helium-neon laser excitation source and 1800 gr / mm grating. The laser power and accumulation times are specified in the figure captions for each individual experiment. Commercial reporter labelled nanotags were added to glass vials and analysed with the inverted laser system equipped with a 20x objective (NA 0.4). Chalcogen reporter labelled nanotags were analysed through transparent bottom 96 well micro-titre plates with 300 µl of the appropriate nanotag solution placed in each well on the standard laser system with a 5x objective (NA 0.15).

785 nm

785 nm solution SERS spectra were recorded using a Renishaw inVia microscope system with a diode laser excitation source and 1200 gr / mm grating. The incident laser power and accumulation times are specified in the figure captions for each individual experiment. Commercial reporter labelled nanotags were added to glass vials and analysed with the inverted laser system equipped with a 20x objective (NA 0.4). Chalcogen reporter labelled nanotags were analysed through transparent bottom 96 well micro-titre plates with 300

µl of the appropriate nanotag solution placed in each well on the standard laser system with a 5x objective (NA 0.15).

1064 nm

1064 nm solution SERS spectra were recorded in glass cuvettes using a Real Time Analyzer FT-Raman spectrometer with an Nd:YAG laser excitation source. Spectra were obtained by scanning 3 replicates of each sample with 20 s acquisition time under a laser incident power of 600 mW.

1280 nm

1280 nm solution SERS spectra were recorded in glass cuvettes using a SnRI portable S14 Raman spectrometer. Spectra were obtained by scanning 3 replicates of each sample with a 10 s acquisition time and laser incident power of 100 mW.

7.6 Cell Preparation

All cell preparation was carried out by Corinna Wetherill at The University of Strathclyde. CHO cells were grown in Dulbecco's Modified Eagle Medium (DMEM) with heat-inactivated foetal bovine serum (10 %), L-glutamine (1 %) and penicillin/streptomycin (1 %) at 37 ˚C in a humidified 5% CO_2 atmosphere.

7.6.1 Nanotag Incubation Directly on to Coverslips

Cells were cultured as above. After reaching confluence, cells were harvested and seeded at 1×10^6 cells per well in a 24-well sterile tissue culture plate to which 13 mm round glass coverslips had been previously applied. The cells were incubated overnight at 37 ˚C, 5 % CO_2 in order to allow the cells to adhere to the coverslips. The stabilised nanotag solutions (500 µL) were added to the cells and incubated for 1 hour. Following incubation and in order to remove any extracellular material the cells were washed four times with PBS before fixation with paraformaldehyde (4 %). After 15 min the coverslips were washed consecutively with PBS and dH_2O. After

fixation the coverslips were air dried for approximately 2 hours before being mounted on labelled microscope slides using distyrene-plasticiser-xylene (DPX) mountant.

7.6.2 Nanotag Incubation in Culture Flasks

After reaching confluence the cells (1×10^6 cells/mL) were transferred to a T25 tissue culture flask with 5 mL of the appropriate media and 500 µL of the stabilised nanotags was added. The cells were left to incubate overnight at 37 ˚C and following this cells were harvested and counted to create the required suspension of cells (4×10^5 cells/mL). 2 mL aliquots were removed and incubated with coverslips for 24 hours at 37 ˚C. Following incubation the media was removed and the cells were washed four times with PBS (1 mL) with gentle agitation for 5 mins with each wash before fixation with paraformaldehyde (4 %, 1 mL). After 15 min the coverslips were washed consecutively with PBS and dH_2O. After fixation the coverslips were air dried for approximately 2 hours before being mounted on labelled slides using DPX mountant.

7.6.3 Cell Toxicity Studies

Cells were harvested as above. After reaching confluence, cells were harvested and seeded at 1×10^6 cells per well in a 96-well plate. Various concentrations of the appropriate nanotag solution (500 µL) were added and incubated for one hour at 37 ˚C. Samples were prepared in triplicate for each concentration and control samples were prepared by adding media with no cells (media background), cells and no nanoparticles (live control), and cells treated with Triton X (0.1 %) (dead control). AlamarBlue® reagent (10 µL) was added to each well and samples were incubated at 37 ˚C for 4 hours. After 4 hours the produced fluorescence was measured using a Varian Cary Eclipse Fluorescence Spectrophotometer at an excitation wavelength of 570 nm and an emission wavelength of 585 nm. The integration time was set to 0.1 sec and the slits widths were 5 nm for both excitation and emission. To the same wells Sytox® Green (10 µL, 50 µM) was added and samples were incubated for

15 min at 37 ˚C and the fluorescence signal was measured at an excitation wavelength of 504 nm and emission wavelength of 523 nm.

7.6.4 Analysis of cell slides

In section 4.4.2 samples were interrogated with a Renishaw inVia Raman spectrometer/ Leica DMI 5000 M microscope with a 785 nm diode laser excitation source and 50x objective (NA 0.75) at 5% laser power (6.6 mW). A grating of 1200 lines / mm was used with a RenCam CCD (1046 × 256 pixels). A step size of x,y 1 µm was employed and static maps were centred at 1600 cm^{-1} with a 5 s acquisition time while extended scan maps had a 10 s acquisition time with a spectral range of 600 – 1800 cm^{-1}. Analysis of the collected data was performed using WiRE 4.0 (the same interface used for data collection). Signal to baseline maps is a method by which to monitor signal intensity within a specified range, the limits of which are set by the operator. This was used to create false colour intensity maps based on the dominant spectral peaks within each dataset.

In section 4.4.3 a WITec Alpha300-R instrument with a 785 nm diode laser excitation source and 100x objective (NA 0.9) at 25% laser power (270 µW) was used to produce higher resolution images than in the previous section. A step size of x,y 0.5 µm and 0.5 s acquisition time were used for all samples. WiTec project 2.10 software was used for further data processing as detailed in the main body of the text in section 4.4.3.

7.7 Chemometrics

All principal component analysis (PCA) was performed by Alexandre Girard (The University of Strathclyde) using Matlab software version R2012a (The MathWorks, Natick, MA, USA). Data were baseline corrected and scaled before analysis. PCA was carried out to assess the reproducibility in the spectra (pH studies, Section 4.3.3) and to separate and individually identify unique components within each dye (cell studies, Section 4.4.3).

8 References

1. N. R. Panyala, E. M. Peña-Méndez and J. Havel, *J. Appl. Biomed.*, 2009, **7**, 75-91.
2. S. Jiang, K. Y. Win, S. Liu, C. P. Teng, Y. Zheng and M.-Y. Han, *Nanoscale*, 2013, **5**, 3127-3148.
3. P. Ghosh, G. Han, M. De, C. K. Kim and V. M. Rotello, *Adv. Drug Deliv. Rev.*, 2008, **60**, 1307-1315.
4. L. Dykman and N. Khlebtsov, *Chem. Soc. Rev.*, 2012, **41**, 2256-2282.
5. M.-C. Daniel and D. Astruc, *Chem. Rev.*, 2004, **104**, 293-346.
6. M. A. El-Sayed, *Acc. Chem. Res.*, 2004, **37**, 326-333.
7. M. A. El-Sayed, *Acc. Chem. Res.*, 2001, **34**, 257-264.
8. J. Z. Zhang, *Acc. Chem. Res.*, 1997, **30**, 423-429.
9. J. Z. Zhang, *J. Phys. Chem. Lett*, 2010, **1**, 686-695.
10. R. Elghanian, J. J. Storhoff, R. C. Mucic, R. L. Letsinger and C. A. Mirkin, *Science*, 1997, **277**, 1078-1081.
11. A. J. Haes and R. P. Van Duyne, *J. Am. Chem. Soc.*, 2002, **124**, 10596-10604.
12. P. Sharma, S. Brown, G. Walter, S. Santra and B. Moudgil, *Adv. Colloid Interface Sci.*, 2006, **123**, 471-485.
13. Y. Cheng, A. C. Samia, J. D. Meyers, I. Panagopoulos, B. Fei and C. Burda, *J. Am. Chem. Soc.*, 2008, **130**, 10643-10647.
14. R. Hong, G. Han, J. M. Fernández, B.-J. Kim, N. S. Forbes and V. M. Rotello, *J. Am. Chem. Soc.*, 2006, **128**, 1078-1079.
15. X. Huang, I. H. El-Sayed, W. Qian and M. A. El-Sayed, *J. Am. Chem. Soc.*, 2006, **128**, 2115-2120.
16. A. M. Gobin, M. H. Lee, N. J. Halas, W. D. James, R. A. Drezek and J. L. West, *Nano Lett.*, 2007, **7**, 1929-1934.
17. W. Lu, C. Xiong, G. Zhang, Q. Huang, R. Zhang, J. Z. Zhang and C. Li, *Cancer Res.*, 2009, **15**, 876-886.
18. E. Hutter and J. H. Fendler, *Adv. Mater.*, 2004, **16**, 1685-1706.
19. A. Moores and F. Goettmann, *New J. Chem.*, 2006, **30**, 1121-1132.
20. G. Mie, *Ann. Phys.*, 1908, **330**, 377-445.
21. J. Z. Zhang and C. Noguez, *Plasmonics*, 2008, **3**, 127-150.
22. A. M. Schwartzberg and J. Z. Zhang, *J. Phys. Chem. C*, 2008, **112**, 10323-10337.
23. A. M. Schwartzberg, T. Y. Olson, C. E. Talley and J. Z. Zhang, *J. Phys. Chem. B*, 2006, **110**, 19935-19944.
24. S. J. Oldenburg, S. L. Westcott, R. D. Averitt and N. J. Halas, *J. Chem. Phys.*, 1999, **111**, 4729-4735.
25. V. Vongsavat, B. M. Vittur, W. W. Bryan, J. H. Kim and T. R. Lee, *ACS Appl. Mater. Interfaces*, 2011, **3**, 3616-3624.
26. J.-H. Kim, W. W. Bryan and T. Randall Lee, *Langmuir*, 2008, **24**, 11147-11152.
27. A. R. Lowery, A. M. Gobin, E. S. Day, N. J. Halas and J. L. West, *Int. J. Nanomedicine*, 2006, **1**, 149.
28. R. R. Anderson and J. A. Parrish, *J. Invest. Dermatol.*, 1981, **77**, 13-19.
29. A. D. McFarland, M. A. Young, J. A. Dieringer and R. P. Van Duyne, *J. Phys. Chem. B*, 2005, **109**, 11279-11285.
30. K. Kneipp, H. Kneipp, I. Itzkan, R. R. Dasari and M. S. Feld, *J. Phys.: Condens. Matter*, 2002, **14**, R597-R624.
31. H. P. Liang, L. J. Wan, C. L. Bai and L. Jiang, *J. Phys. Chem. B*, 2005, **109**, 7795-7800.

32. H. Xie, I. A. Larmour, Y.-C. Chen, A. W. Wark, V. Tileli, D. W. McComb, K. Faulds and D. Graham, *Nanoscale*, 2013, **5**, 765-771.
33. O. Muskens, D. Christofilos, N. Del Fatti and F. Vallée, *J. Opt. A: Pure Appl. Opt.*, 2006, **8**, S264-S272.
34. J. You, G. Zhang and C. Li, *ACS nano*, 2010, **4**, 1033-1041.
35. H. Xie, I. A. Larmour, W. E. Smith, K. Faulds and D. Graham, *J. Phys. Chem. C*, 2012, **116**, 8338-8342.
36. H. Xie, I. A. Larmour, V. Tileli, A. L. Koh, D. W. McComb, K. Faulds and D. Graham, *J. Phys. Chem. C*, 2011, **115**, 20515-20522.
37. Y. Sun and Y. Xia, *Anal. Chem.*, 2002, **74**, 5297-5305.
38. Y. Sun and Y. Xia, *Nano Lett.*, 2003, **3**, 1569-1572.
39. Y. Sun and Y. Xia, *J. Am. Chem. Soc.*, 2004, **126**, 3892-3901.
40. S. Preciado-Flores, D. Wang, D. A. Wheeler, R. Newhouse, J. K. Hensel, A. Schwartzberg, L. Wang, J. Zhu, M. Barboza-Flores and J. Z. Zhang, *J. Mater. Chem.*, 2011, **21**, 2344-2350.
41. M. P. Melancon, M. Zhou and C. Li, *Acc. Chem. Res.*, 2011, **44**, 947-956.
42. W. Cai, T. Gao, H. Hong and J. Sun, *Nanotechnol. Sci. Appl.*, 2008, **1**, 17-32.
43. J. Turkevich, P. C. Stevenson and J. Hillier, *Discuss. Faraday Soc.*, 1951, **11**, 55-75.
44. I. A. Larmour, K. Faulds and D. Graham, *J. Phys. Chem. C*, 2010, **114**, 13249-13254.
45. K. L. Knappenberger, Jr., A. M. Schwartzberg, A. M. Dowgiallo and C. A. Lowman, *J. Am. Chem. Soc.*, 2009, **131**, 13892-13893.
46. B. D. Chithrani, A. A. Ghazani and W. C. Chan, *Nano Lett.*, 2006, **6**, 662-668.
47. B. E. Brinson, J. B. Lassiter, C. S. Levin, R. Bardhan, N. Mirin and N. J. Halas, *Langmuir*, 2008, **24**, 14166-14171.
48. H. Chon, S. Lee, S. W. Son, C. H. Oh and J. Choo, *Anal. Chem.*, 2009, **81**, 3029-3034.
49. H. Chon, C. Lim, S.-M. Ha, Y. Ahn, E. K. Lee, S.-I. Chang, G. H. Seong and J. Choo, *Anal. Chem.*, 2010, **82**, 5290-5295.
50. R. Kumar, A. Maitra, P. Patanjali and P. Sharma, *Biomaterials*, 2005, **26**, 6743-6753.
51. M. P. Melancon, W. Lu, Z. Yang, R. Zhang, Z. Cheng, A. M. Elliot, J. Stafford, T. Olson, J. Z. Zhang and C. Li, *Mol. Cancer Ther.*, 2008, **7**, 1730-1739.
52. A. M. Schwartzberg, T. Y. Oshiro, J. Z. Zhang, T. Huser and C. E. Talley, *Anal Chem*, 2006, **78**, 4732-4736.
53. J. Jackson, S. Westcott, L. Hirsch, J. West and N. Halas, *Appl. Phys. Lett.*, 2003, **82**, 257.
54. G. Wu, A. Mikhailovsky, H. A. Khant, C. Fu, W. Chiu and J. A. Zasadzinski, *J Am Chem Soc*, 2008, **130**, 8175-8177.
55. N. R. Jana, L. Gearheart and C. J. Murphy, *J. Phys. Chem. B*, 2001, **105**, 4065-4067.
56. Y. Y. Yu, S. S. Chang, C. L. Lee and C. R. C. Wang, *J. Phys. Chem. B*, 1997, **101**, 6661-6664.
57. A. McLintock, N. Hunt and A. W. Wark, *Chem. Commun.*, 2011, **47**, 3757-3759.
58. Y. Xia, W. Li, C. M. Cobley, J. Chen, X. Xia, Q. Zhang, M. Yang, E. C. Cho and P. K. Brown, *Acc. Chem. Res.*, 2011, **44**, 914-924.
59. J. Chen, F. Saeki, B. J. Wiley, H. Cang, M. J. Cobb, Z.-Y. Li, L. Au, H. Zhang, M. B. Kimmey and X. Li, *Nano Lett.*, 2005, **5**, 473-477.
60. R. Weissleder, *Nat. Biotechnol.*, 2001, **19**, 316-316.
61. J. Chen, D. Wang, J. Xi, L. Au, A. Siekkinen, A. Warsen, Z.-Y. Li, H. Zhang, Y. Xia and X. Li, *Nano Lett.*, 2007, **7**, 1318-1322.
62. J. Yguerabide and E. E. Yguerabide, *Anal. Biochem.*, 1998, **262**, 137-156.
63. I. H. El-Sayed, X. Huang and M. A. El-Sayed, *Nano Lett.*, 2005, **5**, 829-834.

64. P. K. Jain, K. S. Lee, I. H. El-Sayed and M. A. El-Sayed, *J. Phys. Chem. B*, 2006, **110**, 7238-7248.
65. L. Scaffardi, N. Pellegri, O. De Sanctis and J. Tocho, *Nanotechnology*, 2005, **16**, 158.
66. X. Liu, M. Atwater, J. Wang and Q. Huo, *Colloids Surf. B*, 2007, **58**, 3-7.
67. *The Zeta Potential*, www.colloidal-dynamics.com, Accessed 10 May, 2015.
68. *Malvern Instruments Ltd.*, http://www.malvern.com/en/products/measurement-type/zeta-potential/default.aspx, Accessed 10 May, 2015.
69. Y. Xuan, Q. Li and W. Hu, *AIChE Journal*, 2003, **49**, 1038-1043.
70. J. Goldstein, D. E. Newbury, D. C. Joy, C. E. Lyman, P. Echlin, E. Lifshin, L. Sawyer and J. R. Michael, *Scanning Electron Microscopy and X-ray Microanalysis: Third Edition*, Springer US, 2012.
71. J. Gao, X. Huang, H. Liu, F. Zan and J. Ren, *Langmuir*, 2012, **28**, 4464-4471.
72. X. Zhang, M. R. Servos and J. Liu, *J. Am. Chem. Soc.*, 2012, **134**, 9910-9913.
73. X. Zhang, M. R. Servos and J. Liu, *Langmuir*, 2012, **28**, 3896-3902.
74. M. Roper, M. Skegg, C. Fisher, J. Lee, V. Dhanak, D. Woodruff and R. G. Jones, *Chem. Phys. Lett.*, 2004, **389**, 87-91.
75. C. A. Alves, E. L. Smith and M. D. Porter, *J. Am. Chem. Soc.*, 1992, **114**, 1222-1227.
76. H. Häkkinen, *Nat. Chem.*, 2012, **4**, 443-455.
77. M. Hasan, D. Bethell and M. Brust, *J. Am. Chem. Soc.*, 2002, **124**, 1132-1133.
78. D. V. Leff, L. Brandt and J. R. Heath, *Langmuir*, 1996, **12**, 4723-4730.
79. A. Kumar, S. Mandal, P. Selvakannan, R. Pasricha, A. Mandale and M. Sastry, *Langmuir*, 2003, **19**, 6277-6282.
80. T. Sainsbury, T. Ikuno, D. Okawa, D. Pacile, J. M. Frechet and A. Zettl, *J. Phys. Chem. C*, 2007, **111**, 12992-12999.
81. A. Ulman, *Chem. Rev.*, 1996, **96**, 1533-1554.
82. D. J. Revell, J. R. Knight, D. J. Blyth, A. H. Haines and D. A. Russell, *Langmuir*, 1998, **14**, 4517-4524.
83. S. Watanabe, H. Seguchi, K. Yoshida, K. Kifune, T. Tadaki and H. Shiozaki, *Tetrahedron Lett.*, 2005, **46**, 8827-8829.
84. F. Geng, K. Song, J. Z. Xing, C. Yuan, S. Yan, Q. Yang, J. Chen and B. Kong, *Nanotechnology*, 2011, **22**, 285101.
85. X. Zhang, J. Z. Xing, J. Chen, L. Ko, J. Amanie, S. Gulavita, N. Pervez, D. Yee, R. Moore and W. Roa, *Clin. Invest. Med.*, 2008, **31**, E160-E167.
86. T. Kong, J. Zeng, J. Yang, Y. Yao, X. Wang, P. Li, A. Yang, W. Roa, J. Xing and J. Chen, Life Science Systems and Applications Workshop, Bethesda, USA, 2007.
87. T. Kong, J. Zeng, X. Wang, X. Yang, J. Yang, S. McQuarrie, A. McEwan, W. Roa, J. Chen and J. Z. Xing, *Small*, 2008, **4**, 1537-1543.
88. X. Jiang, A. Housni, G. Gody, P. Boullanger, M. T. Charreyre, T. Delair and R. Narain, *Bioconjug. Chem.*, 2010, **21**, 521-530.
89. J. Zhang, D. Roll, C. D. Geddes and J. R. Lakowicz, *J. Phys. Chem. B*, 2004, **108**, 12210-12214.
90. K. Aslan, J. Zhang, J. R. Lakowicz and C. D. Geddes, *J. Fluoresc.*, 2004, **14**, 391-400.
91. M. Labib, M. Hedstrom, M. Amin and B. Mattiasson, *Anal Chim Acta*, 2010, **659**, 194-200.
92. S. Lee and V. H. Perez-Luna, *Anal Chem*, 2005, **77**, 7204-7211.
93. X. Wang, G. Li, T. Chen, M. Yang, Z. Zhang, T. Wu and H. Chen, *Nano Lett.*, 2008, **8**, 2643-2647.
94. L. C. Martin, I. A. Larmour, K. Faulds and D. Graham, *Chem. Commun.*, 2010, **46**, 5247-5249.

95. S. Lee, S. Kim, J. Choo, S. Y. Shin, Y. H. Lee, H. Y. Choi, S. Ha, K. Kang and C. H. Oh, *Anal. Chem.*, 2007, **79**, 916-922.
96. I. Pastoriza-Santos and L. M. Liz-Marzán, *Langmuir*, 2002, **18**, 2888-2894.
97. X. Qian, X. H. Peng, D. O. Ansari, Q. Yin-Goen, G. Z. Chen, D. M. Shin, L. Yang, A. N. Young, M. D. Wang and S. Nie, *Nat. Biotechnol.*, 2007, **26**, 83-90.
98. V. Mohanraj and Y. Chen, *Trop. J. Pharm. Res.*, 2007, **5**, 561-573.
99. H. Sun, J. Hong, F. Meng, P. Gong, J. Yu, Y. Xue, S. Zhao, D. Xu, L. Dong and S. Yao, *Surf. Coat. Technol.*, 2006, **201**, 250-254.
100. B. A. Moffat, G. R. Reddy, P. McConville, D. E. Hall, T. L. Chenevert, R. R. Kopelman, M. Philbert, R. Weissleder, A. Rehemtulla and B. D. Ross, *Mol. Imaging*, 2003, **2**, 324-332.
101. M. Kuruppuarachchi, H. Savoie, A. Lowry, C. Alonso and R. W. Boyle, *Mol. Pharm.*, 2011, **8**, 920-931.
102. W. Tang, H. Xu, E. J. Park, M. A. Philbert and R. Kopelman, *Biochem. Biophys. Res. Commun.*, 2008, **369**, 579-583.
103. A. M. Smith, H. Duan, M. N. Rhyner, G. Ruan and S. Nie, *Phys. Chem. Chem. Phys.*, 2006, **8**, 3895-3903.
104. H. Yiu, S. McBain, A. El Haj and J. Dobson, *Nanotechnology*, 2007, **18**, 435601-435606.
105. T. Xia, M. Kovochich, M. Liong, H. Meng, S. Kabehie, S. George, J. I. Zink and A. E. Nel, *ACS nano*, 2009, **3**, 3273-3286.
106. T. Silva, L. R. Pokhrel, B. Dubey, T. M. Tolaymat, K. J. Maier and X. Liu, *Sci. Total Environ.*, 2014, **468**, 968-976.
107. S. Liu and M. Y. Han, *Chem. Asian J.*, 2010, **5**, 36-45.
108. J. Huang, K. H. Kim, N. Choi, H. Chon, S. Lee and J. Choo, *Langmuir*, 2011, **27**, 10228-10233.
109. T. Ung, L. M. Liz-Marzán and P. Mulvaney, *Langmuir*, 1998, **14**, 3740-3748.
110. W. E. Doering and S. Nie, *Anal. Chem.*, 2003, **75**, 6171-6176.
111. B. Küstner, M. Gellner, M. Schütz, F. Schöppler, A. Marx, P. Ströbel, P. Adam, C. Schmuck and S. Schlücker, *Angew. Chem. Int. Ed.*, 2009, **48**, 1950-1953.
112. L. M. Liz-Marzán, M. Giersig and P. Mulvaney, *Langmuir*, 1996, **12**, 4329-4335.
113. W. Stöber, A. Fink and E. Bohn, *J. Colloid Interface Sci.*, 1968, **26**, 62-69.
114. K. Nozawa, H. Gailhanou, L. Raison, P. Panizza, H. Ushiki, E. Sellier, J. Delville and M. Delville, *Langmuir*, 2005, **21**, 1516-1523.
115. A. Van Blaaderen, J. Van Geest and A. Vrij, *J. Colloid Interface Sci.*, 1992, **154**, 481-501.
116. C. Fernández-López, C. Mateo-Mateo, R. n. A. Álvarez-Puebla, J. Pérez-Juste, I. Pastoriza-Santos and L. M. Liz-Marzán, *Langmuir*, 2009, **25**, 13894-13899.
117. D. Graham, B. J. Mallinder, D. Whitcombe, N. D. Watson and W. E. Smith, *Anal. Chem.*, 2002, **74**, 1069-1074.
118. S. P. Mulvaney, M. D. Musick, C. D. Keating and M. J. Natan, *Langmuir*, 2003, **19**, 4784-4790.
119. W. E. Smith and G. Dent, *Modern Raman spectroscopy: a practical approach*, John Wiley & Sons, 2005.
120. J. W. Strutt, *Philos. Mag.*, 1871, **41**, 107-120.
121. C. V. Raman and K. S. Krishnan, *Nature*, 1928, **121**, 501-502.
122. P. Pagsberg, R. Wilbrandt, K. B. Hansen and K.-V. Weisberg, *Chem. Phys. Lett.*, 1976, **39**, 538-541.
123. J.-X. Cheng and X. S. Xie, *J. Phys. Chem. B*, 2004, **108**, 827-840.
124. M. Fleischmann, P. J. Hendra and A. McQuillan, *Chem. Phys. Lett.*, 1974, **26**, 163-166.
125. M. G. Albrecht and J. A. Creighton, *J. Am. Chem. Soc.*, 1977, **99**, 5215-5217.

126. D. L. Jeanmaire and R. P. Van Duyne, *J. Electroanal. Chem.*, 1977, **84**, 1-20.
127. M. Moskovits, *J. Raman Spectrosc.*, 2005, **36**, 485-496.
128. M. Moskovits, *Rev. Mod. Phys.*, 1985, **57**, 783-826.
129. S. Schlücker, *Angew. Chem. Int. Ed.*, 2014, **53**, 4756-4795.
130. A. Otto, *J. Raman Spectrosc.*, 1991, **22**, 743-752.
131. G. McAnally, C. McLaughlin, R. Brown, D. C. Robson, K. Faulds, D. R. Tackley, W. E. Smith and D. Graham, *Analyst*, 2002, **127**, 838-841.
132. A. Stacy and R. Van Duyne, *Chem. Phys. Lett.*, 1983, **102**, 365-370.
133. S. McAughtrie, K. Lau, K. Faulds and D. Graham, *Chem. Sci.*, 2013, **4**, 3566-3572.
134. C. Krafft, T. Knetschke, A. Siegner, R. H. Funk and R. Salzer, *Vib. Spectrosc.*, 2003, **32**, 75-83.
135. M. S. Bergholt, W. Zheng, K. Lin, K. Y. Ho, M. Teh, K. G. Yeoh, J. B. Yan So and Z. Huang, *Int. J. Cancer*, 2011, **128**, 2673-2680.
136. N. Stone, C. Kendall, J. Smith, P. Crow and H. Barr, *Faraday Discuss.*, 2004, **126**, 141-157.
137. S. Teh, W. Zheng, K. Ho, M. Teh, K. Yeoh and Z. Huang, *Br. J. Surg.*, 2010, **97**, 550-557.
138. R. Manoharan, Y. Wang and M. S. Feld, *Spectrochim. Acta. A: Mol. Biomol. Spectrosc.*, 1996, **52**, 215-249.
139. B. R. Wood, A. Hermelink, P. Lasch, K. R. Bambery, G. T. Webster, M. A. Khiavi, B. M. Cooke, S. Deed, D. Naumann and D. McNaughton, *Analyst*, 2009, **134**, 1119-1125.
140. R. Shukla, V. Bansal, M. Chaudhary, A. Basu, R. R. Bhonde and M. Sastry, *Langmuir*, 2005, **21**, 10644-10654.
141. E. E. Connor, J. Mwamuka, A. Gole, C. J. Murphy and M. D. Wyatt, *Small*, 2005, **1**, 325-327.
142. A. M. Alkilany and C. J. Murphy, *J. Nanopart. Res.*, 2010, **12**, 2313-2333.
143. C. M. Goodman, C. D. McCusker, T. Yilmaz and V. M. Rotello, *Bioconjug. Chem.*, 2004, **15**, 897-900.
144. A. M. Chen and M. D. Scott, *BioDrugs*, 2001, **15**, 833-847.
145. N. Martin and M. Modi, *Clin Pharmacokinet*, 2001, **40**, 539-551.
146. J. You, J. Zhou, M. Zhou, Y. Liu, J. D. Robertson, D. Liang, C. Van Pelt and C. Li, *Part. Fibre Toxicol.*, 2014, **11**, 26-39.
147. L. Y. Chou, K. Ming and W. C. Chan, *Chem. Soc. Rev.*, 2011, **40**, 233-245.
148. D. P. O'Neal, L. R. Hirsch, N. J. Halas, J. D. Payne and J. L. West, *Cancer Lett.*, 2004, **209**, 171-176.
149. S. Schlücker, *ChemPhysChem*, 2009, **10**, 1344-1354.
150. A. Pallaoro, G. B. Braun, N. Reich and M. Moskovits, *Small*, 2010, **6**, 618-622.
151. X. Qian, X.-H. Peng, D. O. Ansari, Q. Yin-Goen, G. Z. Chen, D. M. Shin, L. Yang, A. N. Young, M. D. Wang and S. Nie, *Nat. Biotechnol.*, 2008, **26**, 83-90.
152. S. Lee, H. Chon, M. Lee, J. Choo, S. Y. Shin, Y. H. Lee, I. J. Rhyu, S. W. Son and C. H. Oh, *Biosens. Bioelectron.*, 2009, **24**, 2260-2263.
153. C. L. Zavaleta, B. R. Smith, I. Walton, W. Doering, G. Davis, B. Shojaei, M. J. Natan and S. S. Gambhir, *Proc. Natl. Acad. Sci.*, 2009, **106**, 13511-13516.
154. D. Schmaljohann, *Adv. Drug Deliv. Rev.*, 2006, **58**, 1655-1670.
155. S. Liu and M. Han, *Adv. Funct. Mater.*, 2005, **15**, 961-967.
156. J. Manson, D. Kumar, B. J. Meenan and D. Dixon, *Gold Bull.*, 2011, **44**, 99-105.
157. M. C. Daniel and D. Astruc, *Chem. Rev.*, 2004, **104**, 293-346.
158. S. Moreton, K. Faulds, N. C. Shand, M. A. Bedics, M. R. Detty and D. Graham, *Nanoscale*, 2015, **7**, 6075-6082.
159. Y. Xiong, Q. Chen, N. Tao, J. Ye, Y. Tang, J. Feng and X. Gu, *Nanotechnology*, 2007, **18**, 345301-345305.

160. J. F. Li, X. D. Tian, S. B. Li, J. R. Anema, Z. L. Yang, Y. Ding, Y. F. Wu, Y. M. Zeng, Q. Z. Chen and B. Ren, *Nat. Protoc.*, 2013, **8**, 52-65.
161. W. P. Wuelfing, S. M. Gross, D. T. Miles and R. W. Murray, *J. Am. Chem. Soc.*, 1998, **120**, 12696-12697.
162. N. J. Lang, B. Liu, X. Zhang and J. Liu, *Langmuir*, 2013, **29**, 6018-6024.
163. N. G. Greeneltch, A. S. Davis, N. A. Valley, F. Casadio, G. C. Schatz, R. P. Van Duyne and N. C. Shah, *J. Phys. Chem. A*, 2012, **116**, 11863-11869.
164. A. Bashkatov, E. Genina, V. Kochubey and V. Tuchin, *J. Phys. D: Appl. Phys.*, 2005, **38**, 2543-2555.
165. E. Le Ru, E. Blackie, M. Meyer and P. G. Etchegoin, *J. Phys. Chem. C*, 2007, **111**, 13794-13803.
166. S. L. Kleinman, R. R. Frontiera, A.-I. Henry, J. A. Dieringer and R. P. Van Duyne, *Phys. Chem. Chem. Phys.*, 2013, **15**, 21-36.
167. C. E. Talley, J. B. Jackson, C. Oubre, N. K. Grady, C. W. Hollars, S. M. Lane, T. R. Huser, P. Nordlander and N. J. Halas, *Nano Lett.*, 2005, **5**, 1569-1574.
168. Y. Lu, G. L. Liu, J. Kim, Y. X. Mejia and L. P. Lee, *Nano Lett.*, 2005, **5**, 119-124.
169. I. A. Larmour, E. A. Argueta, K. Faulds and D. Graham, *J. Phys. Chem. C*, 2012, **116**, 2677-2682.
170. K. K. Maiti, U. Dinish, C. Y. Fu, J.-J. Lee, K.-S. Soh, S.-W. Yun, R. Bhuvaneswari, M. Olivo and Y.-T. Chang, *Biosens. Bioelectron.*, 2010, **26**, 398-403.
171. L. He, N.-J. Kim, H. Li, Z. Hu and M. Lin, *J. Agric. Food Chem.*, 2008, **56**, 9843-9847.
172. M. Chandra, A.-M. Dowgiallo and K. L. Knappenberger Jr, *J. Am. Chem. Soc.*, 2010, **132**, 15782-15789.
173. Z. Zhuang, J. Cheng, H. Jia, J. Zeng, X. Han, B. Zhao, H. Zhang, G. Zhang and W. Zhao, *Vib. Spectrosc.*, 2007, **43**, 306-312.
174. H. Kearns, N. Shand, W. E. Smith, K. Faulds and D. Graham, *Phys. Chem. Chem. Phys.*, 2015, **17**, 1980-1986.
175. Z. Zhuang, X. Shi, Y. Chen and M. Zuo, *Spectrochim. Acta. A: Mol. Biomol. Spectrosc.*, 2011, **79**, 1593-1599.
176. P. L. Stiles, J. A. Dieringer, N. C. Shah and R. P. Van Duyne, *Annu. Rev. Anal. Chem.*, 2008, **1**, 601-626.
177. M. Bedics, H. Kearns, J. Cox, S. Mabbott, F. Ali, N. Shand, K. Faulds, J. Benedict, D. Graham and M. Detty, *Chem. Sci.*, 2015, **6**, 2302-2306.
178. A. Dube, A. R. Chadeayne, M. Sharma, P. T. Wolczanski and J. R. Engstrom, *J. Am. Chem. Soc.*, 2005, **127**, 14299-14309.
179. T. Nakamura, R. Kimura, F. Matsui, H. Kondoh, T. Ohta, H. Sakai, M. Abe and M. Matsumoto, *Langmuir*, 2000, **16**, 4213-4216.
180. S. Abalde-Cela, S. Ho, B. Rodríguez-González, M. A. Correa-Duarte, R. A. Álvarez-Puebla, L. M. Liz-Marzán and N. A. Kotov, *Angew. Chem.*, 2009, **121**, 5430-5433.
181. T. Huang and R. W. Murray, *Langmuir*, 2002, **18**, 7077-7081.
182. C. Xue, Y. Xue, L. Dai, A. Urbas and Q. Li, *Adv. Optical Mater.*, 2013, **1**, 581-587.
183. G. Schneider, G. Decher, N. Nerambourg, R. Praho, M. H. Werts and M. Blanchard-Desce, *Nano Lett.*, 2006, **6**, 530-536.
184. R. Tantra, R. J. Brown and M. J. Milton, *J. Raman Spectrosc.*, 2007, **38**, 1469-1479.
185. D.-H. Kim, R. M. Jarvis, Y. Xu, A. W. Oliver, J. W. Allwood, L. Hampson, I. N. Hampson and R. Goodacre, *Analyst*, 2010, **135**, 1235-1244.
186. *Life Technologies*, http://www.lifetechnologies.com/uk/en/home/brands/molecular-probes/key-molecular-probes-products/alamarblue-rapid-and-accurate-cell-health-indicator.html#what, Accessed 22 April, 2015.

187. *Invitrogen*, http://tools.lifetechnologies.com/content/sfs/manuals/mp07020.pdf, Accessed 22 April, 2015.
188. A. Kroll, M. H. Pillukat, D. Hahn and J. Schnekenburger, *Eur. J. Pharm. Biopharm.*, 2009, **72**, 370-377.
189. C. Hoskins, L. Wang, W. P. Cheng and A. Cuschieri, *Nanoscale Res. Lett.*, 2012, **7**, 1-12.
190. N. M. Sirimuthu, C. D. Syme and J. M. Cooper, *Anal. Chem.*, 2010, **82**, 7369-7373.
191. A. Kamińska, I. Dzięcielewski, J. L. Weyher, J. Waluk, S. Gawinkowski, V. Sashuk, M. Fiałkowski, M. Sawicka, T. Suski and S. Porowski, *J. Mater. Chem.*, 2011, **21**, 8662-8669.

Appendix 1: Raman Reporter Spectral Assignments

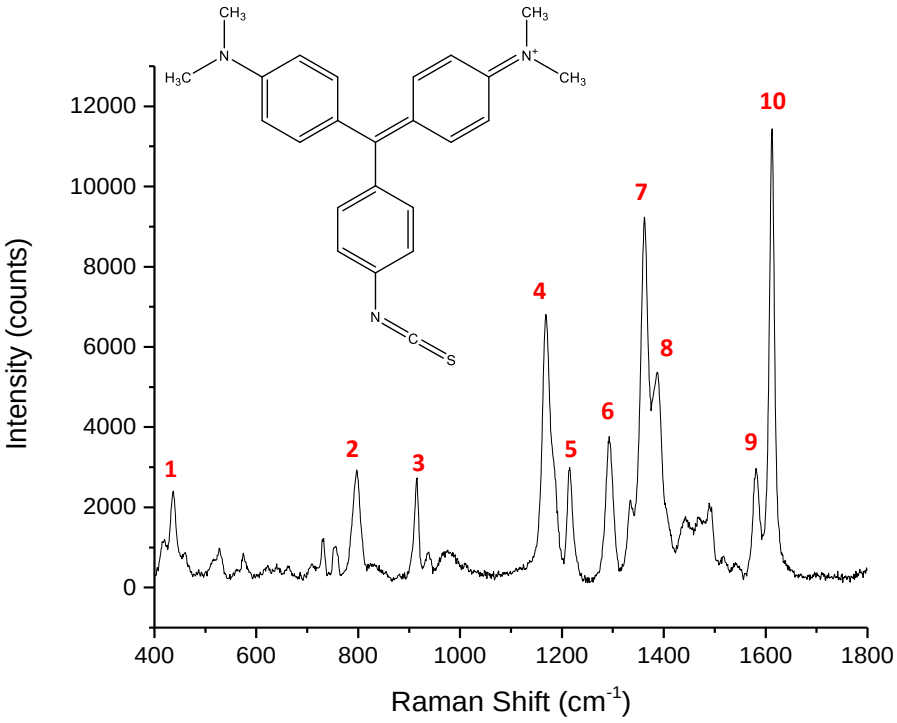

Figure 46: Representative SERS spectrum from MG at 633 nm laser excitation with structure inset.

Table 2: SERS peaks from MG at 633 nm excitation (numbers labelled in red correspond to the labelled peaks in Figure 1), and reported spectral assignments.[171, 191]

Raman Shift (cm^{-1})	Spectral Assignment
(1) 437	Benzene ring deformation
(2) 797	C-H bend from benzene ring
(3) 915	In plane benzene vibration
(4) 1168	In plane vibrations of ring C-H
(5) 1214	C-H rocking
(6) 1293	In plane C-H and C-C-H
(7) 1362	N-Ph ring stretch
(8) 1387	N-Ph ring stretch
(9) 1581	In plane ring, stretch and bend
(10) 1613	N-Ph ring and C-C stretch

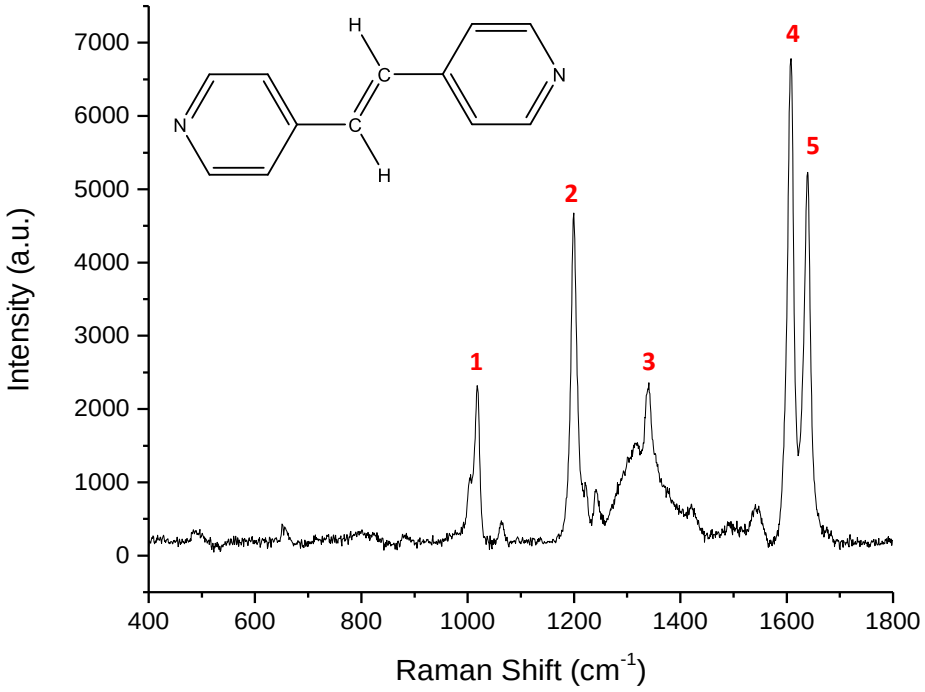

Figure 47: Representative SERS spectrum from BPE at 785 nm laser excitation with structure inset.

Table 3: SERS peaks from BPE at 785 nm excitation (numbers labelled in red correspond to the labelled peaks in Figure 2), and reported spectral assignments.[174, 175]

Raman Shift (cm^{-1})	Spectral Assignment
(1) 1018	Ring deformation
(2) 1199	C-C stretch, C-N and C-H bend from pyridyl ring
(3) 1341	In plane C-H and C=C bend
(4) 1608	C-C stretch, C-N and C-H bend from pyridyl ring
(5) 1639	C=C stretch

Due to the novel nature of the chalcogen dyes there have been no published peak assignments within the literature, however DFT calculations are currently being undertaken within the group. Therefore, it was only possible to present estimated spectral assignments for the main peaks associated with each dye.

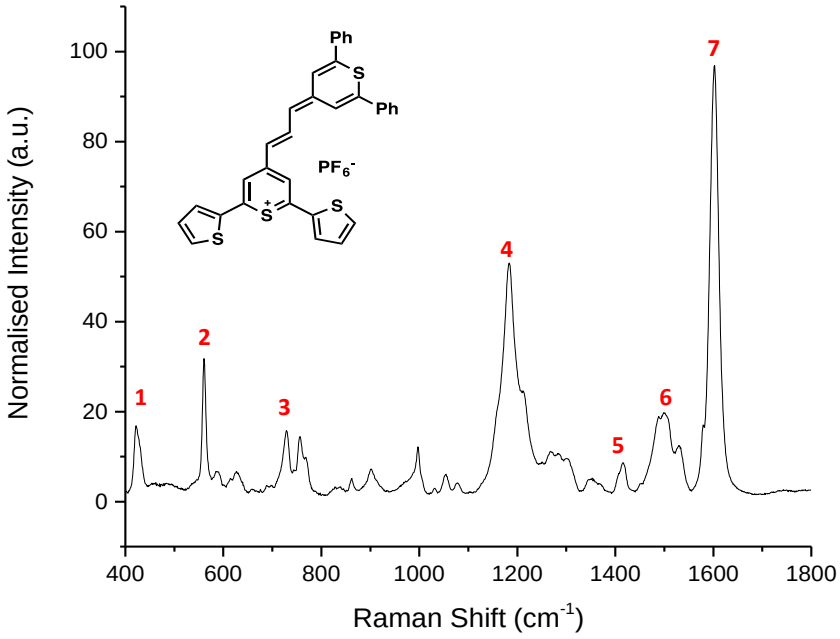

Figure 48: Representative SERS spectrum from dye 1 at 785 nm laser excitation with structure inset.

Table 4: SERS peaks from dye 1 at 785 nm excitation (numbers labelled in red correspond to the labelled peaks in Figure 3), and suggested spectral assignments.

Raman Shift (cm^{-1})	Spectral Assignment
(1) 421	C-C, C-H and C-S stretch in S rings, bridge C=C, C-H rocking
(2) 561	Bridge C=C, C-H rocking
(3) 728	S ring breathing mode C-S, C-C and C-H
(4) 1183	Bridge C=C, C-H
(5) 1415	S ring vibrations C-S, C-C and C-H
(6) 1499	C-C, C-H and C-S vibrations from thiopyran and phenyl rings, bridge C=C, C-H
(7) 1603	C-C, C-H and C-S vibrations from thiopyran rings and phenyl aromatic vibrations

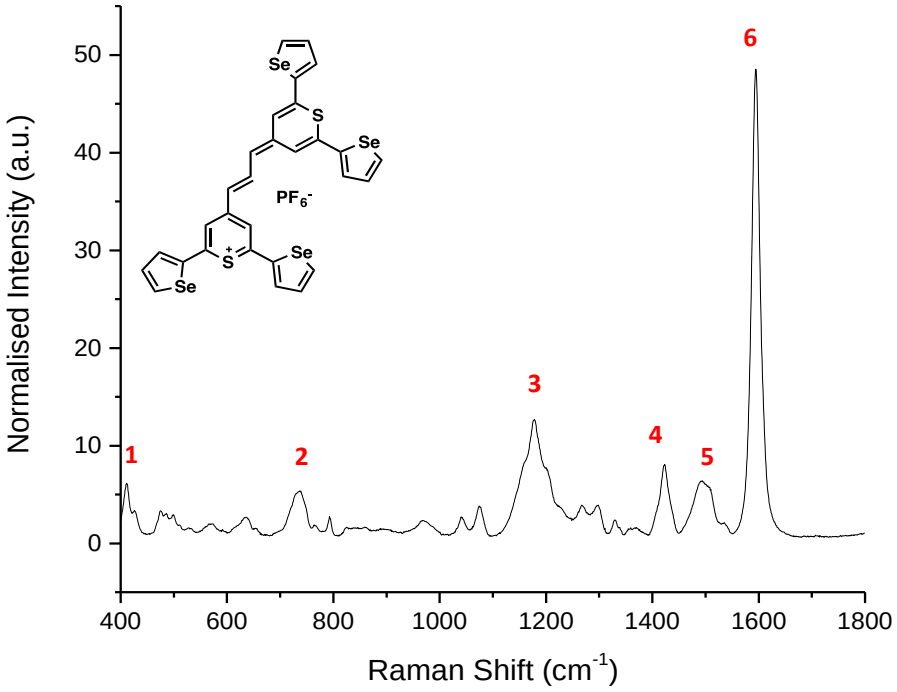

Figure 49: Representative SERS spectrum from dye 2 at 785 nm laser excitation with structure inset.

Table 5: SERS peaks from dye 2 at 785 nm excitation (numbers labelled in red correspond to the labelled peaks in Figure 4), and suggested spectral assignments.

Raman Shift (cm^{-1})	Spectral Assignment
(1) 411	C-C, C-H and C-S stretch in S rings, bridge C=C, C-H rocking
(2) 737	S ring breathing mode C-S, C-C and C-H; extended to Se rings C-Se, C-C, C-H
(3) 1179	Bridge C=C, C-H with extension to Se rings C-Se, C-C and C-H
(4) 1423	S and Se ring vibrations C-S, C-Se, C-C and C-H
(5) 1494	C-C, C-H, C-S and C-Se vibrations from thiopyran and selenophene rings, bridge C=C, C-H
(6) 1594	C-C, C-H, C-S and C-Se vibrations from thiopyran and selenophene rings

Appendix 2

Publication

- "Functionalisation of hollow gold nanospheres for use as stable, red-shifted SERS nanotags", **S. Moreton**, K. Faulds, N. C. Shand, M. A. Bedics, M. R. Detty and D. Graham, *Nanoscale*, 2015, **7**, 6075-6082

Conference Presentations

- "Stabilisation of Hollow Gold Nanospheres for use in Biomedical Applications", **S. Moreton**, K. Faulds, N. C. Shand, M. A. Bedics, M. R. Detty and D. Graham, SCIX Conference, September 2014, Reno, Nevada, USA

- "Synthesis and Surface Functionalisation of Hollow Gold Nanospheres", **S. Moreton**, K. Faulds, N. C. Shand, D. Graham, University of Strathclyde Inorganic Section Meeting, June 2013, West Brewery